Studying the Synthesis and Reactivity of Crystalline Materials using *In Situ* X-ray Diffraction

Saul Joseph Moorhouse

A thesis submitted in part fulfilment of the requirements for the degree of Doctor of Philosophy at the University of Oxford

Somerville College

Oxford

June 2013

The work described in this thesis was undertaken in the Chemistry Research Laboratory, Mansfield Road, Oxford, from October 2009 to June 2013 under the supervision of Professor Dermot O'Hare. All the work described is my own unless stated to the contrary, and has not been submitted for any degree at this or any other university.

Saul Joseph Moorhouse

June 2013

Abstract

Studying the Synthesis and Reactivity of Crystalline Materials using *In Situ* X-ray Diffraction

Saul J. Moorhouse — Somerville College
D.Phil Thesis — Trinity Term 2013

The use of *in situ* X-ray diffraction (XRD) to investigate reactions involving crystalline materials is the focus of the work described in this thesis. The development of procedures for probing chemical reactions *in situ*, and the application of this technique for studying in detail the mechanisms and kinetics of solid-state processes, is reported.

The information in **Chapter One** provides a background to the *in situ* study of chemical reactions, with specific emphasis on the application of X-ray diffraction. Three distinct families of inorganic materials are introduced, including layered double hydroxides, Aurivillius phases, and metal-organic frameworks, and the relevance of each in contemporary technologies, is discussed.

Chapter Two incorporates an account of the design, construction, and development of a chemical reaction furnace, the Oxford-Diamond *In Situ* Cell (ODISC), for the *in situ* study of solid-state reactions. The capabilities of this apparatus are discussed, including the efficient and controlled heating of samples to temperatures in excess of 1000 °C, optional sample stirring, and successful incorporation of a range of different sample vessels. Details of the implementation and optimisation of this equipment for use at Beamline I12 at the Diamond Light Source are provided.

The synthesis and characterisation of a new series of ternary layered double hydroxides (LDHs) with general formula $[M_xM'_{2-x}Al_8(OH)_{24}](NO_3)_4{\cdot}yH_2O$ (M, M' = Zn, Ni or Co), is detailed in **Chapter 3**. It was discovered that these materials exhibit finely tuneable cation ratios in the intralayer regions. A study of the intercalation chemistry of this family is reported, including *in situ* energy-dispersive and angular-dispersive X-ray diffraction experiments. The chapter concludes with details of an *in situ* XRD investigation into the synthesis of these materials *via* direct reaction of metal salts with $Al(OH)_3$, which was observed to proceed in four stages.

Chapter Four is concerned with the molten salt synthesis and characterisation of novel cation-doped compounds with the Aurivillius structure. The limited extent of substitution on the B-sites of the parent $Bi_5Ti_3FeO_{15}$ material was observed to be highly dependent on the nature of the di- or tri-valent substituent. The impact of varying reaction conditions, such as dwell duration and nature of the molten salt, upon pure product formation is described. A comprehensive *in situ* XRD investigation into the molten salt synthesis of a novel doped Aurivillius phase is detailed in **Chapter Five**. A discussion of the synthesis mechanism, in addition to a description of the role of the molten salt in product formation, is provided.

A brief *in situ* XRD study of the mechanism and kinetics of crystallisation of metal-organic frameworks (MOFs) is detailed in **Chapter Six**. The use of ion-exchanged polymer resin beads to direct the synthesis of MOFs is probed in real time, and the route to formation is compared to that for the conventional solvothermal technique.

Experimental procedures pertaining to all of the above chapters are provided in **Chapter Seven**. Supplementary data are included in the **Appendices**.

Acknowledgements

I would like to thank Professor Dermot O'Hare for his support and guidance throughout my time in his research group. Working under his supervision has been a great experience. Thank-you also to Dr. Michael Drakopoulos, my second supervisor, for the assistance and advice when out at Diamond and his encouragement for me to showcase my work.

I must express my warmest gratitude to Dr. Gareth Williams who has helped me enormously along the way. Not only for his supervision when I joined the group, but for the useful discussions about chemistry throughout, his help with analysis techniques, and for his company in the darkest of beamtimes. I am also very thankful to Dr. Andrew Jupe, who has given up much of his time to help with XRD data analysis. Also, to the both of them for help proof reading this thesis, thank-you.

Thank-you to the staff of Diamond Light Source. The support of Thomas Connelly, Christina Reinhard, Leigh Connor, Michael Hart, Bob Humphreys, Stuart Gurney, Ulrik Pederson, Andy Foster, and Fajin Juan, was outstanding during the most stressful of times. Also, to Michelle Warren for helping with numerous beamtime proposals in the early days. In addition, thank-you to the staff at Hasylab in Hamburg, namely Joern Donges and Andre Rothkirch, for help during beamtime out there. I spent the loneliest times of my life under that staircase next to Beamline F3, but nevertheless, it was emotional to see the back of DESY.

I am indebted to all the staff of the University of Oxford who came together with the aim of producing ODISC. Thank-you to Nenad Vranješ and Paul Smith in the University of Oxford Electronics Design and Fabrication Facility for the construction of the ODISC furnace controller. I appreciate the work Nen set aside to help with this project; he was forever able to accommodate my ever-evolving requirements. Likewise, to Charlie Evans in the PTCL Workshop for his considerable help with constructing the components of ODISC. To Terri Adams in the ICL Glassblowing workshop for advice on materials for ODISC and also for last-minute (always) manipulation of glassware before beamtime. To Paul Bircher and Mike Tacon in the Department of Physics for help in the early days in pulling the old furnaces back from the dead. Many thanks also to Richard Makin in the Thin Films Facility at the University of Oxford for the gold-coating of ODISC.

Thank-you to the many other staff at the University of Oxford whose help has enabled my DPhil to progress so smoothly. Dr. Norman Charnley in the Department of Earth Sciences for teaching me how to use the SEM machine, and for being such a nice chap. To Dr. Phil Wiseman for work behind the scenes in keeping both diffractometers and magnetometers up and running. A special thank-you to the ladies of the ICL Reception: Pam, Trish, Shirley, and Hazel, without whose day-to-day efficiency things would have been difficult for me.

Thank-you to those who have helped with the science at some point along the way. To Fabio for help with TGA, Dr. Andrew Fogg for assistance at DESY, Dr. Andrew Goodwin for helpful diffraction discussions, and Dr. Jonathan Burley for the peak-fitting routines. I am indebted to Miss Hannah Buckley for all of her help and intelligent thoughts, as well as her friendship.

I must thank all of my colleagues, the members of the O'Hare group for their support both academically and socially in the last four years. Dr. Robert Cooper for providing all manner of welcome distractions, Mr. Mark Chadwick, for being an amazing housemate and because our morning coffees were so often the highlight of my day, Miss Anchalee Wongariyakawee for being a great person and a great chemist, Mr. Henry Fisher for always making me feel like I'm working hard, Miss Sam Binding and Mr. Tom Arnold for both of their support, particularly in the last few months. Thanks also to Mark and Sam for guiding my brief foray into crystallography. Thanks to the original solid-staters, Dr. Charles Markland and Dr. Chengle Wang, for being excellent DPhils to look up to, and to Joyce for running TEM. Thank you to Dr. JC Buffet and Dr. Zoë Turner for their very helpful advice in the latter stages of my DPhil. An extra thank-you to all of those who gave their time to proof-read this thesis, you are so kind. Thanks additionally to the O'Hare group members gone-by, who have made this group the very best: Shuangde, Andy, Qiang, Ian, Hasna, and all the rest.

To those in the outside world who have made the last few years a truly pleasurable experience, I offer you my most heartfelt thanks. To Mr. Timothy Rooney for being a considerate and fun person to live with, and a very good friend. To the rest of the Catz crowd, Mr. and Mrs. Shenton, Mr. Woolley, Mr. Burfoot, Mr. Hindle, and Mr. Charles, for your friendship and keeping me sane. In particular, thank-you to Russell for regularly sharing with me the highs and lows of a life in research, albeit from a distance. Thank-you to my home crowd, specifically Tom, Greg and Patrick, because a get-together means living the dream. Thanks especially to Sam and Jane, for being good family, and for giving me a date to aim for.

I must certainly extend my thanks to Professor Peter Battle, Professor John Foord, and Dr. Jim Thomson for their tutoring in my days as a Catz undergraduate. Peter, in particular, kick-started my fondness for solids. I owe a lot to Dr. Mike Hayward, my undergraduate Part II supervisor, without whom I would not have been inspired to embark on this journey of research. I must also thank Mike for setting me up at Somerville. Thank-you to Professor Penny Handford for giving me the opportunity to teach undergraduate chemistry during my graduate years. Thanks to both Dr. Edward Dixon and Dr. David Williamson for their advice to me as an undergraduate a long time ago, but also more recently in the planning of my future.

Thank you to the EPSRC and Diamond Light Source for the provision of funding, and also to Somerville College not just for accepting me as a member, but for making me a scholar.

Most importantly, thank-you Ceri. It has not been easy, but you have made the difficult bits less difficult and I could not have done this without you. Thank-you most of all to my parents, Bryn and Lynda. Your support has mattered the most since the very beginning and you have guided me every step of the way.

This thesis is dedicated to my parents, and to Ceri – for whom the next chapter is reserved.

Abbreviations

1D	One-dimensional
1,4-BDC	1,4-benzenedicarboxylate
2D	Two-dimensional
3D	Three-dimensional
a.u.	Arbitrary units
DEF	Diethylformamide
DMF	Dimethylformamide
E	Energy
EA	Elemental analysis
EDX	Energy-dispersive X-ray spectroscopy
EDXRD	Energy dispersive X-ray diffraction
Et	Ethyl
FWHM	Full width at half maximum
GSAS	General Structure Analysis System
IR	Infrared
ID	Inner diameter
JEEP	Joint Engineering, Environmental, and Processing beamline
LDH	Layered double hydroxide
LED	Light-emitting diode
$M_xM'_{2-x}Al_8$-NO_3	$[M_xM'_{2-x}Al_8(OH)_{24}](NO_3)_4{\cdot}yH_2O$
M	mol L^{-1}
Me	Methyl
MOF	Metal-organic framework
MSS	Molten salt synthesis
n	Reaction exponent
NDC	2,6-naphthalenedicarboxylate
NMR	Nuclear magnetic resonance
OD	Outside diameter
ODISC	Oxford-Diamond *In Situ* Cell
PBT	Polybutylene terephthalate
PID	Proportional, Integral, Derivative
PTFE	Polytetrafluoroethylene
SAXS	Small angle X-ray scattering
SEM	Scanning electron microscopy
SQUID	Superconducting quantum interference device
t	Time
TEM	Transmission electron microscopy
T	Temperature
TGA	Thermogravimetric analysis
XRD	X-ray diffraction

Contents

Chapter 1: Introduction

1.1 Synthesising inorganic solids

In general, the preferred synthesis route towards many functional inorganic solids is the high-temperature 'ceramic' method, which involves heating mixtures of solid reagents to elevated temperatures, often in excess of 1000 °C. Due to slow diffusion of the ions in the solid starting materials, extended annealing times and multiple regrinding steps are typically required with this technique. Comparatively little control over the nature of the products is possible under ceramic synthesis conditions due to the thermodynamic driving force at elevated temperatures. Recently, emphasis has been placed on the discovery and improvement of alternatives to the ceramic method for the formation of extended solids. Techniques such as co-precipitation, sol-gel synthesis, hydrothermal synthesis, and molten salt synthesis have been investigated.

A deeper knowledge of some well-established synthesis techniques has led to their wider application in the preparation of functional solids. Low-temperature soft chemical ('*chimie douce*') methods, such as solvothermal synthesis, are now being applied as a route to known perovskite materials and their related oxides.[1] Alternatives to the high-temperature ceramic route can facilitate subtle control over particle size and morphology, ultimately facilitating the optimisation of product properties for a specific application.[2] However, the main obstacle towards the ultimate synthetic 'design' of new materials using such techniques, is the lack of detailed understanding of the complex processes occurring during their formation.

Three synthetic routes to crystalline solids that are relevant to the work discussed in this thesis are introduced in the ensuing sections.

1.1.1 Intercalation

Intercalation refers to the process of incorporating guest species into a one-, two-, or three-dimensional lattice without significant structural reorganisation of the host.[3] The position adopted by the guest in the intercalation product is predetermined by the structure of the host material. The earliest reports of intercalation in chemistry focussed on reactions involving graphite,[4] which have since been extended to the formation of

C_8K, a material that is applicable in organic synthesis.[5] More recently, this type of chemical reaction has been harnessed to facilitate efficient separation of anionic isomers.[6, 7]

Owing to the breaking of comparatively weak bonds which often exist between host and guest, intercalation reactions can occur with very little energetic input, and tend to be undertaken at ambient temperatures. The structures of the starting materials and products are usually closely related due to the topotactic nature of the reaction process. However, in many cases the physical properties of the product material are somewhat different to those of the precursor. Very recently, intercalation reactions involving layered selenides have resulted in profound enhancement of the superconducting properties of the product relative to the host material.[8]

1.1.2 Molten salt synthesis

The molten salt synthesis (MSS) method involves mixing stoichiometric amounts of starting material oxides with an excess of solid salt at room temperature and heating the mixture above the melting point of the salt. Synthesising materials *via* the molten salt, or 'flux growth', method, can involve the use of a high-temperature melt as a reaction 'solvent'. Simple inorganic compounds, or combinations of such, are most commonly used as solvent fluxes. Examples include metal nitrates, sulphates, halides, and carbonates, bismuth oxide, lead oxide, and lead fluoride.[9-12] Molten salts are often preferable to other solvents as they can be resistant to destruction by vigorous reactions, can dissolve high concentrations of various materials, and can accommodate reactions that are adversely affected by water.

The implementation of molten salt synthesis over the ceramic method has several advantages. Reactions are undertaken with significantly greater time and energy efficiency, because reduced temperatures are facilitated by the flux melting point and shorter reaction durations are possible due to greater reagent mobility.[13, 14] The dissolution and reprecipitation processes resulting from the presence of molten salt enable the use of cheaper, lower purity reagents than those required for solid-solid reactions. The preferred attributes of molten fluxes for the synthesis of quaternary oxides are discussed in a recent review by Bugaris and zur Loye.[15] They include: (a) a comparatively low melting point, (b) a high capacity for reagent dissolution, (c) a propensity for facile

removal following formation of the products and cooling, (d) an aversion for side reactions with the starting materials or reaction vessel, (e) a low volatility, and (f) a low cost.

A range of crystalline materials have been successfully prepared using molten salt synthesis, including zeolites,[16, 17] perovskites,[18-20] and binary metal oxides.[21, 22] One of the most widely-investigated advantages of the molten salt method is the ability to regulate the morphology of product particles.[23] The technique has also been applied to facilitate the fine-tuning of magnetic properties of materials.[24] A thorough investigation by Zhou and co-workers detailed the effects of a systematic variation in molten salt synthesis conditions, such as the amount and nature of the salt, upon the purity, morphology, and size of $BaZrO_3$ perovskite particles.[19] They found that reliable morphological control could be achieved through varying the annealing time. However, solubility and reactivity effects associated with different salts were found to significantly impact on the success of pure product formation.

Various reaction mechanisms have been postulated for different molten salt systems. Hedden *et al*. identified the presence of a reactive intermediate in the formation of $RTaO_4$ (R = Gd, Y, Lu), which forms through initial reaction with a Li_2SO_4 flux.[25] Additionally, Geselbracht *et al.* determined that interaction between K_2CO_3 starting material and an RbCl flux was crucial in the synthesis reaction of $RbCa_2Nb_3O_{10}$.[26] However, it still remains unclear in many cases whether MSS occurs *via* dissolution-reprecipitation or rather by interactions on solid surfaces that are mediated by the flux.

1.1.3 Solvothermal synthesis

The hydrothermal technique involves synthesis of crystalline materials in sealed vessels, using water as a solvent and at temperatures above the boiling point of the water. Under such elevated temperatures and pressures, the physical properties of water are different to those experienced under room temperature conditions. As a result, features such as the considerable reduction in H_2O viscosity are said to facilitate an increase in the mobility, and hence reactivity, of reagents in solution.

The term ‘solvothermal’ is used to describe the wider family of homogeneous and heterogeneous reactions in which any solvent, including water, is heated above room

temperature in a sealed vessel at a pressure greater than 1 bar. Examples of solvothermal synthesis and its many advantages are discussed in separate reviews by Demazeau and Walton.[27, 28] Owing to the great number of synthetic parameters associated with a solvothermal reaction, the predictive preparation and design of desired materials is still a major challenge using this technique. Indeed, formation of a variety of materials *via* one-pot syntheses involving identical reagents is not uncommon.[29, 30] It is therefore of high importance that the mechanisms of such chemical processes are probed thoroughly, with a view to controlling and then optimising the formation of new compounds for industrial and commercial use. An emphasis should additionally be placed on the elucidation of kinetic information, such as the contribution from diffusion, nucleation, and growth to crystallisation, as well as the activation energy of the process.

In recent years, *in situ* X-ray diffraction has risen to prominence as an excellent probe for the examination of solvothermal processes.[31, 32] The crystallisation mechanisms of various titanate materials have been probed in-depth using EDXRD.[33] Croker *et al.* observed that successful synthesis of $CaTiO_3$, as well as the rate of product formation, is dependent upon the use of $CaCO_3$ or hydrogarnet as the source of Ca.[34] *In situ* neutron diffraction techniques have also been employed to monitor the dissolution-precipitation mechanism of $BaTiO_3$ formation.[35, 36] Kinetic information about crystallisation reactions undertaken in autoclaves can be obtained through the application of mathematical models to the *in situ* data.[37] Michailovski and co-workers determined, through the use of a combination of X-ray absorption spectroscopy and EDXRD techniques, that the solvothermal growth of MoO_3 fibers occurs *via* a dissolution-precipitation mechanism.[38] *In situ* EDXRD is also very useful for the observation of intermediate phases in solvothermal reactions. McIntyre *et al.* discovered that hydrothermal synthesis of the 3D framework structure, $Yb_4O(OH)_9NO_3$, occurs *via* two sequential intermediates: the 2D layered compounds, $Yb_2(OH)_5NO_3{\cdot}2H_2O$ and $Yb_2(OH)_5NO_3{\cdot}H_2O$.[39]

1.2 Monitoring chemical reactions in the solid-state

The term '*in situ*' is a Latin phrase which translates literally to mean 'in position'. In chemistry, the term refers to an occurrence 'within the reaction mixture', which can be either a chemical process or a method of probing that mixture. On the contrary, *ex situ* refers specifically to processes undertaken on the mixture when it is no longer reacting.

Various methods of monitoring the crystallisation of solids *in situ* were discussed in a recent review by Pienack and Bensch.[40] This section is focussed specifically on solid-state *in situ* probes.

1.2.1 Non-invasive in situ *probes*

When studying reactions in real-time, it is important that the method of investigation does not interfere with the progress of the reaction. Data from *ex situ* quenching experiments can often be unrepresentative of the reaction medium due to the disruptive impact of the quenching process and its propensity to influence structural and chemical characteristics of the system being studied. In contrast to *ex situ* methods, non-invasive *in situ* probes facilitate the detection and subsequent monitoring of any transient intermediate phases present during reaction, including their conversion to the final product. An important advantage of using *in situ* over *ex situ* techniques is the vastly greater amount of data obtained throughout the course of a chemical reaction, with considerably less labour required. As a result of these factors, novel, non-invasive, *in situ* probes are sought.

An in-depth understanding of the complexities of formation of crystalline materials is still in the early stages of development. Several elegant non-invasive methods have been employed to facilitate the *in situ* study of solid-state reactions,[41] such as small-angle X-ray scattering (SAXS),[42] X-ray absorption fine structure (XAFS),[43] Raman,[44] NMR,[45] neutron diffraction,[46] and X-ray diffraction (XRD).[47] It is important to recognise that monitoring the behaviour of amorphous phases *in situ*, using techniques such as X-ray diffraction, can provide valuable complimentary information to that obtained purely from crystalline solids.[48] Data acquired from such investigations are crucial for improving our understanding of the kinetics and mechanisms by which transformations in chemistry proceed.

It must be emphasised that *in situ* methods are not without their limitations. In order for reactions to be probed under non-ambient conditions, custom-designed reactor cells are often necessary, with specific requirements depending on the sample environment and the technique itself (discussed further in Chapter 2). In the case of XRD measurements, very dense materials may degrade the data because of their X-ray absorbance, and for some

phases, particularly with low-symmetry crystal structures, there may be significant detection limits.

1.2.2 In situ *X-ray diffraction*

Energy-dispersive X-ray diffraction (EDXRD) is an appropriate technique for the non-invasive study of a range of chemical reactions involving crystalline materials.[49, 50] The diffraction properties of high energy, polychromatic, 'white beam' X-rays generated from synchrotron sources are well suited for *in situ* studies of bulk chemical systems. The total photon flux across this energy range is extremely high. State-of-the-art EDXRD detectors, positioned at fixed angle (2θ) to the diffracted beam, enable data collection across a wide range of q values ($q = 2\pi/d$) to be undertaken simultaneously and rapidly. High quality data acquisition is therefore possible on the timescale of seconds, which is suitable for *in situ* measurements. Furthermore, the high energy X-rays and large photon flux permit penetration of dense materials and large sample volumes. Diffraction using this technique occurs from a 'lozenge'-shaped gauge volume, which is defined by the 2θ angle and the collimation geometry.[51] The principal disadvantage of EDXRD is the low data resolution owing, in part, to the large sample volume and poor energy-resolution of existing solid-state detectors. This has prevented application of advanced analysis techniques to EDXRD data, such as detailed structure refinement.

More recently, the availability of high energy, single-wavelength X-rays in conjunction with high-speed area detectors, has facilitated time-resolved studies using angular-dispersive XRD.[52] Data collection on the millisecond scale is now possible due to the emergence of novel detector systems, including both 'flat-panel' and 'rotating-arm' designs. The resolution of data measured using this technique is considerably greater than that obtained from EDXRD studies, thus facilitating structure refinement. Until recently, the main disadvantage of the angular-dispersive technique was the lower flux of the monochromatic beam, which hindered penetration of thick-walled sample vessels and large sample volumes. However, facilities such as Beamline I12 at the Diamond Light Source now enable high-flux, angular-dispersive diffraction at far higher energies ($\geq$ 53 keV) than were previously available. In addition to the exceptional data resolution, a considerably greater d-spacing range is also accessible due to the absence of any fixed-2θ constraints experienced with EDXRD. A disadvantage of angular-dispersive

diffraction is the detection of Bragg reflections from the sample vessel and equipment due to the absence of a predefined gauge volume with this configuration.

A considerable limitation of the *in situ* X-ray diffraction technique is the requirement for synchrotron radiation. Whilst high-temperature X-ray diffraction (HTXRD) studies are now possible using laboratory diffractometers, this method often does not facilitate monitoring of reactions on a representative scale or under standard laboratory conditions. Access to facilities which enable *in situ* XRD studies requires the submission and acceptance of a beamtime proposal, a process which is usually highly competitive. If successful, the resulting time allowance for *in situ* XRD studies at Diamond Light Source, for instance, is typically no more than three days per six month allocation period. Application of both energy-dispersive and angular-dispersive X-ray diffraction in the study of chemical reactions using Beamline I12 is discussed in greater detail throughout the following chapters, in addition to the following section.

1.2.3 Beamline I12 at the Diamond Light Source

Beamline I12 is a multi-purpose facility at the Diamond Light Source. The high intensity, high energy beam of X-rays available at this facility can be harnessed for imaging/tomography, X-ray diffraction, and small angle X-ray scattering (SAXS) experiments. The beam is provided by a superconducting multi-pole wiggler which is positioned in the storage ring. Beamline I12 is otherwise known as the Joint Engineering, Environmental and Processing Beamline (JEEP), which emphasises its wide applicability for studies across a broad spectrum of physical sciences.

This beamline produces a continuous spectrum of X-rays in the region $50 \leq E \,/\, \text{keV} \leq 150$. In energy-dispersive mode, reacting samples are irradiated with a continuous series of X-rays with energies across this entire range. The photon flux at 50 keV is *ca.* 1.8×10^{12} photons.s^{-1}. Following interaction with the sample, the diffracted X-ray beam passes through two post-sample collimator slits and onto the detector. A 23-element Ge energy-dispersive detector is used to record diffraction data from the polychromatic beam throughout a chemical reaction. The radial 'take-off' angle, 2θ, for each element of the detector is 5°. In addition, Beamline I12 offers the use of a Thales Pixium RF4343 detector for angular-dispersive studies. This flat-panel detector hardware, in combination with a custom-designed high-energy monochromator, allows angular

dispersive diffraction using X-rays of a specified energy, with $E \geq 53$ keV. The Pixium detector-sample distance can be adjusted in conjunction with the beam energy to optimise the observable *d*-spacing region.

1.3 Layered metal hydroxides

1.3.1 Aluminium hydroxide

Naturally occurring aluminium hydroxide, $Al(OH)_3$, has four structural variants: gibbsite,[53] bayerite,[54, 55] nordstrandite,[56] and doyleite.[57] The general structure of this material is based upon lamellae of edge-sharing AlO_6 octahedra, which interact *via* hydrogen bonding. Al atoms are ordered in two thirds of the octahedral sites within each layer (Figure 1.1).

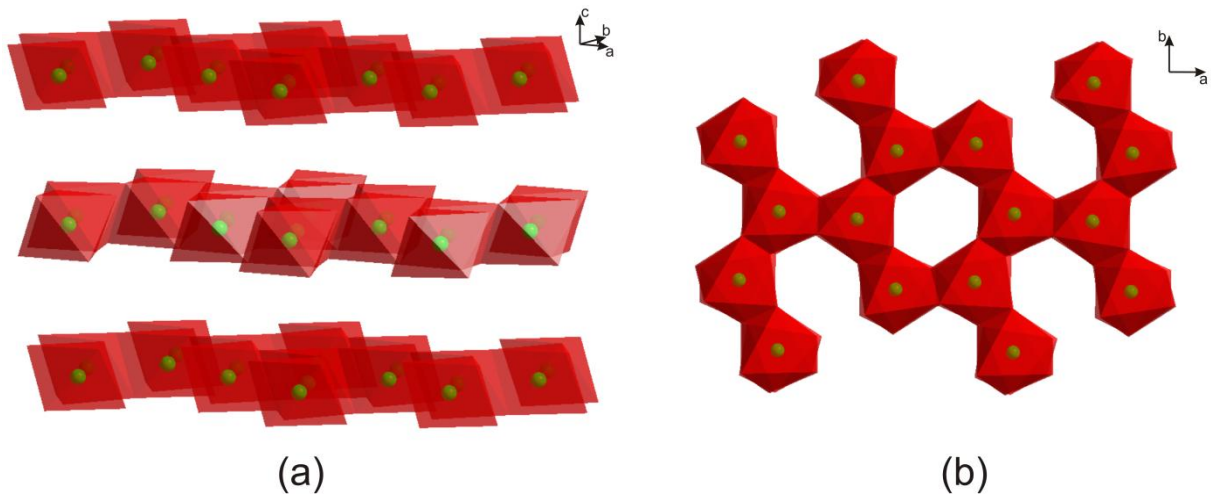

Figure 1.1: Structure of the gibbsite polymorph of $Al(OH)_3$ including (a) layer stacking and (b) view parallel to the *c*-axis. Al atoms are shown in green and O_6 octahedra in red. H atoms have been omitted for clarity.

The different polymorphs of $Al(OH)_3$ exhibit a similar layer structure, but each has a unique stacking sequence of those layers. Gibbsite has an *aba* stacking sequence, in contrast to bayerite which exhibits *aa* stacking (Figure 1.2). This feature is important when discussing the intercalation chemistry of the aluminium hydroxide variants.

When subject to direct reaction with lithium salts (LiX), $Al(OH)_3$ undergoes topotactic 'imbibition' of both Li^+ and X^- ions. The cations become incorporated into the octahedral holes within the layers, and the anions reside between the layers alongside co-intercalated water molecules. Reaction of lithium salts with different $Al(OH)_3$ polymorphs results in LDHs with different layer-stacking sequences. The use of gibbsite produces layered double hydroxides with pseudo-hexagonal symmetry (a two-layer *aba* stacking sequence),[58] whilst reaction with the bayerite and nordstrandite polymorphs has been shown to form the pseudo-rhombohedral (three-layer *abca* stacking) alternative.[59, 60] Britto *et al.* have also suggested such systems may undergo slight structural distortion resulting in monoclinic symmetry.[61]

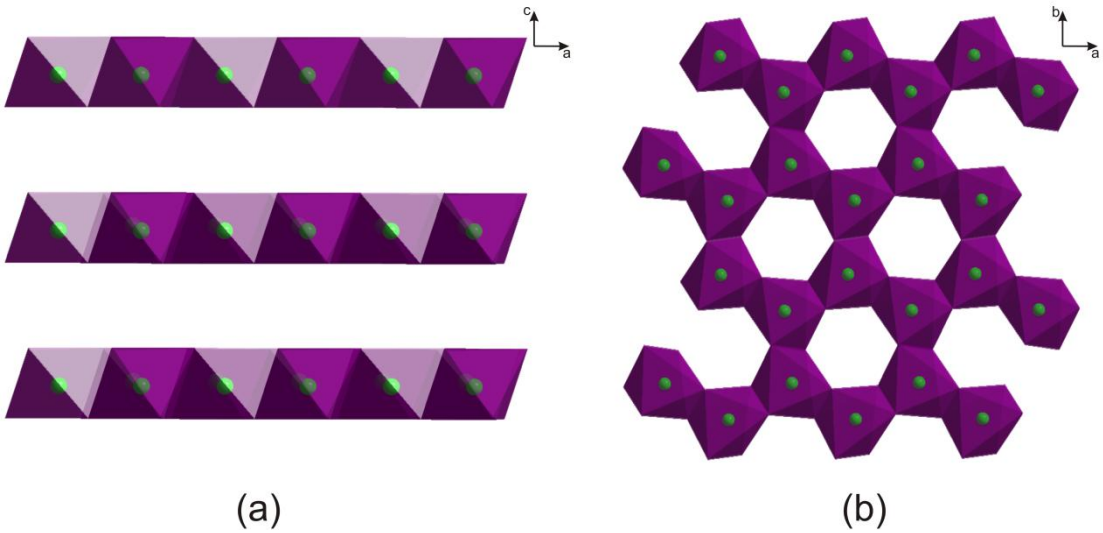

Figure 1.2: Structure of the bayerite polymorph of $Al(OH)_3$, including (a) layer stacking and (b) view parallel to the *c*-axis. Al atoms are shown in green and O_6 octahedra in purple. H atoms have been omitted for clarity.

More recently, incorporation of transition metal nitrate salts into the gibbsite structure has been reported, but the reaction only proceeds following pre-activation of the solid $Al(OH)_3$ precursor through ball-milling. The resulting product materials feature M^{2+} ions in only half the octahedral holes in the layers,[62] and are described in more detail in Chapter 3.

1.3.2 Layered Double Hydroxides

Layered double hydroxides (LDH) are an extensive family of both naturally occurring and synthetic, layered inorganic materials. Knowledge of their chemistry dates back to 1915, when the chemical formula of naturally occurring hydrotalcite,

$Mg_6Al_2(OH)_{16}{\cdot}4H_2O$, was correctly reported by Manasse.[63] The first comprehensive structure analyses of layered hydroxide minerals were undertaken over 50 years later using single crystal X-ray diffraction (XRD).[64-67] LDHs are now the most widely investigated metal hydroxide compounds.

The structure of an LDH, an example of which is shown in Figure 1.3, is based upon that of the brucite mineral, $Mg(OH)_2$ (which exhibits a CdI_2 structure type). $Mg(OH)_2$ comprises infinite sheets of edge-sharing MgO_6 octahedra, which are linked by hydrogen bonding between the layers. The LDH structure can be derived from brucite by substitution of a fraction of the Mg^{2+} ions for M^{3+} ions in the octahedral holes between alternate pairs of OH planes. In this way, the layers acquire a net positive charge, which is balanced by the intercalation of anions between the layers. It is a feature of most LDHs that water molecules also co-intercalate alongside the anions between the layers.[68, 69]

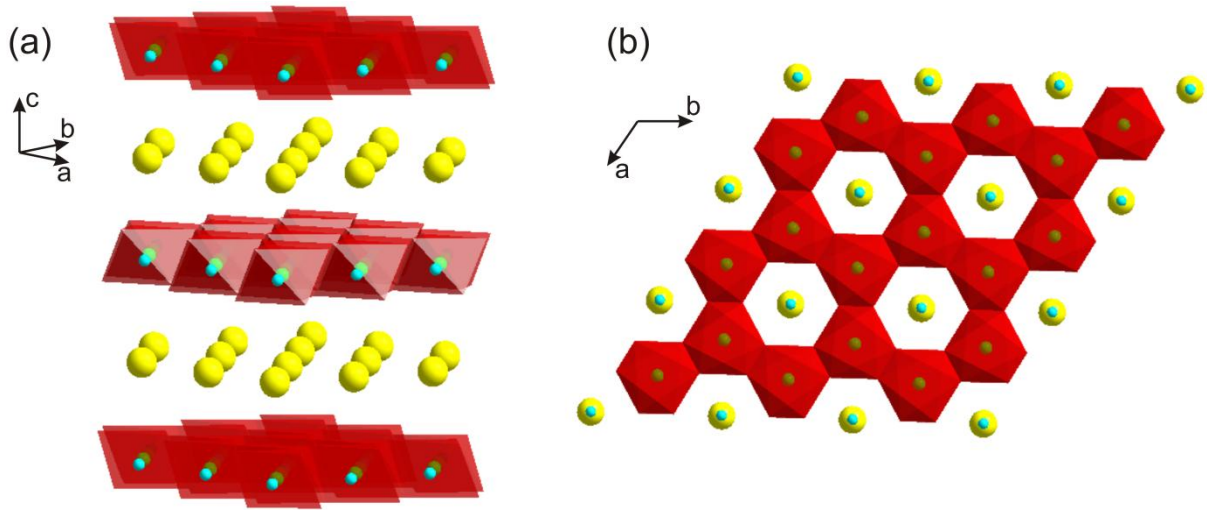

Figure 1.3: Structure of the $[LiAl_2(OH)_6]Cl{\cdot}yH_2O$ LDH,[58] including (a) layer stacking and (b) view parallel to the *c*-axis. ● represents Li^+ cations, ● represents Al^{3+} cations, ● represents interlayer Cl^- anions, and MO_6 octahedra are coloured red. H atoms and interlayer water molecules have been omitted for clarity.

The majority of hydrotalcite-like LDH compounds can be described by the general formula $[M^{2+}_{1-x}M^{3+}_x(OH)_2]^{a+}(X^{n-})_{a/n}{\cdot}yH_2O$, where M^{2+} ions are commonly Mg^{2+}, Ca^{2+}, Mn^{2+}, Fe^{2+}, Co^{2+}, Ni^{2+}, Zn^{2+}, and M^{3+} ions can be Al^{3+}, Cr^{3+}, Mn^{3+}, Fe^{3+}, Co^{3+}, Ni^{3+}, or Ga^{3+}. Pure LDHs have been formed in the range $0.2 \leq x \leq 0.33$, but additional reports suggest that a wider range of metal ratios within the LDH layers is possible, including $0.1 \leq x \leq 0.5$. The limits of x are governed by the proximity of M^{3+} to one another within the layers. Recently, a series of LDHs with unusual chemical formula,

$[MAl_4(OH)_{12}](NO_3)_2{\cdot}yH_2O$ (M = Co, Ni, Cu, Zn), have been synthesised and their reactivity probed.[62, 70, 71] Synthesis of these materials *via* hydrothermal reaction of activated $Al(OH)_3$ gibbsite with highly-concentrated solutions of metal nitrates, results in incorporation of M^{2+} ions in only half of the octahedral holes in the LDH layers (Figure 1.4).

It is important to note that several LDH species exist that cannot be described by the above formula. Many ternary LDHs, containing mixtures of greater than one type of M^{2+} or M^{3+} ion within the layers, have been prepared.[72] Even examples of quaternary systems have been reported.[73] The substitution of some M^{4+} for M^{3+} cations in ternary LDH materials have been reported, including Ti^{4+}, Zr^{4+}, and Sn^{4+}.[74-77] In addition to LDHs containing M^{II-IV} ions, the $[LiAl_2(OH)_6]X{\cdot}yH_2O$ materials, which contain Li^+ and Al^{3+} in the intralayer interstices, have been the subject of considerable investigation.[58, 78, 79] Due to the difference in size and charge of the two cations, ordering is observed within the layers of these '$LiAl_2$-X' systems. The route to synthesis of $LiAl_2$-X LDHs was described in the previous section.

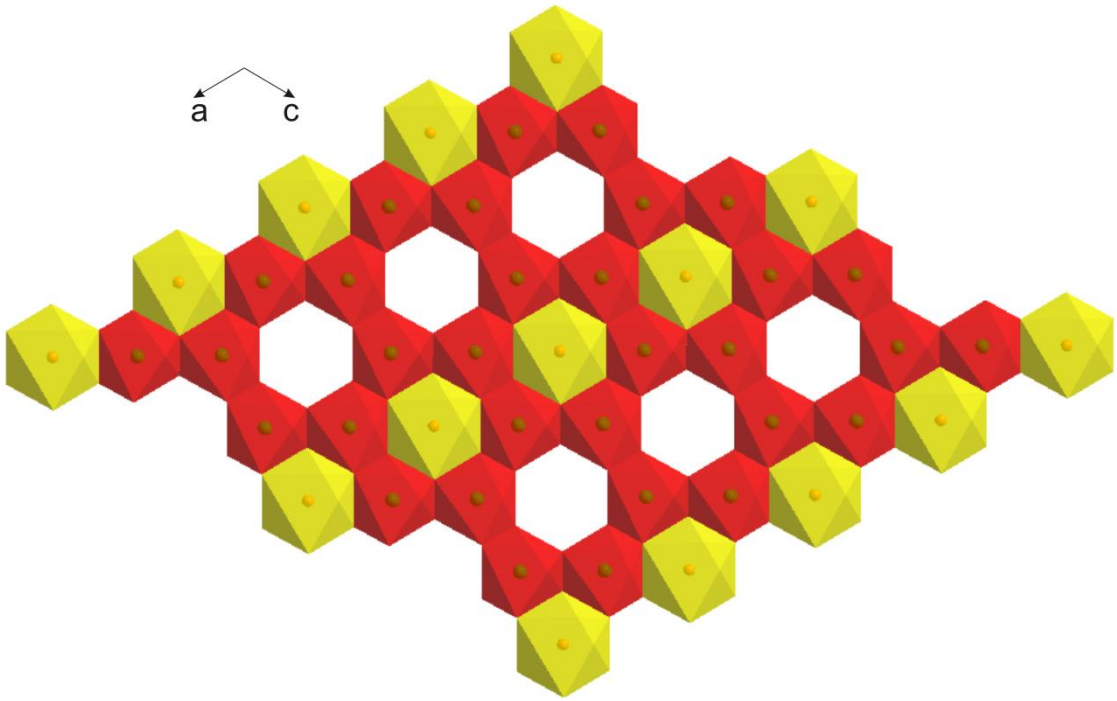

Figure 1.4: Idealised structure of the cation-ordered $[ZnAl_4(OH)_{12}](NO_3)_2{\cdot}yH_2O$ LDH,[62] showing one layer viewed parallel to the *b*-axis. ● represents Al cations within red AlO_6 octahedra and ● represents Zn cations within yellow ZnO_6 octahedra.

Preparation of LDHs has been achieved using a broad spectrum of chemical techniques. The most commonly applied method is simple coprecipitation from solution.[80] This one-pot, direct synthesis approach involves combining mixtures of the relevant metal salts under pH control and has two main variants. Performing at so-called 'low-supersaturation' requires simultaneous addition of metal salts and base to an aqueous solution of the desired interlayer anion,[81-83] whereas at 'high-supersaturation', the mixture of metals salts are added to a basic solution containing the anions at a slow and steady rate.[84-86] Synthesis *via* coprecipitation generally leads to products of higher crystallinity as the rate of crystal growth is greater than the rate of nucleation. Homogeneous precipitation using the urea hydrolysis method is an alternative to coprecipitation, whereby the *in situ* hydrolysis reaction to give ammonia and hydrogen carbonate maintains the pH of the reaction at *ca.* 9.[87, 88] Product crystallisation from solution tends to form hexagonal platelets.[89] In addition to these and the direct intercalation method detailed in Section 1.1.1, synthesis of LDHs has also been undertaken using the reconstruction method,[90, 91] the salt-oxide method,[92, 93] and hydrothermal reaction.[94]

The intercalation chemistry of LDHs is vast and varied.[95, 96] The facile and reversible substitution of interlayer anions has enabled the incorporation of a broad range of interesting and technologically relevant anionic species into the structure of these layered inorganic hosts.[97-99] In part due to the high ion-exchange capacities of LDHs, many applications of them are known, including in catalysis,[100, 101] polymer science,[102, 103] and separation science.[71, 104]

1.3.3 In situ *XRD studies*

In situ EDXRD as a tool for monitoring the interesting intercalation reactivity of metal hydroxides has been discussed in a number of reviews.[80, 105] The decline and growth of starting material and product reflections, in addition to those of crystalline intermediate phases, can be simultaneously, accurately, and non-invasively probed using this technique. As layered crystalline solids, metal hydroxides commonly exhibit several intense Bragg reflections in their X-ray diffraction patterns, making them highly suitable for *in situ* XRD studies.[106] The kinetics and mechanisms of chemical processes involving these materials are often highly unusual, and small changes to the reaction conditions can have a significant impact on the route to product formation.

Precipitation of both the gibbsite and bayerite forms of aluminium hydroxide from solution have been probed using EDXRD.[107] It was noted that they exhibited contrasting behaviour at elevated temperatures, but a transition between the two polymorphs was not observed. The reactivity of metal hydroxides has also been monitored *in situ*. The synthesis of $[LiAl_2(OH)_6]X{\cdot}H_2O$ LDHs *via* the direct intercalation method with $Al(OH)_3$, described in the preceding sections, was studied by Fogg and O'Hare using *in situ* EDXRD.[108] The rate of direct conversion of the gibbsite starting material to the cation-ordered LDH product was found to be highly temperature-dependant.

Investigation into the reactivity of LDHs using time-resolved X-ray diffraction has been the focus of much attention in recent years. Examples of reaction intermediates and staging have been observed during *in situ* investigations of LDH intercalation reactions, and the kinetics of these processes have also been monitored.[104, 109-114] Comprehensive insight into the mechanisms of dehydration and thermal decomposition of LDHs and their layered analogues has been gained through the use of both laboratory and synchrotron X-ray diffraction facilities.[115-120]

1.4 Compounds with the Aurivillius structure

In the early 1950s, Bengt Aurivillius reported the first perovskite-like layered bismuth-containing solid oxides.[121-123] The subsequently-derived 'Aurivillius' family of layered oxides can be described by the general formula $[Bi_2O_2][A_{n-1}B_nO_{3n+1}]$, where A represents one or more bulky cations such as Bi^{3+}, Pb^{2+}, Ba^{2+}, Sr^{2+}, Ca^{2+}, K^+, and Na^+, and B corresponds to smaller cations that are well-suited to octahedral coordination, such as W^{6+}, Nb^{5+}, Zr^{4+}, Ti^{4+}, Fe^{3+}, Cr^{3+}, and Mn^{3+}.[124] The structure of a so-called 'Aurivillius phase' comprises regular intergrowths of fluorite-like $[Bi_2O_2]^{2+}$ layers and pseudo-perovskite $[A_{n-1}B_nO_{3n+1}]^{2-}$ blocks, where n corresponds to the number of sheets of corner-sharing BO_6 octahedra in the perovskite-like slab. Typically, n is an integer number in the range 1 – 4, although various homologous series with $n > 4$ have been reported, up to $n = 9$.[125] The annotated idealised structure of an $n = 2$ Aurivillius phase is provided in Figure 1.5.

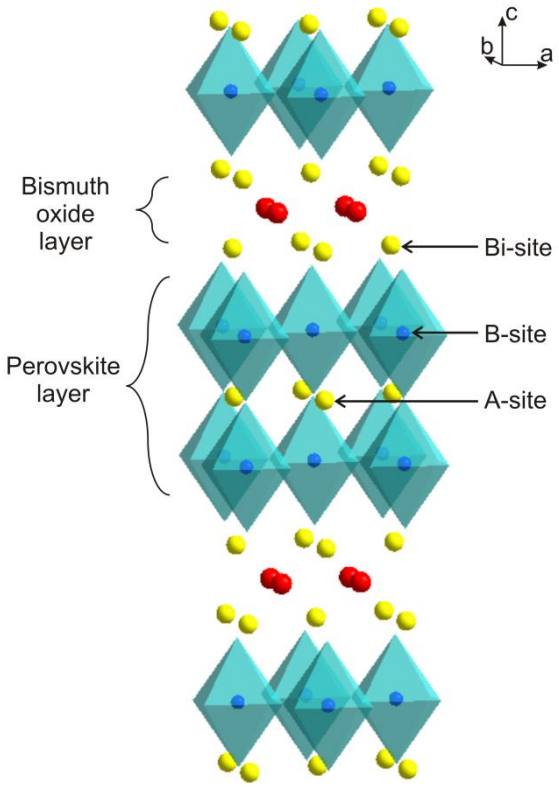

Figure 1.5: Unit cell for the n = 2 Aurivillius structure (e.g. Bi_3TiNbO_9) ● denotes Bi cations and perovskite-layer A-site cations, ● denotes O anions, and ● denotes B-site cations.

Recurrent intergrowth phases also exist in the Aurivillius family, which exhibit long-range ordered structures with alternating perovskite blocks of different n, separated by bismuth oxide layers (Figure 1.6).[126, 127] Such materials are often denoted with non-integer values of n, where most commonly n = 1.5, 2.5, and 3.5. Alternatively, these phases can be described by the general formula $Bi_4A_{(m+n)-2}B_{(m+n)}O_{3(m+n)+6}$, where $m = n \pm 1$. The preferential location of B-site cations in intergrowth layers of specific n has been reported by Sneddon *et al.*[128] High-resolution transmission electron microscopy (HRTEM) has been adopted as a powerful tool not only for confirming the existence of, but observing the relationship between, different perovskite layers in recurrent intergrowth structures.[129] The remarkable comprehensive ordering of intergrowth layers in Aurivillius phases has been explained by the long-range repulsive interactions arising from elastic forces that exist throughout the structure.[130, 131]

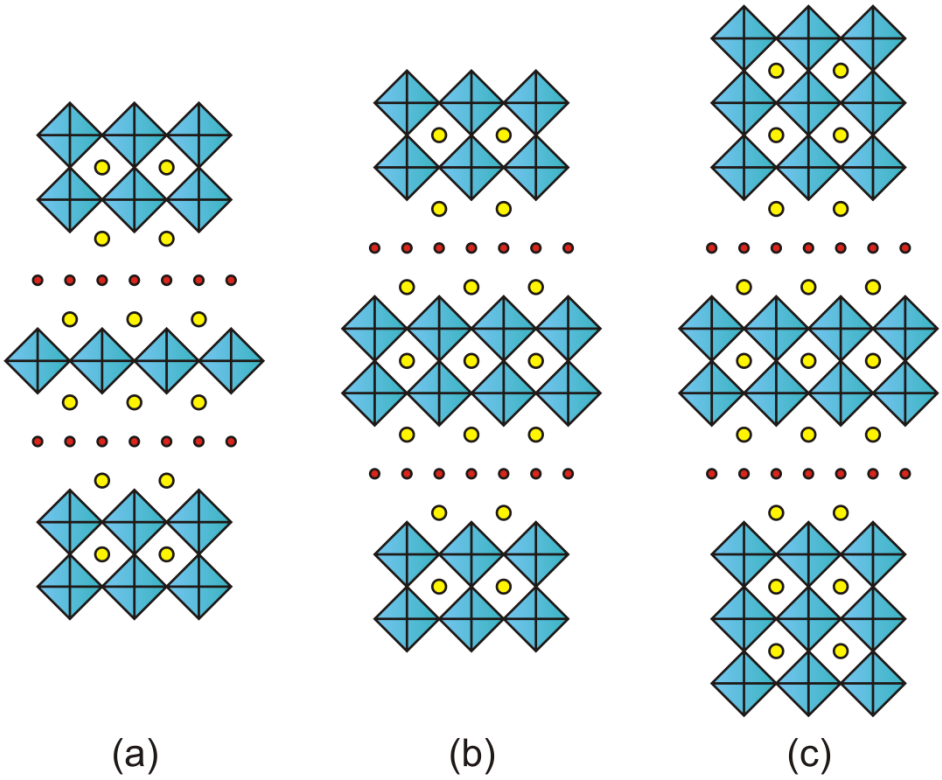

Figure 1.6: Schematic illustration of the structures of three members of the Aurivillius family, including (a) n = 1/2 recurrent intergrowth phase, (b) n = 2 phase, and (c) n = 2/3 recurrent intergrowth phase. ● denotes Bi cations and perovskite-layer A-site cations, ● denotes O anions.

At room temperature, compounds in the Aurivillius family can be tetragonal, or close to tetragonal with slight orthorhombic distortion. In the case of distorted structures, octahedral rotations in the perovskite layers lead to a doubling of the *ab* plane with respect to the tetragonal polytype, resulting in the lattice parameter relationship: $a_{orth} \approx b_{orth} \approx \sqrt{2}a_{tet} \approx 5.4$ Å. The *c*-parameter of the unit cell correlates linearly with variation in *n*. Displacement of B-site cations, to an 'off-centre' position within their coordination octahedra, results in an ionic polarisation and corresponding lowering of crystal symmetry as the octahedral coordination becomes irregular. The symmetries of Aurivillius compounds with odd or even *n* are described by different orthorhombic space groups (*Aba*2 or $A2_1am$, respectively), owing to the in-phase or out-of-phase octahedral rotations about the *c*-axis. It has been reported that orthorhombic distortion in Aurivillius phases is highly dependent upon the radii of cations residing on the perovskite layer A-sites, as well as on the B-sites.[132]

1.4.1 Synthetic routes to Aurivillius phase formation

A broad spectrum of synthetic techniques has been employed to facilitate the formation of Aurivillius compounds. Due to low reagent homogeneity and slow ionic diffusion, conventional solid-state reaction (referred to as the 'ceramic method') is often undertaken at temperatures in excess of 1000 °C and can involve multiple regrinding and pelletizing steps.[133] Use of the Bi_2O_3 reagent, which is volatile at high temperatures, to synthesise Aurivillius phases under such conditions can lead to compositional changes, impurity formation, or defects in the Bi_2O_2 layers. Alternative routes to the ceramic method for synthesis of compounds with the Aurivillius structure are therefore continually being sought. The properties of the resulting materials can be highly dependent upon the synthesis method employed.[134]

The 2008 report by Kong *et al.* provides an excellent summary of the mechanochemical route towards pure-phase formation of compounds with the Aurivillius structure.[135] Mechanochemical activation to form an amorphous Aurivillius product, followed by subsequent calcination, is an appropriate variation on this technique.[136-138] Synthesis of A-site substituted Aurivillius phases has been reported using a 'soft chemical' route.[139] Pure phases with the $n = 4$ structure were formed following precipitation of nitrates onto the surface of TiO_2 particles, however this procedure still required calcination steps undertaken at 750 °C and 950 °C. Alternatively, hydrothermal synthesis of Aurivillius compounds facilitates one-step product formation at temperatures below 250 °C.[140, 141] Sardar and Walton have reported the synthesis of $Bi_4Ti_3O_{12}$ using $NaBiO_3{\cdot}2H_2O$ reagent as a reactive source of Bi^{5+}.[30] Sol-gel and coprecipitation methods have also been applied.[142-145]

Molten salt synthesis (MSS) is a comparatively newer technique than the sol-gel and ceramic methods, and, as a result, it has been much less extensively applied and explained. Few examples of Aurivillius phase synthesis that employ this method have been published.[146-149] Existing examples are discussed in more detail in Chapter 4.

1.4.2 Properties and applications of compounds with the Aurivillius structure

The physical properties exhibited by this layered bismuth family of solid-oxide compounds have been extensively investigated. Initial interest in these materials focussed

on their suitability as lead-free ferroelectrics.[133, 150, 151] The structural basis for ferroelectricity in the bismuth titanate family was discussed by Newnham *et al.*; the main polarisation vector is observed parallel to the *a*-axis, but there is also a small component in the *c*-direction.[152] Withers *et al.* in 1991,[153] and Frit and Mercurio in 1992,[154] reported that the principal structural drive towards ferroelectricity in these compounds originates from displacement of the Bi atoms residing on the perovskite A-sites, and not *via* octahedral off-centring of the B-site cations. It has subsequently been demonstrated that substitution of cations onto the A-sites of the Aurivillius structure results in significant variation of the ferroelectric properties.[155] As a consequence of this interesting behaviour, ferroelectric materials of the Aurivillius family are currently being widely studied for potential uses in non-volatile memory: the use of $SrBi_2Ta_2O_9$ thin films as dynamic random access memories (DRAMs) has been summarised by Scott.[156]

Several reports also detail the propensity for the use of bismuth titanate based layered compounds as high-temperature piezoelectrics.[157, 158] The A-site doped $n = 4$ Aurivillius phase, $Na_{0.5}Bi_{4.5}Ti_4O_{15}$, exhibits excellent piezoelectric properties, a high resistivity, and a high Curie temperature (T_c > 600 °C).[159] This material is commercially available and has been used in accelerometers at temperatures up to 400 °C.[160] Systematic substitution of Ba cations onto the perovskite A-sites of this material, however, leads to a gradual decrease in the ferroelectric to paraelectric phase transition, resulting from reduced structural distortion due to doping of the larger Ba ion.[161]

More recently, focus on the applications of Aurivillius phases has shifted towards their use as oxide ion conductors.[162] The $n = 1$ $Bi_2VO_{5.5}$ material exhibits intrinsic oxygen vacancies,[163, 164] and at elevated temperatures (> 570 °C) disorder of these vacancies in the perovskite layer results in high oxide ion conductivity.[165, 166] A range of metal ions (Me) has been doped for vanadium in this compound, resulting in the BIMEVOX family of doped Bi-V oxides.[167-170]

1.4.3 The $Bi_4Ti_3O_{12}$-$BiFeO_3$ system as a template for multiferroicity

Many forms of modern technology rely upon, and are ultimately derived from, the properties of magnetism and ferroelectricity, and materials that exhibit these features are therefore highly desirable. The simultaneous occurrence of ferromagnetism and

ferroelectricity in a single phase is rare,[171] and a coupling between the two properties, referred to as 'multiferroicity', is rarer still.[172] The reason for this scarcity is primarily due to the opposing origins of the two types of behaviour. Transition metal ions with partially filled *d*-orbitals are required for magnetic interactions, whereas the collective shift of cations within a structure resulting in electric polarisation, is induced by the movement of electrons between oxygen *p*-orbitals and transition metal empty *d*-orbitals. As a result, an additional driving force such as a structural distortion, is required for ferromagnetism and ferroelectricity to coexist.[173]

Aurivillius phases are excellent candidates for multiferroic behaviour. The majority exhibit ferroelectricity due to off-site displacement of A-site and d^0 B-site cations. Accordingly, if suitable substitution of transition metals with partially-filled *d*-orbitals onto the B-sites were to result in strong magnetic interactions, it is entirely possible the two properties could become coupled. The structural, magnetic, and dielectric properties of compounds in the $Bi_4Ti_3O_{12}$-$BiFeO_3$ Aurivillius system ($n = 3 – 9$) therefore, with d^0 and d^n cations on the B-sites, have been the subject of extensive scrutiny.[125, 174-178] The $n = 4$ member of this series, $Bi_5Ti_3FeO_{15}$, has been under particular investigation,[179] and reports indicate that it exhibits a co-existence of ferroelectricity and weak ferromagnetism.[180] B-site doped analogues of the $n = 4$ phase are therefore currently being sought, some existing examples of which are discussed in the introduction to Chapter 4.

1.5 Metal-organic frameworks

In general, metal-organic frameworks (MOFs) are materials that are composed of inorganic clusters interconnected by rigid polydentate organic moieties to produce an ordered porous framework.[181, 182] This family of materials has been the subject of significant and increasing investigation in recent years. The potential industrial applications of MOFs are extensive,[183] and they are currently being investigated for use as hydrogen storage materials,[184-187] as shape selective catalysts,[188] in drug delivery,[189] and in carbon dioxide capture and storage.[190] The importance of the interesting magnetic behaviour exhibited in several MOFs, in particular those containing cobalt centres, has been highlighted by Kurmoo.[191]

Scientific focus on the synthesis and characterisation of new metal-organic frameworks has increased considerably over the last two decades.[192] A vast number and range of synthetic routes towards MOF formation are now available to the modern chemist.[181] These include solvothermal, microwave-assisted, vapour-diffusion, mechanochemical and electrochemical synthesis methods.[193] A variation on the solvothermal technique, termed the 'resin-assisted' method, has also been employed as a route to MOF formation,[194, 195] and is discussed in greater detail in Chapter 6. Successful attempts to improve the speed and scale of MOF synthesis have also recently been reported.[196] However, despite our ever-improving knowledge of the functionality of organic bridging ligands as well as the preferable coordination environments of inorganic metal centres, the synthesis and interconversion of frameworks with various topologies is still very much exploratory. Understanding and influencing the relationship between fundamental factors influencing MOF formation, in addition to the crucial kinetics of their crystallisation, is at the heart of research into this important family of materials. *In situ* probes are extremely valuable for determining the interactions between related framework species during synthesis, as well as the precise kinetics of their crystallisation and the specific conditions under which certain materials form preferentially over others.

There exist several difficulties associated with probing solvothermal syntheses in real time: the reactions are often undertaken in thick-walled steel autoclaves at elevated temperatures, the reagents and products can be present in low concentrations, and the reactions can take up to several days to reach completion. Only a relatively small number of *in situ* EDXRD experiments have been undertaken on solvothermal MOF crystallisation reactions. In 2011, Ahnfeldt *et al.*[197] highlighted the only existing examples of EDXRD MOF crystallisation studies as those probing the formation of Fe-MIL-53, MOF-14, and HKUST-1.[198, 199] In the latter study by Millange and co-workers, the kinetics of HKUST-1 formation were successfully analysed using a model that separates nucleation and growth into two discrete terms, which yielded important information about the crystallisation of this material. Within the last two years, several further *in situ* studies into the formation mechanisms and kinetics of various metal-organic frameworks have been reported, using both XRD and light-scattering techniques.[200-206]

1.6 Aims of this thesis

The principal aim of the work described in this thesis was to facilitate the study of a broad spectrum of solid-state chemical processes using *in situ* X-ray diffraction, through the design and construction of a multifunctional chemical reaction furnace. A proportion of the funding and scientific support for this research was provided by the Diamond Light Source, the UK's national synchrotron, specifically for studies using the high-energy X-ray Beamline, I12.

Following construction and commissioning of the new equipment, the focus was then to demonstrate the capabilities of the apparatus for studying a varied range of chemical reactions involving crystalline materials, in addition to showcasing the wide-applicability of the *in situ* X-ray diffraction technique on Beamline I12. The ultimate target, succeeding furnace construction, was to make available this equipment to the wider scientific community and to continue the development of the apparatus based on the requirements of the users.

Three fields of inorganic chemistry were initially selected for study: the synthesis and intercalation reactivity of layered double hydroxides, the molten salt synthesis of compounds with the Aurivillius structure, and the resin-assisted crystallisation of metal-organic frameworks. These areas were chosen firstly with the intention of understanding more comprehensively their interesting, and occasionally poorly understood, chemistries. An *in situ* exploration of the route to product formation was undertaken in each case to gain an insight into the kinetics and mechanisms of these processes. Not only was the reactivity of these materials vastly different, but the contrasting requirements for their study using X-ray diffraction, such as the observable range of relevant *d*-spacings from Bragg diffraction, enabled the extensive capabilities of Beamline I12 to be demonstrated. Additionally, the range of chemical environments required to undertake such reactions represented those most widely applied in the field of solid-state. Throughout this research, emphasis was placed upon improving, adapting, and diversifying *in situ* XRD data analysis to yield new and important information about the processes being studied.

1.7 References

1. D. R. Modeshia and R. I. Walton, *Chemical Society Reviews*, 2010, **39**, 4303-4325.
2. X. Yang, I. D. Williams, J. Chen, J. Wang, H. Xu, H. Konishi, Y. Pan, C. Liang and M. Wu, *Journal of Materials Chemistry*, 2008, **18**, 3543-3546.
3. J. Aleman, A. V. Chadwick, J. He, M. Hess, K. Horie, R. G. Jones, P. Kratochvil, I. Meisel, I. Mita, G. Moad, S. Penczek and R. F. T. Stepto, *Pure and Applied Chemistry*, 2007, **79**, 1801-1827.
4. K. Fredenhagen and G. Cadenbach, *Z. Anorg. Allg. Chem.*, 1926, **158**, 259.
5. D. Savoia, C. Trombini and A. Umanironchi, *Pure and Applied Chemistry*, 1985, **57**, 1887-1896.
6. L. X. Lei, F. Millange, R. I. Walton and D. O'Hare, *Journal of Materials Chemistry*, 2000, **10**, 1881-1886.
7. F. Millange, R. I. Walton, L. X. Lei and D. O'Hare, *Chemistry of Materials*, 2000, **12**, 1990-1994.
8. M. Burrard-Lucas, D. G. Free, S. J. Sedlmaier, J. D. Wright, S. J. Cassidy, Y. Hara, A. J. Corkett, T. Lancaster, P. J. Baker, S. J. Blundell and S. J. Clarke, *Nature Materials*, 2013, **12**, 15-19.
9. P. Afanasiev and C. Geantet, *Coordination Chemistry Reviews*, 1998, **178**, 1725-1752.
10. J. Yang, R. S. Li, J. Y. Zhou, X. C. Li, Y. M. Zhang, Y. L. Long and Y. W. Li, *Journal of Alloys and Compounds*, 2010, **508**, 301-308.
11. T. Kojima, K. Nomura, Y. Miyazaki and K. Tanimoto, *Journal of the American Ceramic Society*, 2006, **89**, 3610-3616.
12. D. G. Porob and P. A. Maggard, *Journal of Solid State Chemistry*, 2006, **179**, 1727-1732.
13. M. J. Geselbracht, L. D. Noailles, L. T. Ngo, J. H. Pikul, R. I. Walton, E. S. Cowell, F. Millange and D. O'Hare, *Chemistry of Materials*, 2004, **16**, 1153-1159.
14. C. Mao, G. Wang, X. Dong, Z. Zhou and Y. Zhang, *Materials Chemistry and Physics*, 2007, **106**, 164-167.
15. D. E. Bugaris and H.-C. zur Loye, *Angewandte Chemie-International Edition*, 2012, **51**, 3780-3811.
16. M. Park, C. L. Choi, W. T. Lim, M. C. Kim, J. Choi and N. H. Heo, *Microporous and Mesoporous Materials*, 2000, **37**, 81-89.
17. M. Park, C. L. Choi, W. T. Lim, M. C. Kim, J. Choi and N. H. Heo, *Microporous and Mesoporous Materials*, 2000, **37**, 91-98.
18. M. Thirumal, P. Jain and A. K. Ganguli, *Materials Chemistry and Physics*, 2001, **70**, 7-11.
19. H. Zhou, Y. Mao and S. S. Wong, *Chemistry of Materials*, 2007, **19**, 5238-5249.
20. S. Gopalan, K. Mehta and A. V. Virkar, *Journal of Materials Research*, 1996, **11**, 1863-1865.
21. Y.-Z. Zheng and M.-L. Zhang, *Materials Letters*, 2007, **61**, 3967-3969.
22. B. Roy, S. P. Ahrenkiel and P. A. Fuierer, *Journal of the American Ceramic Society*, 2008, **91**, 2455-2463.
23. B. Brahmaroutu, G. L. Messing and S. Trolier-McKinstry, *Journal of the American Ceramic Society*, 1999, **82**, 1565-1568.
24. R. H. Arendt, *Journal of Solid State Chemistry*, 1973, **8**, 339-347.
25. D. B. Hedden, C. C. Torardi and W. Zegarski, *J. Solid State Chem.*, 1995, **118**, 419-421.
26. M. J. Geselbracht, R. I. Walton, E. S. Cowell, F. Millange and D. O'Hare, *Chem. Mat.*, 2002, **14**, 4343-4349.
27. R. I. Walton, *Chemical Society Reviews*, 2002, **31**, 230-238.

28. G. Demazeau, *Journal of Materials Chemistry*, 1999, **9**, 15-18.
29. J. X. Chen, *Chemistry Letters*, 2011, **40**, 886-887.
30. K. Sardar and R. I. Walton, *Journal of Solid State Chemistry*, 2012, **189**, 32-37.
31. J. Murray, L. Kirwan, M. Loan and B. K. Hodnett, *Hydrometallurgy*, 2009, **95**, 239-246.
32. M. Feyand, C. Naether, A. Rothkirch and N. Stock, *Inorganic Chemistry*, 2010, **49**, 11158-11163.
33. A. Laumann, K. M. O. Jensen, C. Tyrsted, M. Bremholm, K. T. Fehr, M. Holzapfel and B. B. Iversen, *European Journal of Inorganic Chemistry*, 2011, 2221-2226.
34. D. Croker, M. Loan and B. K. Hodnett, *Crystal Growth & Design*, 2009, **9**,2207-2213.
35. R. I. Walton, R. I. Smith, F. Millange, I. J. Clark, D. C. Sinclair and D. O'Hare, *Chemical Communications*, 2000, 1267-1268.
36. R. I. Walton, F. Millange, R. I. Smith, T. C. Hansen and D. O'Hare, *Journal of the American Chemical Society*, 2001, **123**, 12547-12555.
37. Y. Zhou, E. Antonova, W. Bensch and G. R. Patzke, *Nanoscale*, 2010, **2**, 2412-2417.
38. A. Michailovski, J. D. Grunwaldt, A. Baiker, R. Kiebach, W. Bensch and G. R. Patzke, *Angewandte Chemie-International Edition*, 2005, **44**, 5643-5647.
39. L. J. McIntyre, T. J. Prior and A. M. Fogg, *Chemistry of Materials*, 2010, **22**, 2635-2645.
40. N. Pienack and W. Bensch, *Angewandte Chemie-International Edition*, 2011, **50**, 2014-2034.
41. R. I. Walton and D. O'Hare, *Chemical Communications*, 2000, 2283-2291.
42. D. Grandjean, A. M. Beale, A. V. Petukhov and B. M. Weckhuysen, *Journal of the American Chemical Society*, 2005, **127**, 14454-14465.
43. R. Le Toquin, W. Paulus, A. Cousson, C. Prestipino and C. Lamberti, *Journal of the American Chemical Society*, 2006, **128**, 13161-13174.
44. E. Boccaleri, F. Carniato, G. Croce, D. Viterbo, W. van Beek, H. Emerich and M. Milanesio, *Journal of Applied Crystallography*, 2007, **40**, 684-693.
45. F. Taulelle, M. Haouas, C. Gerardin, C. Estournes, T. Loiseau and G. Ferey, *Colloids and Surfaces a-Physicochemical and Engineering Aspects*, 1999, **158**, 299-311.
46. G. R. Williams, A. J. Norquist and D. O'Hare, *Chemistry of Materials*, 2006, **18**, 3801-3807.
47. M. Morcrette, Y. Chabre, G. Vaughan, G. Amatucci, J. B. Leriche, S. Patoux, C. Masquelier and J. M. Tarascon, *Electrochimica Acta*, 2002, **47**, 3137-3149.
48. D. A. Keen, A. L. Goodwin, M. G. Tucker, J. A. Hriljac, T. D. Bennett, M. T. Dove, A. K. Kleppe, A. P. Jephcoat and M. Brunelli, *Physical Review B*, 2011, **83**, 064109.
49. M. R. Rowles, M. J. Styles, I. C. Madsen, N. V. Y. Scarlett, K. McGregor, D. P. Riley, G. A. Snook, A. J. Urban, T. Connolley and C. Reinhard, *Journal of Applied Crystallography*, 2012, **45**, 28-37.
50. J. Kikuma, M. Tsunashima, T. Ishikawa, S.-Y. Matsuno, A. Ogawa, K. Matsui and M. Sato, *Journal of the American Ceramic Society*, 2010, **93**, 2667-2674.
51. M. R. Rowles, *Journal of Synchrotron Radiation*, 2011, **18**, 938-941.
52. N. A. S. Webster, M. J. Loan, I. C. Madsen, R. B. Knott and J. A. Kimpton, *Hydrometallurgy*, 2011, **109**, 72-79.
53. H. Saalfeld and M. Wedde, *Zeitschrift Fur Kristallographie*, 1974, **139**.
54. Rothbaue.R, F. Zigan and H. Odaniel, *Zeitschrift Fur Kristallographie Kristallgeometrie Kristallphysik Kristallchemie*, 1967, **125**.
55. F. Zigan, W. Joswig and N. Burger, *Zeitschrift Fur Kristallographie*, 1978, **148**, 3-4.
56. H. J. Bosmans, *Acta Crystallographica Section B-Structural Crystallography and Crystal Chemistry*, 1970, **B 26**, 649.

57. G. Y. Chao, J. Baker, A. P. Sabina and A. C. Roberts, *Canadian Mineralogist*, 1985, **23**, 21-28.
58. A. V. Besserguenev, A. M. Fogg, R. J. Francis, S. J. Price, D. Ohare, V. P. Isupov and B. P. Tolochko, *Chemistry of Materials*, 1997, **9**, 241-247.
59. S. Britto and P. V. Kamath, *Inorganic Chemistry*, 2009, **48**, 11646-11654.
60. A. M. Fogg, A. J. Freij and G. M. Parkinson, *Chemistry of Materials*, 2002, **14**, 232-234.
61. S. Britto, G. S. Thomas, P. V. Kamath and S. Kannan, *Journal of Physical Chemistry C*, 2008, **112**, 9510-9515.
62. A. M. Fogg, G. R. Williams, R. Chester and D. O'Hare, *Journal of Materials Chemistry*, 2004, **14**, 2369-2371.
63. E. Manasse, *Nat. Proc. Verb.*, 1915, 92.
64. A. E. Moore and H. F. W. Taylor, *Acta Crystallographica Section B-Structural Crystallography and Crystal Chemistry*, 1970, **B 26**, 386-393.
65. H. F. W. Taylor, *Mineralogical Magazine*, 1969, **37**, 338-342.
66. H. F. W. Taylor, *Mineralogical Magazine*, 1973, **39**, 377-389.
67. R. Allmann, *Acta Crystallographica Section B-Structural Crystallography and Crystal Chemistry*, 1968, **B 24**, 972.
68. G. Marcelin, N. J. Stockhausen, J. F. M. Post and A. Schutz, *Journal of Physical Chemistry*, 1989, **93**, 4646-4650.
69. S. Miyata, *Clays and Clay Minerals*, 1975, **23**, 369-375.
70. G. R. Williams, T. G. Dunbar, A. J. Beer, A. M. Fogg and D. O'Hare, *Journal of Materials Chemistry*, 2006, **16**, 1222-1230.
71. G. R. Williams, T. G. Dunbar, A. J. Beer, A. M. Fogg and D. O'Hare, *Journal of Materials Chemistry*, 2006, **16**, 1231-1237.
72. F. Cavani, F. Trifiro and A. Vaccari, *Catalysis Today*, 1991, **11**, 173-301.
73. A. J. Marchi and C. R. Apesteguia, *Applied Clay Science*, 1998, **13**, 35-48.
74. S. Velu, V. Ramaswamy, A. Ramani, B. M. Chanda and S. Sivasanker, *Chemical Communications*, 1997, 2107-2108.
75. S. Velu, K. Suzuki, T. Osaki, F. Ohashi and S. Tomura, *Materials Research Bulletin*, 1999, **34**, 1707-1717.
76. S. Velu, K. Suzuki, M. Okazaki, T. Osaki, S. Tomura and F. Ohashi, *Chemistry of Materials*, 1999, **11**, 2163-2172.
77. N. Das and A. Samal, *Microporous and Mesoporous Materials*, 2004, **72**, 219-225.
78. K. R. Poeppelmeier and S. J. Hwu, *Inorganic Chemistry*, 1987, **26**, 3297-3302.
79. J. P. Thiel, C. K. Chiang and K. R. Poeppelmeier, *Chemistry of Materials*, 1993, **5**, 297-304
80. Evans. D.G. and Duan. X., *Layered Double Hydroxides*, Springer, 2006.
81. S. K. Yun and T. J. Pinnavaia, *Chemistry of Materials*, 1995, **7**, 348-354.
82. F. Prinetto, G. Ghiotti, P. Graffin and D. Tichit, *Microporous and Mesoporous Materials*, 2000, **39**, 229-247.
83. K. Klemkaite, I. Prosycevas, R. Taraskevicius, A. Khinsky and A. Kareiva, *Central European Journal of Chemistry*, 2011, **9**, 275-282
84. V. R. L. Constantino and T. J. Pinnavaia, *Inorganic Chemistry*, 1995, **34**, 883-892.
85. E. Gardner, K. M. Huntoon and T. J. Pinnavaia, *Advanced Materials*, 2001, **13**, 1263-1266.
86. S. Carlino and M. J. Hudson, *Journal of Materials Chemistry*, 1995, **5**, 1433-1442.
87. U. Costantino, F. Marmottini, M. Nocchetti and R. Vivani, *European Journal of Inorganic Chemistry*, 1998, 1439-1446.
88. J. M. Oh, S. H. Hwang and J. H. Choy, *Solid State Ionics*, 2002, **151**, 285-291.
89. M. Adachi-Pagano, C. Forano and J. P. Besse, *Journal of Materials Chemistry*, 2003, **13**, 1988-1993.

90. T. S. Stanimirova, G. Kirov and E. Dinolova, *Journal of Materials Science Letters*, 2001, **20**, 453-455.
91. K. L. Erickson, T. E. Bostrom and R. L. Frost, *Materials Letters*, 2005, **59**, 226-229.
92. L. Li, Q. S. Luo and X. Duan, *Journal of Materials Science Letters*, 2002, **21**, 439-441.
93. V. P. Isupov, L. E. Chupakhina and R. P. Mitrofanova, *Journal of Materials Synthesis and Processing*, 2000, **8**, 251-253.
94. M. Ogawa and S. Asai, *Chemistry of Materials*, 2000, **12**, 3253-3255.
95. A. I. Khan and D. O'Hare, *Journal of Materials Chemistry*, 2002, **12**, 3191-3198.
96. S. Carlino, *Solid State Ionics*, 1997, **98**, 73-84.
97. J. Twu and P. K. Dutta, *Chemistry of Materials*, 1992, **4**, 398-401.
98. S. Aisawa, S. Takahashi, W. Ogasawara, Y. Umetsu and E. Narita, *Journal of Solid State Chemistry*, 2001, **162**, 52-62.
99. T. Kwon, G. A. Tsigdinos and T. J. Pinnavaia, *Journal of the American Chemical Society*, 1988, **110**, 3653-3654.
100. A. Monzon, E. Romeo, C. Royo, R. Trujillano, F. M. Labajos and V. Rives, *Applied Catalysis a-General*, 1999, **185**, 53-63.
101. S. Abello, S. Dhir, G. Colet and J. Perez-Ramirez, *Applied Catalysis a-General*, 2007, **325**, 121-129.
102. C. Taviot-Gueho and F. Leroux, *Layered Double Hydroxides*, 2006, **119**, 121-159.
103. C. O. Oriakhi, I. V. Farr and M. M. Lerner, *Journal of Materials Chemistry*, 1996, **6**, 103-107.
104. A. M. Fogg, J. S. Dunn, S. G. Shyu, D. R. Cary and D. O'Hare, *Chemistry of Materials*, 1998, **10**, 351-355.
105. G. R. Williams and D. O'Hare, *Journal of Materials Chemistry*, 2006, **16**, 3065-3074.
106. N. A. S. Webster, I. C. Madsen, M. J. Loan, R. B. Knott, F. Naim, K. S. Wallwork and J. A. Kimpton, *Journal of Applied Crystallography*, 2010, **43**, 466-472.
107. J. S. C. Loh, A. M. Fogg, H. R. Watling, G. M. Parkinson and D. O'Hare, *Physical Chemistry Chemical Physics*, 2000, **2**, 3597-3604.
108. A. M. Fogg and D. O'Hare, *Chemistry of Materials*, 1999, **11**, 1822-1832.
109. Y. Zhang, H. Tan, J.-x. Zhao, X. Li, H. Ma, X. Chen and X. Yang, *Physical Chemistry Chemical Physics*, 2012, **14**,14238-14242.
110. G. R. Williams and D. O'Hare, *Chemistry of Materials*, 2005, **17**, 2632-2640.
111. C. Taviot-Gueho, Y. J. Feng, A. Faour and F. Leroux, *Dalton Transactions*, 2010, **39**, 5994-6005.
112. J. Pisson, C. Taviot-Gueho, Y. Israeli, F. Leroux, P. Munsch, J. P. Itie, V. Briois, N. Morel-Desrosiers and J. P. Besse, *Journal of Physical Chemistry B*, 2003, **107**, 9243-9248.
113. Y. J. Feng, G. R. Williams, F. Leroux, C. Taviot-Gueho and D. O'Hare, *Chemistry of Materials*, 2006, **18**, 4312-4318.
114. C. Taviot-Gueho, F. Leroux, C. Payen and J. P. Besse, *Applied Clay Science*, 2005, **28**, 111-120.
115. M. Wei, S. X. Shi, J. Wang, Y. Li and X. Duan, *Journal of Solid State Chemistry*, 2004, **177**,2534-2541.
116. J. H. Meng, H. Zhang, D. G. Evans and X. Duan, *Chinese Science Bulletin*, 2005, **50**, 2575-2581.
117. A. Piskova, P. Bezdicka, D. Hradil, E. Kafunkova, K. Lang, E. Vecernikova, F. Kovanda and T. Grygar, *Applied Clay Science*, 2010, **49**, 363-371.
118. H. J. Bray, S. A. T. Redfern and S. M. Clark, *Mineralogical Magazine*, 1998, **62**, 647-656.
119. W. L. Huang, W. A. Bassett and T. C. Wu, *American Mineralogist*, 1994, **79**, 683-691.

120. G. R. Williams, A. Clout and J. C. Burley, *Physical chemistry chemical physics : PCCP*, 2013, **15**, 8616-8628.
121. B. Aurivillius, *Arkiv for Kemi*, 1950, **1**, 463-480.
122. B. Aurivillius, *Arkiv for Kemi*, 1950, **1**, 499-512.
123. B. Aurivillius, *Arkiv for Kemi*, 1951, **2**, 519-527.
124. R. A. Armstrong and R. E. Newnham, *Materials Research Bulletin*, 1972, **7**, 1025-1034.
125. N. A. Lomanova, M. I. Morozov, V. L. Ugolkov and V. V. Gusarov, *Inorganic Materials*, 2006, **42**, 189-195.
126. C. N. R. Rao and J. M. Thomas, *Accounts of Chemical Research*, 1985, **18**, 113-119.
127. J. Gopalakrishnan, A. Ramanan, C. N. R. Rao, D. A. Jefferson and D. J. Smith, *Journal of Solid State Chemistry*, 1984, **55**, 101-105.
128. A. Snedden, D. O. Charkin, V. A. Dolgikh and P. Lightfoot, *Journal of Solid State Chemistry*, 2005, **178**, 180-184.
129. J. L. Hutchison, J. S. Anderson and C. N. R. Rao, *Proceedings of the Royal Society of London Series a-Mathematical Physical and Engineering Sciences*, 1977, **355**, 301-312.
130. T. Kikuchi, *Materials Research Bulletin*, 1979, **14**, 1561-1569.
131. D. A. Jefferson, M. K. Uppal, C. N. R. Rao and D. J. Smith, *Materials Research Bulletin*, 1984, **19**, 1403-1409.
132. S. M. Blake, M. J. Falconer, M. McCreedy and P. Lightfoot, *Journal of Materials Chemistry*, 1997, **7**, 1609-1613.
133. E. C. Subbarao, *Physical Review*, 1961, **122**, 804-807.
134. Z. Lazarevic, B. D. Stojanovic and J. A. Varela, *Science of Sintering*, 2005, **37**, 199-216.
135. L. B. Kong, T. S. Zhang, J. Ma and F. Boey, *Progress in Materials Science*, 2008, **53**, 207-322.
136. A. Castro, P. Millan, L. Pardo and B. Jimenez, *Journal of Materials Chemistry*, 1999, **9**, 1313-1317.
137. L. Pardo, A. Castro, P. Millan, C. Alemany, R. Jimenez and B. Jimenez, *Acta Materialia*, 2000, **48**, 2421-2428.
138. J. Ricote, L. Pardo, A. Castro and P. Millan, *Journal of Solid State Chemistry*, 2001, **160**, 54-61.
139. S. K. Rout, E. Sinha, A. Hussian, J. S. Lee, C. W. Ahn, I. W. Kim and S. I. Woo, *Journal of Applied Physics*, 2009, **105**, 024105.
140. Y. H. Shi, S. H. Feng and C. S. Cao, *Materials Letters*, 2000, **44**, 215-218.
141. Y. H. Shi, C. S. Cao and S. H. Feng, *Materials Letters*, 2000, **46**, 270-273.
142. P. C. Joshi, A. Mansingh, M. N. Kamalasanan and S. Chandra, *Applied Physics Letters*, 1991, **59**, 2389-2390.
143. P. C. Joshi and S. B. Krupanidhi, *Journal of Applied Physics*, 1992, **72**, 5827-5833.
144. Y. M. Kan, X. H. Jin, P. L. Wang, Y. X. Li and Y. B. Cheng, *Journal of Inorganic Materials*, 2002, **17**, 51-55.
145. X. W. Dong, K. F. Wang, J. G. Wan, J. S. Zhu and J. M. Liu, *Journal of Applied Physics*, 2008, **103**, 4.
146. D. G. Porob and P. A. Maggard, *Materials Research Bulletin*, 2006, **41**, 1513-1519.
147. L. Fuentes, M. Garcia, D. Bueno, M. E. Fuentes and A. Munoz, *Ferroelectrics*, 2006, **336**, 81-89.
148. M. Garcia-Guaderrama, L. Fuentes, M. E. Montero-Cabrera, A. Marquez-Lucero and M. E. Villafuerte-Castrejon, *Integrated Ferroelectrics*, 2005, **71**, 233-239.
149. Zulhadjri, B. Prijamboedi, A. A. Nugroho, N. Mufti, A. Fajar, T. T. M. Palstra and Ismunandar, *Journal of Solid State Chemistry*, 2011, **184**, 1318-1323.
150. E. C. Subbarao, *Journal of Physics and Chemistry of Solids*, 1962, **23**, 665-676.

151. E. C. Subbarao, *Journal of Chemical Physics*, 1961, **34**, 695.
152. R. E. Newnham, R. W. Wolfe and J. F. Dorrian, *Materials Research Bulletin*, 1971, **6**, 1029-1039.
153. R. L. Withers, J. G. Thompson and A. D. Rae, *Journal of Solid State Chemistry*, 1991, **94**, 404-417.
154. B. Frit and J. P. Mercurio, *Journal of Alloys and Compounds*, 1992, **188**, 27-35.
155. P. Duran-Martin, A. Castro, P. Millan and B. Jimenez, *Journal of Materials Research*, 1998, **13**, 2565-2571.
156. J. F. Scott, *Annual Review of Materials Science*, 1998, **28**, 79-100.
157. A. Moure, A. Castro and L. Pardo, *Progress in Solid State Chemistry*, 2009, **37**, 15-39.
158. M. D. Maeder, D. Damjanovic and N. Setter, *Journal of Electroceramics*, 2004, **13**, 385-392.
159. R. C. Turner, P. A. Fuierer, R. E. Newnham and T. R. Shrout, *Applied Acoustics*, 1994, **41**, 299-324.
160. P. A. Angleton, Ceramic transducer elements and accelerometers, 1967.
161. D. Ben Jannet, M. El Maaoui and J. P. Mercurio, *Journal of Electroceramics*, 2003, **11**, 101-106.
162. K. R. Kendall, C. Navas, J. K. Thomas and H. C. zurLoye, *Chemistry of Materials*, 1996, **8**, 642-649.
163. Bush. AA, *Russ. J. Inorg. Chem.*, 1986, **31**, 769.
164. M. F. Debreuille-Gresse, PhD Thesis, Universite de Lille, 1986.
165. F. Abraham, M. F. Debreuillegresse, G. Mairesse and G. Nowogrocki, *Solid State Ionics*, 1988, **28**, 529-532.
166. K. B. R. Varma, G. N. Subbanna, T. N. G. Row and C. N. R. Rao, *Journal of Materials Research*, 1990, **5**, 2718-2722.
167. F. Abraham, J. C. Boivin, G. Mairesse and G. Nowogrocki, *Solid State Ionics*, 1990, **40-1**, 934-937.
168. S. Lazure, C. Vernochet, R. N. Vannier, G. Nowogrocki and G. Mairesse, *Solid State Ionics*, 1996, **90**, 117-123.
169. C. Pirovano, R. N. Vannier, E. Capoen, G. Nowogrocki, J. C. Boivin, G. Mairesse, M. Anne, E. Dooryhee and P. Strobel, *Solid State Ionics*, 2003, **159**, 167-179.
170. C. Pirovano, R. N. Vannier, G. Nowogrocki, J. C. Boivin and G. Mairesse, *Solid State Ionics*, 2003, **159**, 181-191.
171. N. A. Hill, *Journal of Physical Chemistry B*, 2000, **104**, 6694-6709.
172. S. W. Cheong and M. Mostovoy, *Nature Materials*, 2007, **6**, 13-20.
173. N. A. Hill, *Annual Review of Materials Research*, 2002, **32**, 1-37.
174. A. Srinivas, M. M. Kumar, S. V. Suryanarayana and T. Bhimasankaram, *Materials Research Bulletin*, 1999, **34**, 989-996.
175. A. Srinivas, S. V. Suryanarayana, G. S. Kumar and M. M. Kumar, *Journal of Physics-Condensed Matter*, 1999, **11**, 3335-3340.
176. A. Srinivas, D. W. Kim, K. S. Hong and S. V. Suryanarayana, *Materials Research Bulletin*, 2004, **39**, 55-61.
177. K. R. S. Preethi Meher and K. B. R. Varma, *Journal of Applied Physics*, 2009, **106**, 034113.
178. E. Jartych, M. Mazurek, A. Lisinska-Czekaj and D. Czekaj, *Journal of Magnetism and Magnetic Materials*, 2010, **322**, 51-55.
179. F. Kubel and H. Schmid, *Ferroelectrics*, 1992, **129**, 101-112.
180. X. Y. Mao, W. Wang and X. B. Chen, *Solid State Communications*, 2008, **147**, 186-189.
181. J. L. C. Rowsell and O. M. Yaghi, *Microporous and Mesoporous Materials*, 2004, **73**, 3-14.

182. G. Ferey, *Chemical Society Reviews*, 2008, **37**, 191-214.
183. A. U. Czaja, N. Trukhan and U. Mueller, *Chemical Society Reviews*, 2009, **38**, 1284-1293.
184. S. S. Kaye, A. Dailly, O. M. Yaghi and J. R. Long, *Journal of the American Chemical Society*, 2007, **129**, 14176-14177.
185. J. L. C. Rowsell and O. M. Yaghi, *Angewandte Chemie-International Edition*, 2005, **44**, 4670-4679.
186. B. Panella, M. Hirscher and S. Roth, *Carbon*, 2005, **43**, 2209-2214.
187. B. Panella, M. Hirscher, H. Putter and U. Muller, *Advanced Functional Materials*, 2006, **16**, 520-524.
188. U. Ravon, M. E. Domine, C. Gaudillere, A. Desmartin-Chomel and D. Farrusseng, *New Journal of Chemistry*, 2008, **32**, 937-940.
189. P. Horcajada, C. Serre, G. Maurin, N. A. Ramsahye, F. Balas, M. Vallet-Regi, M. Sebban, F. Taulelle and G. Ferey, *Journal of the American Chemical Society*, 2008, **130**, 6774-6780.
190. R. Vaidhyanathan, S. S. Iremonger, G. K. H. Shimizu, P. G. Boyd, S. Alavi and T. K. Woo, *Science*, 2010, **330**, 650-653.
191. M. Kurmoo, *Chemical Society Reviews*, 2009, **38**, 1353-1379.
192. J. R. Long and O. M. Yaghi, *Chemical Society Reviews*, 2009, **38**, 1213-1214.
193. N. Stock and S. Biswas, *Chemical Reviews*, 2012, **112**, 933-969.
194. Y. Du, A. L. Thompson and D. O'Hare, *Chemical Communications*, 2008, 5987-5989.
195. Y. Du, A. L. Thompson, N. Russell and D. O'Hare, *Dalton Transactions*, 2010, **39**, 3384-3395.
196. M. Gimeno-Fabra, A. S. Munn, L. A. Stevens, T. C. Drage, D. M. Grant, R. J. Kashtiban, J. Sloan, E. Lester and R. I. Walton, *Chemical Communications*, 2012, **48**, 10642-10644.
197. T. Ahnfeldt, J. Moellmer, V. Guillerm, R. Staudt, C. Serre and N. Stock, *Chemistry-a European Journal*, 2011, **17**, 6462-6468.
198. F. Millange, M. I. Medina, N. Guillou, G. Ferey, K. M. Golden and R. I. Walton, *Angewandte Chemie-International Edition*, 2010, **49**, 763-766.
199. F. Millange, R. El Osta, M. E. Medina and R. I. Walton, *Crystengcomm*, 2011, **13**, 103-108.
200. T. Ahnfeldt and N. Stock, *Crystengcomm*, 2012, **14**, 505-511.
201. H. Reinsch and N. Stock, *Crystengcomm*, 2013, **15**, 544-550.
202. J. Cravillon, C. A. Schroder, H. Bux, A. Rothkirch, J. Caro and M. Wiebcke, *Crystengcomm*, 2012, **14**, 492-498.
203. E. Stavitski, M. Goesten, J. Juan-Alcaniz, A. Martinez-Joaristi, P. Serra-Crespo, A. V. Petukhov, J. Gascon and F. Kapteijn, *Angewandte Chemie-International Edition*, 2011, **50**, 9624-9628.
204. M. P. Attfield and P. Cubillas, *Dalton Transactions*, 2012, **41**, 3869-3878.
205. J. Juan-Alcaniz, M. Goesten, A. Martinez-Joaristi, E. Stavitski, A. V. Petukhov, J. Gascon and F. Kapteijn, *Chemical Communications*, 2011, **47**, 8578-8580.
206. J. Cravillon, C. A. Schroeder, R. Nayuk, J. Gummel, K. Huber and M. Wiebcke, *Angewandte Chemie-International Edition*, 2011, **50**, 8067-8071.

Chapter 2: The Oxford Diamond *In Situ* Cell (ODISC) for Studying Chemical Reactions using Time-Resolved X-ray Diffraction

2.1 Introduction

The preparation of inorganic crystalline materials is often undertaken using complex apparatus to deliver extreme reaction conditions, such as elevated temperatures and pressures. Custom designed reactor cells and furnaces are therefore required for *in situ* diffraction studies on these reactions, to recreate the appropriate sample environment whilst allowing X-rays or neutrons to penetrate the sample. For X-ray diffraction experiments, a considerable flux of photons in the high energy spectral region is necessary to penetrate thick-walled reaction vessels and to facilitate collection of data with acceptable time resolution. As a result, it can be problematic to monitor such processes *in situ* using conventional laboratory equipment and techniques. Exploratory *in situ* techniques that can be applied to bulk systems, under conditions representative of those used in laboratory syntheses or in industry, are required.

The design, construction and commissioning of a new, versatile, infrared-heated chemical reaction cell for the *in situ* study of a range of chemical syntheses using time-resolved energy-dispersive X-ray diffraction (EDXRD) and angular-dispersive XRD on Beamline I12 at the Diamond Light Source is described in this chapter.

2.2 Existing equipment for *in situ* studies

Two existing *in situ* diffraction furnaces were refurbished and commissioned for use at Diamond Light Source.[7, 8] The stirrer function and the heating system of a hydrothermal cell were repaired and this furnace was used to undertake feasibility studies on Beamline I12 during the commissioning period in 2010. A steel insert was constructed to improve the heating efficiency of a separate high-temperature furnace, which was used to undertake preliminary studies on the molten salt reactions detailed in Chapter 5. During commissioning time, the requirements for high-quality *in situ* diffraction data collection using this very new facility were established. Such factors included optimum detector

position, appropriate sample containment, and the most effective method of remote equipment control.

Use of the two existing furnaces for *in situ* experiments during this time had several drawbacks. The hardware itself was old and often unreliable. Both furnaces were constructed with very specific purposes in mind and were optimised only for these studies. The regular switching between cells on the mounting stage and subsequent sample realignment resulted in valuable beamtime being lost. The time required for heating and cooling of both furnaces was also extensive. However, when functioning effectively, the fundamental features of these apparatuses facilitated good-quality diffraction data collection. Integrated heating, stirring, and precise sample centring were the key elements required for a highly versatile *in situ* reaction cell. These features would provide the basis upon which the new cell would be designed.

2.3 Design criteria for the development of a multifunctional *in situ* cell

Prior to designing and building the new *in situ* chemical reaction cell, a number of important criteria were established. These were concerned with the principal functions of the cell, in addition to its suitability for operation at synchrotron beamlines. Several experienced furnace users and potential stakeholders were consulted about their ideas for building an efficient, highly-applicable reaction furnace. Providing a user-facility for I12 was the overriding aim, and the main attributes required for this were included in the initial criteria.

The furnace should operate at temperatures up to 1200 °C. The heating and cooling of samples should be controllable across this entire heating range and be precise to 0.1 °C.min^{-1}. The option for rapid sample heating and cooling should be available, which, in addition to allowing reactions under such conditions to be probed, will also serve to improve the efficiency of sample changeovers.

The *in situ* cell should be as versatile as possible in terms of accommodating a broad spectrum of chemical reactions. It should be operational with a range of sample vessel sizes and shapes, including capillaries, cylindrical reaction tubes, and steel autoclaves. It is important that reactions can be undertaken on a representative laboratory scale using the equipment.

Passage of the incident X-ray beam into the sample, and of the diffracted beam from the sample to the detector should be subject to minimal obstruction. A window bisecting the furnace should take into account the angle at which the diffracted beam passes onto the fixed angle EDXRD and angular-dispersive detectors.

Optional sample stirring should be available whilst measurements are being undertaken. This will allow agitation of the reacting sample, ensuring a constant amount of solid is present in the beam-path and preventing sample settling.

It is essential that the furnace be reliably controllable from a remote location. A controller box with remote access capabilities will be constructed. This controller should also facilitate and monitor the safe operation of the furnace.

2.4 The Oxford-Diamond *In Situ* Cell (ODISC) design and assembly

Numerous specialised furnaces and reaction cells have been constructed to enable *in situ* diffraction and imaging studies on samples under non-ambient conditions.[8-12] Several design ideas were investigated prior to deciding on the most appropriate method of sample heating for ODISC. 'Clam-shell' furnaces, oil-heated furnaces and induction furnaces were all explored as potential designs. However, following detailed consideration of the initial criteria, sample heating using infrared radiation was deemed to be highly suited to the requirements of the *in situ* chemical reaction furnace.

Furnaces that heat samples by focussing high-intensity infrared radiation onto strongly absorbing reaction vessels are becoming more prevalent due to the advantages of this 'radiative transfer' heating approach.[13] IR-furnaces with low thermal mass permit significantly faster sample heating and cooling than ovens that heat *via* thermal contact. Infrared radiation can be highly focussed, which facilitates localised heating, making high temperatures very accessible.[14] Such furnaces contain halogen lamps and reflectors with very specific geometry, which enables maximum heat transfer onto the focal point at the centre of the furnace. An arrangement of elliptical reflectors in the furnace walls creates a central chamber, which is ideal for accommodating varying sample sizes and shapes. Additionally, sample vessels positioned within this open chamber do not become contaminated through contact with components of the furnace.

2.4.1 Furnace construction

A schematic of the Oxford Diamond *In Situ* Cell (ODISC) is provided in Figure 2.1.

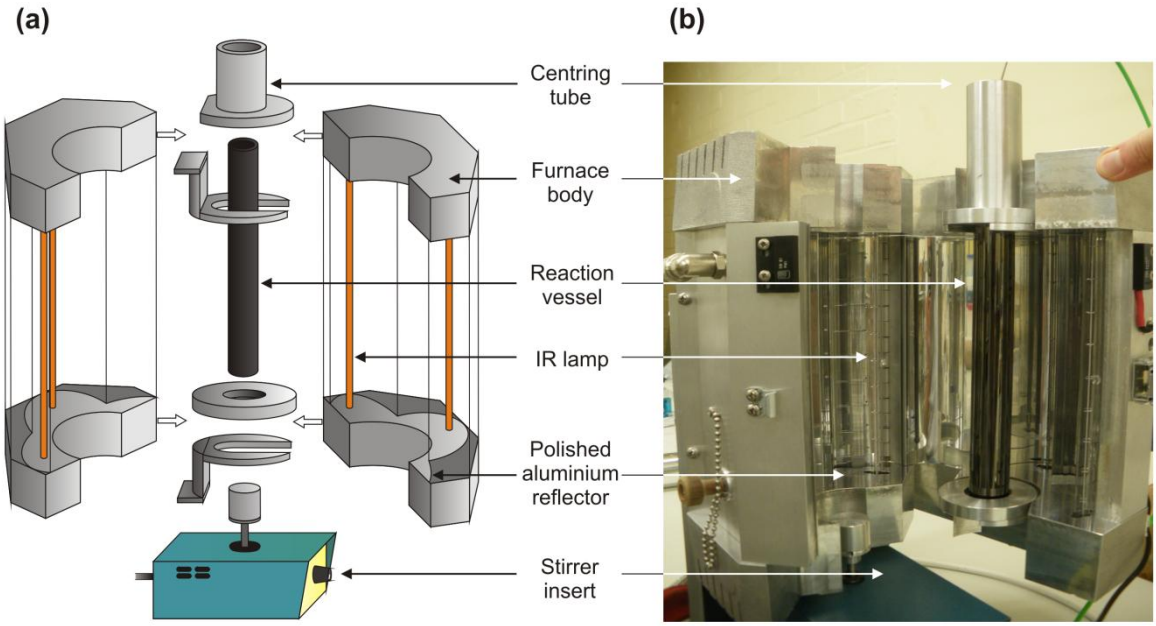

Figure 2.1: (a) Schematic of the ODISC furnace, alongside (b) a photograph of the internal furnace set-up.

Samples positioned inside the furnace are heated *via* radiative transfer. The furnace shell and heating set-up were assembled using commercially available components. The heating system uses highly-polished aluminium elliptical reflectors to focus high-intensity, short-wave IR radiation from four tungsten filament lamps onto a cylindrical sample at the centre of the furnace. At maximum operating voltage each lamp produces 1.5 kW of power, totalling 6.0 kW when all four lamps are in operation.

The furnace body is cooled using an external water flow. A 16 mm (outer diameter (OD)) hose connects the furnace to a continuous water-cooling unit. For applications above 400 °C, it is necessary to further cool the IR lamps using air cooling. In these cases, a supply of clean, dry air is distributed to each of the lamps.

The furnace is vertically mounted upon a bracket attached to a base-plate (Figure 2.2). The base-plate is fully compatible with the sample stage at Beamline I12 at the Diamond Light Source. The sample to stage distance is 141 mm. A cylindrical window runs horizontally through the centre of the furnace, 24 mm above the base of the furnace chamber. This allows unobstructed passage of the incident X-ray beam to the sample and of the diffracted beam from the sample to the detector. A quartz panel in the window

prevents heat loss *via* convection through the opening. The diameter of the window, 16 mm, is such that heat loss is minimised but a clear path at an angle of 5° from the sample to the detector is maintained.

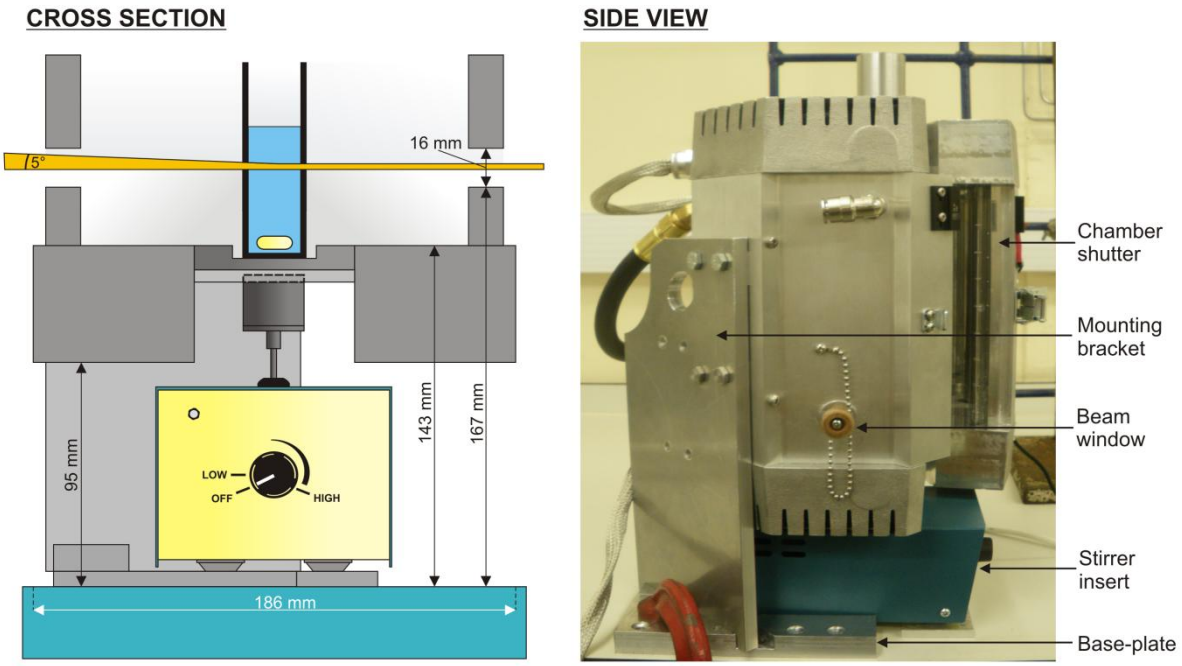

Figure 2.2: Cross section diagram of the lower section of the cell alongside photographic side view showing the mounted furnace.

2.4.2 Cell inserts

Due to constraints on sample heating, cylindrical vessels up to 65 mm maximum diameter can be incorporated into the large, open-chamber inside the furnace body. Exchangeable mounting disks and centring tubes were constructed in order to accommodate the differing dimensions of various reaction configurations. Three bespoke chemical reaction cell systems were initially developed to integrate with the IR furnace design: the *low-temperature*, *high-temperature*, and *hydrothermal* chemical reactor systems illustrated in Figure 2.3.

Accurate sample centring is imperative to ensure that the beam passes through the centre of the sample container and that the volume of sample in the beam is maximised. Low temperature sample vessels made from glassy carbon (dimensions: OD 26 mm × inner diameter (ID) 20 mm × length 300 mm) were positioned centrally in the furnace by a centring tube mounted on a support in the top section of the furnace and a mounting disc located on a support in the lower section of the furnace. The inner diameter of the

centring tube is 27 mm and the recess in the mounting disc has a diameter of 28 mm. Likewise, high temperature sample vessels (dimensions OD 22 mm × ID 16 mm × length 305 mm) were positioned using a centring tube with inner diameter 23 mm and mounting disc with recess 23 mm diameter. The hydrothermal system was configured differently due to the incorporation of an autoclave, which has an outer diameter of 30 mm in the bottom section. The mounting disc has a recess of 36 mm diameter to accommodate a glassy carbon sheath that is required to transfer heat to the vessel. The top section of the hydrothermal set-up is held using two opposing centring plates that rest on the upper support. Once in position, the shaft from the autoclave is located centrally at the top of the furnace.

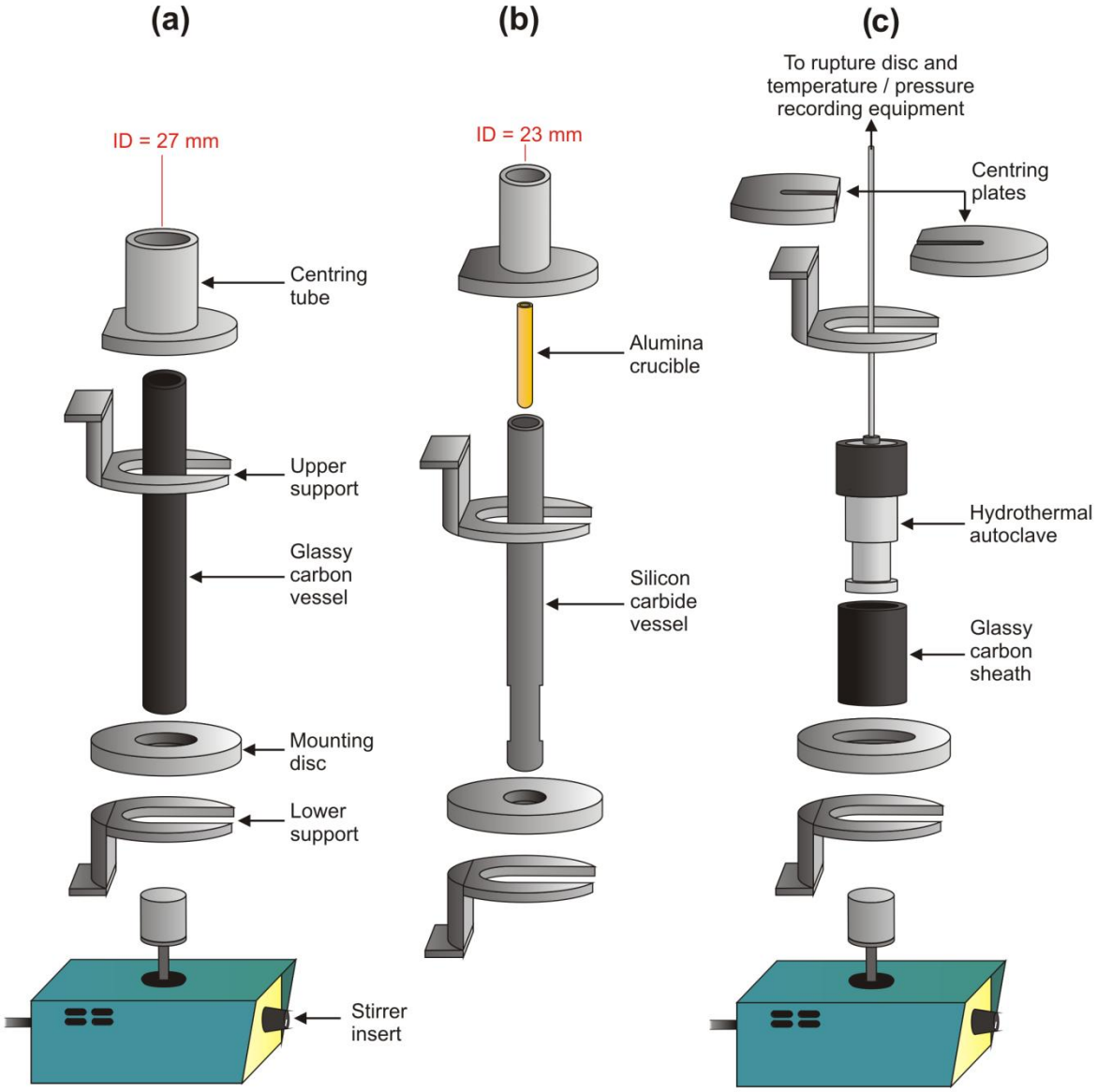

Figure 2.3: Schematic showing three chemical reactor configurations; (a) low-temperature system, (b) high-temperature system, and (c) hydrothermal configuration.

IR heating imposes several constraints upon the choice of chemical reaction vessel. The efficiency of sample heating is dependent upon the IR absorptivity, thermal conductivity, and emissivity of the container material.[15] Sample containment materials were therefore selected based on their capacity to absorb radiation in the infrared region, in addition to their operational requirements and chemical compatibility. Matt black, glassy carbon tubes, that are transparent to X-rays, were employed for reactions below 500 °C and silicon carbide tubes for temperatures greater than 500 °C. A recrystallized alumina crucible positioned inside the silicon carbide tube was utilized to accommodate corrosive reactions. Polytetrafluoroethylene (PTFE)-lined stainless steel autoclaves were used for hydrothermal reactions with heat to the vessel provided *via* a glassy carbon sheath.

The hydrothermal and low temperature configurations incorporate a mechanical stirrer insert in the lower section of the cell for reactions that require agitation. The stirrer magnet comprises three neodymium disc magnets, (15 mm diameter × 3 mm) mounted vertically inside a cylindrical steel head. The steel head is positioned on top of a 60 mm long cylindrical spindle with diameter 6 mm. A speed-controller printed circuit board drives the 240 V rotating motor, which operates at speeds up to 1000 rpm. The stirrer mechanics are positioned inside a 179 × 97 × 74 mm steel instrument case. High-coercivity, PTFE-coated stirrer bars (15 × 9 mm) with samarium cobalt rare-earth magnets were positioned inside the reaction mixture above the stirrer head.

The four halogen lamps are positioned such that they provide heat to the sample vessel across the entire 188 mm height of the furnace chamber. This prevents any significant temperature gradient at the point where the sample is located, in the lower section of the chamber. The temperature at specific locations inside the furnace was recorded using a 500 mm length × 1.5 mm diameter K-type thermocouple. Temperature data were processed by a Eurotherm temperature controller to drive the heating of the furnace. The temperature of the reacting samples was recorded at different positions depending upon the sample configuration. In the low temperature set-up, the thermocouple was positioned directly inside the reacting sample. In the high-temperature set-up, two thermocouples were positioned inside the silicon carbide tube; one between the alumina crucible and the silicon carbide vessel, and one inside the reacting sample. For hydrothermal reactions, one 0.5 mm diameter thermocouple was positioned between the glassy carbon sheath and the steel autoclave and another inside the sample volume, in the sealed container.

2.4.3 Furnace controller design and construction

A bespoke power supply and furnace controller was constructed to incorporate several critical safety and control features. These were in compliance with a full risk assessment for remote beamline operation at the Diamond Light Source. The construction of the furnace controller was undertaken by Nenad Vranješ in the ICL Electronics Design and Fabrication Facility. The circuit diagrams for this device are provided in Appendix A.

The temperature of the furnace is controlled by a programmable temperature controller, which is connected to a single phase thyristor unit. The maximum power output and proportional integral derivative (PID) parameters of the temperature controller were tuned to optimise the efficiency and precision of heating profiles for the different sample configurations at various temperatures (Appendix A).

Before power to the furnace can be enabled, six interlocks must be primed in order to form a completed circuit and connect the 'driver unit' to the IR lamps. If any of the interlock switches opens, or if the emergency button on the front panel is pushed, the contactor will be removed from the circuit and the power to the furnace disconnected. Five of the six interlocks are connected to switches positioned throughout the furnace system (Figure 2.4), with the sixth acting as an auxiliary input to allow further switches to be added. The interlocks were designed so that the circuit 'opens' when the operating conditions of the system are deemed unsafe. Each of the interlocks is connected to a labelled light-emitting diode (LED) on the front panel of the controller box to indicate to the user any interlocks that are not primed.

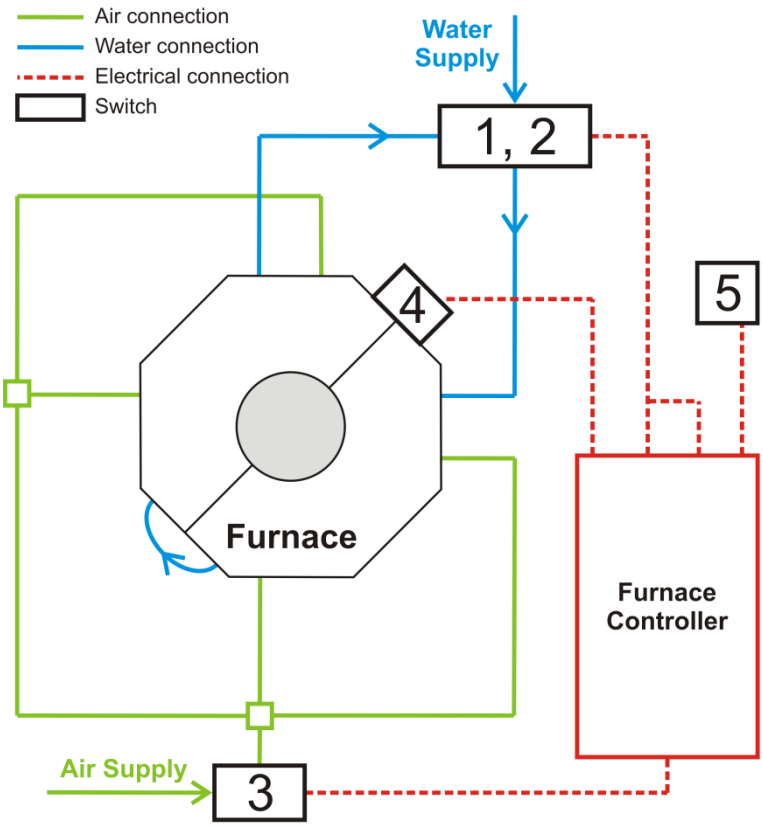

Figure 2.4: Schematic of the ODISC operating system illustrating switch connectivity: 1. Water flow; 2. Water temperature; 3. Air pressure; 4. Chamber shutter; 5. Remote shut-off.

Interlocks 1 and 2 are linked to parameters in the water cooling system. A cable connects the furnace controller to the water cooler *via* a 9-pin 'D' type socket on the rear of the cooler unit. Pins 1 and 2 energise the contact when the water temperature is safely below a preset value. Pins 1 and 3 energise the contact when coolant flow rate is above a preset minimum. The maximum coolant temperature, measured following passage through the furnace and on return to the cooler device, was set to 32 °C. The minimum flow rate was set to 4 gallons per minute.

Interlock 3 is incorporated into the air-cooling system to ensure a constant air flow to the lamps is maintained. A 1.0 MPa reed-type pressure switch was connected to the air-flow system to monitor pressure at the point before the flow is divided onto each of the lamps. In order to maintain a strong, continuous flow of air to the lamps, the minimum pressure at this point was set to 0.2 MPa (2 bar). When low temperature reactions were undertaken and air cooling was not required, the switch was replaced by an override DIN plug to remove this interlock from the system.

Interlock 4 terminates power to the IR lamps when the furnace chamber is open. Even at low operating voltage, the lamps produce very bright light which is potentially damaging to the eyes and skin. A magnetic, reed-type proximity sensor and magnet were attached to either side of the chamber shutter doors and power to the lamps only enabled when the two halves of the switch were in magnetic contact.

The power supply and furnace controller can be operated remotely *via* connection to the Beamline I12 EPICS software.[16, 17] Communication was established *via* an ethernet cable connected to the controller using an RS-232 socket. Interlock 5 is therefore connected to a remote 'emergency-stop' switch, located in the control cabin, so that power can be cut immediately when operating in remote mode.

Only when all six interlocks are primed can the 'Heater On' switch be closed. A green LED on the front panel then indicates that the controller is in communication with the furnace. An additional feature at this point enables the user to switch between 'Remote' and 'Local' modes, whereby control of the furnace can be exchanged from the Eurotherm device to a manual potentiometer dial. This potentiometer controls the furnace output power on a continuous scale of 0 – 100%.

2.4.4 Commissioning at Diamond Light Source

ODISC has been fully commissioned onto the Joint Engineering, Environmental and Processing Beamline I12 (JEEP) of the Diamond Light Source. Figure 2.5 illustrates the compatibility of the ODISC base-plate with the I12 sample stage. Countersunk screw holes on the base-plate are positioned at 25 mm spacings and align with those located on the sample stage. The versatility of the apparatus set-up also enables its use at other high-energy synchrotron X-ray beamlines, such as Beamline F3 of the DORIS synchrotron at Hasylab, Hamburg.

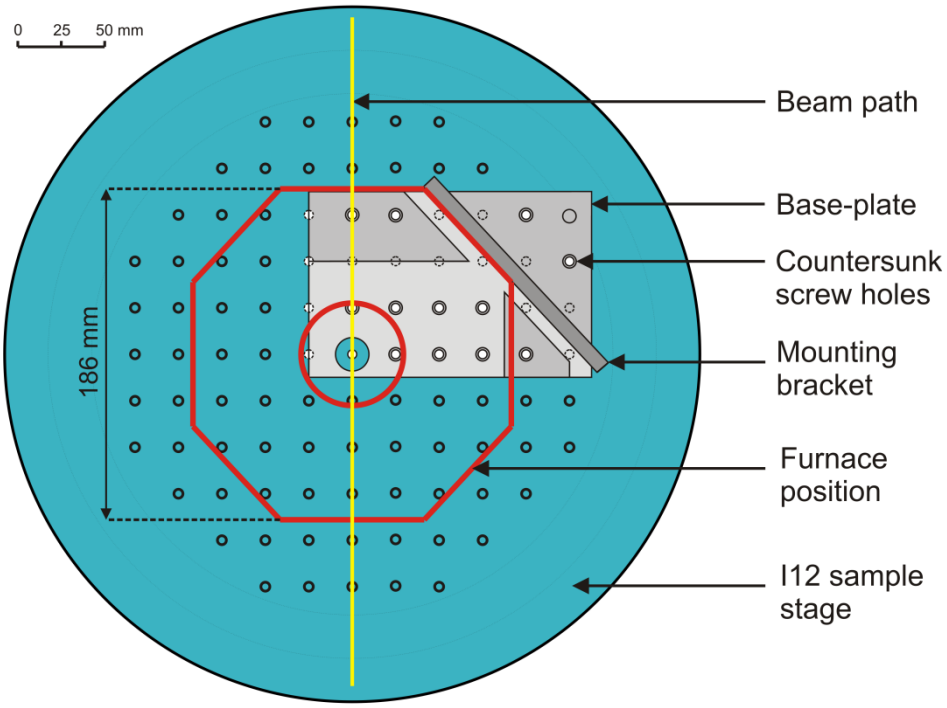

Figure 2.5: Top-view schematic of the I12 sample stage illustrating ODISC base-plate compatibility.

2.5 Further improvements and applications

An increase in the frequency of use of ODISC by members of the wider scientific community was accompanied by a number of requests to adapt and improve its functionality in line with experimental needs. New sample configurations were therefore designed and constructed, and improvements to the basic efficiency of the furnace were implemented.

2.5.1 Low-temperature culture tube configuration

An additional sample configuration was implemented, initially to facilitate low-temperature solvothermal reactions (Figure 2.6). This set-up incorporated 100 mm length × 12 mm OD culture tubes with 20 mm OD polybutylene terephthalate (PBT) screw caps. PTFE-lined magnetic wing stirrers were positioned in the tubes for sample agitation. Heat was transferred to the sample vessel *via* a glassy carbon sheath (dimensions OD 18 mm × ID 14 mm × length 90 mm), located beneath the screw cap and surrounding the culture tube. The temperature of the reacting sample was measured using a K-type thermocouple positioned inside the mixture. A brass ferrule, with an O-ring

positioned between two threaded connectors, enabled the thermocouple to penetrate the cap whilst maintaining the seal to the vessel. The sample was centred using two centring plates on the upper support with 1.5 mm slits to accommodate the thermocouple. The maximum operating temperature of this configuration was dictated by the melting point of the PBT cap, at 150 °C.

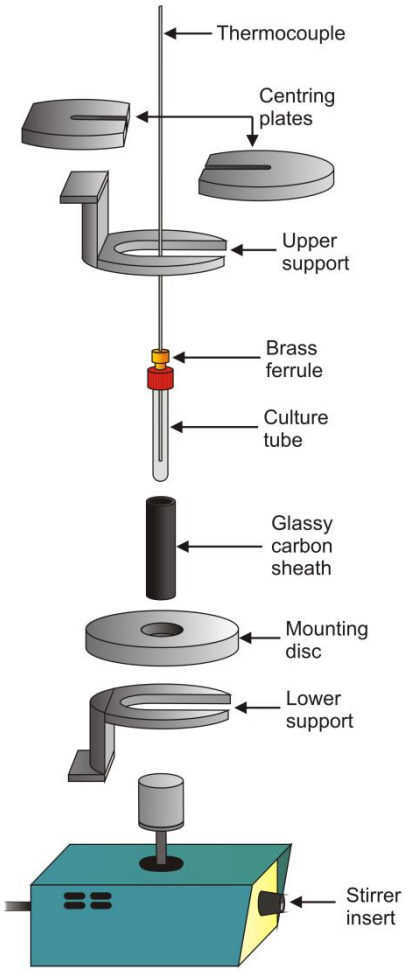

Figure 2.6: Schematic illustrating the low-temperature culture tube chemical reactor configuration.

2.5.2 Gold coating

The tungsten emitter in each of the four halogen lamps produces infrared radiation primarily in the short wavelength region (*ca.* $1000 \leq \lambda$ (nm) ≤ 3000). The reflectance of aluminium is consistently high throughout much of the UV, visible, and IR regions ($\geq$ 80% reflectance over the range $86 \leq \lambda$ (nm) ≤ 5000).[18] However, in the short-wave IR region, gold exhibits the greatest reflectance of all metal thin films ($\geq$ 95% reflectance over the range $620 \leq \lambda$ (nm) ≤ 5000).[19]

In order to improve the operating efficiency of the furnace therefore, the elliptical reflectors inside the chamber were coated with gold (Figure 2.7). Following extensive polishing of the original aluminium surface, gold coating was undertaken on the four separate reflectors by Richard Makin in the Thin Films Facility at the University of Oxford, using the procedure detailed in Chapter 7. Preliminary results illustrated that gold-coating led to an improvement in the efficiency of sample heating by approximately 10%.

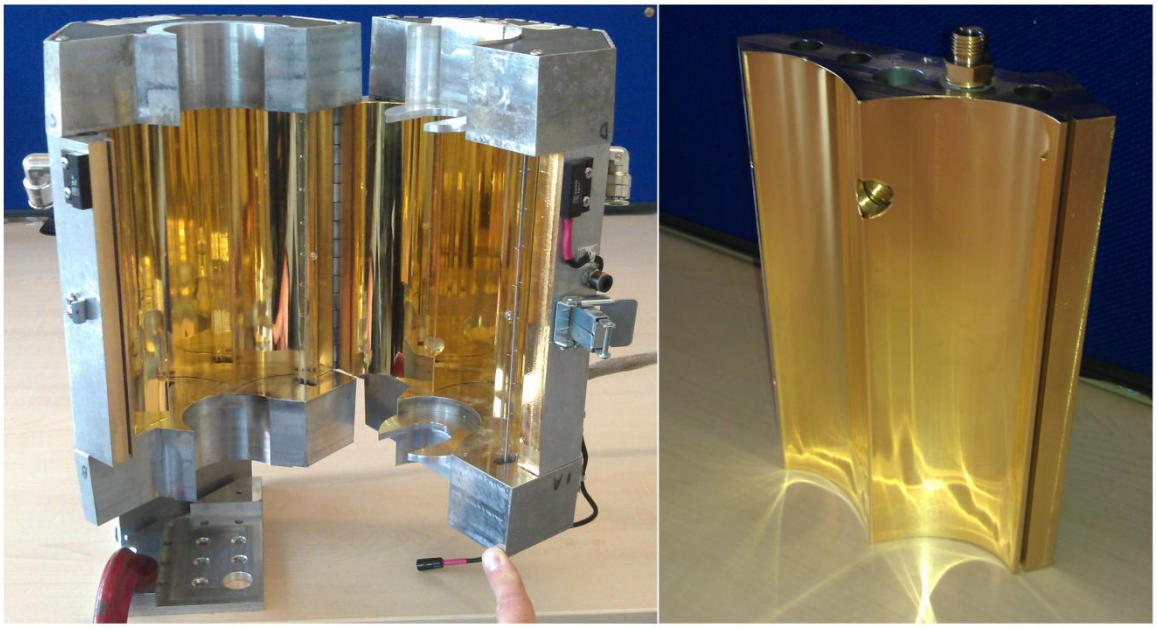

Figure 2.7: Photographs of the gold-coated furnace chamber. LEFT: the furnace interior, and RIGHT: one of the four individual gold-coated reflector segments.

2.5.3 Rapid heating/cooling feasibility study

For the study of phase changes in metals and alloys, samples often require rapid heating to, and cooling from, temperatures in excess of 1000 °C. The suitability of ODISC for undertaking such studies was examined using platinum foil to simulate a metallic sample.

A 1 cm × 1 cm sample of Pt foil was mounted on a ceramic spacer and positioned in the furnace chamber, orthogonal to the X-ray beam path (a schematic of the set-up is provided in Appendix A). A K-type thermocouple was spot-welded to one corner of the foil and used in mounting the sample. The air and water cooling systems were activated for the duration of the experiment. Changes in the temperature of the platinum foil upon varying the output power of the lamps were recorded at 1 second intervals (Figure 2.8).

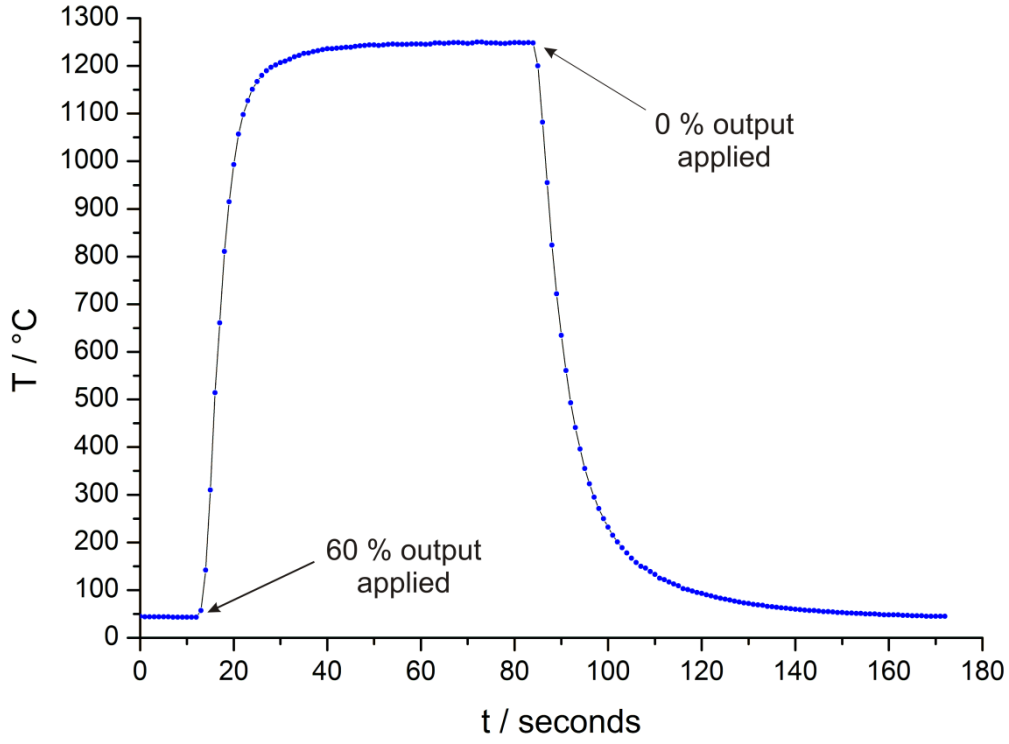

Figure 2.8: Temperature profile for the rapid heating of a sample of platinum foil.

Upon instantaneously applying 60% of the maximum output power to the lamps, the temperature of the sample increased from 43 °C to 1098 °C in 10 seconds. After 60 seconds at 60 % output, the sample temperature plateaus at 1250 °C. 85 seconds into the study, the output voltage was set to 0 V and the temperature decreased by 998 °C in the first 15 seconds. The data illustrate that rapid sample heating can be successfully undertaken to temperatures above 1000 °C at a rate of over 100 °C.sec^{-1}. With the aid of air cooling in the furnace chamber, sample cooling from 1250 °C initially occurs at a rate of over 50 °C.sec^{-1}. To maximise the applicability of this set-up, the PID parameters of the furnace controller were tuned to allow controlled heating and cooling of similar metallic samples at a rate of 1°C.min^{-1} and above (Appendix A).

2.6 Equipment calibration and commissioning

Several calibration scans were undertaken using ODISC before *in situ* experimentation could begin. It was important to establish the quality of data that could be acquired from X-ray diffraction at Beamline I12. A sample of TiO_2 with the rutile structure was selected as an ideal material for study in the preliminary stages of equipment commissioning. Rutile is inexpensive, highly-crystalline, and its structure has been well-characterised.[20]

Bi_2O_3 was chosen for use in temperature calibration scans because of its physical properties. In addition to exhibiting intense Bragg reflections over a wide *q*-range, commercially available Bi_2O_3 exhibits two distinct phase changes upon heating to 900 °C, one of which is a melting transition. Bi_2O_3 was also used as a starting material in experiments undertaken in Chapters 4 and 5 and results from the following calibration scan provided important information about the behaviour of Bi_2O_3 in subsequent reactions. These equipment calibration and commissioning experiments were undertaken before gold-coating was implemented.

2.6.1 Data quality assessment

EDXRD scans, lasting 60 seconds each, were undertaken at room temperature on a crystalline sample of TiO_2. One sample was placed in a glassy carbon tube (low temperature configuration) having a 20 mm length of sample in the beam-path, and another in the alumina crucible inside a silicon carbide vessel (high-temperature configuration), with 11 mm length of sample in the beam path. The data in Figure 2.9 illustrate that it is possible to collect diffraction data of excellent intensity and resolution using data acquisition time intervals analogous to those required for *in situ* studies.

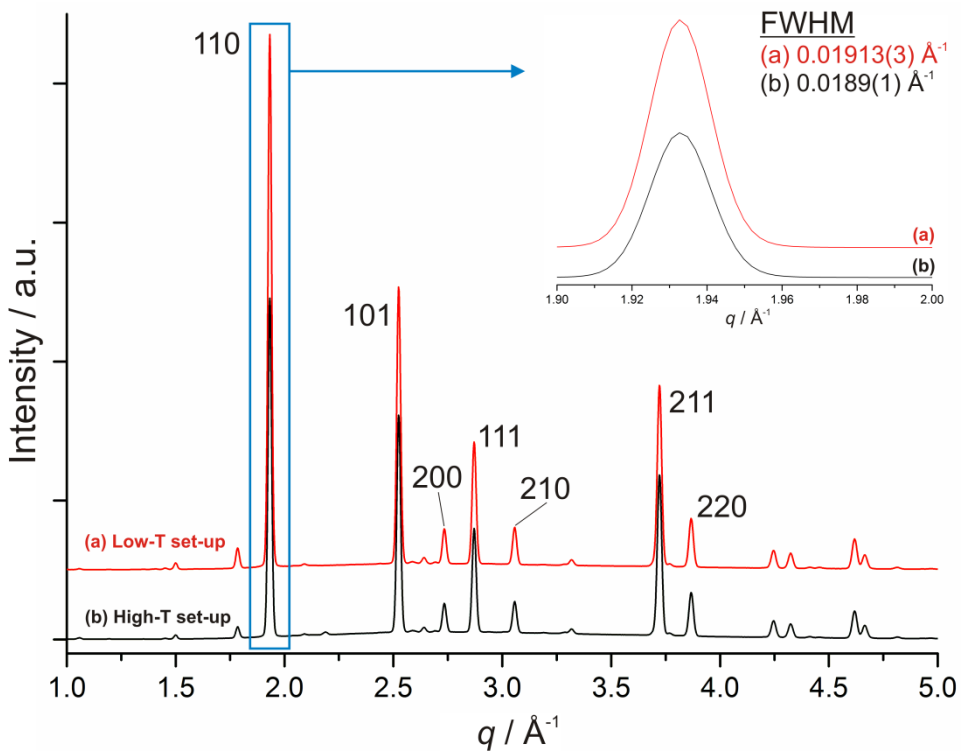

Figure 2.9: EDXRD data for a sample of rutile TiO_2 using (a) the low-temperature reactor configuration and (b) the high-temperature reactor configuration. Inset: the rutile (110) Bragg reflection with full width at half maximum values from data obtained using both configurations.

The full width at half maximum (FWHM) was calculated for the most intense TiO_2 rutile Bragg reflection (110) using a simple Gaussian fit to the data. The FWHM value for the (110) reflection of TiO_2 in the low-temperature set-up was 0.01913(3) $Å^{-1}$ and for TiO_2 in the high-temperature set-up was 0.0189(1) $Å^{-1}$. These values, of comparable magnitude, indicate that despite the greater sample vessel length positioned in the X-ray beam path, data recorded using the low-temperature set-up shows no significant reduction in diffraction intensity or resolution when compared to that from the high-temperature set-up. Furthermore, the use of highly-diffracting crystalline sample vessel materials in the high-temperature set-up has no significant effect upon the diffraction pattern obtained; no intense reflections due to the silicon carbide tube or alumina crucible are detected in the EDXRD data.

In general, the chemical reactions investigated using this equipment occur over a period of minutes and hours. Consequently, it was vital to confirm that high data quality is obtainable from such short scans on crystalline materials. The TiO_2 EDXRD data clearly illustrate that this is the case, as well as indicating that any change in sample configuration has minimal effect upon the quality of the diffraction data obtained.

2.6.2 Temperature calibration: high temperature configuration

The accuracy and precision of cell temperature measurement up to 900 °C was determined by monitoring the phase changes observed upon heating a sample of Bi_2O_3. The calibration run was undertaken using the high temperature set-up.

EDXRD data from the sample were collected for 55 seconds at 60 second intervals for the duration of the experiment. Temperature data were simultaneously recorded at two positions inside the reaction cell at the end point of each 55 second accumulation. The furnace was set to heat the silicon carbide vessel at 10 °C.min^{-1} to 900 °C and hold at that temperature for 10 minutes. The temperature profiles in Figure 2.10 illustrate that there is minimal discrepancy between temperature data collected from the sample vessel (Thermocouple 1) and from within the sample volume (Thermocouple 2). At 900 °C, the difference in temperature between the two thermocouples is less than 4 °C. This demonstrates that samples can be heated to elevated temperatures using the high-temperature set-up, under very accurate control and with no significant lag between the control temperature and the temperature of the reacting sample.

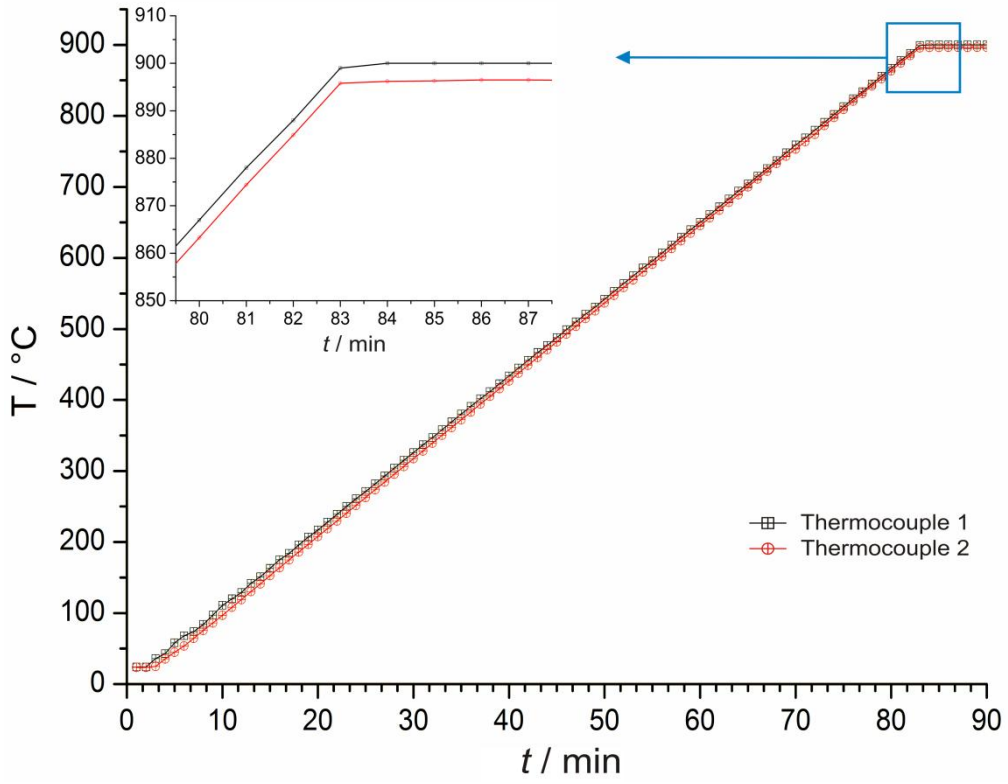

Figure 2.10: Heating profile recorded using the high-temperature configuration. Thermocouple 1 was positioned between the sample tube and crucible. Thermocouple 2 was positioned within the sample volume. INSET: Close-up of the heating profile at the target temperature, 900 °C.

To verify the accuracy of temperature data recorded from the cell, the temperatures at which Bi_2O_3 phase changes occurred were determined precisely using *in situ* EDXRD data. Upon heating, α-Bi_2O_3 undergoes a phase transition, which begins at approximately 729 °C, to the fluorite-related δ-Bi_2O_3 form.[21, 22] δ-Bi_2O_3 exists until the melting point of bismuth oxide at 824 °C.[23] The 3D stack plot in Figure 2.11. clearly illustrates two discrete transformations in the diffraction profile. Bragg reflections corresponding to the starting material are replaced by δ-Bi_2O_3 intermediate reflections at t = 67 mins, and at t = 76 mins a sharp increase in the overall background intensity is indicative of the solid-liquid melting transition.

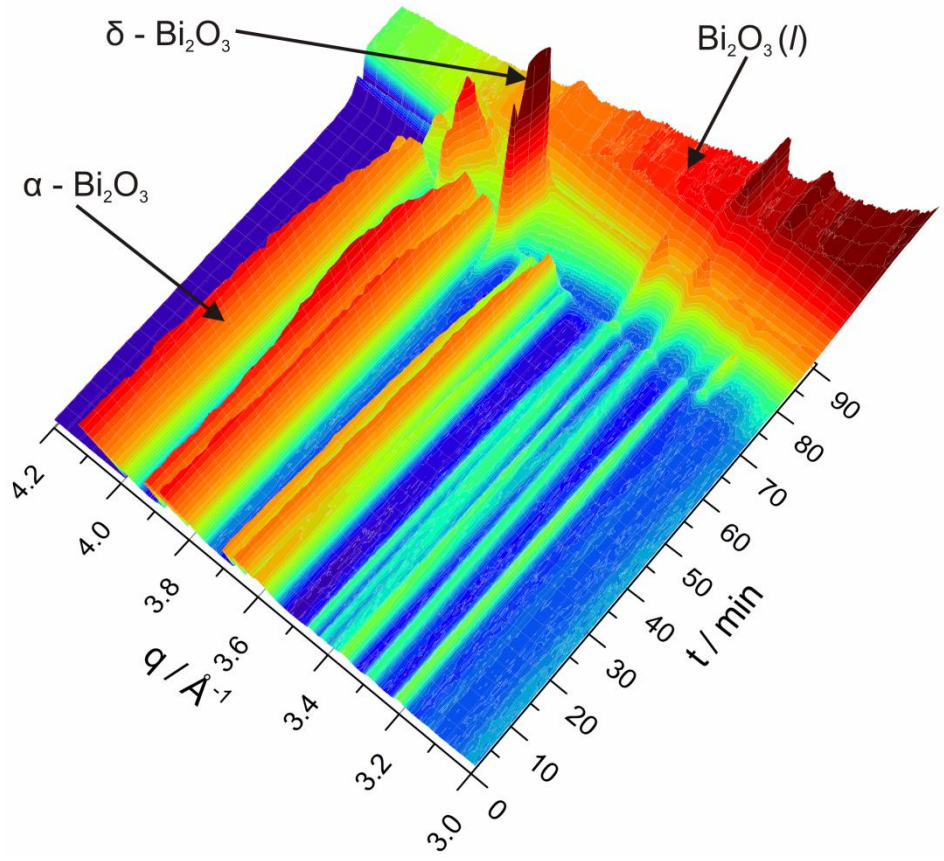

Figure 2.11: 3D stack plot of EDXRD data for a sample of Bi_2O_3 heated to 900 °C. Peaks observed at the conclusion of the reaction correspond to fluorescence peaks due to bismuth.

The contour plot in Figure 2.12(a) shows the diffracted intensity plotted as a function of q and time for the heating of α-Bi_2O_3. The background has been subtracted from the numerous diffraction patterns using a simple but highly effective automatic algorithm.[24] Starting material reflections are observed to shift to lower q as the α-Bi_2O_3 undergoes thermal expansion upon heating. Those reflections that do not shift position with time can be attributed to fluorescence peaks due to bismuth: Kα_1 E = 77.12 keV (q = 3.38 Å^{-1}),

Kα_2 E = 74.81 keV (q = 3.28 Å^{-1}) and Kβ_1 E = 87.34 keV (q = 3.83 Å^{-1}). Such peaks remain even following melting of the sample. Intermediate δ-Bi_2O_3 reflections are observed at q = 3.68 Å^{-1} and q = 3.14 Å^{-1}, which correspond to the respective (311) and (220) reflections.[22]

The extent of reaction, α, is defined as the integrated intensity (I) of a specific reflection at time t, divided by the maximum intensity of that peak [$\alpha = I_{(hkl)}(t)/I_{(hkl)}(\max)$]. A plot of α *vs.* time for the heating of α-Bi_2O_3 (Figure 2.12(b)) shows the precise temperature at which phase changes occur. At $67 \leq t$ (min) ≤ 68 ($722.0 \leq T$ (°C) ≤ 733.0), the intensity of the starting material α-Bi_2O_3 reflections begins a rapid decline as δ-Bi_2O_3 reflections increase in intensity. The α- and δ-Bi_2O_3 curves cross at $\alpha \sim 0.5$ which is indicative of a direct solid-solid conversion in a one step process. The temperature recorded by Thermocouple 2 at this point directly corresponds to the Bi_2O_3 phase-change temperature observed by Schröder *et al.*[25] The melting point provides a more precise indication of sample temperature, as the phase change occurs more rapidly than a solid-solid transformation. The considerable rise in background intensity provides an indication that the material has melted, which is concurrent with a decrease in intensity of the δ-Bi_2O_3 reflections. Data from Thermocouple 2 indicate that Bi_2O_3 melting occurs at $76 \leq t$ (min) ≤ 77 ($820.7 \leq T$ (°C) ≤ 831.6), which is again consistent with the melting point noted by Harwig.[22]

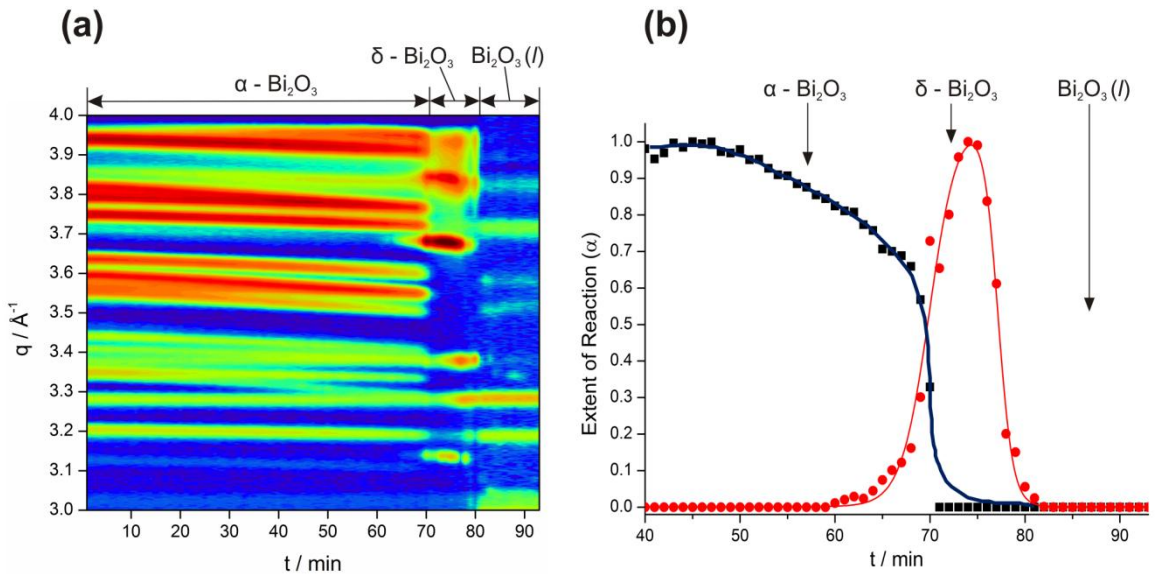

Figure 2.12: Background-subtracted EDXRD data for a sample of Bi_2O_3 heated to 900 °C. (a) Contour plot and (b) extent of reaction *vs.* time plot (the solid lines are a guide for the eye only and have no physical significance).

Furnace operation in the high-temperature configuration was also tested up to 1200 °C. The output power was increased at regular intervals until at 75% of the maximum. A thermocouple measured the temperature of a sample of powdered TiO_2, positioned inside a crucible in the silicon carbide tube. The sample temperature comfortably reached 1202 °C and could be accurately maintained at several dwell temperatures above 1000 °C. The heating profile from this feasibility test is provided in Appendix A.

It is clear that sample temperatures can be accurately monitored and controlled using appropriately positioned thermocouples in each of the configurations. However, where possible, these temperatures were verified using internal calibrants observed experimentally. The *d*-spacing shift of assigned Bragg reflections was monitored upon changes in temperature and compared to known data. The thermal expansion of a PTFE liner in the hydrothermal configuration, and the melting of crystalline RbCl in a molten salt reaction are two such examples of internal calibrants used for reference in the following chapters.

2.6.3 Angular-dispersive X-ray diffraction

Angular-dispersive XRD became available on Beamline I12 in 2011. The option to quickly switch between X-ray beam energies was particularly useful when observing a range of materials with reflections at very different *d*-spacings. A sample of ettringite was synthesised and used as a 2θ calibrant for angular-dispersive studies with ODISC. The mineral ettringite, $Ca_6[Al(OH)_6]_2(SO_4)_3{\cdot}26H_2O$, has a layered structure with $a \sim 11.23$ Å, $c \sim 21.44$ Å. This highly crystalline material was suitable for use as a calibrant due to the multitude of Bragg reflections it exhibits across a wide *q*-range, with the additional advantage of it being relatively simple to synthesise.

Ettringite was synthesised by stirring 10 g $Ca(OH)_2$ and 7.5 g $Al_2(SO_4)_3$ in 100 mL degassed and deionised water at room temperature for two days. Following reaction, the mixture was filtered, and the solid washed with a saturated solution of NH_4Cl. The resulting white powder was analysed using high-resolution powder laboratory XRD to confirm successful formation of the pure phase. Angular-dispersive diffraction was then undertaken on the sample at Beamline I12. In monochromatic beam mode, diffraction data are recorded using the flat panel detector as 2D images of intensity *vs*. detector

pixels, which contain the various Bragg rings of the material being studied. The beam energy, beam centre and sample-detector distance were first accurately determined using data from a sample of CeO_2. Following this, 2D diffraction data obtained from a vial containing the ettringite were converted to a 1D plot of intensity *vs*. 2θ using the Fit2D software program. Rietveld refinement was then undertaken using the 1D angular-dispersive diffraction pattern (Figure 2.13). The structure published by Moore and Taylor was used as an initial model to establish accurate information about the structure of the synthesised phase.[26]

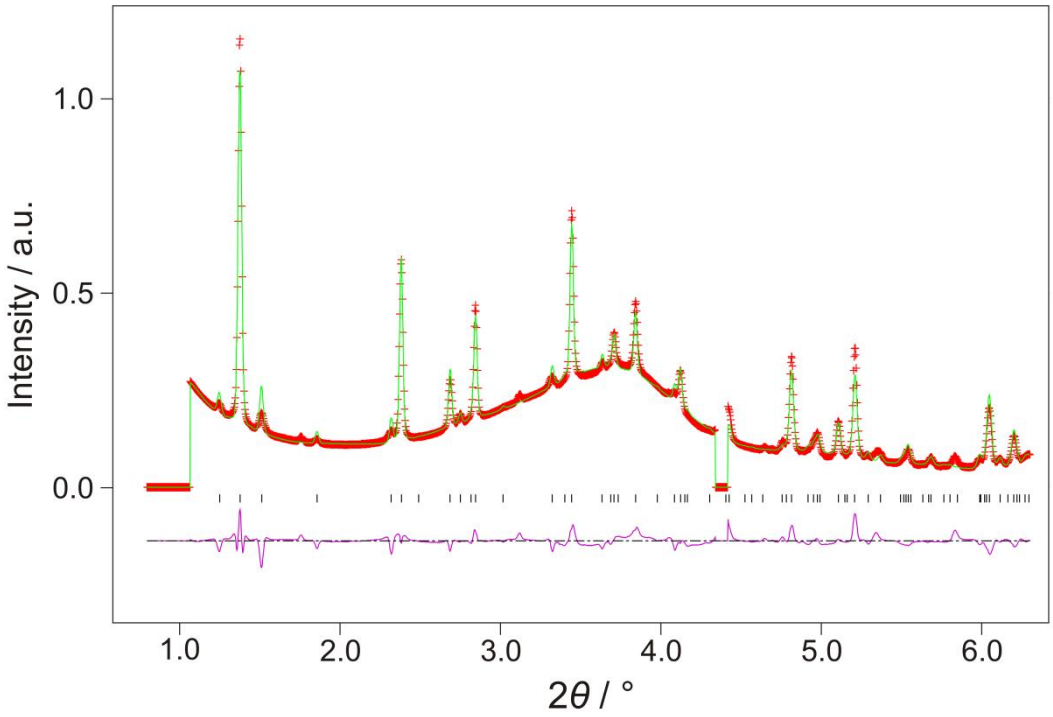

Figure 2.13: Refinement of a hexagonal structure model with angular-dispersive XRD data from a scan of ettringite with 4 sec exposure. Raw data is indicated by the red crosses, the green line indicates the refined model data, and the pink line represents the difference between both experimental and modelled data. wRp = 0.0633, Rp = 0.0425 , χ^2 = 0.6543.

Data collected from the sample of ettringite are of high quality. The intensity and resolution obtained from a scan of 4 sec exposure are comparable those observed in laboratory XRD scans lasting several hours. Structure refinement allowed accurate determination of the *d*-spacings of most Bragg reflections in the data, which could subsequently be plotted as a function of 2θ for calibration purposes.

2.7 Conclusion

A new, versatile, infrared-heated chemical reaction cell, ODISC, has been commissioned for the *in situ* study of a range of chemical syntheses using Beamline I12 at the Diamond Light Source. Specialised reaction configurations have been constructed to enable both EDXRD and angular-dispersive studies on various samples under non-ambient conditions. The cell can incorporate sample vessels such as alumina crucibles, steel hydrothermal autoclaves, and glassy carbon tubes, with the option of motorised stirring for reactions that require agitation. Additionally, an intelligent temperature controller box, incorporating several safety features, has been assembled to facilitate accurate furnace temperature control and to maintain the safe operation of ODISC at all times. The remote access capabilities of the controller allow reaction conditions to be altered without interrupting diffraction data collection.

High quality diffraction measurements from a sample of TiO_2 confirm that data of excellent intensity and resolution can be obtained from crystalline samples using ODISC. Phase changes upon heating a sample of Bi_2O_3 were monitored using EDXRD to demonstrate the impressive accuracy of temperature measurement using the reaction cell. It was found that minimal discrepancy exists between the temperatures of the sample tube and reacting sample in the high-temperature configuration. An additional feasibility study illustrated that the cell is capable of rapidly heating and cooling metallic samples at temperatures in excess of 1000 °C.

The completed ODISC apparatus comprehensively satisfies the initial design criteria detailed in Section 2.3. It has incorporated and improved upon the capabilities of several predecessor cells, in addition to providing new and advanced applications. Crucially, its design and fabrication as a versatile *in situ* furnace has facilitated the study of a broad spectrum of chemical and engineering science using X-ray diffraction.[27] The apparatus became available for use by the wider scientific community in 2012. A user-guide has been written to enable the safe and efficient operation of ODISC for multiple users and uses, and is provided in Appendix F. At the time of writing, June 2013, researchers and academics from seven different institutions worldwide had undertaken *in situ* diffraction studies using this equipment. It is anticipated that future experiments involving ODISC will employ a greater range of high-energy X-ray techniques, such as tomography and

high-speed imaging, and that these studies will instigate further improvements to the equipment.

Detailed examples of the applications of this apparatus for exploring the kinetics and mechanisms of a range of chemical reactions are presented in the following chapters.

2.8 References

1. D. Grandjean, A. M. Beale, A. V. Petukhov and B. M. Weckhuysen, *Journal of the American Chemical Society*, 2005, **127**, 14454-14465.
2. R. Le Toquin, W. Paulus, A. Cousson, C. Prestipino and C. Lamberti, *Journal of the American Chemical Society*, 2006, **128**, 13161-13174.
3. G. R. Williams, A. J. Norquist and D. O'Hare, *Chemistry of Materials*, 2006, **18**, 3801-3807.
4. M. Morcrette, Y. Chabre, G. Vaughan, G. Amatucci, J. B. Leriche, S. Patoux, C. Masquelier and J. M. Tarascon, *Electrochimica Acta*, 2002, **47**, 3137-3149.
5. M. R. Rowles, M. J. Styles, I. C. Madsen, N. V. Y. Scarlett, K. McGregor, D. P. Riley, G. A. Snook, A. J. Urban, T. Connolley and C. Reinhard, *Journal of Applied Crystallography*, 2012, **45**, 28-37.
6. J. Kikuma, M. Tsunashima, T. Ishikawa, S.-Y. Matsuno, A. Ogawa, K. Matsui and M. Sato, *Journal of the American Ceramic Society*, 2010, **93**, 2667-2674.
7. J. S. O. Evans, R. J. Francis, D. O'Hare, S. J. Price, S. M. Clark, J. Flaherty, J. Gordon, A. Nield and C. C. Tang, *Review of Scientific Instruments*, 1995, **66**, 2442-2445.
8. M. J. Geselbracht, R. I. Walton, E. S. Cowell, F. Millange and D. O'Hare, *Review of Scientific Instruments*, 2000, **71**, 4177-4181.
9. K. M. Ok, D. O'Hare, R. I. Smith, M. Chowdhury and H. Fikremariam, *Review of Scientific Instruments*, 2010, **81**, 125107.
10. F. Xia, J. Brugger, G. J. Qian, Y. Ngothai, B. O'Neill, J. Zhao, S. Pullen, S. Olsen and A. Pring, *Journal of Applied Crystallography*, 2012, **45**, 166-173.
11. M. Yashima, K. Ohuchi, M. Tanaka and T. Ida, *Journal of the American Ceramic Society*, 2006, **89**, 1395-1399.
12. M. J. Styles, M. R. Rowles, I. C. Madsen, K. McGregor, A. J. Urban, G. A. Snook, N. V. Y. Scarlett and D. P. Riley, *Journal of Synchrotron Radiation*, 2012, **19**, 39-47.
13. L. F. Siah, W. M. Kriven and J. Schneider, *Measurement Science & Technology*, 2005, **16**, 1291-1298.
14. J. Park, T. Shimomura, M. Yamanaka, S. Watauchi, I. Tanaka and K. Kishio, *Review of Scientific Instruments*, 2005, **76**, 3.
15. M. Bass, *Handbook of Optics: Devices, Measurements, & Properties*, 2nd Edition, Optical Society of America, McGraw-Hill, 1995.
16. M. T. Heron *et al.*, 10th ICALEPCS International Conference on Accelerator & Large Expt. Physics Control Systems, Geneva, 2005.
17. M. T. Heron *et al.*, International Conference on Accelerator and Large Experimental Physics Control Systems 2007, Knoxville, Tennessee, USA, 2007.
18. G. Hass, *Journal of the Optical Society of America*, 1955, **45**, 945-952.
19. H. A. Macleod, *Thin Film Optical Filters*, 3rd Edition, Taylor & Francis Group, 2001.

20. D. T. Cromer and K. Herrington, *Journal of the American Chemical Society*, 1955, **77**, 4708-4709.
21. C. N. R. Rao, G. V. S. Rao and S. Ramdas, *Journal of Physical Chemistry*, 1969, **73**, 672-675.
22. H. A. Harwig, *Zeitschrift Für Anorganische Und Allgemeine Chemie*, 1978, **444**, 151-166.
23. P. Shuk, H. D. Wiemhofer, U. Guth, W. Gopel and M. Greenblatt, *Solid State Ionics*, 1996, **89**, 179-196.
24. S. Bruckner, *Journal of Applied Crystallography*, 2000, **33**, 977-979.
25. F. Schroeder, N. Bagdassarov, F. Ritter and L. Bayarjargal, *Phase Transitions*, 2010, **83**, 311-325.
26. A. E. Moore and H. F. W. Taylor, *Acta Crystallographica Section B-Structural Crystallography and Crystal Chemistry*, 1970, **B 26**, 386-393.
27. G. R. Williams, A. Clout and J. C. Burley, *Physical Chemistry Chemical Physics: PCCP*, 2013, **15**, 8616-8628.

Chapter 3: The Synthesis and Reactivity of Layered Double Hydroxides formed from $Al(OH)_3$

3.1 Introduction

The Li-containing family of Layered Double Hydroxide (LDH) materials, $[LiAl_2(OH)_6]X{\cdot}yH_2O$ ($LiAl_2$-X, where X = e.g. Br, Cl, CO_3, NO_3, OH), was introduced in Section 1.3. A general synthetic route to these materials is *via* the intercalation of lithium salts into aluminium hydroxide.[1, 2] This method involves the direct reaction of highly-concentrated solutions of LiX with different polymorphs of $Al(OH)_3$.[3, 4] $Al(OH)_3$ has a structure comprising sheets made up of double layers of hexagonally packed O atoms, discussed in detail in Chapter 1. Al^{3+} ions occupy two thirds of the octahedral holes in the layers in an ordered fashion. Reaction with lithium salts results in an intercalation process in which both cations and anions are incorporated into the host lattice; the Li^+ cations enter the vacancies in the $Al(OH)_3$ layers and the anions enter the interlayer space. The resultant LDH exhibits cation ordering within the layers.

3.1.1 LDHs formed from $Al(OH)_3$

There are a limited number of examples which demonstrate the potential for LDH formation using aluminium hydroxide as a precursor. Greenwell *et al.* recently reported the successful synthesis of a Mg/Al LDH through hydrothermal reaction of $Al(OH)_3$ and $Mg(OH)_2$ at 150 °C.[5] Additionally, Ogawa and Sugiyama formed a range of Zn/Al LDHs *via* the hydrothermal reaction of $Al(OH)_3$ and ZnO in the presence of benzenesulfonic acid.[6] Various intralayer Zn/Al ratios (spanning the range 1.5 – 4) were achieved using this technique.

In addition to these examples, a related series to the Li/Al LDHs, containing M^{2+} ions, has been synthesised using $Al(OH)_3$ starting material. By reacting 'activated' gibbsite (which had been subject to particle breakdown by ball-milling prior to reaction) with concentrated transition metal nitrate salts under hydrothermal conditions, a novel series of LDHs with the formula $[MAl_4(OH)_{12}](NO_3)_4{\cdot}yH_2O$ (MAl_4-NO_3, M = Co, Ni, Cu, Zn) was synthesised.[7] These materials exhibit a very different stoichiometry to most

previously synthesised LDHs, with a M^{2+} : M^{3+} ratio of 1 : 4 in the layers. The MAl_4-NO_3 materials were determined to have promising shape selective intercalation chemistry.[8, 9] Palladium-doped variants of these LDHs have also been used as precursors to efficient catalysts for the conversion of acetone to methyl isobutyl ketone.[10] Structurally similar LDHs have been formed through hydrothermal reaction using the bayerite polymorph of $Al(OH)_3$ as a starting material.[11] Further to this work, Chitrakar *et al.* employed hydrothermal treatment to $MgCl_2 \cdot 6H_2O$-coated gibbsite in the synthesis of chloride-intercalated $MgAl_4$-Cl LDH, with Mg^{2+} : Al^{3+} ratio of 1 : 4.[12]

3.1.2 Topotactic approaches to LDH formation

Reactions are often labelled 'topotactic' without significant evidence of the occurrence of a structure-conserving process. The concept of topotaxy has been discussed in depth by Figlarz and co-workers.[13] In this work, a topotactic reaction is defined as "a transformation in which one crystalline phase is converted into another with a definite and reproducible crystallographic orientation relationship between the two". No assumptions are made about the mechanism of the reaction in this definition.

Britto and Kamath introduced the concept of metal-hydroxide layer building-blocks as 'structural synthons' in the construction of various polymorphic variations of Li/Al LDHs.[14, 15] In these works, several topotactic pathways are employed to synthesise a number of predicted LDH polytypes, which are then classified based on local symmetry relationships. In addition to direct intercalation of lithium salts into the polymorphs of $Al(OH)_3$, other topotactic methods have been employed to transform brucite-like metal hydroxides into hydrotalcite-like LDHs. Using a unique 'oxidative intercalation process', which involves simultaneous intralayer oxidation of Fe^{2+} to Fe^{3+} and incorporation of I^- ions into the interlayer space, Ma *et al.* have successfully synthesised Co(II)/Fe(III) layered double hydroxides.[16] Further studies revealed a similar method can be applied to systems without iron, where Co^{2+} to Co^{3+} oxidation is favoured by prolonged reaction durations and the use of iodine/bromine reagents in excess.[17, 18] Delamination is an additional effective method of forming novel LDH systems that retain some structural character from the parent material.[19-24] Delamination involves the deconstruction of an LDH into its individual component 'nanosheets'. The constituent layers can then be

reformed into a model lamellar arrangement to create an ideal multilayer thin-film system.

Recent advances in physical methods which probe reactions *in situ* allow the concept of topotaxy to be extended to describe structure-conserving processes, as well as the relationship between materials that exist at the start and end of these processes.

3.1.3 Synthesis of LDHs containing three intralayer cations

It is possible to synthesise LDHs that contain greater than two metal cations in the octahedrally-coordinated sites in the positively charged layers. Synthetic routes to such compounds generally involve a mixture of the relevant concentrated metal ion solutions as starting materials. Liu and co-workers have successfully synthesised the ternary LDHs M/M'/Al-CO_3 (M, M' = Fe, Co, Zn) using a urea hydrolysis method.[25] Despite altering the molar amounts of the relevant starting materials, attempts to vary the M^{2+} : Al^{3+} ratio in the products proved futile, and a ratio of 2 : 1 was consistently obtained. However, by varying the M^{2+} : M'^{2+} ratios in the starting solutions it was possible to alter the ratio of these metal ions within the layers.

Tichit and co-workers have reported the synthesis of Co/Mg/Al and Ni/Mg/Al LDHs using the coprecipitation method under supersaturation conditions.[26, 27] By varying the quantity of metal ions in the starting materials, the ratio of M^{2+} : Al^{3+} (2 – 3 : 1) and M^{2+} : M'^{2+} (0 – 4 : 1) in the intralayer region was tuned. Klemkaite *et al.* further reported the synthesis of M/M'/Al-CO_3 LDHs (M, M' = Co, Ni) with M^{2+} : Al^{3+} ratios close to 3 : 1, using an analogous procedure.[28] The three-metal LDH systems were found to re-form layered materials following high-temperature decomposition and subsequent rehydration.

A study into the thermal decomposition of cobalt-containing LDHs by Johnsen and Norby contains a comparison between the Co/Al-NO_3 and Co/Zn/Al-NO_3 systems.[29] The three metal LDH in this case, $[Co_{0.38}Zn_{0.36}Al_{0.26}(OH)_2](NO_3)_{0.18}(CO_3)_{0.05}\cdot 0.46H_2O$, was synthesised by the coprecipitation method, and exhibits a M^{2+} : M^{3+} ratio of 3 : 1. Other hydrotalcite-like compounds containing mixtures of Al^{3+} and M^{2+} ions in the layers are listed in the seminal paper by Cavani *et al.*[30] The majority of three-metal phases discussed in this work contain Cu^{2+} or Mg^{2+} ions.

3.1.4 Scope of the chapter

Following recent reports into the synthesis and reactivity of MAl_4-LDHs,[7-9] further studies into the hydrothermal formation of related LDHs using aluminium hydroxide as a precursor have been undertaken. Reaction of the gibbsite polymorph of $Al(OH)_3$ with mixtures of M^{2+} salts provides a unique method of forming analogous layered double hydroxides with more than two metal ions in the metal-hydroxide layers. The principal focus of the work described in this chapter centres upon reaction with Co, Ni and Zn salts, but also includes attempts to incorporate other transition metal ions into the layers. An account of the structure, properties and reactivity of the novel series of three-metal layered double hydroxides is provided. The chapter concludes with the description of an *in situ* X-ray diffraction study into the synthesis and reactivity of $Al(OH)_3$-derived LDHs, including the first ever chemical reaction to be probed using Beamline I12 at the Diamond Light Source.

3.2 Synthesising ternary LDH systems

Hydrothermal reaction of $Al(OH)_3$ with concentrated transition metal salts required initial activation of the gibbsite precursor through ball milling. This had the effect of decreasing particle size and increasing the irregularity of particle morphology, thus increasing surface area and promoting reactivity. Forcing hydrothermal conditions were also used, with elevated temperatures, long reaction durations, and highly concentrated metal salt solutions being employed.

Syntheses of three-metal LDHs were performed using the following procedure: 1 g of activated $Al(OH)_3$ was reacted with 5 mL of a 10 M aqueous solution of each of two metal nitrate hydrates ($Zn(NO_3)_2{\cdot}6H_2O$, $Co(NO_3)_2{\cdot}6H_2O$, $Ni(NO_3)_2{\cdot}6H_2O$). The reagents were treated hydrothermally at 150 °C for 48 hours. Following controlled cooling to room temperature at 5 °C.min^{-1}, the products were vacuum filtered, washed with water, and then dried in air for 2 hours to afford the products as pastel coloured powders. The product containing Co/Ni was a light blue-grey, the Co/Zn product was pink-coloured, and the Ni/Zn material was light blue. The observation of coloured compounds suggests the presence of transition metal ions, and is consistent with observations for the analogous two-metal MAl_4-NO_3 compounds.

The compositions of the reaction products were determined using CHN analysis and energy-dispersive X-ray spectroscopy (EDX) (Appendix B). All compounds were synthesised with phase-purity. The general formula for each was found to be $[M_xM'_{2-x}Al_8(OH)_{24}](NO_3)_4{\cdot}yH_2O$, where M, M' = Zn, Ni or Co. For notation purposes, these novel materials will henceforth be referred to collectively as $MM'Al_8\text{-}NO_3$ and individually as $M_xM'_{2-x}Al_8\text{-}NO_3$. The exact compositions, including the number of co-intercalated water molecules determined using thermogravimetric analysis (TGA), are provided in Table 3.1.

Table 3.1: Chemical compositions of the new ternary LDHs.

Formula	**Stoichiometric ratios from EDX**	
	Observed	Calculated
$[CoZnAl_8(OH)_{24}](NO_3)_4{\cdot}5H_2O$	Al : Co : Zn 8.00 : 0.98 (±0.1) : 0.87 (±0.1)	Al : Co : Zn 8.00 : 1.00 : 1.00
$[Ni_{1.9}Zn_{0.1}Al_8(OH)_{24}](NO_3)_4{\cdot}5H_2O$	Al : Ni : Zn 8.00 : 2.18 (±0.2) : 0.06 (±0.1)	Al : Ni : Zn 8.00 : 1.90 : 0.10
$[Co_{0.1}Ni_{1.9}Al_8(OH)_{24}](NO_3)_4{\cdot}4H_2O$	Al : Ni : Co 8.00 : 2.07 (±0.2) : 0.03 (±0.1)	Al : Ni : Co 8.00 : 1.90 : 0.10

EDX was undertaken on an appropriate number of different product particles to ensure that, in each case, two M^{2+} cations were present within the same particle and the sample did not comprise a mixture of the individual $MAl_4\text{-}NO_3$ LDHs containing different M^{II} ions.

3.2.1 X-ray Diffraction

Rietveld refinement has previously been undertaken with X-ray diffraction (XRD) data from the parent structure, $ZnAl_4$-NO_3. Due to disorder invoked by interlayer water molecules, this LDH was dehydrated prior to undertaking XRD measurements and subsequent structural analysis. Results from structure refinement indicate that Zn^{2+} cations occupy one half of the octahedral holes within the $Al(OH)_3$ layers, with some evidence for intralayer cation ordering. The $[ZnAl_4(OH)_{12}]^{2+}$ layers are arranged with *abab* stacking sequence and interlayer separation of 8.32 Å. The structure exhibits monoclinic symmetry with a = 5.1976(8) Å, b = 16.647(2) Å, c = 10.4054(2) Å, β = 119.966(16)°, and space group $P2_1/c$.[31]

The relative compositions of the $MM'Al_8$-NO_3 compounds are comparable to those of the MAl_4-NO_3 materials. It can be expected therefore, that the structures of both families will also be analogous: nitrate-intercalated layered double hydroxides with metal ions incorporated into vacancies in the gibbsite $Al(OH)_3$ layers. Indeed, X-ray diffraction data obtained from the novel materials are typical of LDHs – intense 'basal' reflections corresponding to diffraction from lattice planes parallel to the layers were evident in each case (Figure 3.1).

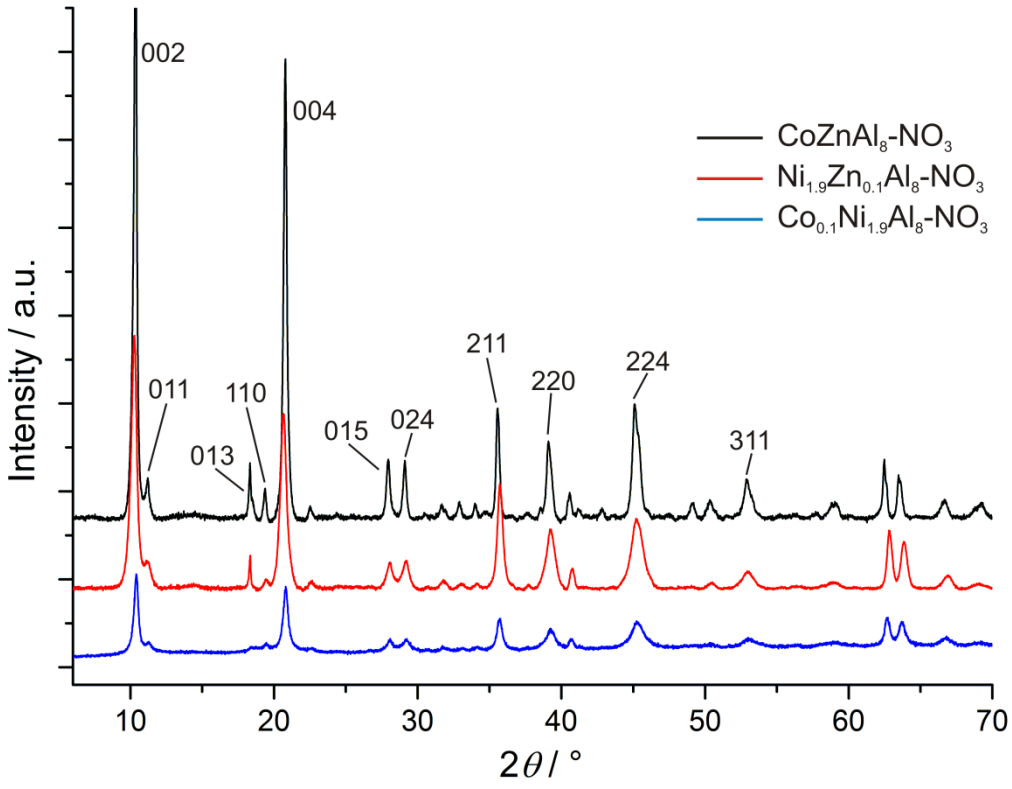

Figure 3.1: X-ray diffraction data for the three-metal LDHs.

By converting the symmetry of the $ZnAl_4$-NO_3 unit cell to become approximately orthorhombic, the lattice parameters from refinement become: a = 5.20 Å, b = 16.65 Å, c = 9.01 Å, and $\beta \sim 90°$. This alteration to the unit cell allowed high-resolution diffraction data for the MM'Al_8-NO_3 materials to be comprehensively indexed. A similar model to the parent material was used for this analysis, $a \sim 5.3$ Å, $b \sim 8.9$ Å and $c \sim 17.0$ Å, but with a slightly expanded c-parameter due to the presence of interlayer water in the hydrated species (Table 3.2). Additionally, the b- and c-parameters were swapped to a non-standard setting where the (00l) Bragg planes lie parallel to the layers, in order to facilitate comparison with similar LDHs. The structural similarity between the binary and ternary 1 : 4 systems suggests an analogous model applies – including, perhaps, ordering of the M^{2+} cations in half of the octahedral vacancies in the $Al(OH)_3$ layers. In a similar study, Britto and Kamath did not observe such ordering in an analogous LDH formed from $ZnSO_4$ and bayerite; they instead recorded a M^{2+} : M^{3+} ratio of closer to 1 : 3 in the layers due to some replacement of Al^{3+} in the bayerite by Zn(II), which could be the reason for this disorder.[11] The ordering of metal ions in the octahedral holes of the MM'Al_8-NO_3 materials is not unexpected given the contrast in size and charge of the metal cations.[32] In comparable fashion to the two-metal $NiAl_4$-NO_3 LDH, the Ni-containing materials have significantly lower crystallinity than the other three-metal systems.

Table 3.2: Refined unit cell parameters for the MM'Al_8-NO_3 LDHs.

LDH	***a*-parameter / Å**	***b*-parameter / Å**	***c*-parameter / Å**
$CoZnAl_8$-NO_3	5.282 (5)	8.904 (9)	17.03 (1)
$Ni_{1.9}Zn_{0.1}Al_8$-NO_3	5.322 (9)	8.909 (7)	17.00 (2)
$Co_{0.1}Ni_{1.9}Al_8$-NO_3	5.306 (7)	8.890 (6)	17.06 (2)

*A list of indexed reflections for each compound is provided in Appendix C.

Attempts at detailed Rietveld refinement using high-resolution XRD data for each material proved problematic owing to the low crystallinity observed. The presence of interlayer water molecules and random orientation of the nitrate guest species within the layers resulted in significant disorder in each case.

3.2.2 IR Spectroscopy

Infrared (IR) spectra for the MM'Al_8-NO_3 materials are provided in Figure 3.2.

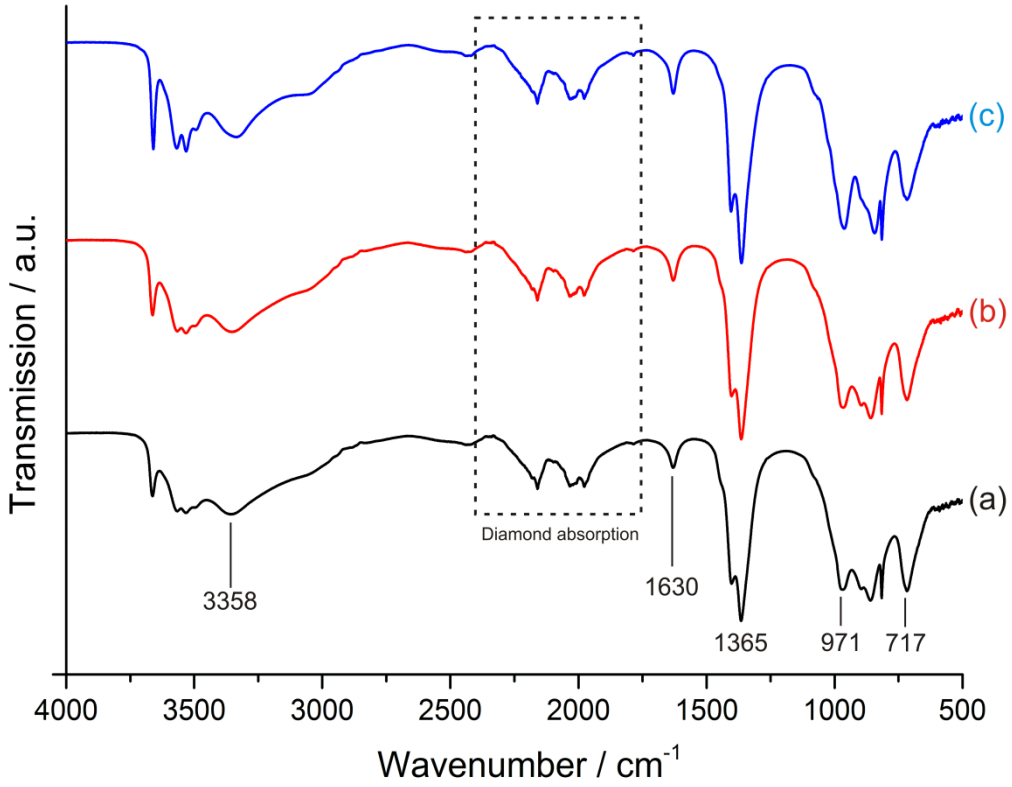

Figure 3.2: IR spectroscopy data for (a) $Co_{0.1}Ni_{1.9}Al_8$-NO_3 (b) $Ni_{1.9}Zn_{0.1}Al_8$-NO_3 and (c) $CoZnAl_8$-NO_3.

The IR data are as expected for an LDH; the broad absorbance at *ca.* 3358 cm^{-1} and the band at 971 cm^{-1} are consistent with the respective O–H stretching and bending vibrations of co-intercalated water molecules and hydroxide groups in the positively-charged layers. The low intensity band at 1630 cm^{-1} corresponds to the δ-vibration of the interlayer water molecules. Bands below *ca.* 800 cm^{-1} are attributable to Al–O and M–O lattice vibrations; in all three spectra, a strong absorption is seen at 717 cm^{-1}. The presence of nitrate in the LDHs is confirmed by the absorbance observed at 1365 cm^{-1}. This band is assigned to N=O, the band appearing split due to overlap of the symmetric and antisymmetric vibration signals.

3.2.3 Thermogravimetric Analysis

Thermogravimetric analysis (TGA) was performed to confirm the number of co-intercalated water molecules in each structure. TGA data for the MM'Al_8-NO_3 LDHs are provided in Figure 3.3.

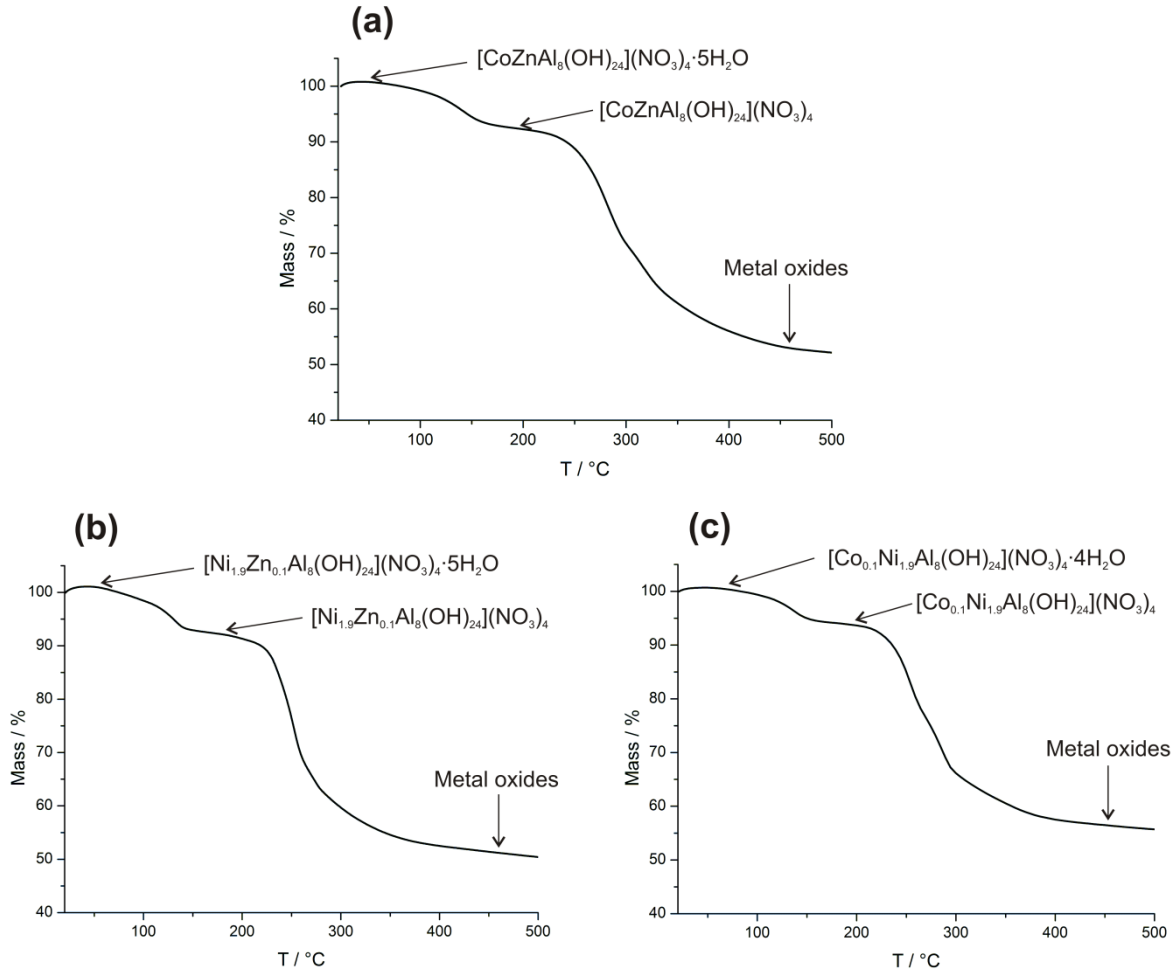

Figure 3.3: TGA data for (a) $CoZnAl_8$-NO_3, (b) $Ni_{1.9}Zn_{0.1}Al_8$-NO_3 and (c) $Co_{0.1}Ni_{1.9}Al_8$-NO_3.

Mass loss occurs in two stages for each LDH. TGA data for $CoZnAl_8$-NO_3 are provided in Figure 3.3(a) and are described here as a representative example. The first stage of mass loss (*ca.* 8.2 %) begins below 100 ℃ and is complete by 200 ℃. This corresponds to loss of the interlayer water molecules, resulting in the dehydrated compound $[CoZnAl_8(OH)_{24}](NO_3)_4$. Above 250 ℃, there is simultaneous dehydration of the layers and decomposition of the nitrate guest (*ca.* 40.1 %) to yield $[CoZnAl_8O_{12}]O_2$, which corresponds to the individual metal oxides. Percentage mass losses for all MM'Al_8-NO_3

LDHs observed in the TGA data agree well with the elemental compositions obtained using CHN and EDX analyses.

3.2.4 Transmission Electron Microscopy

Transmission Electron Microscopy (TEM) studies were undertaken to establish the morphology of the MM'Al_8-NO_3 product particles. Figure 3.4(a) contains a TEM image of the $CoZnAl_8$-NO_3 sample. It is clear that the particles exhibit hexagonal platelet morphology, which is consistent with particle shape observed for the $LiAl_2$-X and MAl_4-NO_3 LDHs, and is indicative of a material with pseudo-hexagonal symmetry.

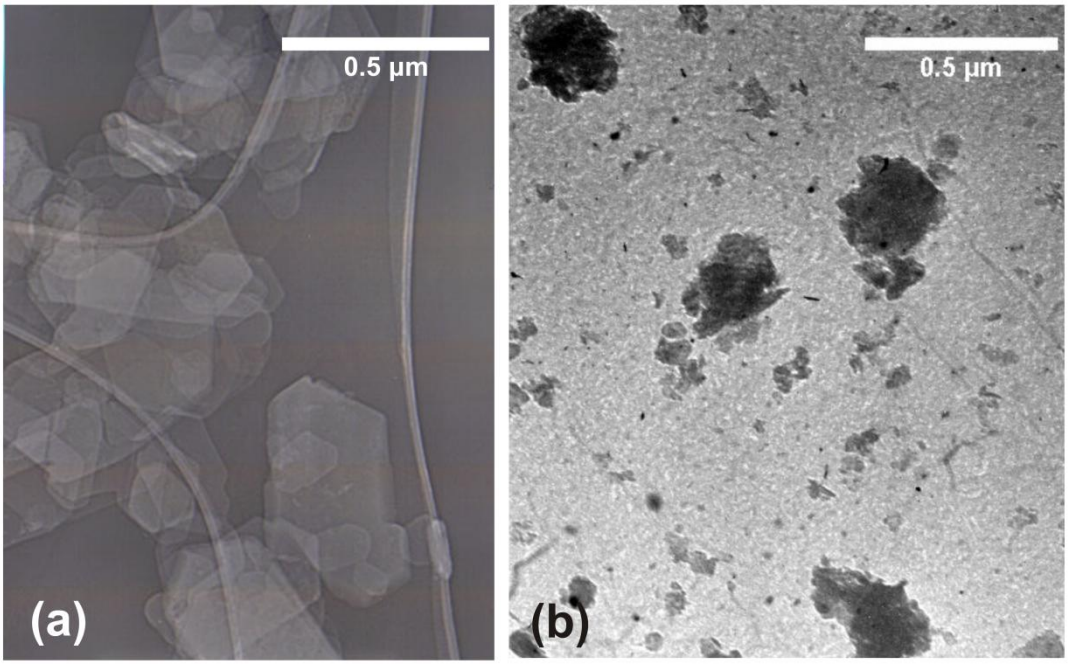

Figure 3.4: Transmission electron micrographs of (a) $CoZnAl_8$-NO_3 and (b) activated gibbsite $Al(OH)_3$.

Wang and O'Hare investigated the topotactic intercalation reaction of lithium salts into gibbsite to form LDH nanorods.[33] They found that the rod-like morphology of the gibbsite precursor particles was conserved in the product phase. In the case of the LDH particles shown in Figure 3.4(a), the morphology does not resemble that of the activated gibbsite starting material in Figure 3.4(b), particles of which are generally smaller and considerably disordered in size and shape. This difference is perhaps indicative of a process that is not topotactic.

3.2.5 Further synthesis of $[MM'Al_8(OH)_{24}](NO_3)_4{\cdot}yH_2O$ systems

The synthesis of ternary LDHs containing other transition metal cations was attempted. The ionic radii of Fe^{2+} (0.780 Å), and Cu^{2+} (0.730 Å) cations are similar to those of Co^{2+} (0.735 Å), Ni^{2+} (0.700 Å), and Zn^{2+} (0.745 Å), which make them ideal candidates for incorporating into similar three-metal systems.[34] Recent reports by Chitrakar *et al.* and Kameda *et al.* detail the synthesis of a $FeAl_4$-Cl LDH.[35, 36] Both groups employed the coprecipitation method with $AlCl_3$ and $FeCl_2$ starting materials, and in each case only small amounts of very poorly crystalline LDH products were formed. Impurity phases, such as goethite (FeOOH), were formed in excess. The formation of pure-phase ternary LDHs containing Fe^{2+} was therefore attempted using gibbsite and the hydrothermal method. The products of all reactions involving Fe^{2+} salts exhibited diffraction patterns that were dominated by Fe_2O_3 and boehmite (AlOOH) impurity phases. No reflections corresponding to a pure LDH phase were observed, which was likely due to the competing oxidation of Fe^{2+} to Fe^{3+} at such elevated temperatures.

The $[CuAl_4(OH)_{12}](NO_3)_2{\cdot}2.5H_2O$ LDH, with 1 : 4 metal ratio, was reported by Fogg and co-workers in 2004.[7] The hydrothermal synthesis of analogous three-metal systems containing Cu^{2+} was therefore attempted. The diffraction data in Figure 3.5 illustrate that formation of three novel copper-containing ternary LDHs was successful. The XRD data are very similar to those of the other $MM'Al_8$-NO_3 materials, with basal spacings of 8.5 – 8.6 Å. Bragg reflections could be indexed using similar lattice parameters to those detailed in Section 3.2.1, $a \sim 5.3$ Å, $b \sim 8.9$ Å, and $c \sim 17.0$ Å, suggesting a similar structural model applies. Despite attempts to optimise sample purity by altering the synthesis conditions, the copper-containing LDHs could only be formed alongside a crystalline impurity phase, $Cu_2(NO_3)(OH)_3$. The X-ray diffraction pattern of the Ni/Cu/Al system indicates a product of lower crystallinity, as is also observed for the nickel-containing $MM'Al_8$-NO_3 materials discussed in Section 3.2.1.

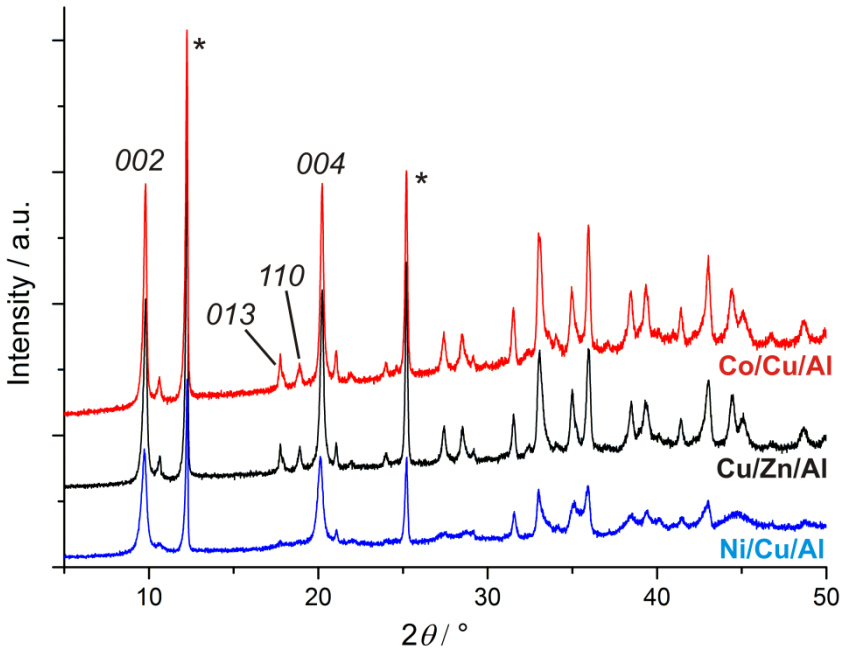

Figure 3.5: X-ray diffraction data for the three novel copper-containing LDHs (Reflections labelled * correspond to the $Cu_2(NO_3)(OH)_3$ impurity).

Further analysis of the Cu^{2+} ternary LDHs was complicated by the presence of the $Cu_2(NO_3)(OH)_3$ impurity. The elemental compositions of each material were estimated using data from CHN and EDX analysis (Table 3.3). A 1 : 1 ratio of Cu : M was evident for LDHs with M = Co and Zn, however a sensible formula for the Ni/Cu/Al LDH could not be derived from elemental analysis data. EDX studies of this compound illustrated that individual particles contained either an excess of nickel and aluminium (corresponding to a two-metal LDH) or an excess of copper (corresponding to $Cu_2(OH)_3NO_3$). Considering this information, it is likely that the LDH in this case contains a significant excess of Ni >> Cu, which is consistent with the previously discussed nickel-containing ternary systems.

Table 3.3: Elemental compositions and basal spacings for the copper-containing ternary LDHs.

Metal ions		**Composition**	***d*-spacing / Å**
M	**M'**		
Co	**Cu**	$[Co_{1.0}Cu_{1.0}Al_8(OH)_{24}](NO_3)_4 \cdot 7H_2O$ + $y[Cu_2(OH)_3NO_3]$	8.5 (1)
Ni	**Cu**	*	8.6 (1)
Cu	**Zn**	$[Cu_{1.0}Zn_{1.0}Al_8(OH)_{24}](NO_3)_4 \cdot 8H_2O$ + $y[Cu_2(OH)_3NO_3]$	8.5 (1)

* illustrates that a consistent formula could not be derived for this system.

3.3 Monitoring changes to the LDH intralayer composition

3.3.1 Tuning the M(II) : M'(II) ratio

It is clear that in the case of the ternary MM'Al_8-NO_3 LDHs discussed in the preceding sections, using a 1 : 1 mixture of metal salts does not always result in a corresponding 1 : 1 ratio of M^{2+} cations in the product. Analysis of the metal compositions gives a ratio of approximately 1 : 1 only for the LDH produced from the Co/Zn/Al system and apparently for the Cu/Zn/Al and Co/Cu/Al materials. The Ni/Zn/Al and Co/Ni/Al LDH (and most likely the Ni/Cu/Al) systems contain a significant excess of nickel cations; the M^{2+} : Ni^{2+} ratio is approximately 1 : 40. It appears, therefore, that where Ni^{2+} is present in the reaction mixture, it is incorporated into the $Al(OH)_3$ with a high degree of selectivity over the other metal ions, producing an LDH which is essentially the $NiAl_4$-NO_3 material. This finding is supported by the fact that the XRD patterns of the products from the M/Ni reactions closely resemble those of $NiAl_4$-NO_3.

The preferential incorporation of transition metal ions into the LDH layers can be summarised as follows:

$$Ni^{2+} >> Co^{2+} \approx Cu^{2+} \approx Zn^{2+}$$

This series generally correlates well with the radii of the ions for the M^{2+} cations. Shannon-Prewitt radii for octahedrally coordinated ions are as follows: Co^{2+} 0.745 Å; Ni^{2+} 0.690 Å; Cu^{2+} 0.730 Å; Zn^{2+} 0.750 Å.[34, 37] It is clear that the smaller Ni^{2+}, with higher charge-density, intercalates preferentially over the larger Co^{2+}, Cu^{2+} and Zn^{2+} cations, which are close in size and show approximately the same propensity to intercalate. Additionally, a recent DFT study by Yan *et al.* using a range of $[M_2Al(H_2O)_9(OH)_4]^{3+}$ clusters in LDHs found that the 2Ni-Al cluster was more stable than the 2Co-Al, 2Cu-Al, and 2Zn-Al analogues due to several factors derived from the electronic structure of the Ni^{2+} cation.[38] It is possible that effects such as Jahn-Teller distortion and binding energies have some influence on the stability of the MM'Al_8-NO_3 LDHs.

As a result of these observations, further experiments were performed in which the ratio of M^{2+} solutions was varied to tune the metal contents of the LDHs. Elemental analysis using EDX was undertaken on the products from these experiments and the results are depicted in Figure 3.6. The reagent and product cobalt and nickel percentages displayed

in this figure were calculated with respect to the other transition metal ion present, *i.e.* Product %M(II) = Observed %M(II) / [%M(II) + %M'(II)].

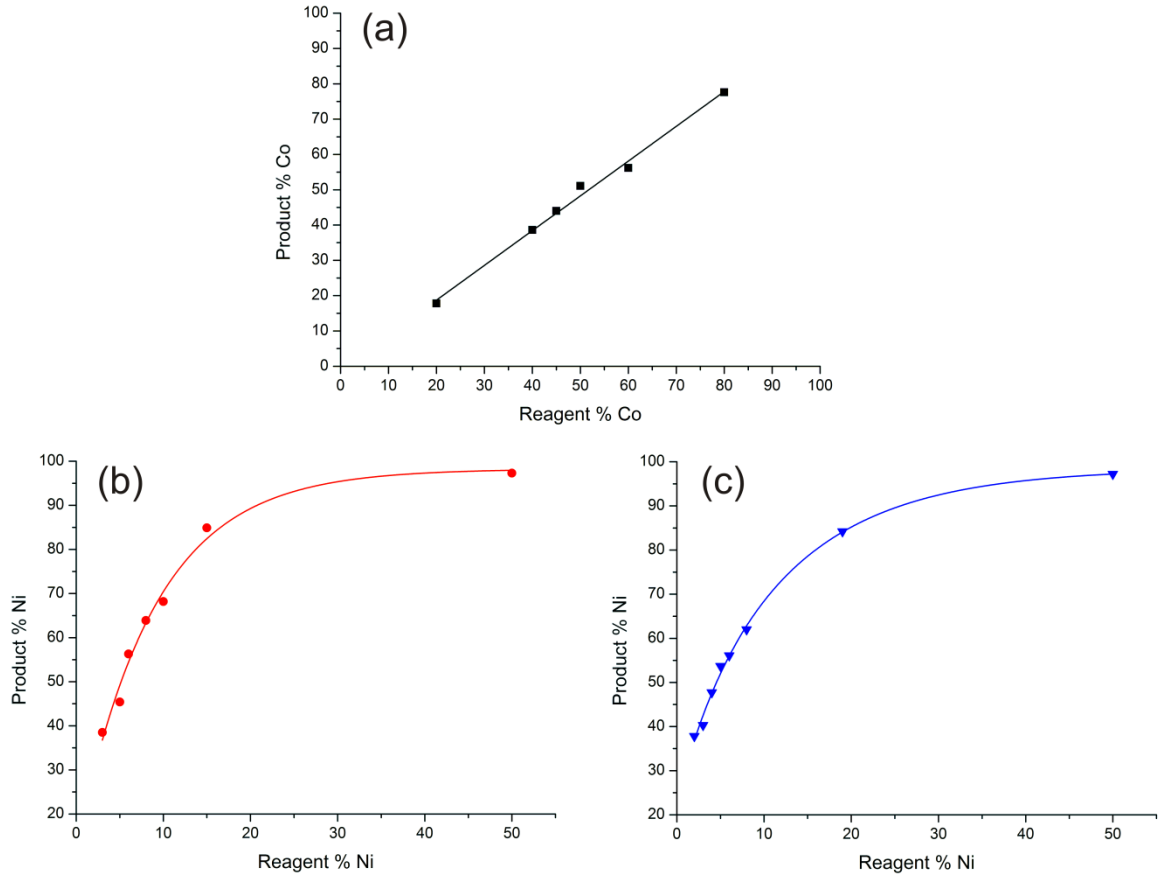

Figure 3.6: Scatter graphs illustrating the relationship between % metal ion in the reagents and products for (a) %Co in $Co_xZn_{2-x}Al_8$-NO_3 (b) %Ni in $Ni_xZn_{2-x}Al_8$-NO_3 (c) %Ni in $Co_xNi_{2-x}Al_8$-NO_3. The fitted lines are provided only as a guide for the trend in each series, and are not based on any physical model.

It is apparent from these results that, by varying the metal composition in the reaction mixture, it is possible to tune the amount of each metal incorporated into the LDH layers. The ratio of Co^{2+} : Zn^{2+} in the product material varies approximately linearly with the change in starting material ratio. In this case, the percentage Co^{2+} incorporated into the LDH layers corresponds to the percentage Co^{2+} in the reaction mixture. This indicates a similar propensity for the two different cations to intercalate. For the LDH materials containing nickel, a significant deviation from a 1 : 1 ratio of the starting materials is required to achieve equal incorporation of M^{2+} ions in the product. A 17 : 1 excess of $Zn(NO_3)_2$ is required to synthesise $NiZnAl_8$-NO_3, and 21 : 1 excess of $Co(NO_3)_2$ is required to form $CoNiAl_8$-NO_3. It is expected that a similar relationship would be observed for a pure phase $Ni_xCu_{2-x}Al_8$-NO_3 system.

3.3.2 Synthesis of $[MM'M''Al_{12}(OH)_{36}](NO_3)_6 \cdot yH_2O$

By restacking delaminated layered double hydroxides, Johnsen and co-workers have successfully formed LDHs with alternating layers containing combinations of cobalt, aluminium, magnesium and gallium cations.[39] The tolerance of MAl_4-LDH systems for incorporating a variety of metal ions in the octahedral holes in the layers was therefore investigated. Bulk synthesis of an $Al(OH)_3$ derived LDH containing Co, Ni, Zn and Al was attempted using an analogous hydrothermal procedure to that described in Section 3.2. The preference for nickel incorporation was taken into account in the volume ratios of the starting materials in an attempt to incorporate a significant proportion of each cation in the product: 4.8 mL $Co(NO_3)_2 \cdot 6H_2O$, 0.4 mL $Ni(NO_3)_2 \cdot 6H_2O$, and 4.8 mL $Zn(NO_3)_2 \cdot 6H_2O$. CHN and EDX analyses undertaken on the product phase confirmed the incorporation of four metal ions into the LDH layers (Appendix B).

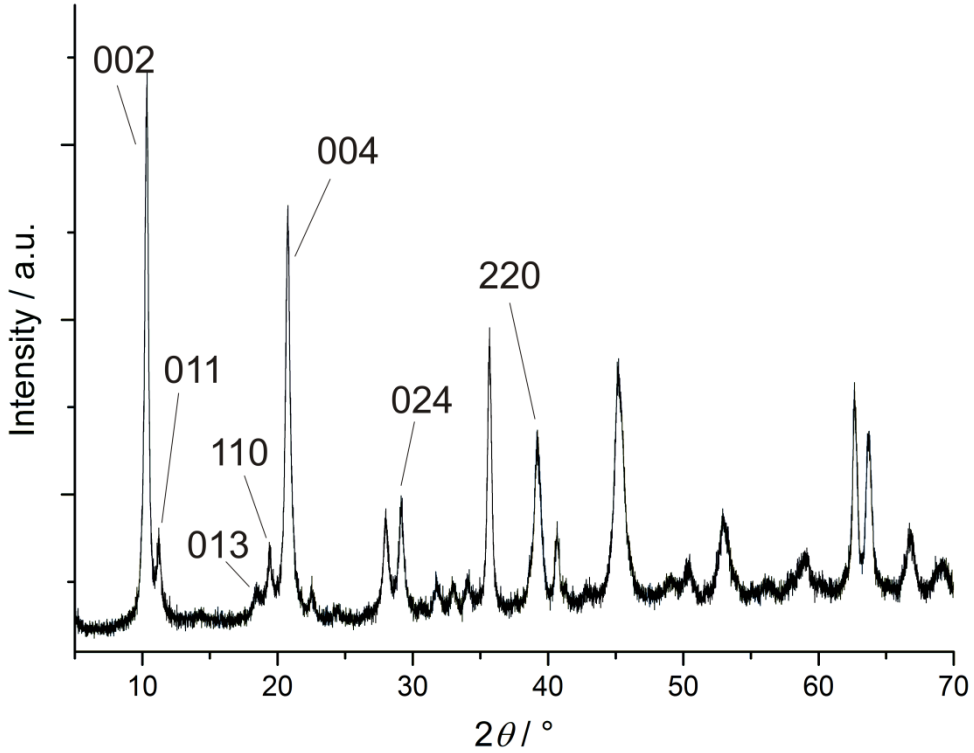

Figure 3.7: Powder XRD data for the $[Co_{0.5}Ni_{1.1}Zn_{0.4}Al_8(OH)_{24}](NO_3)_4 \cdot 2H_2O$ LDH.

The chemical formula of the new material is $[Co_{0.5}Ni_{1.1}Zn_{0.4}Al_8(OH)_{24}](NO_3)_4 \cdot 2H_2O$. Successful LDH formation is indicated by the XRD data in Figure 3.7, which can be indexed to a structure analogous to the MAl_4-NO_3 compounds, with lattice parameters $a \sim 5.3$ Å, $b \sim 8.9$ Å, and $c \sim 17.0$ Å. The presence of non-basal reflections in the diffraction pattern also suggests some degree of intralayer order, which is perhaps

surprising given the number of different cations present on the octahedral sites. The quantity of Ni^{2+} ions in $[Co_{0.5}Ni_{1.1}Zn_{0.4}Al_8(OH)_{24}](NO_3)_4{\cdot}2H_2O$ is slightly greater than Co^{2+} and Zn^{2+}, with the M^{2+} : Al^{3+} ratio once again 1 : 4.

3.3.3 Discussion

The ability to control the extent of metal ion incorporation in the LDH layers presents an interesting opportunity to optimise the physical and chemical properties of these systems. The selective intercalation chemistry of the MAl_4-NO_3 LDHs has already been studied and is considered an area for further exploration with the new ternary systems. Previous investigations into the reactivity of the MAl_4-NO_3 materials illustrate that the preferential intercalation of various anionic isomers is temperature-dependent.[9] For instance, the incorporation of 2, 6-naphthalenedisulfonic acid in preference to the 1,5-naphthalenedisulfonic acid isomer, over the range $20 \leq T / °C \leq 100$, follows an opposing trend for the $CoAl_4$-NO_3 and $ZnAl_4$-NO_3 systems. It is possible, therefore, that by tuning the concentration of the cobalt and zinc cations in the LDH layers, this intercalation reactivity could be optimised for one isomer over the entire temperature range.

3.4 Ion-exchange intercalation chemistry of three-metal LDHs

To demonstrate the characteristic LDH reactivity of the $MM'Al_8$-NO_3 materials, their intercalation chemistry was explored. Five simple organic anions were selected for investigation: fumarate, succinate, phthalate, terephthalate and 2-naphthalenesulfonate (the chemical structures of which are provided in Appendix C). These species were chosen not only for their suitability in observing the basic fundamental reactivity of these novel LDHs, but also because their functional groups are representative of those found in useful organic molecules such as drugs and herbicides.[40]

Most intercalation reactions were undertaken using the LDHs with cation ratios detailed at the beginning of Section 3.2. However, to illustrate the comparable behaviour of the metal-tuned systems, reactions with phthalate were carried out with LDHs containing approximately a 1 : 1 ratio of M : M'. For all intercalation reactions, 0.2 g of the LDH was added to 10 mL of water containing a five- or ten-fold excess of the guest ions and

the mixtures stirred for periods of 2 – 30 hours. A full list of reaction conditions is provided in Chapter 7. It proved possible to intercalate all five organic anions into the MM'Al_8-NO_3 LDHs. The compositions of the products calculated from elemental analysis data, and the basal spacing of each compound calculated from X-ray diffraction data, are summarised in Tables 3.4-3.6.

Table 3.4: Summary of XRD and elemental analysis data for the organic intercalates of $Co_xZn_{2-x}Al_8$-NO_3.

Guest	Formula	*d*-spacing / Å
Fumarate	$[Co_{1.0}Zn_{1.0}Al_8(OH)_{24}](C_4H_2O_4)_{1.5}(CO_3)_{0.5}\cdot 4.5H_2O$	10.7(1)
Succinate	$[Co_{1.0}Zn_{1.0}Al_8(OH)_{24}](C_4H_4O_4)_{1.7}(CO_3)_{0.3}\cdot 6H_2O$	10.7(1)
Terephthalate	$[Co_{1.0}Zn_{1.0}Al_8(OH)_{24}](C_8H_4O_4)_{1.7}(CO_3)_{0.3}\cdot 9.5H_2O$	14.0(1)
2-naphthalenesulfonate	$[Co_{1.0}Zn_{1.0}Al_8(OH)_{24}](C_{10}H_7SO_3)_3(CO_3)_{0.5}\cdot 8H_2O$	17.8(1)
Phthalate	$[Co_{1.0}Zn_{1.0}Al_8(OH)_{24}](C_8H_4O_4)_{1.6}(CO_3)_{0.4}\cdot 10H_2O$	14.5(1)

Table 3.5: Summary of XRD and elemental analysis data for the organic intercalates of $Ni_xZn_{2-x}Al_8$-NO_3.

Guest	Formula	*d*-spacing / Å
Fumarate	$[Ni_{1.9}Zn_{0.1}Al_8(OH)_{24}](C_4H_2O_4)_{1.8}(CO_3)_{0.2}\cdot 8H_2O$	10.7(1)
Succinate	$[Ni_{1.9}Zn_{0.1}Al_8(OH)_{24}](C_4H_4O_4)_{1.7}(CO_3)_{0.3}\cdot 7H_2O$	10.7(1)
Terephthalate	$[Ni_{1.9}Zn_{0.1}Al_8(OH)_{24}](C_8H_4O_4)_{1.8}(CO_3)_{0.2}\cdot 10.5H_2O$	14.0(1)
2-naphthalenesulfonate	$[Ni_{1.9}Zn_{0.1}Al_8(OH)_{24}](C_{10}H_7SO_3)_{2.9}(CO_3)_{0.55}\cdot 7H_2O$	17.9(1)
Phthalate	$[Ni_{1.1}Zn_{0.9}Al_8(OH)_{24}](C_8H_4O_4)_{1.6}(CO_3)_{0.4}\cdot 10H_2O$	14.4(1)

Table 3.6: Summary of XRD and elemental analysis data for the organic intercalates of $Co_xNi_{2-x}Al_8$-NO_3.

Guest	Formula	*d*-spacing / Å
Fumarate	$[Co_{0.1}Ni_{1.9}Al_8(OH)_{24}](C_4H_2O_4)_{1.8}(CO_3)_{0.2}\cdot 7H_2O$	10.8(1)
Succinate	$[Co_{0.1}Ni_{1.9}Al_8(OH)_{24}](C_4H_4O_4)_{1.9}(CO_3)_{0.1}\cdot 10.5H_2O$	10.8(1)
Terephthalate	$[Co_{0.1}Ni_{1.9}Al_8(OH)_{24}](C_8H_4O_4)_{1.9}(CO_3)_{0.1}\cdot 11H_2O$	14.0(1)
2-naphthalenesulfonate	$[Co_{0.1}Ni_{1.9}Al_8(OH)_{24}](C_{10}H_7SO_3)_{2.9}(CO_3)_{0.55}\cdot 7H_2O$	17.9(1)
Phthalate	$[Co_{1.2}Ni_{0.8}Al_8(OH)_{24}](C_8H_4O_4)_{1.6}(CO_3)_{0.4}\cdot 10H_2O$	14.4(1)

3.4.1 X-ray Diffraction

X-ray diffraction data confirmed the complete replacement of nitrate ions in the interlayer region with the respective organic guest ion. The X-ray diffraction patterns of $CoZnAl_8$-NO_3 and $CoZnAl_8$-succinate are shown in Figure 3.8. (00*l*) Bragg reflections of the MM'Al_8-NO_3 materials were completely absent from the powder patterns of the products. New reflections were observed at higher *d*-spacings, which could be indexed on a similar unit cell to the starting material (a ~ 5.3 Å, b ~ 8.8 Å), but with an expanded *c*-parameter. Structural information for the LDH intercalate materials, derived from indexing of the XRD data, is provided in Appendix C.

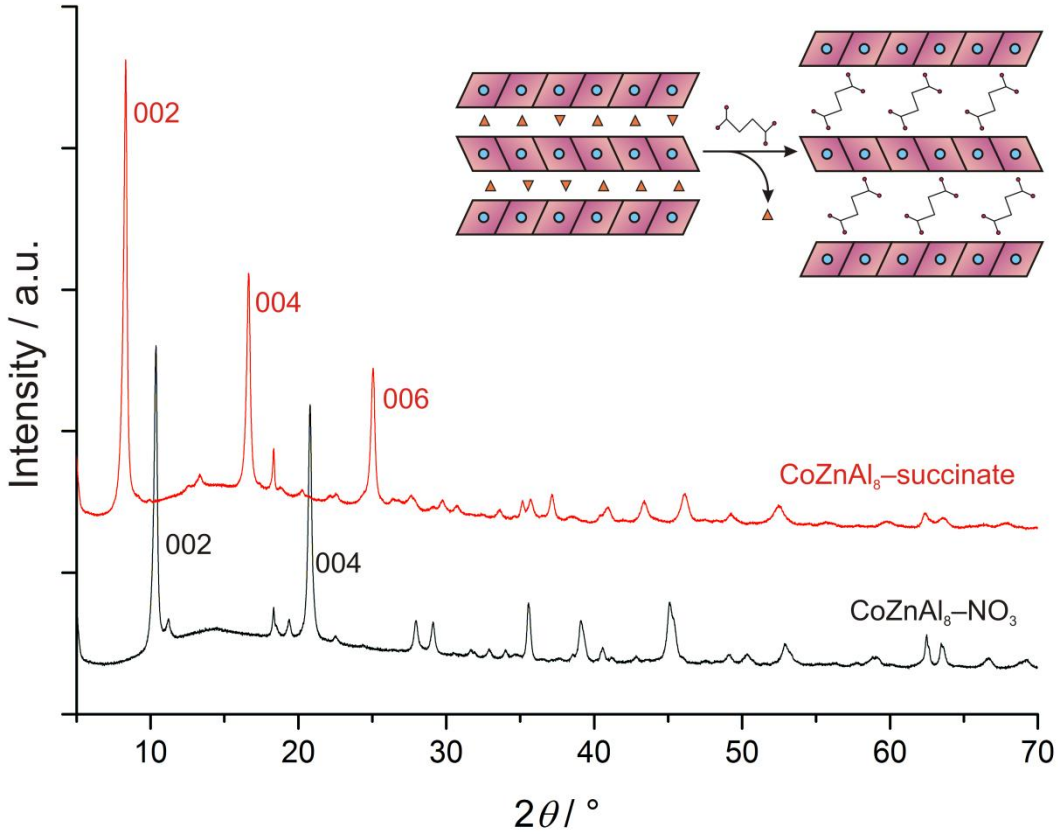

Figure 3.8: X-ray diffraction data for the host $CoZnAl_8$-NO_3 and product $CoZnAl_8$-succinate materials. INSET: Schematic illustrating succinate anion intercalation in place of nitrate anions, and the resulting impact upon the interlayer distance.

3.4.2 IR Spectroscopy

Complete substitution of the guest species is also supported by infrared spectroscopy data. Figure 3.9 contains IR spectra for the succinate intercalate of the $CoZnAl_8$-LDH, alongside reference spectra of sodium succinate and the host material.

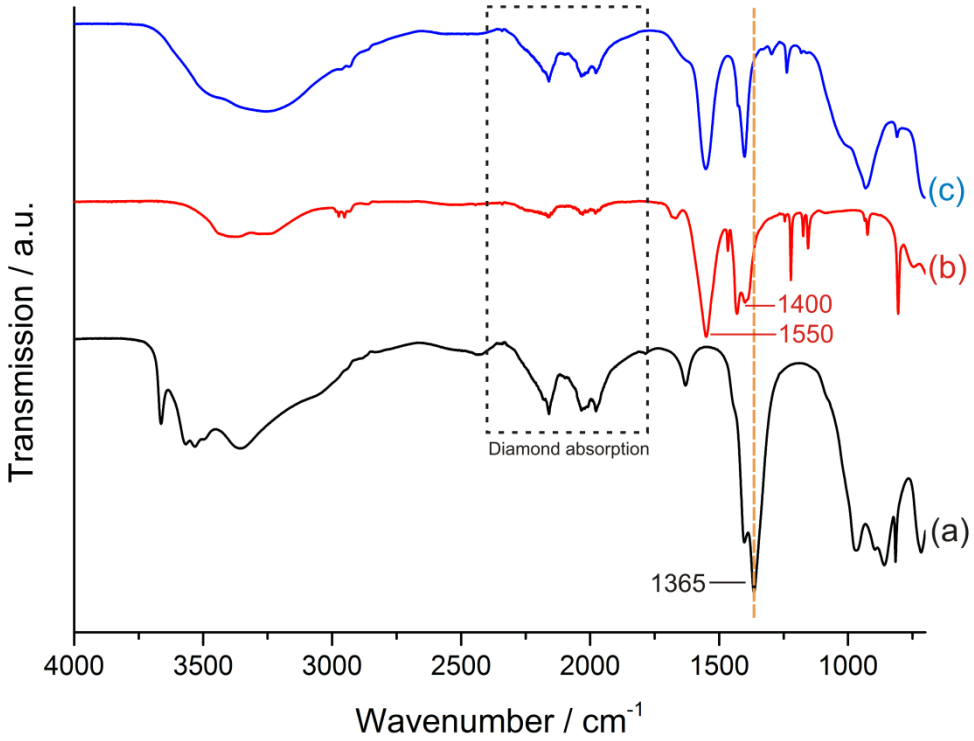

Figure 3.9: IR spectroscopy data for (a) $CoZnAl_8$-NO_3 (b) Na-succinate and (c) $CoZnAl_8$-succinate. The orange dotted line provides a guide for the eye.

The IR spectra of the product LDHs were found to display close similarity to those of the relevant guest species. Crucially, no absorptions attributable to the nitrate group at 1365 cm^{-1} and 1380 cm^{-1} were observed in the product spectrum, which confirmed that all of the starting material had been consumed. Instead, two strong absorption bands at 1550 cm^{-1} and 1400 cm^{-1}, corresponding to the carboxylate functional group of succinic acid, were observed. IR spectra for the additional four intercalates of $CoZnAl_8$-LDH were consistent with complete conversion of $CoZnAl_8$-NO_3 to the guest-intercalated species. Infrared spectroscopy also confirmed successful conversion of the $Ni_{1-x}Zn_xAl$-NO_3 and $Co_{1-x}Ni_xAl$-NO_3 analogues to the relevant carboxylate- and sulfonate-intercalated LDHs.

3.4.3 Thermogravimetric analysis

Thermogravimetric analysis was employed to establish the number of co-intercalated water molecules in each intercalation product. The presence of organic guest species between the LDH layers was also verified by observing the decomposition pathways of the products. TGA data for $CoZnAl_8$-succinate LDH are provided in Figure 3.10.

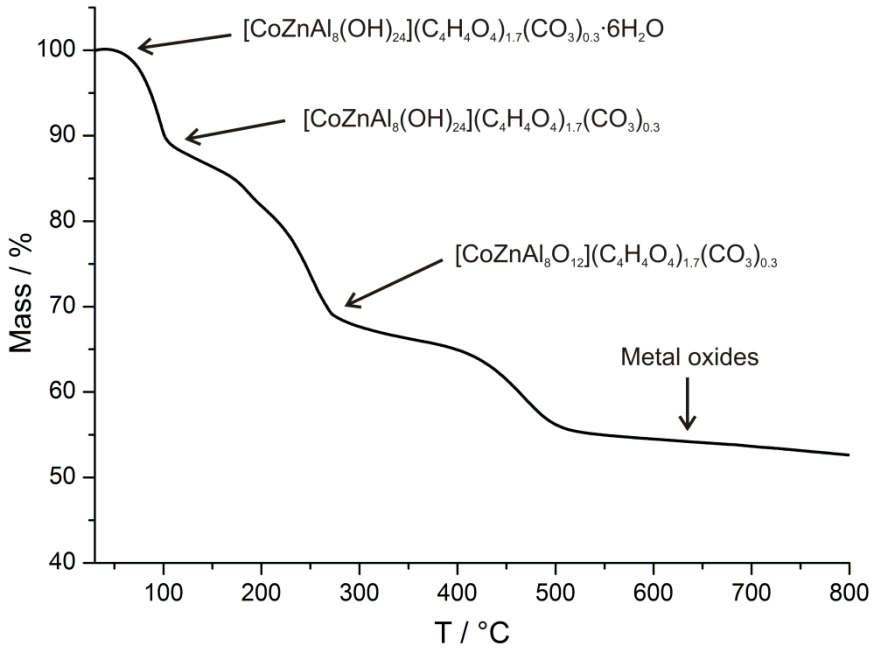

Figure 3.10: Thermogravimetric analysis curve for CoZnAl-succinate.

An initial mass loss of 10.4 % is observed upon heating the $CoZnAl_8$-succinate LDH from room temperature to 103 °C. This corresponds to dehydration of the sample and loss of water molecules from the interlayer regions. A second loss in sample mass of 20.8 % is observed upon heating to 275 °C, which is indicative of further water loss, this time from the intralayer regions. Decomposition of the organic guest species and breakdown of the layered structure occurs beyond 400 °C, with a further 13.5 % loss by 520 °C leaving only metal oxides with the nominal composition $CoZnAl_8O_{14}$. TGA traces for the other intercalate-LDHs are similar to the data described above.

3.4.4 Transmission Electron Microscopy

Transmission electron microscopy studies were undertaken on the products from intercalation reactions. The results indicated that product particle size and shape were comparable to those of the host materials. Figure 3.11 contains TEM images of the $CoZnAl_8$-succinate material. Clearly, particles exhibit hexagonal platelet morphology analogous to the nitrate-intercalated host.

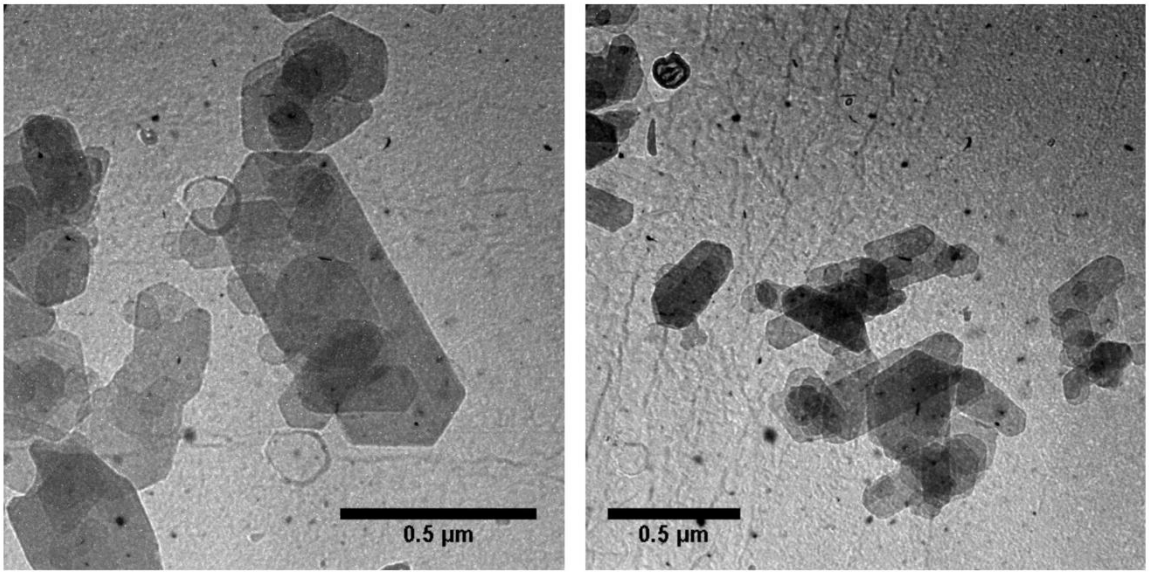

Figure 3.11: Transmission electron micrographs of $CoZnAl_8$-succinate.

3.5 *In situ* X-ray diffraction studies of LDH intercalation reactions

The intercalation of inorganic and organic anions into LDHs results in a structure change that is ideal for study using X-ray diffraction. Because of the difference in *d*-spacing of the basal reflections of the host and product materials, corresponding to the distance between the positively-charged layers in each structure, the process of guest ion intercalation can be effectively monitored. Interesting reaction intermediates, staging, and selective ion-exchange have been detected in previous *in situ* investigations of LDH intercalation reactions.[41-47]

The incorporation of guest species with carboxylate and sulfonate functional groups into LDHs has been the focus of much research; in addition to their industrial and commercial relevance, such anions often exhibit interesting intercalation chemistry. Incorporation of succinate into $[LiAl_2(OH)_6]Cl{\cdot}H_2O$ takes place *via* a 'second-stage' intermediate, in which chloride and succinate anions occupy alternating LDH layers.[48] Carboxylate intercalation reactions involving the parent MAl_4-NO_3 materials, as well as the $[LiAl_2(OH)_6]NO_3{\cdot}H_2O$ species, proceed through one-step transformation of the host to the product. It was of particular interest therefore, to establish the mechanism of intercalation involving the novel tertiary MM'Al_8-NO_3 LDHs.

An advantage of studying these reactions during the commissioning phase of Beamline I12 was their appropriateness for initial feasibility studies and to assess data quality from

in situ XRD measurements. In all cases, the products of reactions undertaken during synchrotron beamtime were confirmed using laboratory XRD data analysis.

3.5.1 Monitoring intercalation reactions using energy-dispersive XRD at Diamond Light Source

In situ energy-dispersive X-ray diffraction (EDXRD) was employed to probe the intercalation of organic carboxylate species into the three novel LDHs: $CoZnAl_8$-NO_3, $Ni_{1.9}Zn_{0.1}Al_8$-NO_3, and $Co_{0.1}Ni_{1.9}Al_8$-NO_3. This was undertaken in an attempt to elucidate information about the mechanisms of these reactions. Carboxylate intercalation into LDHs can be a rapid process, often occurring to completion in under a minute at room temperature. In order to monitor the progress of the reaction therefore, it was necessary to use a syringe pump to add the guest solution dropwise to a suspension of the host material. As a result, kinetic parameters could not be extracted for these reactions. Energy-dispersive diffraction studies of LDH intercalation reactions in this section were undertaken using a refurbished version of the Oxford-Daresbury hydrothermal cell, discussed in Chapter 2.[49]

3.5.1.1 Shifted EDXRD Detector Configuration

Experiments detailed in the following section (Section 3.5.1.2) were carried out during 'in-house' beamtime as part of the commissioning phase of Beamline I12. EDXRD studies were undertaken using the 23-element, semi-annular, Ge-detector. The radial 'take-off' angle, 2θ, for each element in the detector is 5° and the I12 energy range spans $50 \leq E$ / keV ≤ 150. Consequently, the observed range of q values in this set-up is limited to $2.2 \leq q$ (Å^{-1}) ≤ 6.4.

In order to monitor systems outside of this q range therefore (*i.e.* materials such as layered double hydroxides that exhibit reflections at $d \geq 2.85$ Å ($q \leq 2.2$ Å^{-1})), an alternative detector configuration was adopted. This configuration was trialled for the first time in May 2010. It was implemented by shifting the EDXRD detector orthogonally with respect to the beam path, thus altering the respective take-off angles for each detector element. The increased range of detector angles facilitated the detection of reflections over a considerably enlarged d range. However, no standardised q calibration

was available for this configuration, and q values were therefore determined relative to a sample of highly crystalline TiO_2.

Use of the 'shifted-detector configuration' required both collimator slits to be removed from the diffracted-beam path to enable unobstructed passage of the beam to each element in the detector. This had the unfavourable effect of reducing the overall resolution of Bragg reflections, in addition to increasing the intensity of some fluorescence peaks.

3.5.1.2 The first *in situ* experiments on Beamline I12

The room-temperature intercalation of phthalate anions into $CoZnAl_8$-NO_3, $Ni_{1.9}Zn_{0.1}Al_8$-NO_3, and $Co_{0.1}Ni_{1.9}Al_8$-NO_3, was investigated. In each case, the LDH was stirred in a borosilicate tube with deionised water. After a few minutes, an aqueous solution containing a 10-fold excess of phthalate was added drop-wise to the reaction mixture and changes in the diffraction data were monitored. A 3D stack plot containing data from the reaction of phthalate with $CoZnAl_8$-NO_3 is shown in Figure 3.12. At the outset of the reaction, the (002) Bragg reflection of the $CoZnAl_8$-NO_3 starting material is observed at q = 0.74 $Å^{-1}$ (d = 8.5 Å). After 14 minutes, signalling the start of phthalate addition, the starting material reflection declines as the product (002) Bragg reflection appears at q = 0.42 $Å^{-1}$. The product reflection position corresponds to a d spacing of *ca.* 15.0 Å, which is consistent with the data in Table 3.4 and previously reported values for a phthalate intercalated LDH. Additional peaks visible in the plot correspond to fluorescence from heavy elements, such as lead and indium, that are found in hardware in the experimental hutch.

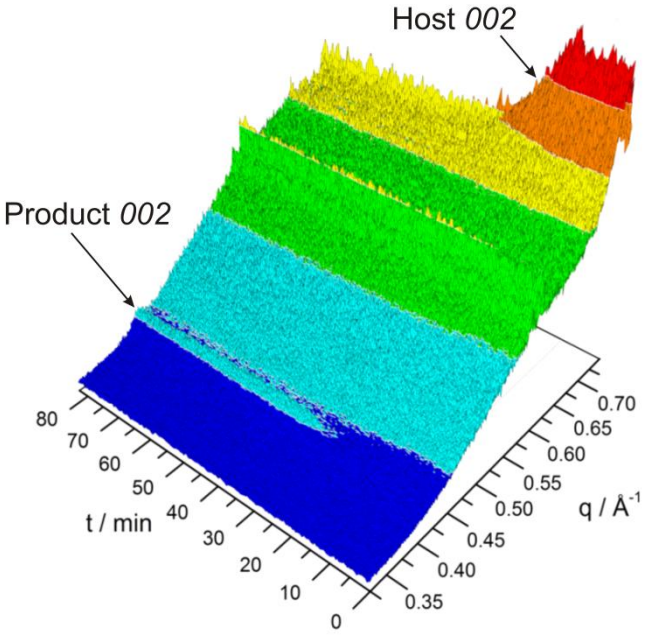

Figure 3.12: 3D stack plot showing the change in intensity of host and product (002) Bragg reflections for the intercalation of phthalate into $CoZnAl_8$-NO_3

The extent of reaction, α, is defined as the integrated intensity of a specific reflection at time t, divided by the maximum intensity of that peak [$\alpha = I_{(hkl)}(t)/I_{(hkl)}(\text{max})$]. A plot of α *vs.* t for the reaction of phthalate with $CoZnAl_8$-NO_3 shows that the host and product curves intersect at $\alpha \sim 0.5$ (Figure 3.13). The loss in coherence of the host is exactly matched by the gain in coherence of the product reflection, which is consistent with a direct conversion of the starting material to the product in a one-step transformation. This one stage process is analogous to previous results obtained for carboxylate intercalation into the MAl_4-NO_3 LDHs.[8]

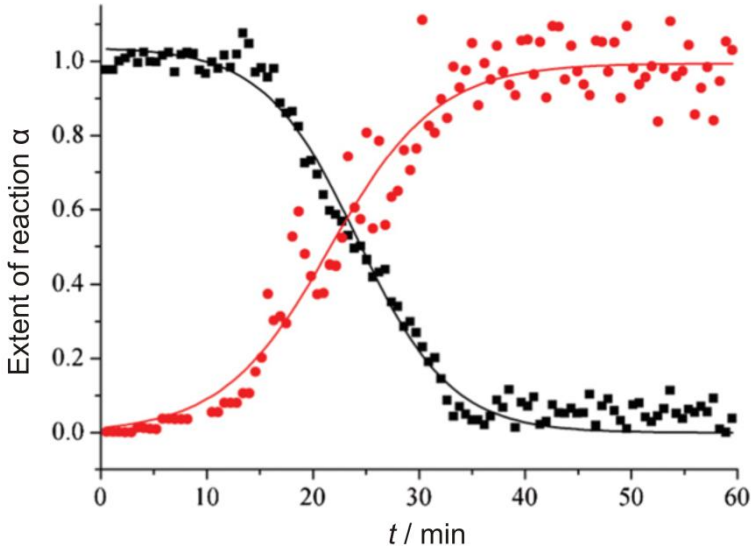

Figure 3.13: Extent of reaction *vs.* time plot for the intercalation of phthalate into $CoZnAl_8$-NO_3 showing evolution of intensity of the host (002) (■) and product (002) (●) Bragg reflections.

EDXRD stack plots for the reaction of phthalate with $Ni_{1.9}Zn_{0.1}Al_8$-NO_3 and $Co_{0.1}Ni_{1.9}Al_8$-NO_3 were very similar to that for $CoZnAl_8$-NO_3. In each case, the (002) reflection corresponding to the crystalline starting material decreases in intensity as the product (002) reflection appears. The data from these reactions comprise the first *in situ* chemical experiments undertaken on Beamline I12 at Diamond, and clearly demonstrate the capabilities of the facility: valuable information could be extracted from data obtained after very little optimisation. The results of these experiments comprised an important part of the commissioning of Beamline I12. Use of the EDXRD detector in the shifted configuration was trialled for the first time and data from these simple intercalation reactions was used to inform the future direction of improvements to this set-up. Discussions into the construction of a bespoke collimator, tuned to the respective take-off angles for each detector element, are ongoing.

3.5.2 Monitoring Intercalation Reactions using EDXRD at Beamline F3, Hasylab

The intercalation of dicarboxylate species into the three-metal systems were probed in more detail using facilities at Beamline F3 of Hasylab, Germany. The intercalation of succinate and terephthalate anions into the 1:1 metal-tuned $CoZnAl_8$-NO_3, $NiZnAl_8$-NO_3, and $CoNiAl_8$-NO_3 were found to proceed *via* single-step processes analogous to those for phthalate. Figure 3.14 shows a 3D stack plot for the reaction of $CoZnAl_8$-NO_3 with succinate, alongside the extent of reaction *vs.* time plot for this reaction.

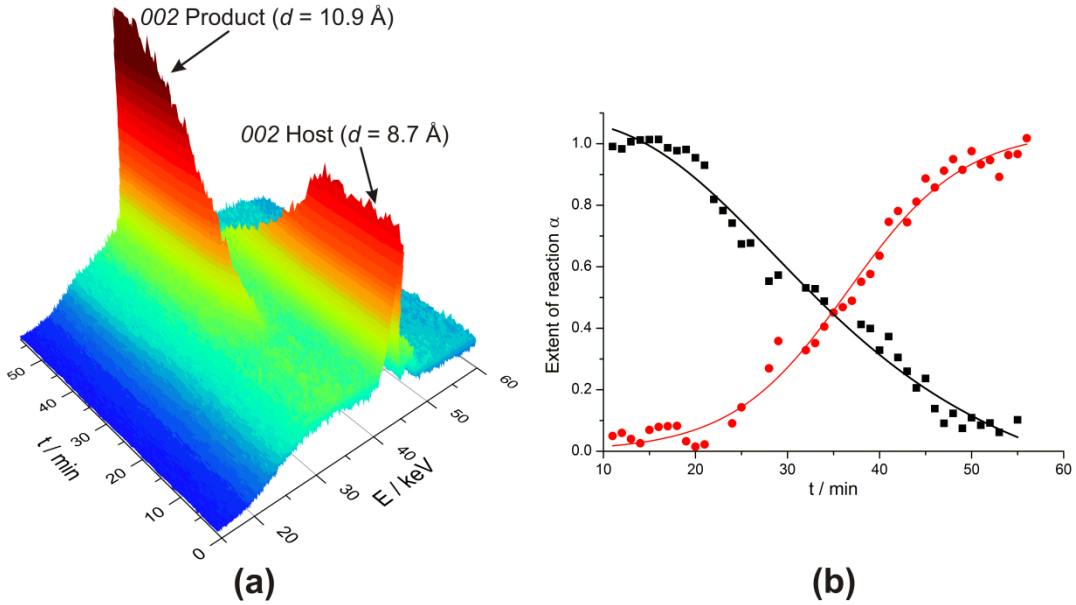

Figure 3.14: Time-resolved *in situ* X-ray diffraction data for the intercalation of succinate into $CoZnAl_8$-NO_3: (a) 3D stack plot showing the change in intensity of host and product (002) reflections and (b) Extent of reaction *vs.* time plot for the host (002) (■) and product (002) (●) reflections.

The one-step nature of the reaction is clear: the host and product α *vs. t* curves cross at *ca.* α = 0.5, supporting a mechanism with direct conversion of the host material to the product. *In situ* EDXRD data for the reaction of $NiZnAl_8$-NO_3 with terephthalate are provided in Figure 3.15.

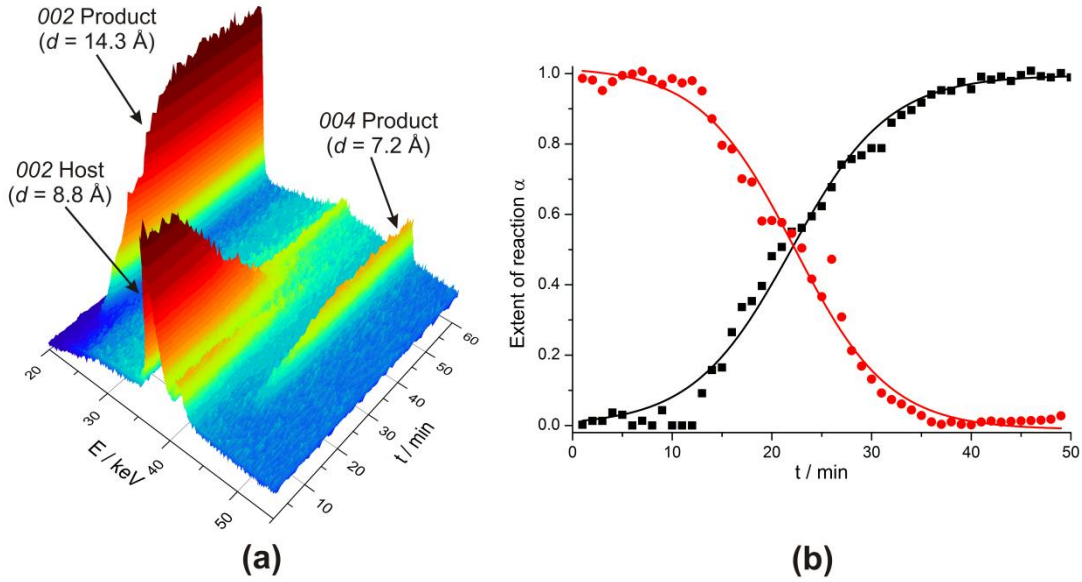

Figure 3.15: Time-resolved *in situ* X-ray diffraction data for the intercalation of terephthalate into $NiZnAl_8$-NO_3: (a) 3D stack plot showing the change in intensity of host and product (002) reflections and (b) Extent of reaction *vs.* time plot for the host (002) (■) and product (002) (●) reflections.

The extent of reaction *vs.* time curves of the host and product phases cross close to α = 0.5 which again indicates a direct transformation. The data obtained from these studies confirm the simple intercalation behaviour of the novel ternary LDHs. Figure 3.15(a) shows that, following optimisation, more than one basal reflection of the product material can be observed during reaction. The product (002) reflection positions for all reactions of succinate and terephthalate are consistent with the *d*-spacings recorded in Tables 3.4-3.6.

3.5.3 Monitoring intercalation reactions using angular-dispersive XRD at Diamond Light Source

Following detailed investigation of facile carboxylate intercalation into the novel three-metal LDHs, these simple reactions were then used to demonstrate the effectiveness of *in situ* angular-dispersive diffraction at the Diamond Light Source. The properties of the angular-dispersive diffraction set-up at Beamline I12 are ideal for probing LDH intercalation reactions. The large-area 2D Thales Pixium RF4343 detector was employed,

in conjunction with the Oxford-Diamond *In Situ* Cell (ODISC) in the low-temperature configuration,[50] to observe the intercalation of succinate into $CoZnAl_8$-NO_3 (Figure 3.16). An aqueous solution containing a five-fold excess of succinate anions was added drop-wise to $CoZnAl_8$-NO_3 stirring in deionised water. Images from the 2D detector were recorded with 4 second exposure at 30 second intervals.

The energy of the monochromated beam was tuned to 53.2442 keV (λ = 0.23286 Å) and the detector was positioned 2501.440 mm from the sample. This enabled Bragg reflections in the high *d*-spacing region ($8 \leq d$ / Å ≤ 23) to be observed at optimum 2θ. The 2D image of concentric Bragg rings was integrated over 360° and converted to a 1D diffraction pattern with intensity *vs.* 2θ. The background due to the sample vessel and water was estimated using an automatic iterative method and subtracted from the raw data.[51].

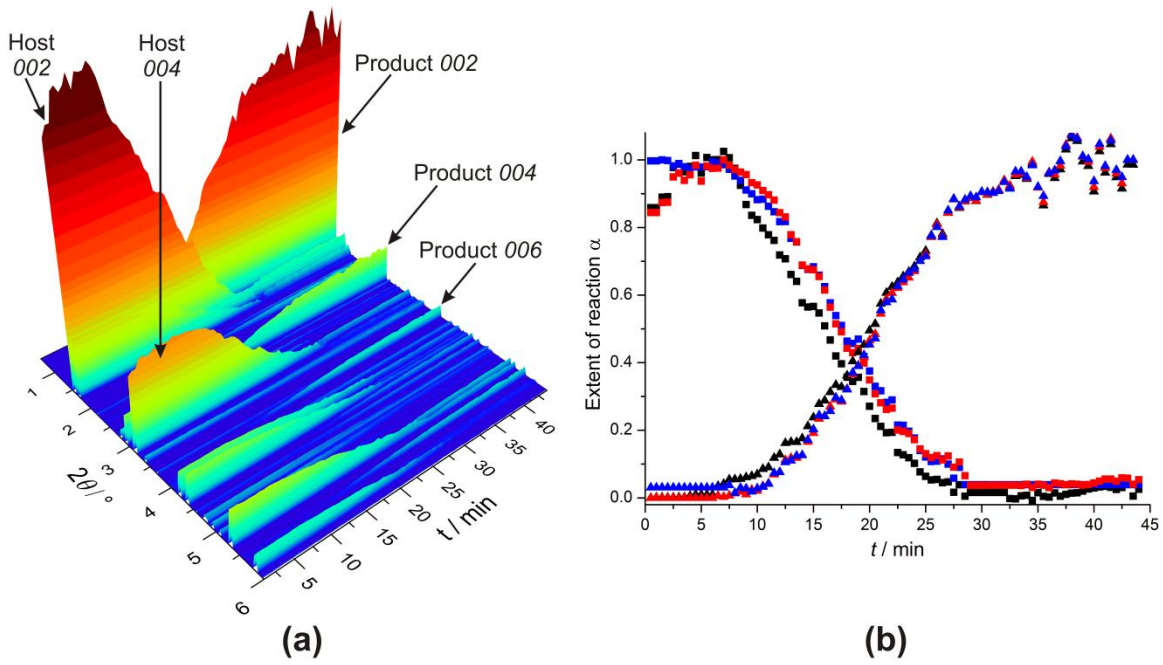

Figure 3.16: Time-resolved *in situ* angular-dispersive XRD data for the intercalation of succinate into $CoZnAl_8$-NO_3: (a) 3D stack plot showing the change in intensity of host and product basal and non-basal Bragg reflections, and (b) Extent of reaction *vs.* time plot for the host (002) (■), (004) (■), (011) (■), and product (002) (▲), (004) (▲), (006) (▲) reflections.

It is clear from the 3D stack plot that with little optimisation, the quality of angular dispersive X-ray diffraction data from the intercalation reaction is vastly superior to data obtained using the shifted EDXRD detector configuration (Section 3.5.1.2). A comparison of the full width at half maximum (FWHM) values of the $CoZnAl_8$-NO_3 (004) reflections, calculated using a Gaussian fit to the data, from an individual Pixium

detector scan with 4 second exposure and data collected over 3 hours using a laboratory diffractometer with Cu-Kα radiation was undertaken. The FWHM of the (004) reflection calculated from data collected at Diamond is d = 0.065(3) Å, whereas the (004) FWHM from laboratory data is d = 0.059(1) Å, which emphasises the comparable data quality.

Several strong basal reflections, some of which are also observed in energy-dispersive data, are clearly visible in both the starting material and product phases. However, additionally observed in the angular-dispersive data are a considerable number of lower intensity non-basal Bragg reflections, which appear in both the starting material and product phases even at high 2θ angles (Figure 3.16). These reflections are indicative of a system that is ordered not just in the direction orthogonal to the layers and their observation emphasises the quality of the angular-dispersive XRD data. Batch peak integration has been undertaken for both basal and non-basal reflections and the resulting α *vs.* t plot in Figure 3.16(b) confirms the one-step nature of the reaction. The starting material and product scans can be fully indexed using similar parameters to those established for the laboratory synthesised samples. Manual indexing suggests the lattice parameters are slightly larger for the *in situ* samples, which can be explained by increased hydration due to the sample presence in solution.

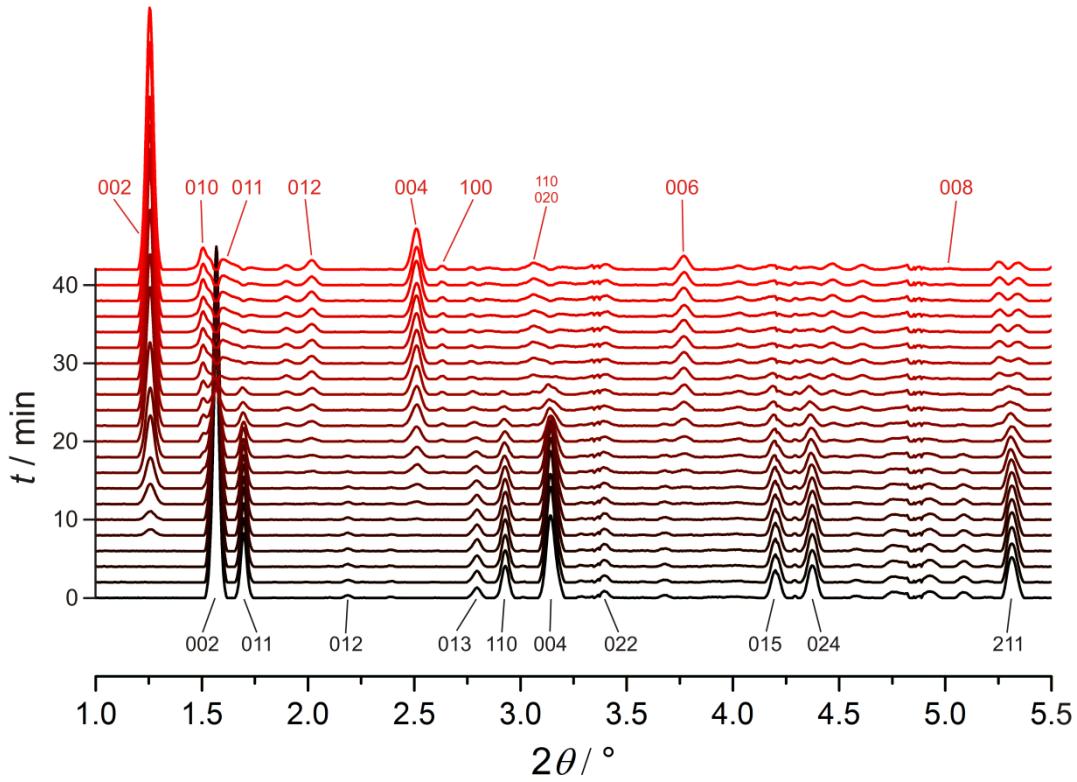

Figure 3.17: A stacked projection of time-resolved *in situ* XRD data recorded during the intercalation of succinate into $CoZnAl_8$-NO_3. Diffraction scans recorded at two minute intervals are shown. Selected Bragg reflections corresponding to the starting material and product are labelled.

A stacked projection of the *in situ* XRD data is shown in Figure 3.17. Due to the high quality data, a more thorough structural examination of the species present in the intercalation reaction is possible using a batch peak-fitting analysis procedure. A preliminary attempt at XRD data fitting *via* the Le Bail method, using the Topas suite of software, was carried out in conjunction with Dr. Leigh Connor at the Diamond Light Source. These initial tests were successful and allowed the phase fractions to be determined for each scan point. It is clear that for future analyses, data is of suitably high quality to allow batch Rietveld refinement on entire reaction sequences, with intricate changes in solid-state structures observed as a function of time.

3.6 An angular-dispersive XRD study of LDH synthesis using $Al(OH)_3$

In addition to reports on low-temperature intercalation reactions, *in situ* investigation into the chemical behaviour of layered double hydroxides has also been extended to LDH synthesis and reactivity at elevated temperatures. The thermal decomposition of LDHs has been monitored using both laboratory and synchrotron X-ray diffraction techniques.[52-54] Synchrotron XRD has also been employed to study dehydration in LDH-like montmorillonite clays.[55, 56]

Reactions involving the various polymorphs of $Al(OH)_3$ have also been the subject of much scrutiny in the field of *in situ* diffraction studies. EDXRD has been employed to observe the contrasting behaviours of gibbsite and bayerite during precipitation from solution at 60 °C and 80 °C.[57] No transition between the two polymorphs was observed at these temperatures. The intercalation of lithium salts into gibbsite to yield $[LiAl_2(OH)_6]X{\cdot}H_2O$ (X = Cl, Br, OH, NO_3, SO_4) has been probed using EDXRD by Fogg and O'Hare.[3] The LDH product was observed to form *via* a single-step transformation from the gibbsite starting material, at a temperature-dependant rate. In contrast to this mechanism, Britto and Kamath proposed that hydrothermal synthesis of the ZnAl-NO_3 LDH (~3 : 1, $M^{II} : M^{III}$) occurs *via* a dissolution-reprecipitation mechanism when using a bayerite precursor.[11] They hypothesised that a highly crystalline product forms due to the slow kinetics of dissolution of bayerite at the solid-liquid interface.

An *in situ* angular-dispersive XRD study was undertaken to instigate a more thorough understanding of the processes involved in high-temperature hydrothermal formation of LDHs from $Al(OH)_3$.

3.6.1 Monitoring the synthesis of $CoAl_4$-NO_3 LDH

Hydrothermal synthesis of the $[CoAl_4(OH)_{12}](NO_3)_2{\cdot}yH_2O$ LDH was monitored *in situ*. ODISC was operated in the hydrothermal set-up to probe the reaction of 10 mL aqueous $Co(NO_3)_2.6H_2O$ (10 M) with 0.5 g activated $Al(OH)_3$ gibbsite, at 250 °C in an autoclave. The temperature was recorded using a thermocouple positioned between the glassy carbon sheath and the autoclave. Beamline I12 was configured in monochromatic beam mode (E = 52.9716 keV, λ = 0.2341 Å), with the detector position set at 2500 mm from the sample. The sample autoclave was heated to 250 °C at a rate of 30 °C.min^{-1} and held at that temperature for 102 mins. Sample cooling was then undertaken at a rate of 2 °C.min^{-1} to room temperature. Images from the 2D Pixium detector were recorded with 4 second exposure at 60 second intervals. Figure 3.18 contains an annotated 3D stack plot for the synthesis reaction. Background intensity was estimated using an automatic iterative method and subtracted from the raw data.[51] The following regions were excluded due to diffraction reflections from the steel autoclave and PTFE liner: 2θ = 2.62 – 2.78, 4.65 – 4.75, and 5.35 – 5.43°.

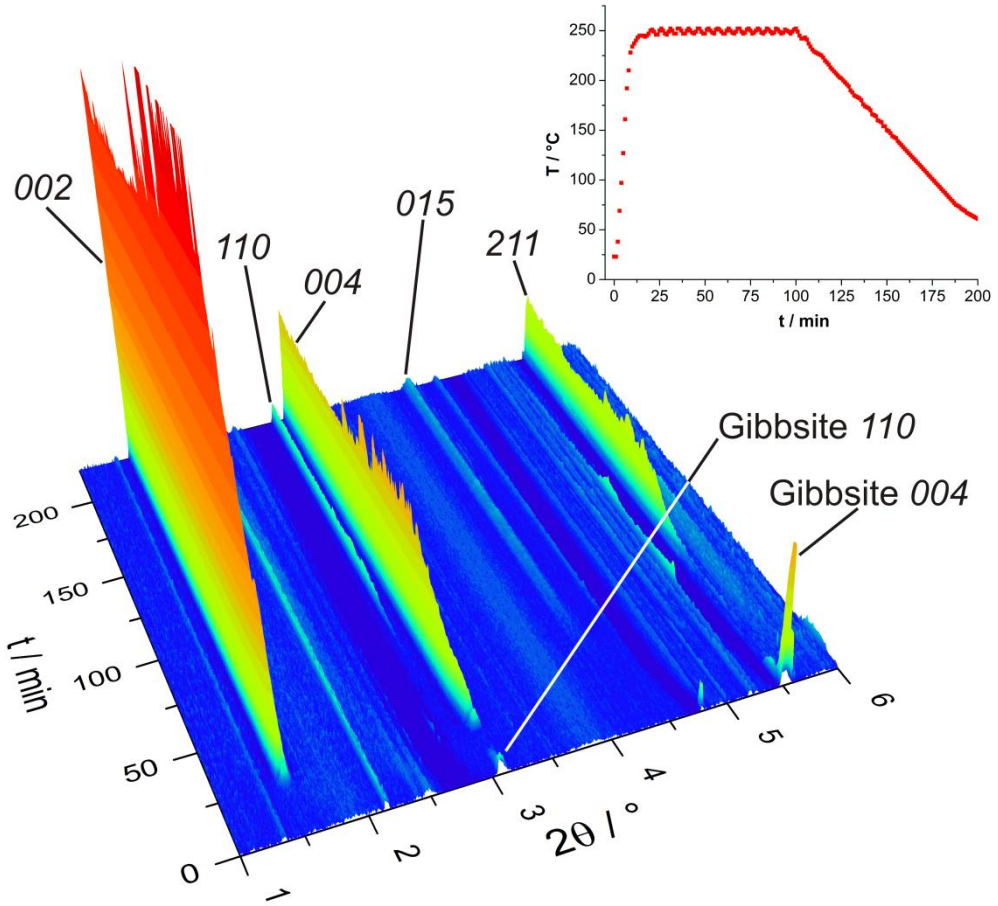

Figure 3.18: Time-resolved *in situ* angular-dispersive XRD data for the synthesis of $CoAl_4$-NO_3. INSET: Temperature profile for the reaction.

Several important phenomena relating to the phases present during reaction can be inferred from the stack plot. The intensities of the (110) and (004) Bragg reflections due to crystalline gibbsite starting material decline to zero upon heating. This suggests complete dissolution of the starting material. During the 10 mins following dissolution of $Al(OH)_3$, in which the autoclave temperature increases from 210 °C to 247 °C, no reflections due to crystalline materials are visible in the diffraction data. At 250 °C, Bragg reflections consistent with the LDH product appear, and grow in intensity. These reflections correspond to the (002) (d = 8.9 Å) and (004) (d = 4.4 Å) basal reflections of $CoAl_4$-NO_3 LDH. Several minutes later, non-basal reflections of the product phase appear, including peaks corresponding to diffraction from the (110), (015), and (211) lattice planes highlighted in the 3D stack-plot.

The intensities of the observed Bragg reflections were integrated using a Gaussian function and the extent of reaction parameter, α, calculated for each phase in the reaction profile. The α *vs.* *t* plot in Figure 3.19 illustrates that the gibbsite peak intensity declines to zero prior to any product formation. It can be inferred that the entirety of the $Al(OH)_3$ reagent dissolves in $Co(NO_3)_2$ aqueous solution before reaction to form the product LDH. It also appears that growth of the non-basal reflections begins approximately when the intensities of the (00*l*) reflections have reached their relative maxima.

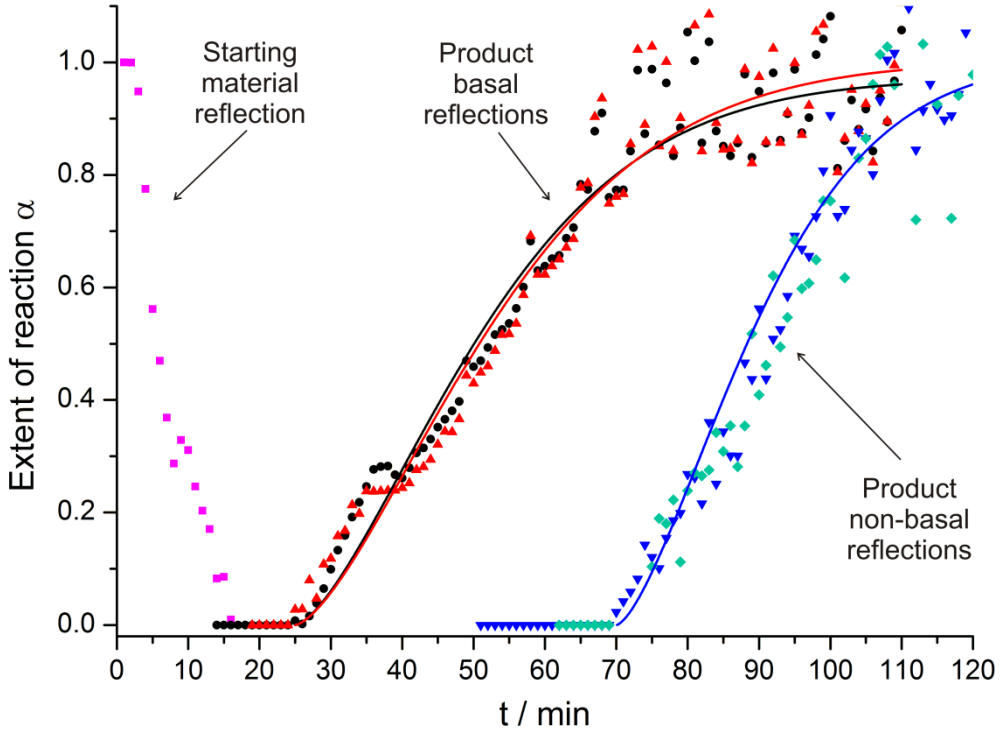

Figure 3.19: Extent of reaction *vs.* time plot for the synthesis of $CoAl_4$-NO_3 LDH showing change in intensity of the gibbsite (110) (■) and product (002) (●), (004) (▲), (110) (▼), and (211) (♦) reflections. The lines correspond to fitting of the Avrami-Erofe'ev rate equation.

The change in α as a function of time for the (00*l*) Bragg reflections was modelled using the Avrami-Erofe'ev equation to provide insight into the mechanism of crystallisation. Initial fitting to both basal reflections yielded Avrami exponents very close to $n = 1.5$. A similar value has been observed in reports on crystal growth from solution.[58] The value is suggestive of crystal growth that is predominantly controlled by nucleation, rather than by diffusion of reagents to the sites of crystallisation. To establish approximate parameters corresponding to the kinetics of growth in each dimension, the exponent n was set constant at 1.5 and Avrami-Erofe'ev modelling undertaken for α corresponding to all reflections. The resulting parameters are provided in Table 3.7. The induction time for each reflection was calculated as the length of time between the autoclave temperature reaching 250 °C and the first observation of non-zero intensity for that reflection. Growth of the basal reflections is effectively coincident, following which there is approximately 48 mins delay before growth of the (110) and (211) reflections begins.

Table 3.7: Kinetic information extracted using Avrami-Erofe'ev modelling ($\alpha = 1 - \exp\{-[k(t - t_0)]^n\}$) to α *vs. t* curves of several product reflections.

Bragg reflection / (*hkl*)	**Induction time (t_0) / min**	**Rate constant (k) / s^{-1}**
(002)	4	3.2 (1)
(004)	5	3.0 (1)
(110)	52	4.3 (2)
(211)	52	3.6 (4)

The growth in intensities of the (00*l*) reflections is accompanied by variations in their peak widths and positions. The decrease in width of the (002) and (004) reflections is most marked within the first 25 minutes of reaction at 250 °C (Figure 3.20(a)). This observation indicates particle growth and increase in product crystallinity as the number of consecutively stacked layers in the structure increases. No asymmetry is observed in the peak shape during formation, which would be indicative of stacking faults perpendicular to the *c*-direction. Following an initial sharp decline, the widths of the (002) and (004) reflections remain approximately constant for the remainder of the reaction.

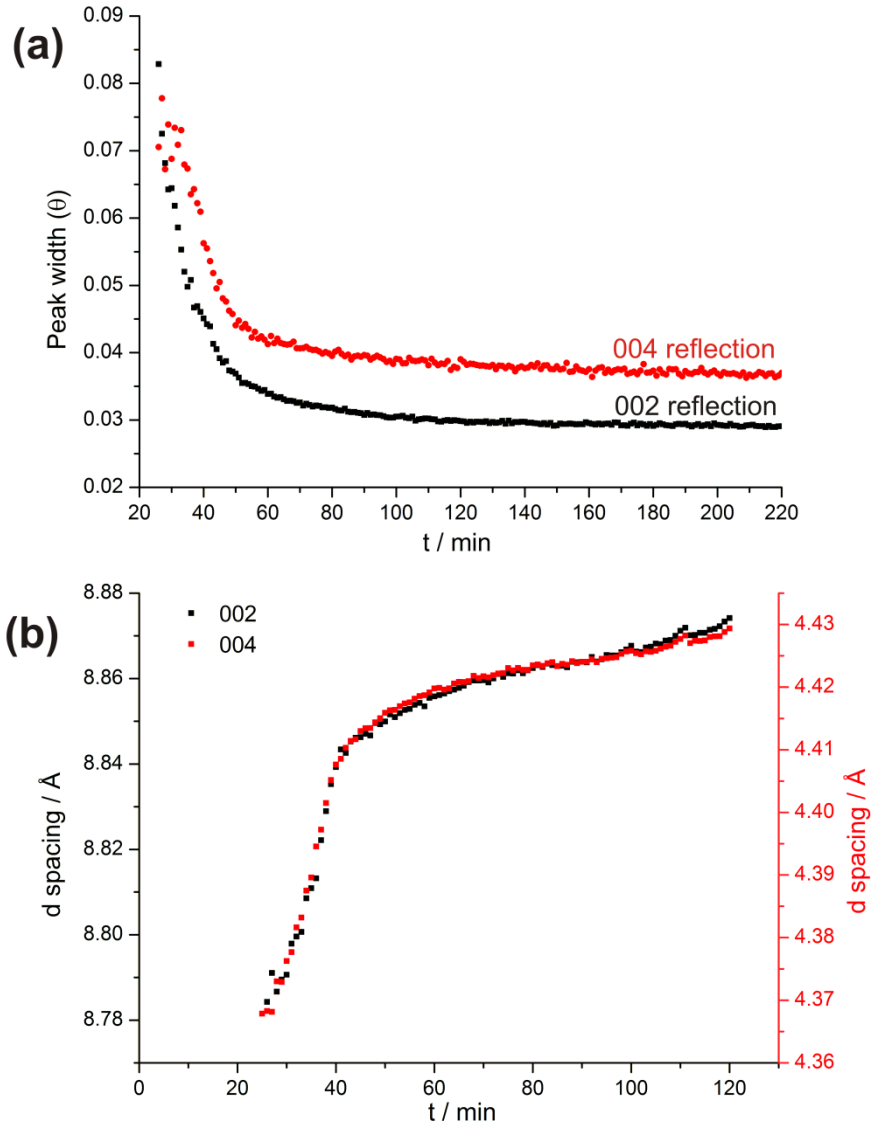

Figure 3.20: Variation in (a) width of the (002) (●) and (004) (●) Bragg reflections and (b) position of the (002) (■) and (004) (●) reflections as a function of reaction duration (NB. The data in (b) are plotted against two different *y*-axes).

The positions of the (00*l*) reflections are also observed to shift on a relatively small scale during product growth (Figure 3.20(b)). Basal reflection position is indicative of the interlayer distance within the product material. The variation in *d*-spacings of the (002) and (004) reflections is comparable throughout the course of the reaction, which is to be expected. The greatest increase in *d* occurs within the first 15 mins of reaction at 250 °C, which is followed by a consistent, but significantly slower, rise in the interlayer spacing. Due to the lower intensity of the (110) and (211) reflections, data corresponding to peak width and position were more difficult to interpret, but it appears that both parameters vary little with time in each case.

3.6.2 Crystal growth analysis

The exceptional resolution observed in the *in situ* angular-dispersive diffraction data allows time-dependent crystallinity to be determined using the Scherrer Equation. Reflection broadening due to the sample volume was taken into account by numerical convolution of the data with a 'top-hat' function of variable width. The width used for each point was $\tau(\tan\theta)$, where τ is the sample thickness. Contributions to peak width from the instrument were then corrected for using diffraction data from a sample of NIST-standard LaB_6. The variation in crystallite size during product formation was derived using the Scherrer Equation ($\tau = 0.89\lambda / \beta\cos\theta$). Figure 3.21 contains a plot of the sample crystallinity, calculated using the width of the (002) Bragg reflection, as a function of time.

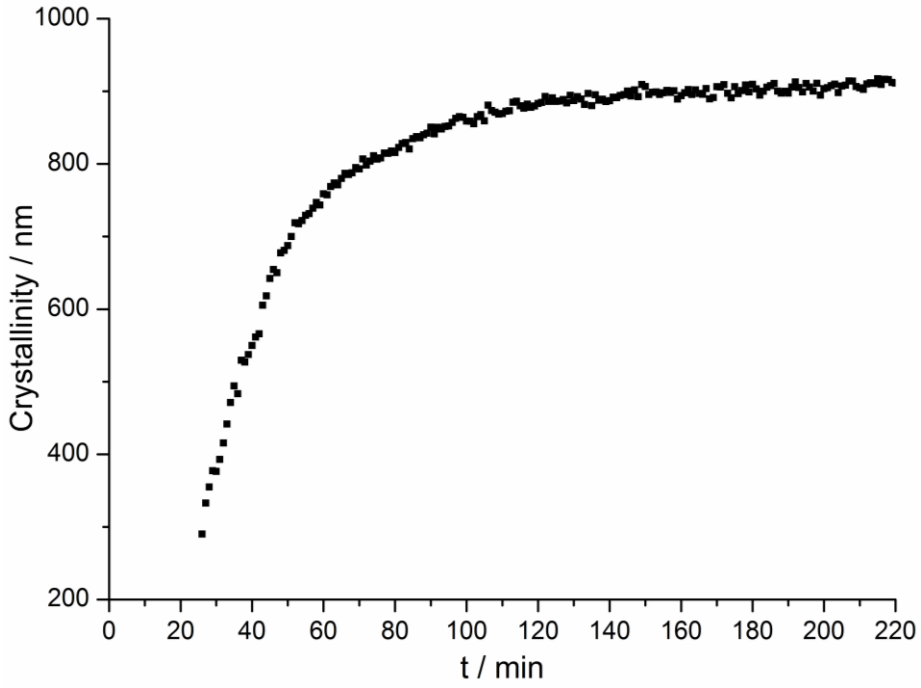

Figure 3.21: The increase in average crystallinity (nm) as a function of reaction duration for the synthesis of $CoAl_4$-NO_3.

The crystallinity calculated using this method relates approximately to the general particle sizes observed in *ex situ* TEM measurements. Analogous calculations were made using some non-basal reflections, but the lower intensity of these peaks led to a much greater spread of values extracted from Scherrer analysis. Nevertheless, sample crystallinity calculated from the (110) and (211) reflections generally remains constant with time, which is indicate of highly anisotropic crystal growth.

3.6.3 Discussion

It can be inferred from the above observations that formation of the $CoAl_4$-NO_3 material occurs *via* a four-stage mechanistic pathway. The first stage involves dissolution of the solid starting material to form the corresponding aqueous ions. The next step begins following complete dissolution of $Al(OH)_3$, when conditions become isothermal after 20 mins. During this stage, termed the 'induction period', the building blocks for LDH growth are formed on the nano-scale, and only broad reflections corresponding to short-range order in the (*h*00) and (0*k*0) planes are expected (Figure 3.22(a)). These reflections have very weak intensity in laboratory LDH XRD data and are not observed in the *in situ* data here. Existing hydrothermal crystallisation studies have suggested that the role of anionic species in the reaction medium, such as OH^-, during this period is as complexing agents to direct growth of the product structure.[59] In the case of LDH formation here, this stage is particularly rapid, taking place in under 5 mins at 250 °C.

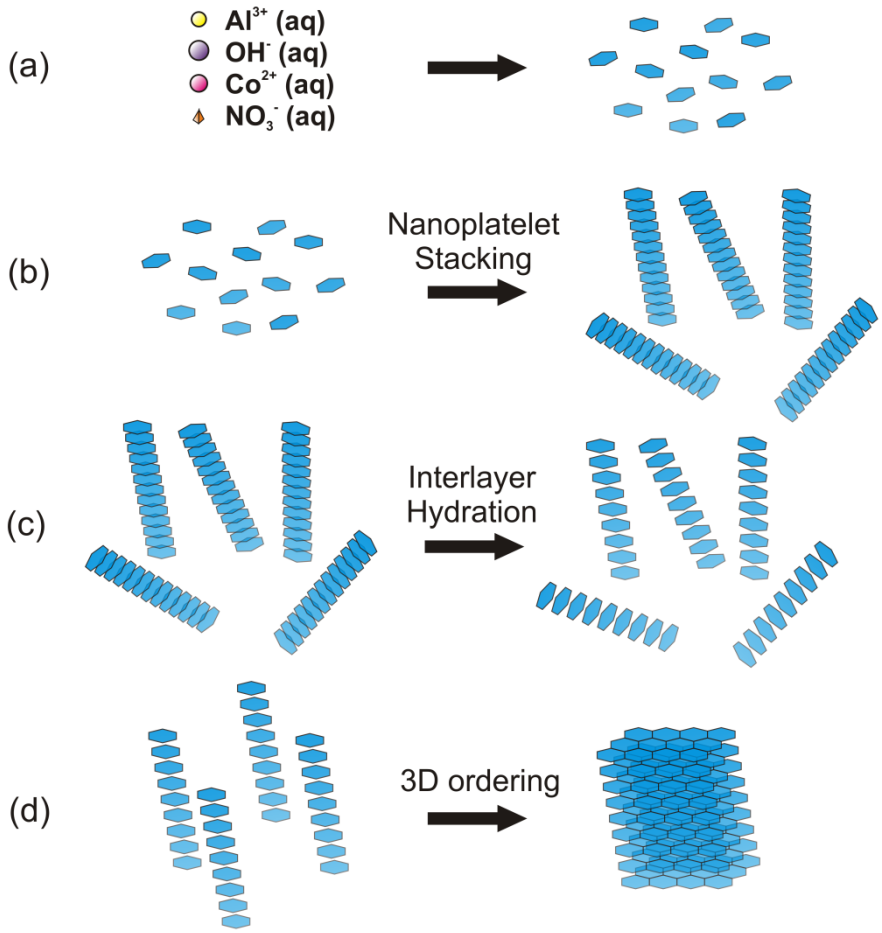

Figure 3.22: Schematic illustrating the various hypothesised stages of hydrothermal LDH formation following dissolution of $Al(OH)_3$. (a) Formation of nano-sheets from solution, (b) sheet stacking to form 'rod-like' structures followed by (c) layer hydration, and (d) final structural ordering in three dimensions.

During the third stage, a poorly-crystalline 'rod-like' layered structure is assembled from the building blocks formed in stage one (Figure 3.22(b)). The new material exhibits long-range order in the direction orthogonal to the newly-stacked layers, corresponding to (00*l*) lattice planes. The formation of this phase is indicated by growth in intensity of the (002) and (004) reflections in the *in situ* XRD data, and occurs in a few minutes. A noticeable variation in the width and position of the basal reflections is also detected during this period. The change in position of these reflections upon formation is an interesting observation. It can be hypothesised that the small increase in *d*-spacing at this point is due to hydration in the interlayer region. Immediately following alternate stacking of the positively-charged layers and anionic guests, molecules of water enter the structure resulting in a swelling and shift in (00*l*) reflection position (Figure 3.22(c)). This effect has been observed in previous *in situ* investigations of 3D framework synthesis; both in the starting materials prior to reaction,[60] and the product materials upon formation.[59]

The fourth and final stage of crystalline LDH formation is indicated by growth in intensity of product reflections in directions which do not correspond to single unit cell axes *i.e.* for which more than one Miller index is non-zero. This is indicative of structural ordering between adjacent positively-charged LDH layers and also in the direction parallel to the layers. The 'rod-like' LDH precursors connect together, forming platelets that are ultimately observed in the *ex situ* SEM measurements. The product layers orient in an *aba* stacking sequence and the intralayer Co^{2+} and Al^{3+} cations order within the octahedral interstices (Figure 3.22(d)). This concluding unification step begins as formation of the nanoparticles with rod-like morphology starts to decline. The rate of adhesion as the rods join to form platelets is closely comparable to the rate of growth of the rods from nanoparticles in the previous step.

Comparisons can be drawn between the mechanism of hydrothermal LDH synthesis and that of the so-called 'urea-method', which employs additional reagents, such as urea or hexamethylenetetramine (HMT), to facilitate LDH product formation. The hydrolysis of these starting materials at high-temperatures causes a release of ammonia and a corresponding increase in alkalinity of the reactant mixture, resulting in dissolution of metal hydroxide reagents.[61] Subsequent formation of the product in solution is followed by homogeneous precipitation of highly-crystalline LDH particles. It appears that hydrothermal LDH synthesis at 250 °C observed here proceeds *via* a similar mechanism.

It is likely that the basic conditions due to highly-concentrated starting material solutions, in addition to pre-activation of the $Al(OH)_3$ precursor, are the catalysts for initial gibbsite dissolution and the resulting homogeneous reprecipitation. This contrasts with the mechanism proposed for hydrothermal synthesis of the $LiAl_2$-X analogue, whereby LDH synthesis occurs *via* direct topotactic intercalation into crystalline gibbsite.

In reference to Section 3.1.2, this synthesis reaction can be defined as topotactic based on the definition of Figlarz *et al.*, where the structure of the LDH product is strongly related to that of the gibbsite precursor. However, the process itself involves complete dissolution of $Al(OH)_3$ prior to product crystallisation, and cannot therefore be described as topotactic. Such a mechanistic route does open up the potential for interconversion between MAl_4-NO_3 LDHs. Complete replacement of intralayer M(II) cations can be achieved upon hydrothermal heating of the LDH in a highly-concentrated solution of the desired metal nitrate substitute, which is almost certainly facilitated by a dissolution of the starting material LDH followed by recombination and precipitation of the product species.[31]

3.7 Synthesis using bayerite

As discussed in Chapter 1, the intercalation of lithium salts into different polymorphs of $Al(OH)_3$ results in formation of LDHs with different layer-stacking sequences. The hydrothermal formation of CoZnAl-NO_3 LDH using an activated bayerite precursor was therefore attempted. Successful reaction required more 'forcing' conditions than the analogous synthesis with gibbsite. 0.2 g of bayerite was treated with a 1 : 1 mixture of $Co(NO_3)_2{\cdot}6H_2O$ and $Zn(NO_3)_2{\cdot}6H_2O$ 10 M aqueous solutions at 225 °C for 110 hours in an autoclave. The diffraction pattern from the product material is provided in Figure 3.23. The product is of low crystallinity and the absence of several non-basal reflections is indicative of a poorly-ordered system. Basal reflections corresponding to LDH layers are clearly visible, but unequivocal reflection indexing was not possible for this phase due to the low number of crystalline Bragg reflections. Comparison of the diffraction data with those detailed in Section 3.2.1 indicates that the bayerite-derived LDH has an analogous structure to that of the gibbsite-derived analogue. The XRD data could be manually indexed on an identical orthorhombic cell to the gibbsite-derived analogues, with marginally larger *c*-parameter: a = 5.3 Å, b = 8.9 Å, c ~ 17.0 Å.

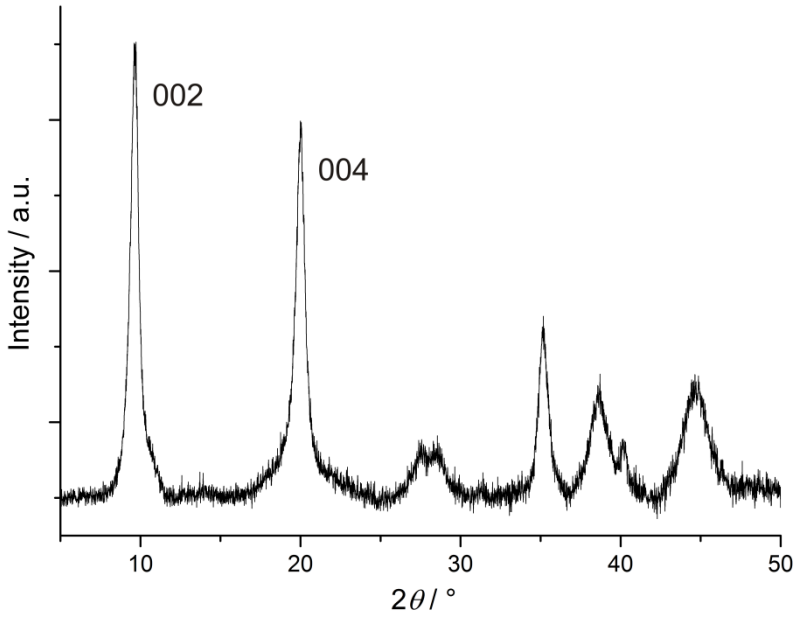

Figure 3.23: X-ray diffraction data corresponding to the bayerite-derived $Co_xZn_{2-x}Al_8$-NO_3 LDH product.

The structural similarity of the two $Al(OH)_3$-derived LDHs is an interesting and relevant observation. XRD data from the gibbsite- and bayerite-derived LDHs are very similar and there exists no indication that the material formed from the bayerite precursor exhibits rhombohedral layer-stacking, as is the case with analogous reaction with lithium salts. Instead, the formation of an LDH with pseudo-hexagonal *aba* stacking geometry, equivalent to that synthesised from gibbsite in Section 3.2, is highly suggestive of a reaction process that is not topotactic – *i.e.* the structure of the product is independent of that of the starting material. It is likely that the reaction with bayerite follows a similar reaction scheme to Figure 3.22, with dissolution of the solid starting material preceding the first stage. In this case, the thermodynamically favoured *aba*-stacked product forms preferentially over the rhombohedral *abca*-stacked alternative. The nature of the LDH product from synthesis with bayerite supports the findings from *in situ* studies; hydrothermal syntheses of LDHs involving $Al(OH)_3$ occur *via* the homogeneous precipitation mechanism.

3.8 Conclusion

The hydrothermal reactivity of $Al(OH)_3$ towards the formation of layered double hydroxides has been explored. The family of MAl_4-NO_3 LDHs, which exhibit an unusual 1 : 4 ratio of M^{2+} : Al^{3+}, has been extended to include species with three metal cations residing in the positively-charged layers. Comprehensive characterisation of this new sub-family of LDHs has been undertaken using XRD, IR spectroscopy, elemental analysis (CHN and EDX), TGA and TEM. The series were observed to exhibit tuneable intralayer cation ratios and successful synthesis of $Co_{1-x}Zn_xAl_8$-NO_3, $Ni_{1-x}Zn_xAl_8$-NO_3, and $Co_{1-x}Ni_xAl_8$-NO_3 for a range of *x* was achieved. The intercalation chemistry of the novel three-metal LDHs has been also been thoroughly investigated. Reaction of $CoZnAl_8$-NO_3 with phthalate was probed *in situ* as part of the first chemical experiments to be undertaken using Beamline I12 at the Diamond Light Source. Data quality from these and subsequent studies of LDH intercalation reactions has influenced improvements to the hardware and software facilities on I12. A crucial aspect of these *in situ* studies has been the optimisation of data collection, quality, and processing for future users studying a broad spectrum of chemical reactions using this facility. High-quality, angular-dispersive X-ray diffraction data provide unprecedented insight into the mechanism by which this family of LDHs form from $Al(OH)_3$.

3.9 References

1. K. R. Poeppelmeier and S. J. Hwu, *Inorganic Chemistry*, 1987, **26**, 3297-3302.
2. J. P. Thiel, C. K. Chiang and K. R. Poeppelmeier, *Chemistry of Materials*, 1993, **5**, 297-304.
3. A. M. Fogg and D. O'Hare, *Chemistry of Materials*, 1999, **11**, 1771-1775.
4. G. R. Williams and D. O'Hare, *Journal of Physical Chemistry B*, 2006, **110**,10619-10629.
5. H. C. Greenwell, W. Jones, S. L. Rugen-Hankey, P. J. Holliman and R. L. Thompson, *Green Chemistry*, 2010, **12**, 688-695.
6. M. Ogawa and Y. Sugiyama, *Journal of the Ceramic Society of Japan*, 2009, **117**, 179-184.
7. A. M. Fogg, G. R. Williams, R. Chester and D. O'Hare, *Journal of Materials Chemistry*, 2004, **14**, 2369-2371.
8. G. R. Williams, T. G. Dunbar, A. J. Beer, A. M. Fogg and D. O'Hare, *Journal of Materials Chemistry*, 2006, **16**, 1222-1230.
9. G. R. Williams, T. G. Dunbar, A. J. Beer, A. M. Fogg and D. O'Hare, *Journal of Materials Chemistry*, 2006, **16**, 1231-1237.
10. R. D. Hetterley, R. Mackey, J. T. A. Jones, Y. Z. Khimyak, A. M. Fogg and I. V. Kozhevnikov, *Journal of Catalysis*, 2008, **258**, 250-255.

11. S. Britto and P. V. Kamath, *Inorganic Chemistry*, 2010, **49**, 11370-11377.
12. R. Chitrakar, Y. Makita, A. Sonoda and T. Hirotsu, *Journal of Hazardous Materials*, 2011, **185**, 1435-1439.
13. M. Figlarz, B. Gerand, A. Delahayevidal, B. Dumont, F. Harb, A. Coucou and F. Fievet, *Solid State Ionics*, 1990, **43**, 143-170.
14. S. Britto and P. V. Kamath, *Inorganic Chemistry*, 2011, **50**, 5619-5627.
15. S. Britto and P. V. Kamath, *Zeitschrift Fur Anorganische Und Allgemeine Chemie*, 2012, **638**, 362-365.
16. R. Ma, Z. Liu, K. Takada, N. Iyi, Y. Bando and T. Sasaki, *Journal of the American Chemical Society*, 2007, **129**, 5257-5263.
17. R. Ma, J. Liang, K. Takada and T. Sasaki, *Journal of the American Chemical Society*, 2011, **133**, 613-620.
18. J. Liang, R. Ma, N. Iyi, Y. Ebina, K. Takada and T. Sasaki, *Chemistry of Materials*, 2010, **22**, 371-378.
19. H. Q. Nie and W. G. Hou, *Acta Physico-Chimica Sinica*, 2011, **27**, 1783-1796.
20. L. Li, R. Z. Ma, Y. Ebina, N. Iyi and T. Sasaki, *Chemistry of Materials*, 2005, **17**, 4386-4391.
21. Z. P. Liu, R. Z. Ma, M. Osada, N. Iyi, Y. Ebina, K. Takada and T. Sasaki, *Journal of the American Chemical Society*, 2006, **128**, 4872-4880.
22. F. Leroux, M. Adachi-Pagano, M. Intissar, S. Chauviere, C. Forano and J. P. Besse, *Journal of Materials Chemistry*, 2001, **11**, 105-112.
23. T. Hibino and W. Jones, *Journal of Materials Chemistry*, 2001, **11**, 1321-1323.
24. S. O'Leary, D. O'Hare and G. Seeley, *Chemical Communications*, 2002, **14**, 1506-1507.
25. Z. P. Liu, R. Z. Ma, Y. Ebina, N. Iyi, K. Takada and T. Sasaki, *Langmuir*, 2007, **23**, 861-867.
26. D. Tichit, F. Medina, B. Coq and R. Dutartre, *Applied Catalysis General*, 1997, **159**, 241-258.
27. S. Ribet, D. Tichit, B. Coq, B. Ducourant and F. Morato, *Journal of Solid State Chemistry*, 1999, **142**, 382-392.
28. K. Klemkaite, I. Prosycevas, R. Taraskevicius, A. Khinsky and A. Kareiva, *Central European Journal of Chemistry*, 2011, **9**, 275-282.
29. R. E. Johnsen and P. Norby, *Journal of Applied Crystallography*, 2008, **41**, 991-1002.
30. F. Cavani, F. Trifiro and A. Vaccari, *Catalysis Today*, 1991, **11**, 173-301.
31. G. R. Williams, S. J. Moorhouse, T. J. Prior, A. M. Fogg, N. H. Rees and D. O'Hare, *Dalton Transactions*, 2011, **40**, 6012-6022.
32. L. Aimoz, C. Taviot-Gueho, S. V. Churakov, M. Chukalina, R. Dahn, E. Curti, P. Bordet and M. Vespa, *Journal of Physical Chemistry C*, 2012, **116**, 5460-5475.
33. C. J. Wang and D. O'Hare, *Journal of Materials Chemistry*, 2012, **22**, 23064-23070.
34. R. D. Shannon and C. T. Prewitt, *Acta Crystallographica Section B-Structural Crystallography and Crystal Chemistry*, 1970, **B 26**, 1046-1048.
35. R. Chitrakar, Y. Makita, A. Sonoda and T. Hirotsu, *Journal of Colloid and Interface Science*, 2011, **354**, 798-803.
36. T. Kameda, N. Yagihashi, K. S. Park, G. Grause and T. Yoshioka, *Fresenius Environmental Bulletin*, 2009, **18**, 1006-1010.
37. R. D. Shannon and C. T. Prewitt, *Acta Crystallographica Section B-Structural Crystallography and Crystal Chemistry*, 1969, **B 25**, 925-946.
38. H. Yan, M. Wei, J. Ma, F. Li, D. G. Evans and X. Duan, *Journal of Physical Chemistry A*, 2009, **113**, 6133-6141.
39. R. E. Johnsen, Q. L. Wu, A. O. Sjastad, O. B. Vistad, F. Krumeich and P. Norby, *Journal of Physical Chemistry C*, 2008, **112**, 16733-16739.

40. A. I. Khan, A. Ragavan, B. Fong, C. Markland, M. O'Brien, T. G. Dunbar, G. R. Williams and D. O'Hare, *Industrial & Engineering Chemistry Research*, 2009, **48**, 10196-10205.
41. Y. Zhang, H. Tan, J.-x. Zhao, X. Li, H. Ma, X. Chen and X. Yang, *Physical Chemistry Chemical Physics*, 2012, **14**, 9067-9075.
42. A. M. Fogg, J. S. Dunn, S. G. Shyu, D. R. Cary and D. O'Hare, *Chemistry of Materials*, 1998, **10**, 351-355.
43. G. R. Williams and D. O'Hare, *Chemistry of Materials*, 2005, **17**, 2632-2640.
44. C. Taviot-Gueho, Y. J. Feng, A. Faour and F. Leroux, *Dalton Transactions*, 2010, **39**, 5994-6005.
45. J. Pisson, C. Taviot-Gueho, Y. Israeli, F. Leroux, P. Munsch, J. P. Itie, V. Briois, N. Morel-Desrosiers and J. P. Besse, *Journal of Physical Chemistry B*, 2003, **107**, 9243-9248.
46. Y. J. Feng, G. R. Williams, F. Leroux, C. Taviot-Gueho and D. O'Hare, *Chemistry of Materials*, 2006, **18**, 4312-4318.
47. C. Taviot-Gueho, F. Leroux, C. Payen and J. P. Besse, *Applied Clay Science*, 2005, **28**, 111-120.
48. A. M. Fogg, J. S. Dunn and D. O'Hare, *Chemistry of Materials*, 1998, **10**, 356-360.
49. J. S. O. Evans, R. J. Francis, D. O'Hare, S. J. Price, S. M. Clark, J. Flaherty, J. Gordon, A. Nield and C. C. Tang, *Review of Scientific Instruments*, 1995, **66**, 2442-2445.
50. S. J. Moorhouse, N. Vranjes, A. Jupe, M. Drakopoulos and D. O'Hare, *Review of Scientific Instruments*, 2012, **83**, 084101-084108.
51. S. Bruckner, *Journal of Applied Crystallography*, 2000, **33**, 977-979.
52. M. Wei, S. X. Shi, J. Wang, Y. Li and X. Duan, *Journal of Solid State Chemistry*, 2004, **177**, 2534-2541.
53. J. H. Meng, H. Zhang, D. G. Evans and X. Duan, *Chinese Science Bulletin*, 2005, **50**, 2575-2581.
54. A. Piskova, P. Bezdicka, D. Hradil, E. Kafunkova, K. Lang, E. Vecernikova, F. Kovanda and T. Grygar, *Applied Clay Science*, 2010, **49**, 363-371.
55. H. J. Bray, S. A. T. Redfern and S. M. Clark, *Mineralogical Magazine*, 1998, **62**, 647-656.
56. W. L. Huang, W. A. Bassett and T. C. Wu, *American Mineralogist*, 1994, **79**, 683-691.
57. J. S. C. Loh, A. M. Fogg, H. R. Watling, G. M. Parkinson and D. O'Hare, *Physical Chemistry Chemical Physics*, 2000, **2**, 3597-3604.
58. F. Millange, M. I. Medina, N. Guillou, G. Ferey, K. M. Golden and R. I. Walton, *Angewandte Chemie-International Edition*, 2010, **49**, 763-766.
59. R. J. Francis, S. O'Brien, A. M. Fogg, P. S. Halasyamani, D. O'Hare, T. Loiseau and G. Ferey, *Journal of the American Chemical Society*, 1999, **121**, 1002-1015.
60. P. Norby, *Journal of the American Chemical Society*, 1997, **119**, 5215-5221.
61. N. Iyi, T. Matsumoto, Y. Kaneko and K. Kitamura, *Chemistry Letters*, 2004, **33**, 1122-1123.

Chapter 4: Molten Salt Synthesis and Characterisation of Oxides with the Aurivillius Structure

4.1 Introduction

Since the discovery of compounds with the Aurivillius structure (shown in Figure 4.1) in the 1950s,[1-3] the ability to dope cations of different sizes and charges onto both the perovskite-layer A-sites and Bi_2O_3-layer Bi-sites in these materials has been demonstrated.[4] However, doping of cations onto the perovskite B-sites of such structures has been found to be much less facile, with far fewer examples existing in the literature. One sub-family of Aurivillius compounds with B-site solid solution behaviour is the so-called 'BIMEVOX' series of materials. The substitution of transition metal cations (M^{II-IV}) for V^V on the B-sites of the n = 1 Aurivillius phase $Bi_2V_{1-x}M_xO_{5.5-y}$ results in a high concentration of oxide vacancies in the structure lattice, leading to high oxide ion conductivity.[5-7] However, the solubility maximum for B-site cation incorporation is often as low as $x = 0.2$ in many BIMEVOX series, which can limit extensive tuning of the physical properties of these materials.

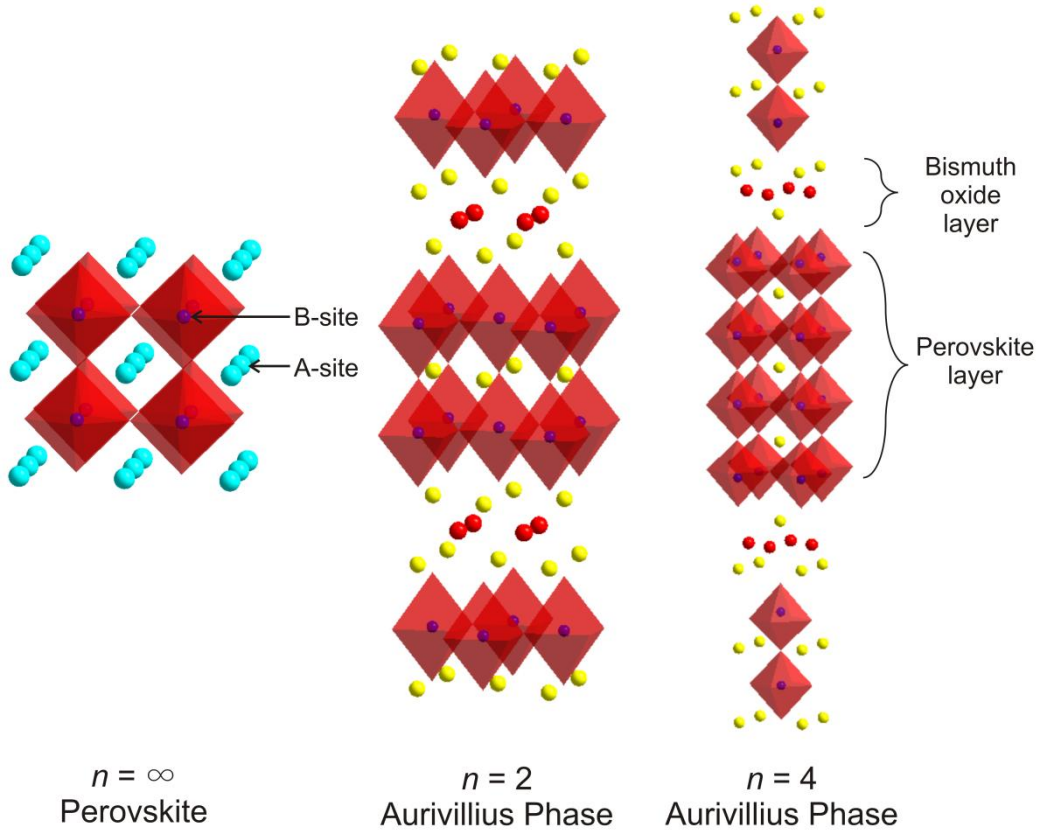

Figure 4.1: Unit cells of the cubic perovskite structure (e.g. $BaTiO_3$), the n = 2 Aurivillius structure (e.g. Bi_3TiNbO_9), and the n = 4 Aurivillius structure (e.g. $Bi_5Ti_3CrO_{15}$). ● denotes perovskite A-site cations, ● denotes Aurivillius Bi cations, ● denotes Aurivillius O anions, and ● denotes all B-site cations.

The research described in this chapter focuses on members of the $n = 4$ family of Aurivillius phases. Many recent articles in this field proclaim the successful formation of novel doped $n = 4$ Aurivillius compounds that exhibit exciting and highly sought-after physical properties. However, it is also evident from several conflicting reports in the literature that synthesis of such novel Aurivillius structures as pure-phases can be challenging. The vast range of synthetically-accessible, structurally-related potential product materials, in addition to common use of relatively volatile reagents such as Bi_2O_3, often leads to formation of undesirable side-products alongside the target material. The existence of such impurities can be difficult to confirm because of their presence in low concentration and their structural similarity to the desired product, therefore care must be taken to comprehensively characterise all product phases formed.

4.1.1 B-site cation-doped compounds with the n = *4 Aurivillius structure*

B-site cation doping can be divided into two categories: isovalent and aliovalent substitution. The term 'isovalent' refers to the direct replacement of a cation in a structure with one of the same oxidation state. Aliovalent substitution involves replacement with an ion of different oxidation state, and takes place with either corresponding loss of oxygen from the structure or parallel aliovalent cation substitution, to balance the overall charge.

The synthesis of B-site doped $n = 4$ Aurivillius ceramics has been dominated by phases containing d^0 cations.[8] Generally, the success of aliovalent B-site cation substitution in Aurivillius phases, leading to non-stoichiometry, is highly-dependent upon the maximum threshold for oxide vacancies in the structure under scrutiny. For Aurivillius phases where $n > 1$, this is typically very low (*ca.* < 5%).[4] The successful substitution of Ga^{3+} for Ti^{4+} to form '$BaBi_4Ti_3GaO_{14.5}$' was initially reported to form a product exhibiting exceptionally high oxide ion conductivity.[9] However, subsequent investigation led to the discovery of a small amount of β-Bi_2O_3 impurity in the product mixture, confirming that incorporation of Ga^{3+} onto the B-sites was significantly lower than the original report suggested.[10] This reappraisal highlights the importance of complete phase characterisation prior to forming definitive conclusions about structure-property relationships in these complex solid state systems.

The $Bi_5Ti_3FeO_{15}$ compound was introduced in Section 1.4. It remains one of the few examples of a structurally characterised $n > 1$ Aurivillius phase that contains a significant stoichiometry of a non-d^0 cation.[11] Clearly, this system represents a template for synthesis of similar transition-metal doped species with highly desirable physical properties, and yet well-defined examples of such are rare. In 2011, whilst preliminary studies were being undertaken on the work described in this chapter, Giddings *et al.* reported the successful synthesis and characterisation of $Bi_5Ti_3CrO_{15}$.[12] This isovalently B-site doped $n = 4$ Aurivillius compound exhibits low-temperature paramagnetism due to Cr/Ti disorder on the B-sites. In the same report, the attempted ceramic synthesis of $Bi_5Ti_3CoO_{15}$ and $Bi_5Ti_3MnO_{15}$ species failed to yield pure $n = 4$ phases.

A study of further reports of attempted Co^{3+} incorporation into $n = 4$ compounds highlights several inconsistencies within the literature. In 2009, Mao and co-workers reported on the multiferroic properties of '$Bi_5Ti_3Fe_{0.5}Co_{0.5}O_{15}$' with $n = 4$ Aurivillius structure.[13] Coexistence of ferroelectricity and ferromagnetism above room temperature in this compound was described, following partial doping of Co^{3+} for Fe^{3+} on the perovskite-layer B-sites. Thin films of this material have also been formed using the chemical solution deposition method.[14, 15] However, subsequent detailed phase analysis on this system indicates that the magnetic behaviour arises instead from a small amount of $CoFe_{2-x}Ti_xO_4$ spinel-type impurity phase formed alongside the Aurivillius compound.[16, 17] In similar work, two very recent articles by Chen and co-workers (2011[18] and 2012[19]) describe the synthesis of the $Bi_5Ti_3Fe_{1-x}Co_xO_{15}$ series in both bulk and thin film form. Despite clear variation in the XRD data observed across members of this series however, they do not report the existence of impurity phases or changes in crystal symmetry for any of the product materials.

Examples of fully structurally characterised four-layer Aurivillius compounds containing other M^{3+} B-site cations are rare. Despite the attempts of Giddings and co-workers, incorporation of Mn^{3+} into perovskite layers of the structure, in various quantities, has been undertaken with some success.[20-23] Synthesis of the gallium-doped $Bi_5Ti_3GaO_{15}$ species (alongside an unidentified impurity phase) was first mentioned by Subbarao in 1962.[24] Strain calculations and the room temperature dielectric properties of this material were subsequently reported,[25, 26] however, this compound and its partially Ga-doped analogues have not been the subject of any further characterisation. Intriguingly, the only example of successful incorporation of trivalent V^{3+} in the place of Fe^{3+} into the $n = 4$

family was claimed by Kan *et al.* for the $0 \leq x \leq 0.05$ members of the '$Bi_{4.5}Sr_{0.5}Ti_4Fe_{0.5-x}V_xO_{15}$' series.[27] However, the *c*-parameters elucidated from structural refinement with materials in this series exhibited notable incongruity with increasing *x*, which is perhaps indicative of the formation of a competing impurity phase alongside the product.

4.1.2 Molten salt synthesis of Aurivillius phases

The technique of molten salt synthesis (MSS) was introduced in Section 1.1.2. The $n = 3$ Aurivillius phase, $Bi_4Ti_3O_{12}$, has been prepared by this method.[28] The nature of the salt species, in addition to its ratio in the reagent mixture, has a significant impact upon both the size and morphology of the resultant bismuth titanate particles.[29, 30] Formation of $Bi_4Ti_3O_{12}$ was hypothesised to proceed *via* liquid-assisted reaction of Bi_2O_3 and TiO_2 above the eutectic point of the Na_2SO_4/K_2SO_4 salt employed (823 °C). Particles formed using this method were larger than those synthesised using a comparable NaCl/KCl salt mix, which was explained by the higher solubility and mass transport rate of the reagents in the sulphate flux.

Synthesis of the 'parent' $Bi_5Ti_3FeO_{15}$ $n = 4$ material has also been successfully undertaken using a eutectic mixture of NaCl/KCl salts in four-fold excess.[31, 32] Particle size and sample crystallinity were observed to vary markedly with changes in synthesis duration. In a parallel study undertaken by Porob and Maggard, $Bi_5Ti_3FeO_{15}$ was synthesised using a seven-fold excess of a eutectic mixture of the Na_2SO_4 and K_2SO_4 salts.[33] They found that the molten flux accelerated the reaction kinetics, and a pure crystalline phase was formed upon reaction at 900 °C for just one hour. Under similar conditions, members of the $Pb_{1-x}Bi_{4+x}Ti_{4-x}Mn_xO_{15}$ series were successfully formed in the presence of excess of Na_2SO_4/K_2SO_4 salt.[34] A limit for incorporation of Mn^{3+} into the perovskite layers of the structure was observed at $x \geq 0.8$ in this report.

Further examples of MSS of B-site doped $n = 4$ Aurivillius phases are uncommon. Palizdar *et al.* attempted the synthesis of $Bi_5Ti_3Fe_{0.5}Co_{0.5}O_{15}$ in NaCl/KCl flux, but the product could only be formed in the presence of impurities.[35] Nevertheless, an interesting comparison of the particle morphology with the product from analogous ceramic synthesis emphasises the applicability of this technique in forming highly-textured platelet materials.[36]

4.1.3 Scope of the chapter

The work described in this chapter focuses on the isovalent doping of several M^{3+} ions (M = V, Cr, Co, Ga) for Fe^{3+} on the B-sites of the parent *n* = 4 Aurivillius phase, $Bi_5Ti_3FeO_{15}$. Ionic radii for the M^{3+} ions are provided in Table 4.1. Cations were selected based on their likelihood to successfully substitute for Fe^{3+} (similar ionic size and charge), as well as their propensity to promote interesting physical properties in the product material (in the case of Cr^{3+} and Co^{3+}, *via* unpaired *d*-electrons). Considering the quantity of publications in this field which report on the synthesis of minor impurity phases alongside target Aurivillius products, particular emphasis was given to comprehensive structural characterisation of each product phase. Where relevant, synthesis parameters were tuned in an attempt to form Aurivillius compounds with phase-purity.

Table 4.1: Summary of the ionic radii of the M^{3+} metal ions investigated.

Metal ion	Ionic Radius* / Å
V^{3+}	0.640
Cr^{3+}	0.615
Fe^{3+} (LS)	0.550
Fe^{3+} (HS)	0.645
Co^{3+} (LS)	0.545
Co^{3+} (HS)	0.610
Ga^{3+}	0.620

* Ionic radii for ions with octahedral coordination obtained from Shannon, 1969.[37]

Given the susceptibility of these systems to small changes in reaction conditions, the molten salt synthesis procedure was employed to facilitate optimisation of the products. Previous reports indicate that use of a 1 : 1 Na_2SO_4/K_2SO_4 mixture is highly appropriate for Aurivillius phase synthesis. This flux exhibits an appropriate eutectic point for synthesis at reduced temperatures, a high solubility in water (aiding product recovery), a low reactivity (therefore unlikely to participate in side reactions), and the individual components are relatively inexpensive.

4.2 Molten salt synthesis of doped Aurivillius phases

The synthesis of four distinct series of B-site cation-doped n = 4 Aurivillius phases, $Bi_5Ti_3Fe_{1-x}M_xO_{15}$ (M = V, Cr, Co, Ga), was attempted using an analogous molten salt method to Porob and Maggard.[33] Stoichiometric amounts of the relevant metal oxide starting materials were ground with an excess of ionic salt to produce a homogeneous mixture. Reactions in this section were undertaken in the presence of a seven-fold excess of an equimolar combination of Na_2SO_4 and K_2SO_4 ionic salts. The mixture was placed in an alumina crucible and heated above the melting point of the salt. Following a dwell period at the synthesis temperature, samples were cooled, washed with warm water to remove the salt, vacuum filtered, and then dried in air for 2 hours.

Molten salt synthesis of the four Aurivillius series was attempted over the range $0.1 \leq x \leq 1.0$, in increments of 0.1. n = 4 Aurivillius phase synthesis was only successful for certain members of each series. The values of x in the starting materials for which Aurivillius phase formation was achieved are provided in Table 4.2.

Table 4.2: Summary of the values of x for successful n = 4 Aurivillius phase formation.

Aurivillius Series	Successful n = 4 product formation
$\mathbf{Bi_5Ti_3Fe_{1-x}V_xO_{15}}$	x = 0.1*, 0.2*, 0.3*
$\mathbf{Bi_5Ti_3Fe_{1-x}Cr_xO_{15}}$	x = 0.1, 0.2, 0.3, 0.4, 0.5, 0.6*, 0.7*, 0.8*, 0.9*
$\mathbf{Bi_5Ti_3Fe_{1-x}Co_xO_{15}}$	x = 0.1*, 0.2*, 0.3*, 0.4*, 0.5*, 0.6*
$\mathbf{Bi_5Ti_3Fe_{1-x}Ga_xO_{15}}$	x = 0.1, 0.2, 0.3*, 0.4*, 0.5*

* indicates formation in the presence of additional impurity phases. x in each case denotes starting material stoichiometry, as opposed to values observed in the products.

Each series exhibits a maximum threshold for the quantity of M^{3+} incorporated onto the B-sites. At higher values of M^{3+} substitution, impurities form alongside the desired phase, until the respective limit in x is reached and an n = 4 Aurivillius phase no longer forms. Similar solubility limits have been observed during attempts at B-site Mn^{3+} doping into analogous n = 4 structures.[34] Product powder samples containing vanadium and chromium ranged from light brown to dark brown, those containing cobalt were dark brown, and those containing gallium ranged from light brown to orange.

The elemental compositions of the reaction products were determined using energy-dispersive X-ray spectroscopy (EDX) (Appendix B). The data were calibrated with respect to a $Bi_5Ti_3FeO_{15}$ standard and the error in each case was determined to be *ca.* ± 5 % from analysis of multiple samples. Those compounds exhibiting chemical formulae consistent with an $n = 4$ Aurivillius phase are listed in Table 4.3.

Table 4.3: Summary of the elemental ratios obtained from EDX data for members of the $Bi_5Ti_3Fe_{1-x}M_xO_{15}$ (M = V, Cr, Co, Ga) series.

Attempted Dopant Stoichiometry	**Chemical Formula**	**Elemental ratios from EDX**	
		Observed	Calculated
$V_{0.1}$*	$Bi_5Ti_3Fe_{0.9}V_{0.1}O_{15}$	Ti : Fe : V 2.97 : 0.88 : 0.12	Ti : Fe : V 3.00 : 0.90 : 0.10
$Cr_{0.1}$	$Bi_5Ti_3Fe_{0.9}Cr_{0.1}O_{15}$	Ti : Fe : Cr 3.10 : 0.92 : 0.08	Ti : Fe : Cr 3.00 : 0.90 : 0.10
$Cr_{0.2}$	$Bi_5Ti_3Fe_{0.8}Cr_{0.2}O_{15}$	Ti : Fe : Cr 2.99 : 0.81 : 0.19	Ti : Fe : Cr 3.00 : 0.80 : 0.20
$Cr_{0.3}$	$Bi_5Ti_3Fe_{0.7}Cr_{0.3}O_{15}$	Ti : Fe : Cr 3.04 : 0.69 : 0.31	Ti : Fe : Cr 3.00 : 0.70 : 0.30
$Cr_{0.4}$	$Bi_5Ti_3Fe_{0.6}Cr_{0.4}O_{15}$	Ti : Fe : Cr 3.04 : 0.60 : 0.40	Ti : Fe : Cr 3.00 : 0.60 : 0.40
$Cr_{0.5}$	$Bi_5Ti_3Fe_{0.5}Cr_{0.5}O_{15}$	Ti : Fe : Cr 3.08 : 0.52 : 0.48	Ti : Fe : Cr 3.00 : 0.50 : 0.50
$Co_{0.1}$*	$Bi_5Ti_3Fe_{0.9}Co_{0.1}O_{15}$	Ti : Fe : Co 3.56 : 0.88 : 0.12	Ti : Fe : Co 3.00 : 0.90 : 0.10
$Co_{0.2}$*	$Bi_5Ti_3Fe_{0.8}Co_{0.2}O_{15}$	Ti : Fe : Co 2.99 : 0.83 : 0.17	Ti : Fe : Co 3.00 : 0.80 : 0.20
$Co_{0.3}$*	$Bi_5Ti_3Fe_{0.8}Co_{0.2}O_{15}$	Ti : Fe : Co 3.41 : 0.75 : 0.25	Ti : Fe : Co 3.00 : 0.70 : 0.30
$Co_{0.4}$*	$Bi_5Ti_3Fe_{0.7}Co_{0.3}O_{15}$	Ti : Fe : Co 4.35 : 0.68 : 0.32	Ti : Fe : Co 3.00 : 0.60 : 0.40
$Ga_{0.1}$	$Bi_5Ti_3Fe_{0.9}Ga_{0.1}O_{15}$	Ti : Fe : Ga 3.08 : 0.91 : 0.09	Ti : Fe : Ga 3.00 : 0.90 : 0.10
$Ga_{0.2}$	$Bi_5Ti_3Fe_{0.8}Ga_{0.2}O_{15}$	Ti : Fe : Ga 3.36 : 0.79 : 0.21	Ti : Fe : Ga 3.00 : 0.80 : 0.20

* indicates samples synthesised alongside additional impurities. The Ti content in some Co-doped phases was slightly higher than anticipated.

Inductively coupled plasma (ICP) atomic emission spectroscopy was used to verify the bulk elemental composition for pure samples listed in Table 4.3. In each case, the M^{3+} metal ratios agreed with those established using EDX analysis.

4.2.1 $Bi_5Ti_3Fe_{1-x}V_xO_{15}$ – X-ray diffraction analysis

Structural characterisation was undertaken on products from the attempted synthesis of $Bi_5Ti_3Fe_{1-x}V_xO_{15}$. Initial reactions were undertaken at 950 °C for 5 hours. Bragg reflections corresponding to an n = 4 Aurivillius phase were observed in samples where $x \leq 0.3$. These reflections were indexed on the basis of an orthorhombic unit cell, $a \sim 5.47$ Å, $b \sim 5.44$ Å, $c \sim 41.00$ Å with space group $A2_1am$. In all cases, Bragg reflections from an impurity phase were additionally observed in the data, which are highlighted for the $0.1 \leq x \leq 0.5$ products in Figure 4.2.

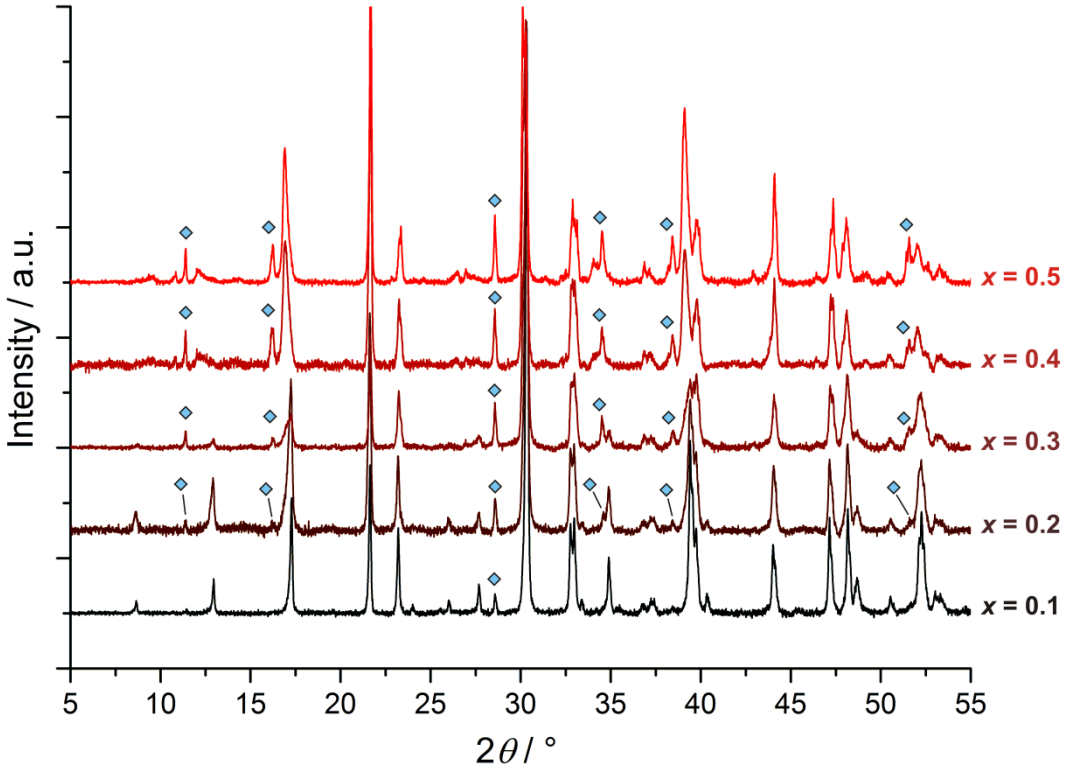

Figure 4.2: Powder XRD data for the products of attempted syntheses of $0.1 \leq x \leq 0.5$ members of the $Bi_5Ti_3Fe_{1-x}V_xO_{15}$ series. Reflections corresponding to a $Bi_4V_2O_{11}$ impurity are labelled (◇).

The observed impurity is consistent with a bismuth vanadium oxide phase, $Bi_4V_2O_{11}$.[38] This material, mentioned in Section 4.1, exhibits room temperature monoclinic symmetry with lattice parameters a = 5.61 Å, b = 15.28 Å, c = 16.60 Å, β = 89.76 °, and space group $C2/m$.[39] The intensity of the $Bi_4V_2O_{11}$ reflections increases with increasing x. For samples where $x \geq 0.4$, several Aurivillius (00l) reflections at low angle are not visible in the XRD data, which indicates that an n = 4 stacked phase no longer forms under these conditions. Instead, a mixture of several other phases predominates, including $Bi_4V_2O_{11}$ and the n = 3 Aurivillius phase $Bi_4Ti_3O_{12}$.[40]

The reaction conditions were varied in an attempt to encourage the formation of a pure $n = 4$ product phase. However, an increase in reaction duration to 12.5 hours and dwell temperature to 1050 °C did not change the nature of the resulting phases. Additionally, ceramic synthesis of the $Bi_5Ti_3Fe_{0.5}V_{0.5}O_{15}$ and $Bi_5Ti_3VO_{15}$ materials was attempted at 1200 °C, using pelletized reagents and prolonged synthesis durations, but pure $n = 4$ Aurivillius phase formation was not possible. $Bi_4Ti_3O_{12}$ and $Bi_4V_2O_{11}$ were again identified as the major products from the XRD data.

4.2.2 $Bi_5Ti_3Fe_{1-x}Cr_xO_{15}$ – X-ray diffraction analysis

Laboratory powder X-ray diffraction analysis was undertaken on the products of $Bi_5Ti_3Fe_{1-x}Cr_xO_{15}$ synthesis. Following reaction at 950 °C for 5 hours, pure $n = 4$ Aurivillius phase formation was successful for values of $x \leq 0.5$. Reflections were indexed using a similar unit cell to the parent compound, $Bi_5Ti_3FeO_{15}$ ($a \sim 5.46$ Å, $b \sim 5.43$ Å, $c \sim 41.10$ Å, space group $A2_1am$). As the Cr^{3+} stoichiometry in the starting material mixture increased in this range, (00*l*) Bragg reflections of the product were observed to shift to higher angle, corresponding to a decrease in the *c*-parameter (discussed in more detail in Section 4.3).

For samples of $Bi_5Ti_3Fe_{1-x}Cr_xO_{15}$ where $x \geq 0.6$, asymmetric reflection broadening in the powder diffraction data is clearly visible (Figure 4.3). The asymmetry is observed only for (*hkl*) reflections with an *l*-dependence (in this case, corresponding to diffraction planes which have some component in the *c*-axis). This observation is indicative of stacking faults, or turbostratic disorder, along this axis. For the $x = 0.8$ congener, the broadened peaks show signs of splitting into new reflections, indicating formation of an additional phase, which eventually exists preferentially at $x = 1.0$. Indexing of the diffraction data confirmed this phase to have a closely related structure to the $n = 4$ Aurivillius compound, but with a reduced *c*-parameter. This material corresponds to a recurrent-intergrowth phase consisting of alternating $n = 3$ and $n = 4$ layers and has the formula $Bi_9Ti_6MO_{27}$ (where M = Fe or Cr).[41] All Bragg reflections were indexed to an orthorhombic unit cell with structural parameters $a = 5.46$ Å, $b = 5.44$ Å and $c \sim 37.0$ Å, and space group *Cmm2* (where $c \sim 37.0$ Å is an approximate average of the *c*-parameter for the $n = 3$ and $n = 4$ Aurivillius phases).

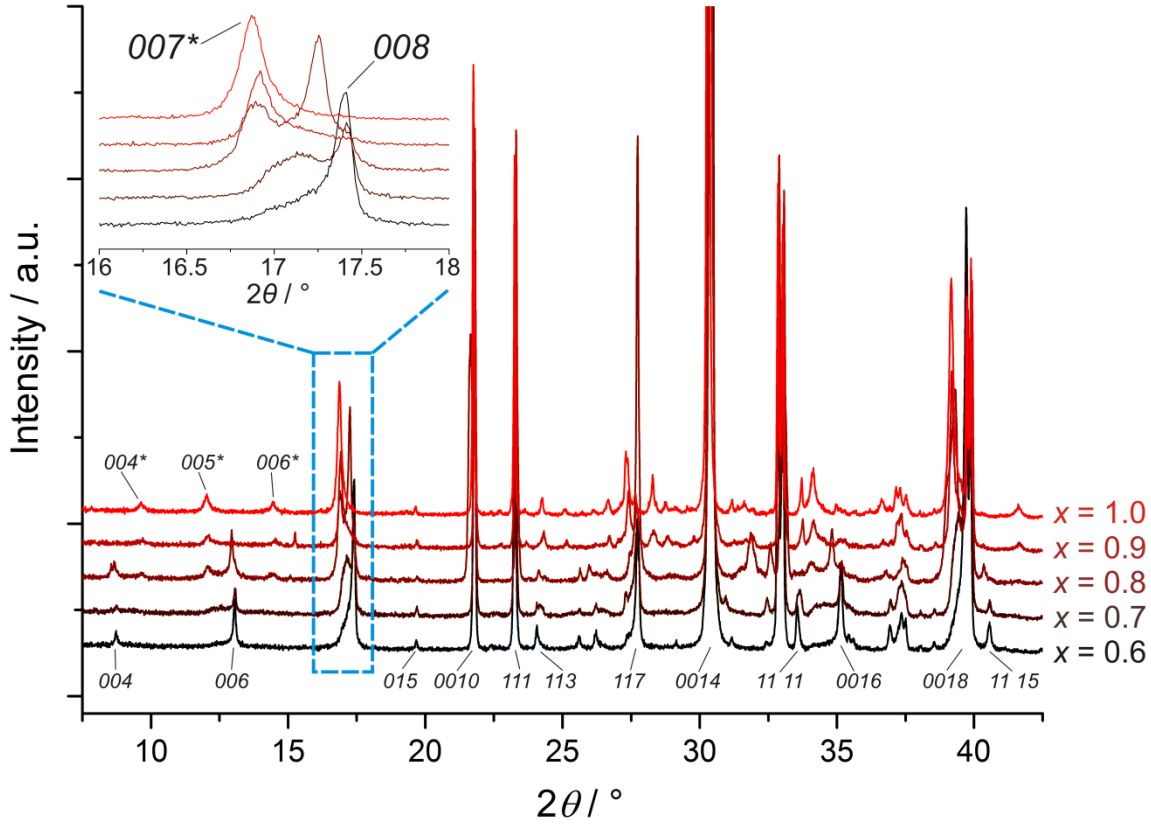

Figure 4.3: Powder XRD data for the products of attempted syntheses of $0.6 \leq x \leq 1.0$ members of the $Bi_5Ti_3Fe_{1-x}Cr_xO_{15}$ series. The x = 0.6 sample has been fully indexed and some low-angle reflections corresponding to (00l) planes of the $Bi_9Ti_6MO_{27}$ phase in the x = 1.0 sample are labelled with an asterix. INSET: Variation in peak asymmetry of the n = 4 (008) reflection and subsequent increase in intensity of the n = 3/4 (007) reflection with change in x.

$Bi_5Ti_3CrO_{15}$ was recently synthesised using the ceramic method by Giddings *et al.*[12] For the attempted molten salt synthesis of the x = 1.0 material here (with complete substitution of Cr^{3+} for Fe^{3+}), only an n = 3/4 intergrowth Aurivillius structure forms alongside some oxide impurities. Further experimentation into the effects of reaction duration on molten salt synthesis of $Bi_5Ti_3CrO_{15}$ is discussed in Section 4.5.1.

4.2.3 $Bi_5Ti_3Fe_{1-x}Co_xO_{15}$ – X-ray diffraction analysis

Formation of an n = 4 Aurivillius compound was achievable for $Bi_5Ti_3Fe_{1-x}Co_xO_{15}$ synthesis attempted in the range $0.1 \leq x \leq 0.6$. However, in each case the product material was formed alongside an impurity phase, which is the tetragonal form of bismuth oxide, β-Bi_2O_3.[42] The intensities of the impurity reflections increase as x is increased. The existence of this additional phase suggests the ratio of metal ions in each Aurivillius product may not be of the initial desired stoichiometry.

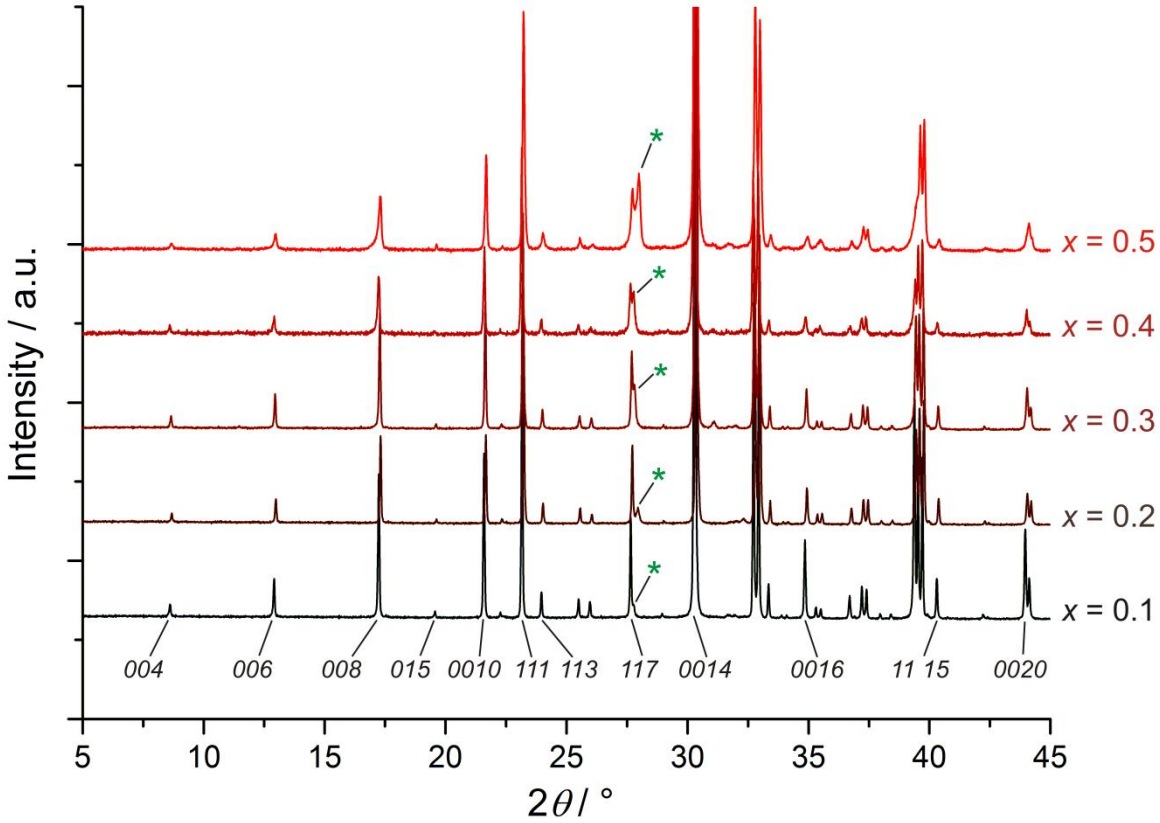

Figure 4.4: Powder XRD data for the products of attempted syntheses of $0.1 \leq x \leq 0.5$ members of the $Bi_5Ti_3Fe_{1-x}Co_xO_{15}$ series. The (201) Bragg reflection of β-Bi_2O_3 is labelled in each diffraction pattern (*).

The (00l) reflections of the product material shift to higher 2θ angles with increasing x. This shift is indicative of incorporation of cobalt in place of iron in the perovskite layers, leading to a reduction in the c-parameter corresponding to the reduced ionic radius of Co^{3+} (Table 4.1). The displacement in reflection position occurs to a lesser degree than that observed for the $Bi_5Ti_3Fe_{1-x}Cr_xO_{15}$ series. Directly analogous to the chromium-doped series however, the basal reflections at low angles exhibit asymmetric broadening at higher dopant quantities. This is most notably observed in the (008) reflection in Figure 4.4. This is attributable to n = 3 intergrowth layers in the product, which arrange

systematically leading to the formation of an n = 3/4 recurrent-intergrowth phase in preference to the pure n = 4 compound at $x \geq 0.7$.

4.2.4 $Bi_5Ti_3Fe_{1-x}Ga_xO_{15}$ – X-ray diffraction analysis

Powder diffraction data indicates that isovalent substitution of Ga^{3+} for Fe^{3+} onto the B-sites in $Bi_5Ti_3Fe_{1-x}Ga_xO_{15}$ is possible for values of $x \leq 0.2$. Beyond this 'solubility limit', where $x \geq 0.3$, Aurivillius phase formation occurs alongside impurities or not at all. Molten salt synthesis of the stoichiometric variants was attempted at 950 °C and a number of different dwell durations (5, 7.5, 10, and 12.5 hours). It was found that an increase in synthesis time did have an effect on the product reflection broadening, but did not increase the quantity of n = 4 Aurivillius phase relative to the impurities formed in the product. XRD data for attempted synthesis of samples in the range $0.1 \leq x \leq 0.5$, at 950 °C for 7.5 hours, are shown in Figure 4.5.

Bragg reflections that do not correspond to the desired n = 4 Aurivillius product are observed to increase in intensity as x increases beyond $x \geq 0.3$. The majority of these can be indexed to the orthorhombic $Bi_2Ga_4O_9$ phase (a = 7.93 Å, b = 8.30 Å, c = 5.89 Å), with a mullite-type structure.[43] The impurity reflections appear at slightly different d-spacings for the different samples, which may be explained by the partial doping of Fe^{3+} into the structure, as has previously been observed in the $Bi_2(Fe_{1-x}Ga_x)_4O_9$ system.[44] As the ratio of Fe^{3+} in the reaction mixture decreases, the propensity for Aurivillius formation also falls, which is indicative of a system where minimum Ga^{3+} is incorporated into the n = 4 structure. This is supported by the observation that (00l) reflections of the product shift minimally with respect to the $Bi_5Ti_3FeO_{15}$ parent material. It also correlates with the results from EDX measurements undertaken on this series.

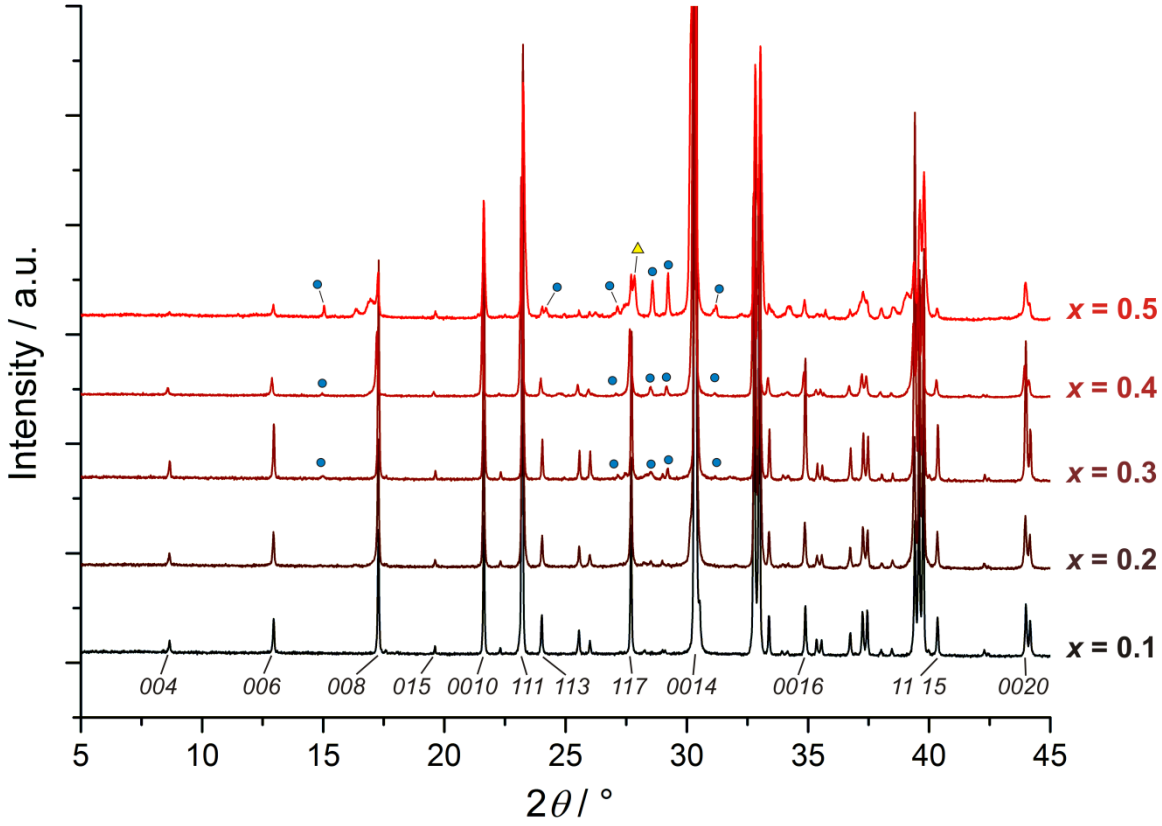

Figure 4.5: Powder XRD data for the products of attempted syntheses of $0.1 \leq x \leq 0.5$ members of the $Bi_5Ti_3Fe_{1-x}Ga_xO_{15}$ series. Some Bragg reflections of the $x = 0.1$ sample are labelled. Reflections corresponding to the $Bi_2Ga_4O_9$ impurity are marked with blue circles (●) and the β-Bi_2O_3 reflection at *ca.* 28° is marked with a yellow triangle (△).

It is interesting to note that broadening of some of the (00*l*) reflections of the $n = 4$ phase is evident in XRD data for $x = 0.4$ and 0.5 (most notable in the (008) reflection at $2\theta \sim 17.3°$). This is again analogous to findings from the $Bi_5Ti_3Fe_{1-x}Cr_xO_{15}$ series, where $n = 3$ intergrowths infiltrate the $n = 4$ structure at higher dopant quantities. This trend continues beyond $x = 0.5$ until an $n = 3/4$ recurrent intergrowth phase forms in preference to the $n = 4$ material.

4.2.5 Discussion

Evidence for the existence of solubility limits in each series arises from the observed shift in product reflection positions. Upon isovalent substitution of cations on the B-sites, in most cases the unit cell contracts along the *c*-direction due to incorporation of smaller M^{3+} cations. Formation of an $n = 4$ Aurivillius phase is often evident beyond the solubility limit, but the observation of no further shift of the (00*l*) Bragg reflections

suggests that the ratio of M^{3+} : Fe^{3+} does not continue to change. This is consistent with EDX data for the products and the detection of additional phases formed alongside the relevant materials.

B-site doping of vanadium for iron into the perovskite layers of $Bi_5Ti_3FeO_{15}$ was not readily achieved. At elevated temperatures, oxidation of V^{3+} to V^{5+} competes with isovalent substitution, resulting in parallel formation of the bismuth vanadium oxide compound, $Bi_4V_2O_{11}$, which has the n = 1 Aurivillius structure. Use of an alternative lower-temperature synthesis technique to the molten salt method, employing less forcing conditions, may result in retention of the +3 oxidation state and more extensive formation of members of the $Bi_5Ti_3Fe_{1-x}V_xO_{15}$ series.[45]

The n = 4 Aurivillius structure appears to be more accommodating towards incorporation of chromium on the B-sites than the other M^{3+} ions studied. The system behaves similarly to the $Bi_5Ti_3Fe_{1-x}Mn_xO_{15}$ series.[20] EDX and XRD analyses are both suggestive of pure Cr^{3+}-doped Aurivillius formation for $Bi_5Ti_3Fe_{1-x}Cr_xO_{15}$, when $0.1 \leq x \leq 0.5$. Beyond this range however, incommensurate intergrowths of n = 3 perovskite blocks infiltrate the n = 4 structure resulting in a deviation from the ideal target stoichiometry. A schematic, summarising the phases formed during molten salt synthesis of $0.1 \leq x \leq 1.0$ members of this series, is shown in Figure 4.6.

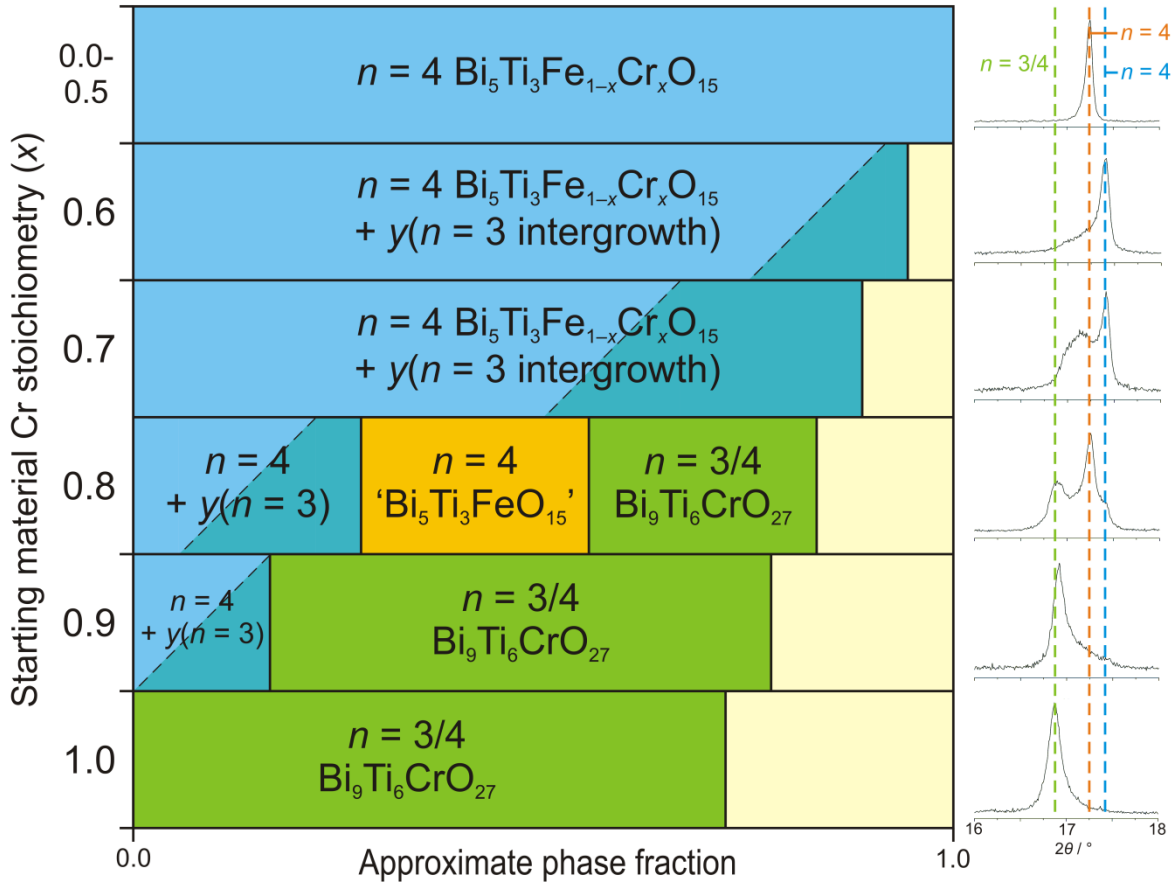

Figure 4.6: Schematic depicting the estimated distribution of crystalline phases formed during attempted synthesis of $Bi_5Ti_3Fe_{1-x}Cr_xO_{15}$, derived using product XRD data and known starting material stoichiometries. The approximate fraction of oxide impurities for each product is represented by the yellow blocks. A section of the XRD data from the $x = 0.1$ and $0.6 \leq x \leq 1.0$ products is shown on the right hand side, labelled with the expected positions of reflections corresponding to a chromium-deficient $n = 4$ phase (orange line), a partially chromium-doped $n = 4$ phase (blue line) and an $n = 3/4$ phase (green line).

As the number of observed $n = 3$ intergrowths increases with increasing x, so must the quantity of impurities formed in conjunction (the yellow blocks in Figure 4.6). Indeed, Bragg reflections corresponding to the β-Bi_2O_3 impurity phase are observed to increase in intensity at consecutively higher values of x. However, no single Ti/Fe/Cr-containing crystalline impurities are detected in the XRD data, as would be expected to balance the stoichiometry across each system. It can be hypothesised that doping of some of these ions may take place into the Bi_2O_3 impurity phase. It is also possible that metal ions are lost from the product mixture as part of the salt-washing procedure prior to XRD analysis.

Through visual comparison of the diffraction data, it is impossible to ascertain preferential location of the different transition metals in distinct $n = 3$ or $n = 4$ blocks.

However, due to the different ionic radii of the B-site species, by observing shifts in the positions of basal reflections, changes in *c*-parameter can be monitored to give an indication of the level of dopant incorporation in each Aurivillius layered-phase. XRD data from the products of attempted synthesis of $Bi_5Ti_3Cr_{0.8}Fe_{0.2}O_{15}$, $x = 0.8$, exhibit reflections corresponding to chromium-deficient $n = 4$ stacked layers (coloured orange in the schematic), highly chromium-doped $n = 4$ stacked layers with disordered $n = 3$ intergrowths (coloured blue/turquoise in the schematic), and chromium-doped alternately-stacked $n = 3/4$ layers (coloured green in the schematic). This is an interesting observation, as it implies segregation of the transition metal cations into different phases; iron is preferentially incorporated into the $n = 4$ stacked layers, with chromium into the $n = 3/4$. This is also consistent with the general trend observed in the products upon increasing chromium over the range $0.1 \leq x \leq 1.0$. Consideration of the perovskite tolerance factor can shed some light on this observation. Subbarao first applied the concept of cation 'tolerance' to the perovskite unit of Aurivillius phases in 1962.[24] He suggested that the tolerance range for cation incorporation decreases, with more stringent regulation on the substituent ionic radii, as the number of layers in the perovskite block (*n*) increases. Subsequently, Newnham *et al.* suggested that cations outside the radius range 0.62 – 0.69 Å could not be tolerated on the B-sites of $Bi_4Ti_3O_{12}$.[46] The ionic radius of octahedral Cr^{3+} (0.615 Å) lies close to the boundary of this range, and as such, may have a stronger preference to reside in the perovskite layers of a system with greater cationic tolerance, corresponding to lower *n*.

Attempted synthesis of the $Bi_5Ti_3Fe_{1-x}Co_xO_{15}$ and $Bi_5Ti_3Fe_{1-x}Ga_xO_{15}$ series led to product formation alongside impurities. The use of Co(II,III) oxide starting material potentially led to non-stoichiometry in the product due to incorporation of some Co^{2+}. Additionally, Co^{3+} and Fe^{3+} possess the greatest discrepancy in ionic radii of all the dopant cations investigated (Table 4.1). It may be that the structural distortion required to incorporate a significant concentration of Co^{3+} is not energetically favourable. EDX data for cobalt-doped species with higher values of *x* suggest a larger than expected quantity of Ti^{4+} resides on the B-sites (Table 4.3). This coincides with the onset of $n = 3$ intergrowth formation, which indicates that the intergrowth layer may be predominantly $Bi_4Ti_3O_{12}$.

4.3 Structure refinement

The crystal structure of $Bi_5Ti_3FeO_{15}$ has been elucidated by Hervoches *et al.*[11] The resulting model was used as a starting point for structure refinement of several novel doped $n = 4$ Aurivillius phases discussed in the preceding sections. Data obtained from laboratory high-resolution powder X-ray diffraction measurements were suitable for Rietveld analysis using GSAS-EXPGUI.[47] An orthorhombic cell (space group: $A2_1am$) with B-site solid solution was refined against samples and an acceptable correlation between model and data was found for refinements with all phases discussed in this section. The result of Rietveld analysis with data from the $Bi_5Ti_3Fe_{0.8}Cr_{0.2}O_{15}$ sample, containing the observed, calculated and difference profiles, is provided in Figure 4.7.

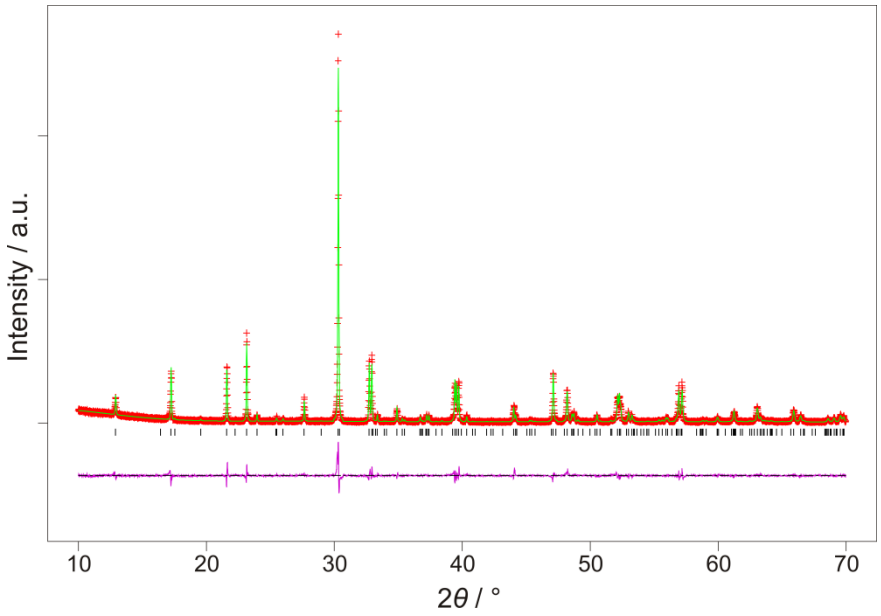

Figure 4.7: Rietveld refinement of an orthorhombic structure model with powder XRD data from a scan of $Bi_5Ti_3Fe_{0.8}Cr_{0.2}O_{15}$. The diagram contains experimental (red), calculated (green) and difference (pink) profiles for the data. Goodness of fit parameters were: $\chi^2 = 1.796$, wRp = 0.1629, and Rp = 0.1238.

Structural information formulated from Rietveld analyses with acceptable goodness of fit parameters are summarised in Table 4.4 and a comprehensive list of refinement data is provided in Appendix C. Strong preferred orientation effects were detected in XRD data for many of the samples. This feature is consistent with previous XRD measurements undertaken on Aurivillius phases synthesised using MSS. Preferential growth along the (001) plane was observed in $Bi_4Ti_3O_{12}$ product particles synthesised in the presence of a K_2SO_4/Na_2SO_4 eutectic flux.[29] As a result of this faceting, the powder diffraction intensities of (00*l*) reflections were often greater than those predicted by the refined model.

Table 4.4: Summary of unit cell parameters obtained from Rietveld refinement of an orthorhombic $n = 4$ Aurivillius structure model against XRD data for members of the $Bi_5Ti_3Fe_{1-x}M_xO_{15}$ (M = V, Cr, Co, Ga) series.

Sample	Lattice parameter			V / Å^3
	a / Å	b / Å	c / Å	
$Bi_5Ti_3Fe_{0.9}V_{0.1}O_{15}$*	5.4701(2)	5.4364(2)	41.166(1)	1224.17(9)
$Bi_5Ti_3Fe_{0.9}Cr_{0.1}O_{15}$	5.4704(2)	5.4363(2)	41.157(1)	1223.97(9)
$Bi_5Ti_3Fe_{0.8}Cr_{0.2}O_{15}$	5.4684(2)	5.4359(2)	41.108(1)	1222.0(1)
$Bi_5Ti_3Fe_{0.7}Cr_{0.3}O_{15}$	5.4675(2)	5.4354(2)	41.069(1)	1220.47(8)
$Bi_5Ti_3Fe_{0.6}Cr_{0.4}O_{15}$	5.4651(2)	5.4348(2)	41.017(1)	1218.3(1)
$Bi_5Ti_3Fe_{0.5}Cr_{0.5}O_{15}$	5.4640(2)	5.4351(2)	40.997(2)	1217.5(1)
$Bi_5Ti_3Fe_{0.9}Co_{0.1}O_{15}$*	5.47111(9)	5.43678(9)	41.1695(6)	1224.59(5)
$Bi_5Ti_3Fe_{0.8}Co_{0.2}O_{15}$*	5.47239(7)	5.43862(8)	41.1561(6)	1224.90(5)
$Bi_5Ti_3Fe_{0.8}Co_{0.2}O_{15}$*	5.4706(1)	5.4318(1)	41.146(1)	1223.89(8)
$Bi_5Ti_3Fe_{0.7}Co_{0.3}O_{15}$*	5.4694(2)	5.4375(2)	41.138(1)	1223.4(1)
$Bi_5Ti_3Fe_{0.9}Ga_{0.1}O_{15}$	5.4705(1)	5.4366(1)	41.1844(8)	1224.86(6)
$Bi_5Ti_3Fe_{0.8}Ga_{0.2}O_{15}$	5.4667(1)	5.4337(1)	41.2181(8)	1224.34(6)

* denotes impure samples which were subject to a multi-phase refinement.

The general trend for the change in unit cell volume across each series is a small but significant decrease upon increased B-site substitution. This is in line with the smaller Shannon-Prewitt effective ionic radii for octahedrally coordinated cations of V^{3+} (0.640 Å), Cr^{3+} (0.615 Å), Co^{3+} (0.610 Å) and Ga^{3+} (0.620 Å), when compared to Fe^{3+} (0.645 Å).[37] Individual lattice parameters vary to different extents depending on the dopant cation. The *a*- and *b*-parameters fluctuate only marginally as the B-site stoichiometry changes. However, upon V-, Cr- and Co-doping, the *c*-parameter decreases markedly as the quantity of iron across the series falls. The *c*-parameters calculated for phases in the $Bi_5Ti_3Fe_{1-x}Cr_xO_{15}$ and $Bi_5Ti_3Fe_{1-x}Co_xO_{15}$ series are plotted in Figure 4.8. A comparison with structural data from the $Bi_5Ti_3FeO_{15}$ phase (a = 5.4698(1) Å, b = 5.4389(1) Å, and c = 41.197(1) Å) was made.

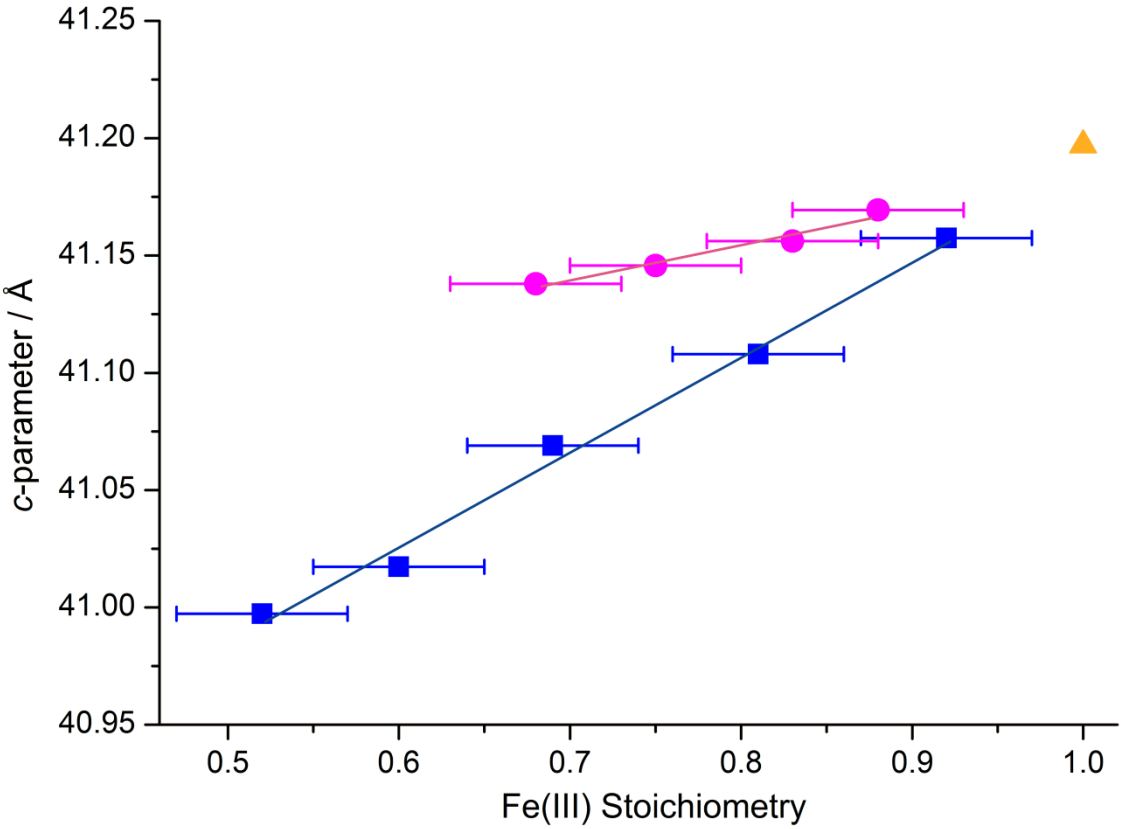

Figure 4.8: The change in *c*-parameter as a function of B-site substitution in the $Bi_5Ti_3Fe_{1-x}M_xO_{15}$ series, for Cr- (■) and Co-doping (●). Data were calculated from structure refinement/EDX analysis and the lattice parameter error in each case is within the data point. The *c*-parameter of $Bi_5Ti_3FeO_{15}$, published by Hervoches *et al.*, is represented by ▲.

The *c*-parameter values for members of the Cr- and Co-series fit well with a linear decrease upon reduction in Fe content. This is in accordance with Vegard's Law, which postulates that unit cell parameters should vary linearly with composition for a solid solution with random distribution of ions.[48] The decrease in *c*-parameter observed for $Bi_5Ti_3Fe_{1-x}Co_xO_{15}$ is smaller than expected when considering the relative cationic radii. Liu *et al.* observed an *increase* in *c*-parameter across the $n = 5$ $Bi_6Fe_{2-x}Co_xTi_3O_{18}$ Co-doped series, which was ascribed to a contribution from radially larger Co^{2+} ions (0.745 Å) present in the lattice.[49] It is possible that a similar redox variation occurs in the $n = 4$ cobalt-doped system, with partial Co^{2+}/Co^{3+} substitution accounting for the lattice parameter variation. The higher than expected Ti : Co ratio calculated from EDX data (Table 4.3), in addition to the β-Bi_2O_3 impurity observed alongside the product, supports the argument for some Co^{2+} inclusion.

The unit cell length along the *c*-axis deviates minimally upon gallium substitution. Early reports on the structure of $Bi_5Ti_3GaO_{15}$ proposed a *c*-parameter of 41.0(5) Å,[24] which suggests a decrease would be expected as the ratio of gallium in the structure is increased (in line with the difference in ionic radii of the Ga^{3+} and Fe^{3+} species). A reason for the absence of this trend could be a failure to incorporate any gallium into the $n = 4$ structure, however this contrasts observations from EDX, ICP and XRD phase-analysis. It is possible that at such low concentrations of dopant, the structure exhibits a 'buffering effect' towards Ga^{3+} incorporation, with the unit cell volume remaining approximately constant as a small quantity of Ga^{3+} locates in the perovskite layer.

The *c*-parameter of the $x = 1.0$ species, $Bi_5Ti_3CrO_{15}$ (40.701 Å), determined by Giddings *et al.*, is consistent with the linear trend for $Bi_5Ti_3Fe_{1-x}Cr_xO_{15}$ detailed here. A comparable reduction in lattice constants upon B-site substitution of Cr^{3+} for Fe^{3+} has also been observed in an $n = 5$ Aurivillius system.[50] The atomic positions of the B-site cations in each Cr-doped phase model were refined where possible. The 'outer' B-site cation of the perovskite layer (labelled 'Ti/Fe/Cr2' in Figure 4.9) exhibits a notable deviation in position from the centre of the surrounding oxide octahedron for all compounds in the Cr-series. An analogous positional shift was recorded for Ti/Mn cations in $Pb_{1-x}Bi_{4+x}Ti_{4-x}Mn_xO_{15}$.[34]

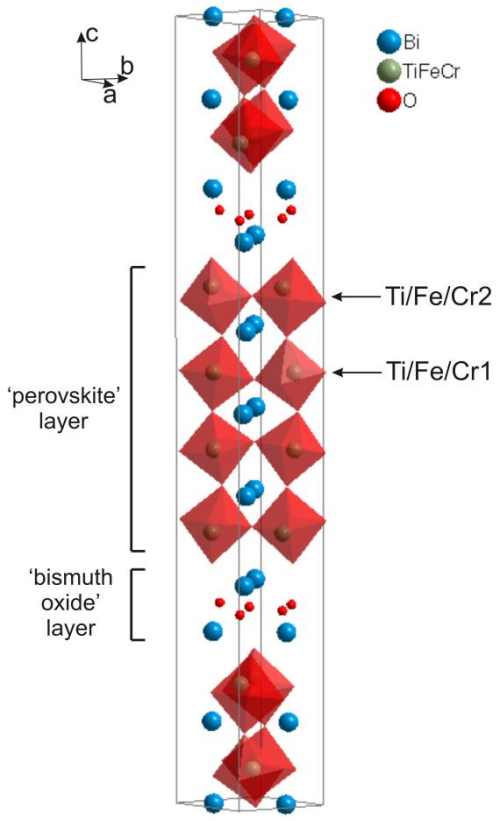

Figure 4.9: Unit cell diagram for the n = 4 Aurivillius compound $Bi_5Ti_3Fe_{0.8}Cr_{0.2}O_{15}$, created using the structural model from Rietveld refinement with powder XRD data.

In the Rietveld refinement of the $Bi_5Ti_3Fe_{1-x}Cr_xO_{15}$ series, the $Ti^{4+}/Fe^{3+}/Cr^{3+}$ cations were randomly distributed over the two distinct perovskite B-sites in their stoichiometric amounts. Instigating competitive B-site occupation in the model did lead to a small preference for Ti^{4+} over Cr^{3+}/Fe^{3+} ions to locate on the Ti/Fe/Cr2 'outer' positions of the n = 4 perovskite block. A similar observation in the $Bi_5Ti_3CrO_{15}$ species was explained by the preference for Ti^{4+} occupation of the more distorted octahedral site at high temperatures due to maximum electrostatic interaction with oxide ions in the fluorite-like bismuth oxide layer.[12] It is likely that this effect would be more pronounced in products formed from MSS due to the shorter reaction durations and faster cooling rates, preventing the cation distribution from equilibrating. Neutron diffraction studies are required to unequivocally confirm the absolute distribution of cations on the B-sites.

4.4 Characterisation of $Bi_5Ti_3Fe_{1-x}Cr_xO_{15}$

Due to the relatively high Cr^{3+} solubility limit of the series, the novel members of the B-site doped family $Bi_5Ti_3Fe_{1-x}Cr_xO_{15}$ were selected for further investigation, and the pure phases formed from molten salt synthesis were characterised.

4.4.1 Thermogravimetric analysis

Thermogravimetric analysis (TGA) was employed to determine the oxygen stoichiometry in each phase, and hence the oxidation state of the B-site metal ions. The propensity for the n = 4 Aurivillius structure to incorporate oxide vacancies is low, and as such, significant deviation from fifteen oxygen atoms per formula unit was not anticipated. TGA data for the x = 0.2 sample are shown in Figure 4.10, and the remaining data for the $0.1 \leq x \leq 0.5$ samples are collated in Appendix D.

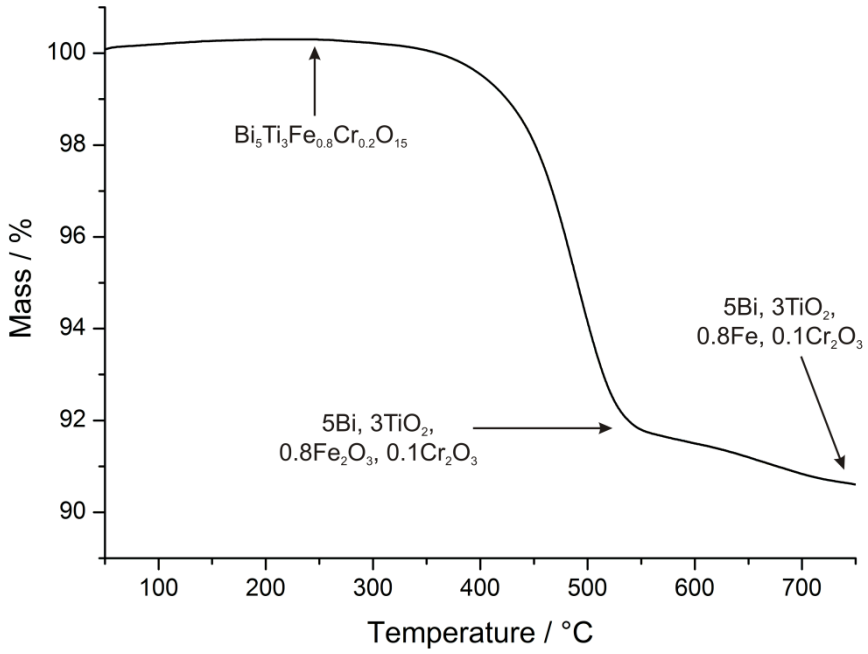

Figure 4.10: TGA data for $Bi_5Ti_3Fe_{0.8}Cr_{0.2}O_{15}$.

Samples were heated to 800 °C at a rate of 5 °C.min^{-1} under a 50 cm^3.min^{-1} flow of hydrogen (25 %) in nitrogen gas and left to dwell at that temperature for one hour. The percentage change in sample mass was recorded as a function of temperature. For each sample, a significant mass loss occurred (*ca.* 8.5 %) between 400 and 550 °C corresponding to the reduction of Bi^{III} to elemental Bi^0. This was followed by a smaller

mass loss of *ca.* 1.0 % due to reduction of Fe^{III} to Fe^{0} upon heating to 750 °C. XRD data from the products of TGA analysis confirmed the presence of Bi and TiO_2 crystalline phases. During the temperature dwell at 800 °C, a small linear decrease in sample mass was observed, which is likely to be due to loss of volatile elemental bismuth above its melting point.

For all compounds in the range $0.1 \leq x \leq 0.5$, the observed mass loss was consistent with reduction of an $n = 4$ Aurivillius compound with fifteen oxygen atoms per formula unit. This further confirms the complete occupancy of perovskite B-sites with Ti^{IV}, Cr^{III}, and Fe^{III} in each case.

4.4.2 Scanning Electron Microscopy

Scanning Electron Microscopy (SEM) was employed to determine the particle size and morphology of the $0.1 \leq x \leq 0.5$ products of $Bi_5Ti_3Fe_{1-x}Cr_xO_{15}$ molten salt synthesis. Aurivillius phases synthesised by hydrothermal and MSS methods have a tendency to form well-defined platelets,[29, 51] with the perovskite *c*-axis positioned perpendicular to the principal surface of these platelets.[52] SEM images for each sample are shown in Figure 4.11.

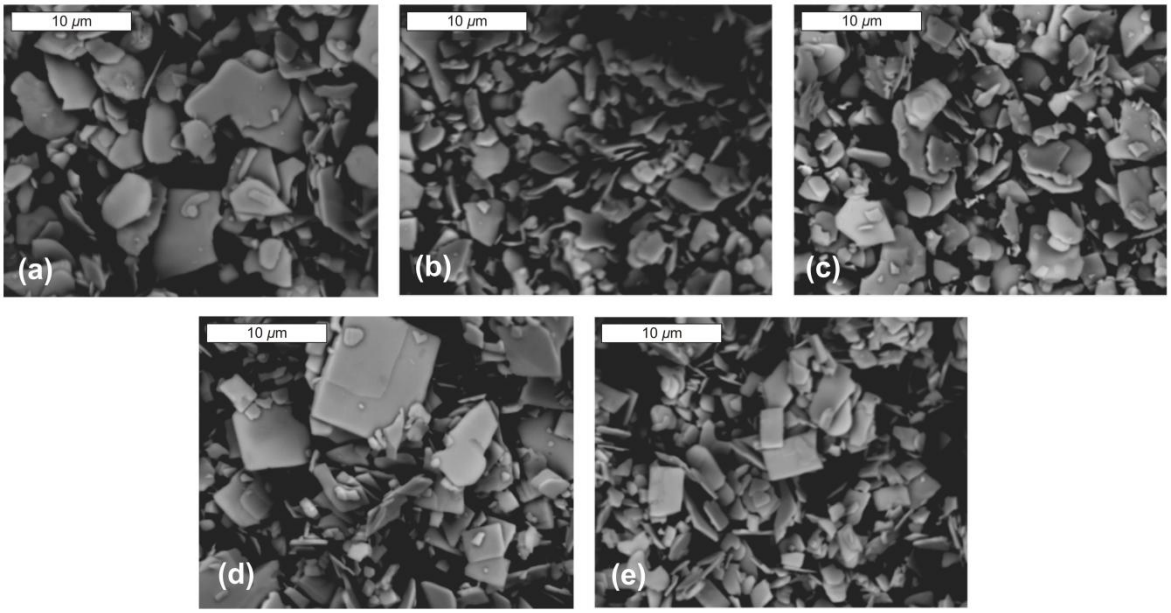

Figure 4.11: SEM images for the (a) $x = 0.1$, (b) $x = 0.2$, (c) $x = 0.3$, (d) $x = 0.4$, and (e) $x = 0.5$ samples of $Bi_5Ti_3Fe_{1-x}Cr_xO_{15}$ synthesised in the presence of molten salt at 950 °C for 5 hours.

As anticipated, the Aurivillius product particles have platelet morphology. Particle size varies significantly within each compound, with an upper limit of approximately 10 μm. No variation in size is evident between samples of different *x*. However, a greater proportion of the x = 0.4 and 0.5 product particles do appear to exhibit regimented rectangular morphology, in contrast to the more random platelet shape at lower *x*.

4.4.3 Magnetic Properties

Figure 4.12 illustrates the temperature dependence of the molar susceptibility (χ_m) of $Bi_5Ti_3Fe_{0.5}Cr_{0.5}O_{15}$ across the range $10 \leq T$ / K ≤ 300. Paramagnetic behaviour is observed in the sample, with no transition to a magnetically ordered state evident at low temperatures. Inset in Figure 4.12 is a plot of the inverse of the molar susceptibility as a function of temperature, and these data have been modelled using the Curie-Weiss Law.

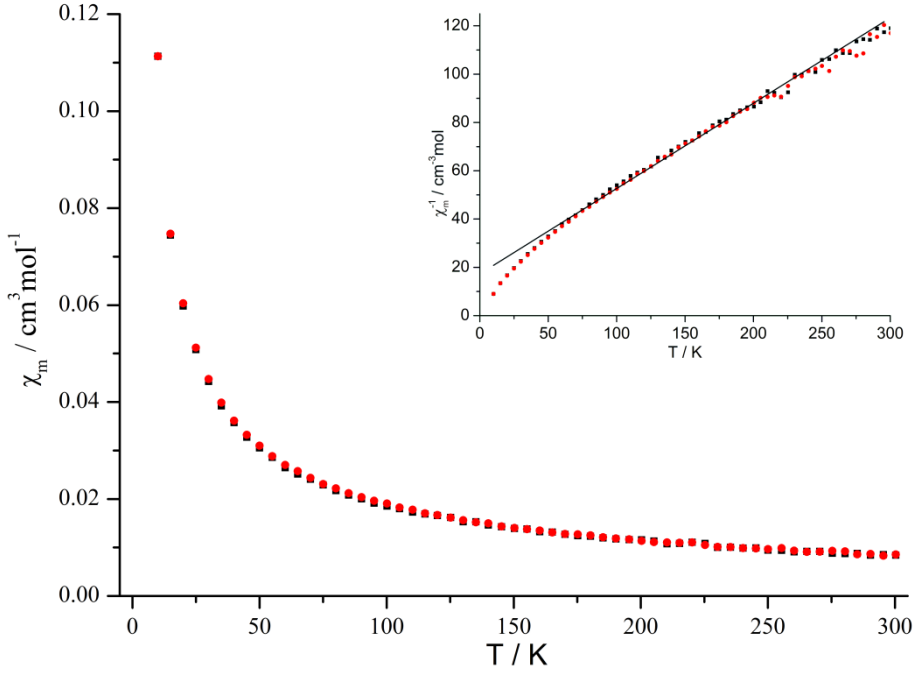

Figure 4.12: Zero field cooled (■) and field cooled (●) molar susceptibility (χ_m) *vs.* temperature plot for the $Bi_5Ti_3Fe_{0.5}Cr_{0.5}O_{15}$ sample. INSET: Plot of reciprocal of χ_m *vs.* temperature including fitting of field cooled data to the Curie-Weiss Law.

The calculated and expected magnetic moments per formula unit (μ_{eff}) for $0.1 \leq x \leq 0.5$ members of the $Bi_5Ti_3Fe_{1-x}Cr_xO_{15}$ series are shown in Table 4.5. In most cases, values agree closely with the spin-only approximation, which is expected for a mixture of Cr^{3+} d^3 and Fe^{3+} d^5 ions.

Table 4.5: Magnetic moment data for the $Bi_5Ti_3Fe_{1-x}Cr_xO_{15}$ $0.1 \leq x \leq 0.5$ congeners.

Chromium stoichiometry (x)	Expected μ_{eff} (spin-only)	Observed μ_{eff} (μ_B)	Weiss Constant (θ) / K
0.1	5.74	5.64 (4)	– 96.1
0.2	5.58	5.00 (6)	– 65.4
0.3	5.39	4.77 (5)	– 53.1
0.4	5.20	4.62 (4)	– 52.8
0.5	5.00	4.75 (5)	– 48.9

Magnetic data for all samples are summarised in Appendix D. Extrapolation of the Curie-Weiss fit yields a negative Weiss constant in each case. A negative value is indicative of antiferromagnetic coupling of spins. Consideration of the superexchange pathway confirms that this is expected for Cr^{3+} d^3-d^3 and Fe^{3+} d^5-d^5 interactions.[53] The paramagnetic behaviour with short-range antiferromagnetic interactions observed here for the partially Cr-doped species is analogous to that reported for isostructural $Bi_5Ti_3CrO_{15}$ and $Bi_5Ti_3FeO_{15}$.[12, 54] The similarity of these magnetic properties is perhaps suggestive of some degree of segregation of the M^{3+} cations within the perovskite layers.

4.4.4 Vibrational Spectroscopy

Immediately following reaction and cooling to room temperature, samples were washed with deionised water and the Aurivillius product separated from the dissolved salt using vacuum filtration. During this washing procedure, it was noted that the filtrate became discoloured for different samples. At lower values of x the aqueous solution was colourless, but for samples where $x \geq 0.5$, the filtrate became increasingly yellow as the quantity of chromium in the starting materials increased (Figure 4.13).

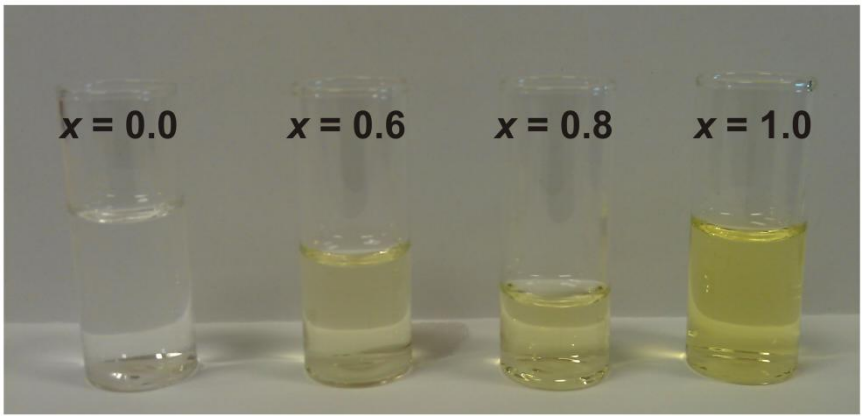

Figure 4.13: Photograph of some filtrates of $Bi_5Ti_3Fe_{1-x}Cr_xO_{15}$ samples obtained following washing.

The yellow discolouration is indicative of a mixed sodium/potassium chromate species present in solution. The nature of the species in each filtrate solution was probed using Raman spectroscopy. Measurements were undertaken using aqueous solutions of the filtrates from the x = 0.6, 0.8, and 1.0 congeners, and on crystals grown from the filtrate of the x = 0.0 compound (Figure 4.14). Strong bands due to SO_4^{2-} are observed at *ca.* 452, 620, 628 and 992 cm^{-1} in all the spectra. Notably, additional bands at *ca.* 464, 645, 1100, 1130 and 1150 cm^{-1} were observed in the spectrum of the x = 0.0 sample, which were attributable to Na_2SO_4 crystals.[55]

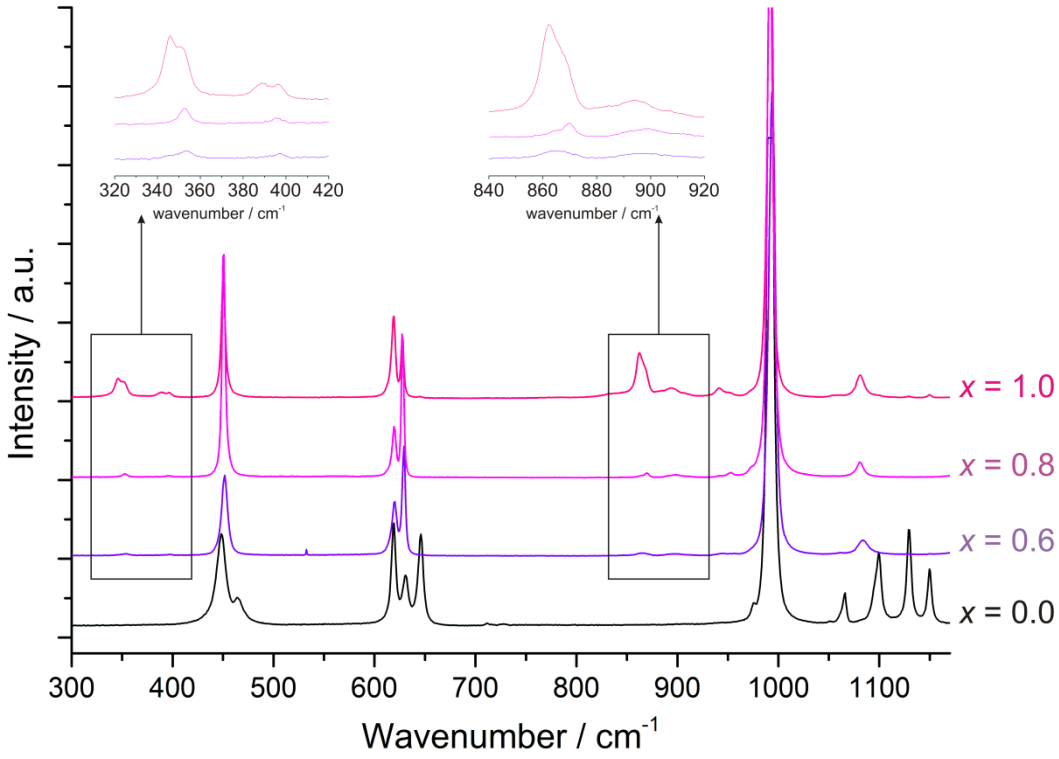

Figure 4.14: Raman data for the aqueous solutions resulting from product washing. Measurements were undertaken on filtrates of selected samples in the $Bi_5Ti_3Fe_{1-x}Cr_xO_{15}$ series.

Additionally observed in spectra for the x = 0.6, 0.8, 1.0 filtrates are bands due to the chromate species, CrO_4^{2-}, highlighted in Figure 4.14. The two stretching frequencies are found at *ca.* 862 and 893 cm^{-1}, and the positions of the two bending vibrations are *ca.* 348 and 392 cm^{-1}.[56] No bands due to $Cr_2O_7^{2-}$ dichromate species were evident in any of the Raman spectra.[57, 58] An additional band was also present at *ca.* 1085 cm^{-1} in data from the x = 0.6, 0.8, and 1.0 filtrates, which corresponds to the sulphite species SO_3^{2-}.

These observations indicate that for the attempted MSS of $Bi_5Ti_3Fe_{1-x}Cr_xO_{15}$ with $0.5 \leq x \leq 1.0$, the excess Cr^{3+} that does not become incorporated into the Aurivillius structure is oxidised to Cr^{6+} by sulphate, which is present in excess. During the reaction at 950 °C, a corresponding reduction of some sulphate SO_4^{2-} ions to sulphite SO_3^{2-} takes place. Both CrO_4^{2-} and SO_3^{2-} are subsequently removed from the product mixture during washing, and are detected in the Raman spectra of the filtrates. This explains the absence of any crystalline Cr-containing impurity phases in the diffraction data of the product materials of higher x.

4.5 Monitoring the effects of varying synthesis conditions

The studies described in the preceding sections illustrate that molten salt synthesis is an appropriate method for producing some members of the $Bi_5Ti_3Fe_{1-x}Cr_xO_{15}$ series in the pure phase. Formation of the x = 0.0, 0.6, and 1.0 members of this series was subject to further examination. Previous investigations indicate that in the case of the MSS technique, slight alterations to synthetic parameters can make significant impacts upon the nature of the products formed. Yang and co-workers observed that by methodically varying the reaction temperature as well as the nature of the molten salt, the synthesis of several $LaMO_3$ (M = Fe, Co, Ni) perovskite phases could be tuned to facilitate optimum product purity, as well as significant changes in the morphology of the resulting particles.[59] This section contains a description of the results from Aurivillius phase synthesis following a systematic variation in two different synthetic conditions: the synthesis duration and the composition of the molten salt.

4.5.1 Varying the reaction duration

Considering the complex relationship between product phases in the $Bi_5Ti_3Fe_{1-x}Cr_xO_{15}$ system (Section 4.2.5), the influence of reaction duration upon layer-stacking and intergrowth formation in the x = 0.6 and x = 1.0 congeners was investigated. Due to the corrosive nature of the molten salt employed, reaction for longer than 12.5 hours led to significant interaction with, and degradation of, the alumina crucible. Consequently, this was the maximum dwell duration probed for this synthesis technique. A section of the diffraction data for products of $Bi_5Ti_3Cr_{0.6}Fe_{0.4}O_{15}$ synthesis at various durations is shown in Figure 4.15.

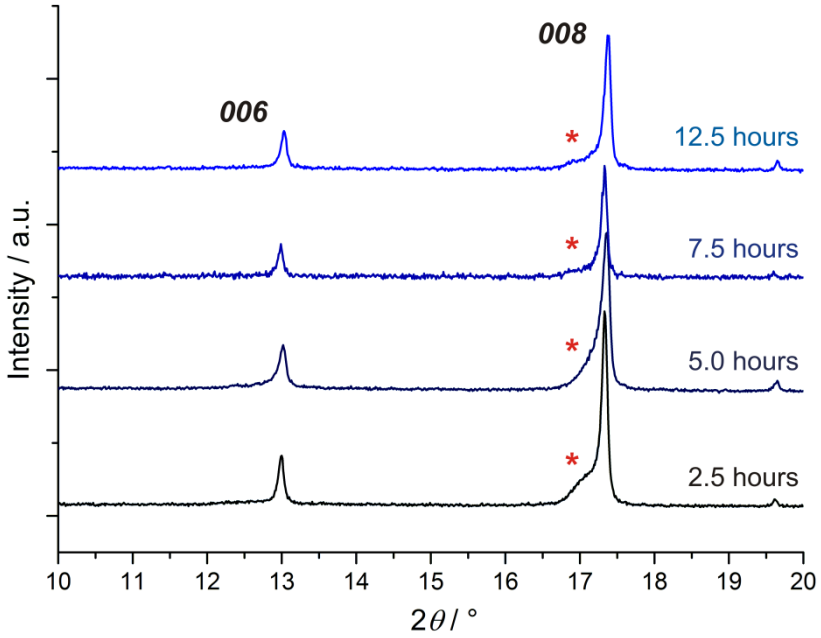

Figure 4.15: XRD data for samples of $Bi_5Ti_3Cr_{0.6}Fe_{0.4}O_{15}$ synthesised at 950 °C with various dwell durations. A shoulder on the (008) reflection, indicating turbostratic disorder, is labelled (*).

The peak asymmetry of several (00*l*) Bragg reflections is less in the products of reaction at longer duration. It can be inferred from this that the quantity of n = 3 intergrowth layers in the product material declines when the sample is reacted for longer timescales, and conversion from a lamellar system, containing disorder in the *c*-direction, to the thermodynamically favoured pure n = 4 system occurs over time. However, in the case of this x = 0.6 sample, it is not possible to completely eradicate intergrowths using the molten salt method at timescales of less than 12.5 hours. SEM images provided in Appendix D illustrate that the x = 0.6 platelet particles formed after 12.5 hours are generally larger than those formed after 2.5 hours.

XRD data for the products of attempted synthesis of $Bi_5Ti_3CrO_{15}$ (x = 1.0), from reactions with various dwell durations, are shown in Figure 4.16. MSS reactions were undertaken separately at 1000 °C for 5.0, 7.5 and 12.5 hours. To complement this investigation, standard ceramic synthesis was also undertaken using pelletized reagents in the absence of salt at 1000 °C for 50 hours.

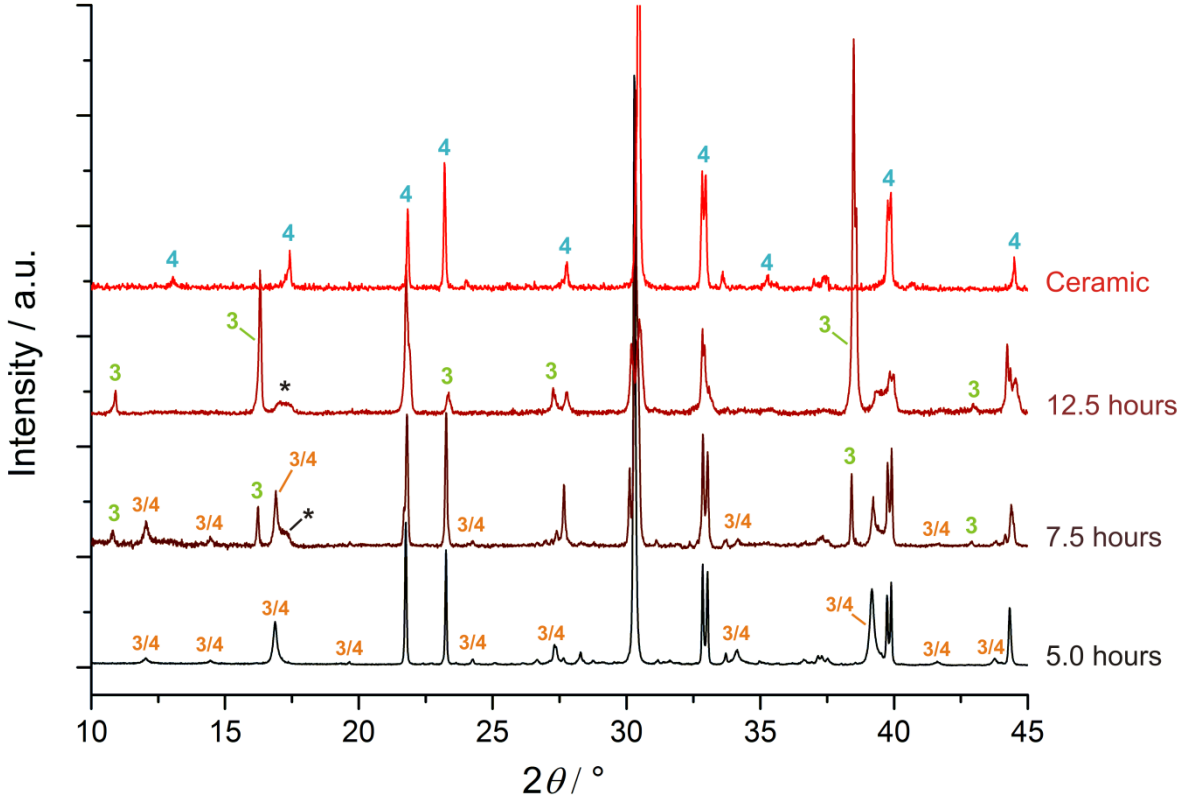

Figure 4.16: XRD data for products of attempted $Bi_5Ti_3CrO_{15}$ molten salt and ceramic syntheses undertaken at 1000 °C with various dwell durations. Selected reflections corresponding to the n = 3 phase $Bi_4Ti_3O_{12}$ (3), the n = 3/4 phase $Bi_9Ti_6CrO_{27}$ (3/4), and the n = 4 phase $Bi_5Ti_3CrO_{15}$ (4) are labelled. * denotes reflection broadening discussed in the text.

Following reaction at 1000 °C in the presence of molten salt for 5.0 hours, the major product detected in XRD data was the recurrent intergrowth species, $Bi_9Ti_6CrO_{27}$, mentioned in Section 4.2.2. Other crystalline phases identified from the data were a small amount of β-Bi_2O_3 and several other starting material metal oxides. Prolonged heating for 7.5 hours leads to formation of the n = 3 $Bi_4Ti_3O_{12}$ phase in addition to the n = 3/4 product. Following extended reaction for 12.5 hours, $Bi_4Ti_3O_{12}$ forms in excess alongside a bismuth-containing impurity. In contrast to the materials produced from molten salt synthesis, the ceramic synthesis method generates only the n = 4 $Bi_5Ti_3CrO_{15}$ product

(which exhibits a small amount of turbostratic disorder evidenced by the asymmetry of the (008) reflection at $2\theta \sim 17.5°$).

The behaviour of the $x = 1.0$ system is different to that of the $x = 0.6$ system. Whereas the XRD data from ceramic synthesis indicate that the $n = 4$ $Bi_5Ti_3CrO_{15}$ material is again the thermodynamic product, prolonged molten salt synthesis no longer instigates formation of this phase. Instead, the system becomes chromium-deficient upon extended reaction, resulting in gradual conversion of the $n = 3/4$ phase to $Bi_4Ti_3O_{12}$, with $n = 3$ structure. An increase in the discolouration of the filtrate following salt removal suggests that competing oxidation of Cr^{3+} to Cr^{6+} by sulphate, analogous to that observed in Section 4.4.4, is the reason for this observation. EDX analysis was undertaken on samples from attempted $x = 1.0$ synthesis and a gradual decrease in chromium content was confirmed in samples synthesised for progressively longer durations (Appendix D). Accompanying the loss in coherence of reflections corresponding to the $n = 3/4$ phase is a significant broadening of reflections in those regions where $n = 4$ basal reflections may be expected (labelled * in Figure 4.16). This is suggestive of $Bi_4Ti_3O_{12}$ formation from $Bi_9Ti_6CrO_{27}$ *via* a disordered phase containing a randomised mixture of $n = 3$ and $n = 4$ layers. Such a mechanism has been observed using high-resolution TEM for the conversion between $n = 3$ and $n = 4$ phases,[60] and this is discussed in greater depth in Chapter 5.

4.5.2 Varying the Molten Flux

As outlined in Section 1.1.2, a broad range of fluxes have been studied and their suitability for a variety of molten salt syntheses has been assessed.[61, 62] RbCl has been successfully employed as a molten salt to enable the rapid synthesis of perovskite-like compounds. Geselbracht *et al.* reported that formation of the $RbCa_2Nb_3O_{10}$ Dion-Jacobson phase in RbCl occurs within minutes at 800 °C.[63] Additionally, Yang and co-workers synthesised the $LaFeO_3$ perovskite using both $NaNO_2$ and a $NaNO_3/KNO_3$ 1 : 1 eutectic flux.[59] Existing reports of MSS of $n = 4$ Aurivillius phases have principally focused on use of the NaCl/KCl and Na_2SO_4/K_2SO_4 fluxes, at temperatures in excess of 800 °C.[33]

The molten salt synthesis of $Bi_5Ti_3FeO_{15}$ was attempted using three different fluxes: $NaNO_2$ (melting point 271 °C), a $NaNO_3/KNO_3$ eutectic (melting point 228 °C),[64] and RbCl (melting point 718 °C). These materials were selected based on their existing

successful use in the synthesis of perovskite-like compounds, in addition to their lower melting points relative to Na_2SO_4/K_2SO_4 and their high solubility in water (to enable product recovery). A summary of the results from attempted synthesis of $Bi_5Ti_3FeO_{15}$ (x = 0.0) with the different molten salts under various reaction conditions is provided in Table 4.6.

Table 4.6: Summary of the products from attempted synthesis of $Bi_5Ti_3FeO_{15}$ using various molten salts.

Salt Components	Reaction Conditions			Identifiable Products in XRD Data
	Salt Excess	Temperature	Duration	
$NaNO_3/KNO_3$*	10 : 1	450 °C	5 hours	β-Bi_2O_3, TiO_2, Fe_2O_3
$NaNO_3/KNO_3$*	10 : 1	550 °C	5 hours	$Bi_{12}TiO_{20}$, β-Bi_2O_3, TiO_2, Fe_2O_3
$NaNO_2$	17 : 1	450 °C	5 hours	$Bi_{12}TiO_{20}$, $Na_{0.5}Bi_{0.5}TiO_3$
$NaNO_2$	17 : 1	550 °C	5 hours	$Bi_{12}TiO_{20}$, $Na_{0.5}Bi_{0.5}TiO_3$
RbCl	30 : 1	800 °C	5 hours	Broad starting material oxide reflections
RbCl	30 : 1	835 °C	5 hours	n = 4 $Bi_5Ti_3FeO_{15}$
RbCl	30 : 1	1000 °C	12.5 hours	n = 4 $Bi_5Ti_3FeO_{15}$

* the ratio of $NaNO_3$: KNO_3 in the salt mixture was 1 : 1.

Reaction with the $NaNO_3/KNO_3$ salt did not lead to formation of the target $Bi_5Ti_3FeO_{15}$ phase. Instead, a mixture of the starting materials was observed in the XRD data from the products, as well as reflections corresponding to the sillenite-type phase $Bi_{12}TiO_{20}$ in data from the reaction at 550 °C. This material, with cubic cell, a = 10.188 Å and space group $I23$,[65] is a commonly synthesised member of the Bi_2O_3-TiO_2 system. A slight deviation in the observed lattice parameters of this phase from the literature reported values may be due to a small amount of Fe^{3+}-doping.[66]

Intriguingly, use of the nitrite salt results in formation of different products than with the nitrate materials, despite the identical reaction conditions. This suggests that the molten $NaNO_2$ interacts with the solid reagents to facilitate an alternative reaction. Phase analysis of the XRD data reveals that only two detectable crystalline phases form at both 450 and 550 °C; the body-centred cubic $Bi_{12}TiO_{20}$ and the pseudo-rhombohedral

$Na_{0.5}Bi_{0.5}TiO_3$ (NBT) phases. NBT has the distorted perovskite structure with a = 5.49 Å, c = 13.50 Å, and space group $R3c$,[67] although recent studies also indicate an appropriate monoclinic model for this phase at room temperature.[68] NBT has been investigated as a lead-free piezoelectric material for use in sensors.[69] Molten salt synthesis of this material has been achieved using a NaCl/KCl eutectic above 950 °C,[70, 71] but to our knowledge this is the first example of NBT synthesis *via* incorporation of sodium from molten $NaNO_2$ at these comparatively low temperatures.

MSS of $Bi_5Ti_3FeO_{15}$ was attempted at three temperatures using RbCl. The XRD pattern from products synthesised at 800 °C contained reflections attributable to TiO_2, in addition to several other broad, low intensity reflections. Formation of the n = 4 phase was successful at 835 and 1000 °C. The stark contrast in observed product materials between 800 and 835 °C is highly indicative of a reaction 'barrier' somewhere in this temperature range. It appears that a different chemical feature of the system, rather than the melting of the salt at 718 °C, is required to be overcome before successful reaction can occur. It was mentioned in Section 2.6.2 that the melting point of Bi_2O_3 is 824 °C. It is highly possible that this physical change is the driving force towards n = 4 Aurivillius formation. This hypothesis is discussed in more depth in Chapter 5.

4.6 B-site substitution involving divalent cations

Octahedral B-site cations in Aurivillius phases tend to be small and highly-charged. Incorporation of a divalent M^{2+} cation onto the B-sites of an $n > 1$ Aurivillius phase has never been reported.[72] The ionic radius of the Ni^{2+} cation is within the tolerance threshold required for successful perovskite substitution hypothesised by Newnham *et al.*[46] Synthesis of the $Bi_5Ti_{3+x}Fe_{1-2x}Ni_xO_{15}$ series was attempted in increments of 0.1 over the range $0.1 \leq x \leq 0.5$. To account for the difference in charge between Fe^{3+} and Ni^{2+}, the stoichiometry of Ti^{4+} was increased to maintain charge neutrality upon nickel-doping. As a result, although this is an example of attempted aliovalent B-site doping, no corresponding increase in oxygen vacancies in the structure was required to incorporate Ni^{2+}.

Reflection indexing and phase analysis of the XRD data indicated that the products of x = 0.1 and 0.2 synthesis were phase pure compounds with the n = 4 Aurivillius structure.

The $x = 0.3$ member of the series was formed in the presence of minor impurities. The chemical compositions calculated using EDX and TGA data are provided in Table 4.7.

Table 4.7: Summary of the chemical compositions of $0.1 \leq x \leq 0.3$ members of the $Bi_5Ti_{3+x}Fe_{1-2x}Ni_xO_{15}$ series, derived from EDX data. Bulk sample Fe : Ni ratios from ICP analysis are also provided.

Chemical Formula	B-site ratios from EDX	Fe : Ni ratio from ICP
$\mathbf{Bi_5Ti_{3.1}Fe_{0.8}Ni_{0.1}O_{15}}$	Ti : Fe : Ni 3.13(±0.2) : 0.78(±0.1) : 0.09(±0.1)	0.79: 0.10(±0.1)
$\mathbf{Bi_5Ti_{3.2}Fe_{0.6}Ni_{0.2}O_{15}}$	Ti : Fe : Ni 3.24(±0.2) : 0.60(±0.1) : 0.16(±0.1)	0.59: 0.20(±0.1)
$\mathbf{Bi_5Ti_{3.3}Fe_{0.4}Ni_{0.3}O_{15}}$	Ti : Fe : Ni 3.31(±0.2) : 0.43(±0.1) : 0.26(±0.1)	0.52: 0.22(±0.1) *

* indicates deviation from expected due to presence of additional impurities in the bulk sample.

High-resolution XRD data obtained from the $0.1 \leq x \leq 0.3$ samples can be indexed to an orthorhombic cell analogous to that applied for the other $n = 4$ Aurivillius series. Considerable intensity variations for many of the (00*l*) reflections resulted from preferred orientation effects from the platelet particles. Structural parameters elucidated from peak-fitting analysis of the three samples are provided in Table 4.8.

Table 4.8: Unit cell parameters for members of the $Bi_5Ti_{3+x}Fe_{1-2x}Ni_xO_{15}$ series.

Sample	Lattice parameter			V / Å^3
	a / Å	b / Å	c / Å	
$\mathbf{Bi_5Ti_{3.1}Fe_{0.8}Ni_{0.1}O_{15}}$	5.461(2)	5.426(2)	40.957(16)	1213.7(9)
$\mathbf{Bi_5Ti_{3.2}Fe_{0.6}Ni_{0.2}O_{15}}$	5.462(4)	5.430(3)	40.895(15)	1212.9(8)
$\mathbf{Bi_5Ti_{3.3}Fe_{0.4}Ni_{0.3}O_{15}}$	5.464(3)	5.431(5)	40.877(16)	1212.9(8)

Systematic replacement of larger Ni^{2+} (0.690 Å) for Fe^{3+} on the B-sites does not result in an increase in the overall unit cell volume, as may be anticipated. Instead, the decrease observed in both V and the c-parameter can be attributed to a greater effect from the corresponding increase in concentration of smaller Ti^{4+} cations (0.605 Å) in the lattice.

As the number of non-titanium ions in the perovskite unit decrease, the influence from these cations upon the size of the unit cell is depleted.

Scanning electron microscopy studies confirmed the morphology of the samples to be characteristic of Aurivillius compounds formed from molten salt synthesis (Figure 4.17). Samples exhibited distinctive platelet morphology with moderately homogeneous size distribution between 5 and 10 μm.

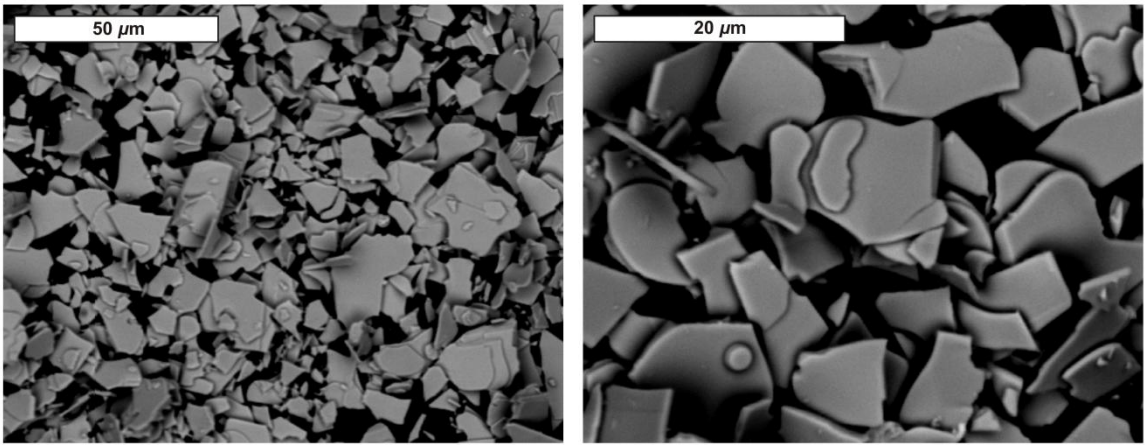

Figure 4.17: SEM images of $Bi_5Ti_{3.1}Fe_{0.8}Ni_{0.1}O_{15}$.

4.7 Conclusion

Doping into the perovskite-layer B-sites of the Aurivillius compound, $Bi_5Ti_3FeO_{15}$, has been accomplished using a range of cations. The extent to which successful substitution of Fe^{III} for V^{III}, Cr^{III}, Co^{III}, Ni^{II}, and Ga^{III} was achieved was found to be highly dependent upon the nature of the substituent. Definitive limits were established in each case for the maximum quantity of each ion that could be incorporated into the $n = 4$ Aurivillius structure.

The molten salt synthesis method was employed in the formation of all novel compounds described in this chapter. Structure refinement and SEM studies on the $Bi_5Ti_3Fe_{1-x}Cr_xO_{15}$ series indicate that highly-pure crystalline product platelets can be formed using this technique, following reaction for just 5 hours. However, XRD analysis in conjunction with Raman spectroscopy brought to light a crucial disadvantage of the procedure. Undesirable side-reactions involving the flux, such as formation of Na_2CrO_4/K_2CrO_4 in the case of $Bi_5Ti_3Fe_{1-x}Cr_xO_{15}$ $(0.6 \leq x \leq 1.0)$ synthesis, can lead to oxidation and

subsequent isolation of important reagents from the reaction mixture. Sometimes however, these side-reactions can also facilitate the formation of highly desirable phases, as was observed in the first example of $NaNO_2$-induced formation of $Na_{0.5}Bi_{0.5}TiO_3$.

Aurivillius phases, specifically those with greater values of *n*, are highly intricate systems and it is clear from the findings detailed in this chapter that complex relationships exist between the $n = 3$ and $n = 4$ structures. The existence of perovskite-layer intergrowths has been shown to be dependent upon both synthesis duration and the relative stoichiometry of B-site dopant. The drive towards interconversion and ordered-mixing of these two related lamellar systems remains unclear. Questions have also arisen over the true function of the molten salt. Multifarious reports in the literature describe the effects of 'improved ionic mobility' accompanying the molten salt method, leading to lower synthesis temperatures and reaction durations, with specific references to reactions involving compounds with the $n = 4$ Aurivillius structure. However, preliminary findings detailed in this chapter suggest that the temperature threshold for molten salt synthesis of a pure Aurivillius phase may be entirely independent of the flux.

Chapter 5, immediately succeeding this, contains the description of a detailed *in situ* X-ray diffraction investigation into the molten salt synthesis of some of the novel $n = 4$ Aurivillius phases described above.

4.8 References

1. B. Aurivillius, *Arkiv for Kemi*, 1950, **1**, 463-480.
2. B. Aurivillius, *Arkiv for Kemi*, 1950, **1**, 499-512.
3. B. Aurivillius, *Arkiv for Kemi*, 1951, **2**, 519-527.
4. R. A. Armstrong, and R. E. Newnham, *Materials Research Bulletin*, 1972, **7**, 1025-1034.
5. S. K. Kim and M. Miyayama, *Solid State Ionics*, 1997, **104**, 295-302.
6. F. Abraham, J. C. Boivin, G. Mairesse and G. Nowogrocki, *Solid State Ionics*, 1990, **40-1**, 934-937.
7. S. Lazure, C. Vernochet, R. N. Vannier, G. Nowogrocki and G. Mairesse, *Solid State Ionics*, 1996, **90**, 117-123.
8. A. Chakrabarti and J. Bera, *Current Applied Physics*, 2010, **10**, 574-579.
9. J. K. Thomas, K. R. Kendall and H. C. Zurloye, *Solid State Ionics*, 1994, **70**, 225-228.
10. A. Snedden, S. M. Blake and P. Lightfoot, *Solid State Ionics*, 2003, **156**, 439-445.

11. C. H. Hervoches, A. Snedden, R. Riggs, S. H. Kilcoyne, P. Manuel and P. Lightfoot, *Journal of Solid State Chemistry*, 2002, **164**, 280-291.
12. A. T. Giddings, M. C. Stennett, D. P. Reid, E. E. McCabe, C. Greaves and N. C. Hyatt, *Journal of Solid State Chemistry*, 2011, **184**, 252-263.
13. X. Y. Mao, W. Wang, X. B. Chen and Y. L. Lu, *Applied Physics Letters*, 2009, **95**, 082901.
14. H. Sun, X. M. Lu, T. T. Xu, J. Su, Y. M. Jin, C. C. Ju, F. Z. Huang and J. S. Zhu, *Journal of Applied Physics*, 2012, **111**, 6.
15. H. Sun, T. T. Xu, J. Su and C. C. Ju, *Integrated Ferroelectrics*, 2012, **140**, 64-70.
16. L. Keeney, S. Kulkarni, N. Deepak, M. Schmidt, N. Petkov, P. F. Zhang, S. Cavill, S. Roy, M. E. Pemble and R. W. Whatmore, *Journal of Applied Physics*, 2012, **112**, 10.
17. M. Palizdar, T. P. Comyn, M. B. Ward, A. P. Brown, J. Harington, S. Kulkarni, L. Keeney, S. Roy, M. Pemble, R. Whatmore, C. Quinne, S. H. Kilcoyne, A. J. Bell and Ieee, *2011 International Symposium on Applications of Ferroelectrics (Isaf/Pfm) and 2011 International Symposium on Piezoresponse Force Microscopy and Nanoscale Phenomena in Polar Materials*, 2011, 4.
18. W. Wang, X. H. Wu, X. Y. Mao and X. B. Chen, *Chinese Physics B*, 2011, **20**, 7.
19. W. L. Yang, C. Y. Chen, X. Y. Mao and X. B. Chen, *Chinese Physics B*, 2012, **21**, 5.
20. S. Ahn, Y. Noguchi, M. Miyayama and T. Kudo, *Materials Research Bulletin*, 2000, **35**, 825-834.
21. M. M. Kumar, A. Srinivas, G. S. Kumar and S. V. Suryanarayana, *Solid State Communications*, 1997, **104**, 741-746.
22. S. V. Suryanarayana and A. Srinivas, *Electronic Ceramic Materials and Devices*, 2000, **106**, 277-299.
23. M. B. Suresh, E. V. Ramana, S. N. Babu and S. V. Suryanarayana, *Ferroelectrics*, 2006, **332**, 57-63.
24. E. C. Subbarao, *Journal of the American Ceramic Society*, 1962, **45**, 166-169.
25. E. C. Subbarao, *Journal of Physics and Chemistry of Solids*, 1962, **23**, 665-676.
26. T. Kikuchi, *Materials Research Bulletin*, 1979, **14**, 1561-1569.
27. A. Kan, H. Ogawa, K. Kawada and T. Moriyama, *Ferroelectrics*, 2012, **427**, 129-136.
28. T. Kimura and T. Yamaguchi, *Ceramics International*, 1983, **9**, 13-17.
29. Y. M. Kan, X. H. Jin, P. L. Wang, Y. X. Li, Y. B. Cheng and D. S. Yan, *Materials Research Bulletin*, 2003, **38**, 567-576.
30. T. Kimura, T. Kanazawa and T. Yamaguchi, *Journal of the American Ceramic Society*, 1983, **66**, 597-600.
31. M. Garcia-Guaderrama, L. Fuentes, M. E. Montero-Cabrera, A. Marquez-Lucero and M. E. Villafuerte-Castrejon, *Integrated Ferroelectrics*, 2005, **71**, 233-239.
32. L. Fuentes, M. Garcia, D. Bueno, M. E. Fuentes and A. Munoz, *Ferroelectrics*, 2006, **336**, 81-89.
33. D. G. Porob and P. A. Maggard, *Materials Research Bulletin*, 2006, **41**, 1513-1519.
34. Zulhadjri, B. Prijamboedi, A. A. Nugroho, N. Mufti, A. Fajar, T. T. M. Palstra and Ismunandar, *Journal of Solid State Chemistry*, 2011, **184**, 1318-1323.
35. M. Palizdar, T. Comyn, S. Kulkarni, L. Keeney, S. Roy, M. Pemble, R. Whatmore, A. Bell and Ieee, *International Symposium on the Applications of Ferroelectrics (Isaf)*, 2010.
36. M. Palizdar, T. P. Comyn, M. B. Ward, A. P. Brown, J. P. Harrington, S. Kulkarni, L. Keeney, S. Roy, M. Pemble, R. Whatmore, C. Quinn, S. H. Kilcoyne and A. J. Bell, *Journal of Applied Physics*, 2012, **112**, 8.
37. R. D. Shannon and C. T. Prewitt, *Acta Crystallographica Section B-Structural Crystallography and Crystal Chemistry*, 1969, **B 25**, 925-946.

38. F. Abraham, M. F. Debreuillegresse, G. Mairesse and G. Nowogrocki, *Solid State Ionics*, 1988, **28**, 529-532.
39. O. Joubert, A. Jouanneaux and M. Ganne, *Materials Research Bulletin*, 1994, **29**, 175-184.
40. J. F. Dorrian, R. E. Newnham, M. I. Kay and D. K. Smith, *Ferroelectrics*, 1971, **3**, 17-27.
41. G. N. Subbanna, T. N. G. Row and C. N. R. Rao, *Journal of Solid State Chemistry*, 1990, **86**, 206-211.
42. S. K. Blower and C. Greaves, *Acta Crystallographica Section C-Crystal Structure Communications*, 1988, **44**, 587-589.
43. J. Schreuer, M. Burianek, M. Muehlberg, B. Winkler, D. J. Wilson and H. Schneider, *Journal of Physics-Condensed Matter*, 2006, **18**, 10977-10988.
44. T. Debnath, C. H. Ruescher, P. Fielitz, S. Ohmann and G. Borchardt, *Journal of Solid State Chemistry*, 2010, **183**, 2582-2588.
45. D. R. Modeshia and R. I. Walton, *Chemical Society Reviews*, 2010, **39**, 4303-4325.
46. R. E. Newnham, R. W. Wolfe and J. F. Dorrian, *Materials Research Bulletin*, 1971, **6**, 1029-1039.
47. A.C. Larson and R.B.V. Dreele, Los Alamos National Laboratory Report LAUR, 2004, 86-748.
48. A. R. Denton and N. W. Ashcroft, *Physical Review A*, 1991, **43**, 3161-3164.
49. Z. Liu, J. Yang, X. W. Tang, L. H. Yin, X. B. Zhu, J. M. Dai and Y. P. Sun, *Applied Physics Letters*, 2012, **101**, 4.
50. J. Yang, W. Tong, Z. Liu, X. B. Zhu, J. M. Dai, W. H. Song, Z. R. Yang and Y. P. Sun, *Physical Review B*, 2012, **86**, 7.
51. K. Sardar and R. I. Walton, *Journal of Solid State Chemistry*, 2012, **189**, 32-37.
52. L. Pardo, A. Castro, P. Millan, C. Alemany, R. Jimenez and B. Jimenez, *Acta Materialia*, 2000, **48**, 2421-2428.
53. J. Kanamori, *Journal of Physics and Chemistry of Solids*, 1959, **10**, 87-98.
54. X. W. Dong, K. F. Wang, J. G. Wan, J. S. Zhu and J. M. Liu, *Journal of Applied Physics*, 2008, **103**, 4.
55. I. A. Degen and G. A. Newman, *Spectrochimica Acta Part a-Molecular and Biomolecular Spectroscopy*, 1993, **49**, 859-887.
56. H. Stammreich, D. Bassi and O. Sala, *Spectrochimica Acta*, 1958, **12**, 403-405.
57. W. Scheuerm and G. J. Ritter, *Journal of Molecular Structure*, 1970, **6**, 240-245.
58. G. Michel and R. Machiroux, *Journal of Raman Spectroscopy*, 1983, **14**, 22-27.
59. J. Yang, R. S. Li, J. Y. Zhou, X. C. Li, Y. M. Zhang, Y. L. Long and Y. W. Li, *Journal of Alloys and Compounds*, 2010, **508**, 301-308.
60. S. Mallick, K. J. Bowman and A. H. King, *Applied Physics Letters*, 2005, **86**, 2.
61. D. E. Bugaris and H.-C. zur Loye, *Angewandte Chemie-International Edition*, 2012, **51**, 3780-3811.
62. H. Zhou, Y. Mao and S. S. Wong, *Chemistry of Materials*, 2007, **19**, 5238-5249.
63. M. J. Geselbracht, R. I. Walton, E. S. Cowell, F. Millange and D. O'Hare, *Chemistry of Materials*, 2002, **14**, 4343-4349.
64. P. Afanasiev and C. Geantet, *Coordination Chemistry Reviews*, 1998, **178**, 1725-1752.
65. D. C. N. Swindells and J. L. Gonzalez, *Acta Crystallographica Section B-Structural Science*, 1988, **44**, 12-15.
66. F. Mersch, K. Buse, W. Sauf, H. Hesse and E. Kratzig, *Physica Status Solidi a-Applied Research*, 1993, **140**, 273-281.
67. G. O. Jones and P. A. Thomas, *Acta Crystallographica Section B-Structural Science*, 2002, **58**, 168-178.

68. A. O'Brien, D. I. Woodward, K. Sardar, R. I. Walton and P. A. Thomas, *Applied Physics Letters*, 2012, **101**, 142902.
69. E. Aksel and J. L. Jones, *Sensors*, 2010, **10**, 1935-1954.
70. J. T. Zeng, K. W. Kwok, W. K. Tam, H. Y. Tian, X. P. Jiang and H. L. W. Chan, *Journal of the American Ceramic Society*, 2006, **89**, 3850-3853.
71. W. Zhao, H. Zhou, Y. Yan and D. Liu, *Journal of the American Ceramic Society*, 2008, **91**, 1322-1325.
72. V. A. Isupov, *Inorganic Materials*, 2006, **42**, 1094-1098.

Chapter 5: Investigating the Synthesis of Aurivillius Phases using *In Situ* X-ray Diffraction

5.1 Introduction

The successful molten salt syntheses (MSS) of several novel members of the doped series of Aurivillius phases, $Bi_5Ti_3Fe_{1-x}M_xO_{15}$ (M = V, Cr, Co, Ga, and $0.0 \leq x \leq 1.0$), were described in Chapter 4. Many of the $n = 4$ product materials exhibit subtle differences upon small changes to the synthetic conditions. Interconversion between related Aurivillius phases with different *n*, where *n* denotes the number of MO_6 sheets in the perovskite layers, in addition to the formation of recurrent intergrowth species, was discovered to be highly dependent upon reaction temperature and duration. Synthesis of layered materials such as these can be interesting to observe *in situ*, as the mechanisms of their formation often proceed *via* related higher-symmetry structural analogues from the same family. The features of these synthesis reactions, in addition to the properties of compounds in the Aurivillius family, make them ideal for study using *in situ* synchrotron X-ray diffraction: pure product phase formation occurs on an appropriate timescale (*ca.* 5 hours) at temperatures accessible using the Oxford Diamond *In Situ* Cell (< 1000 °C). Additionally, the product materials are well-characterised and highly crystalline.

A limited number of studies of the synthesis mechanisms of Aurivillius phases exist. Both *in situ* and *ex situ* methods have been employed to study these reactions, sometimes leading to conflicting conclusions over the precise nature of observed intermediate phases. The mechanism of formation is also highly dependent on the synthesis method and starting materials employed. The kinetics and mechanisms by which the $n = 2$ Aurivillius compound, $SrBi_2Ta_2O_9$ (SBT), forms have been studied using *in situ* laboratory diffraction techniques. The sol-gel synthesis of B-site substituted SBT thin films was probed by Sung and co-workers.[1, 2] The activation energy as well as the purity of the product was observed to be dependent upon the nature of the dopant, which was explained by the lower dissociation energy of various substituent M–O bonds. Rate of conversion of a fluorite-type δ-Bi_2O_3 intermediate to the final Aurivillius product was found to increase upon Ti-doping when compared to the parent SBT.[3] Alternatively, pre-

reaction of Bi_2O_3 and Ta_2O_5 to form $BiTaO_4$, prior to reaction with $SrCO_3$, was found to be an effective method of suppressing intermediate formation *en route* to SBT.[4]

The synthesis route to Aurivillius phases with $n > 2$ has also been reported for different synthesis procedures. The formation of $Bi_4Ti_3O_{12}$ from solid-state reaction of the oxide precursors has been monitored using laboratory *in situ* XRD.[5, 6] Rapid formation of this $n = 3$ Aurivillius product was reported to proceed *via* a stabilised Ti-doped variant of the γ-form of Bi_2O_3: the $Bi_{12}TiO_{20}$ cubic sillenite phase. *Ex situ* experiments indicate that pure Aurivillius product formation can be achieved at a temperature of 800 °C and above.[7] Alternatively, the use of reactive templates with 'core-shell' structure facilitates the formation of dense single-crystal nanorods of $Bi_4Ti_3O_{12}$.[8] A topotactic reaction occurs between Bi_2O_3 and TiO_2 anatase using this method, which does not proceed *via* the intermediate sillenite phase. This observation is explained using a growth mechanism involving diffusion of Bi^{3+} and O^{2-} through the titanate lattice. Attempted solid-state synthesis of the analogous $n = 3$ Aurivillius phase, $Bi_2Sr_2Nb_2TiO_{12}$, was monitored using *in situ* XRD by Peterson *et al.*.[9] In this investigation, a number of Aurivillius phases of varying *n* were observed to form alongside the product at high temperature, including an $n = \infty$ perovskite. This is indicative of a system where conversion *via* a layered Aurivillius analogue with higher or lower *n*, ultimately affords the $n = 3$ product. Recent *ex situ* studies indicate that the $n = 3/4$ $Bi_4Ti_3O_{12}$-$CaBi_4Ti_4O_{15}$ recurrent-intergrowth phase forms *via* the $n = 3$ $Bi_4Ti_3O_{12}$ analogue.[10]

The precise role of the molten salt in assisting Aurivillius product formation remains unclear. Porob and Maggard have demonstrated that use of a Na_2SO_4/K_2SO_4 eutectic mixture accelerates the reaction kinetics of $Bi_5Ti_3FeO_{15}$ formation.[11] It has been suggested by Zulhadjri and co-workers that the molten salt can act as a medium to facilitate the dissolution of reagents resulting in homogeneous mixing and rapid product precipitation.[12]

A description of several novel B-site doped $n = 4$ Aurivillius series was provided in Chapter 4. The synthesis of one member of these series, $Bi_5Ti_3Fe_{0.5}Cr_{0.5}O_{15}$, was selected for further study using *in situ* XRD. This material was chosen based on its high dopant incorporation and propensity to form as a pure phase. The experiments detailed in this chapter focus primarily upon the use of *in situ* XRD to probe the mechanism of $Bi_5Ti_3Fe_{0.5}Cr_{0.5}O_{15}$ Aurivillius phase formation. The impact of the molten salt in assisting

the synthesis reaction, in addition to the effects of its absence, was ascertained. An investigation into the effect of changing both the reaction dwell temperature and the composition of the molten salt upon the mechanism is also described. Both energy-dispersive and angular-dispersive XRD techniques are employed in experiments detailed throughout the chapter, and a critical comparison between the two is provided.

5.2 *Ex situ* quenching studies

It is important to complement results from *in situ* studies with data from other analysis techniques. When undertaking experiments during allotted beamtime at synchrotrons, time constraints can enforce a reduction in the number of experimental repeats, ultimately impacting on the reliability of the *in situ* data. *Ex situ* 'quenching' studies were therefore undertaken prior to synchrotron diffraction experiments to provide a comparison with the *in situ* data. *Ex situ* studies had the advantage of being undertaken using identical equipment to the laboratory experiments described in Chapter 4. However, products obtained following quenching are often atypical of the true reaction medium due to adverse physical and chemical changes induced by the quenching process itself.

Stoichiometric quantities of starting material oxides required to synthesise the $Bi_5Ti_3Fe_{0.5}Cr_{0.5}O_{15}$ product were ground with a seven-fold excess (relative to the product) of Na_2SO_4 and placed in an alumina crucible. Separate samples were heated at 5 °C.min^{-1} to 800, 830, and 860 °C, and then quenched immediately using liquid N_2. Following sample washing, vacuum filtration and drying in air, X-ray diffraction measurements were undertaken with each of the product powders. The results are shown in Figure 5.1.

XRD data from the product quenched at 800 °C exhibit reflections corresponding to a mixture of crystalline phases, including Bi_2O_3. XRD data from products quenched at both 830 and 860 °C contain Bragg reflections which can be indexed to the room-temperature structure of the $Bi_4Ti_3O_{12}$ phase, with a = 5.45 Å, b = 5.41 Å, c ~ 32.8 Å, and space group $B2cb$.[13, 14] Results from these quenching experiments suggest that the onset of n = 3 Aurivillius phase formation occurs in the narrow temperature range $800 \leq T / °C \leq 830$, and that this precedes formation of the final n = 4 product.

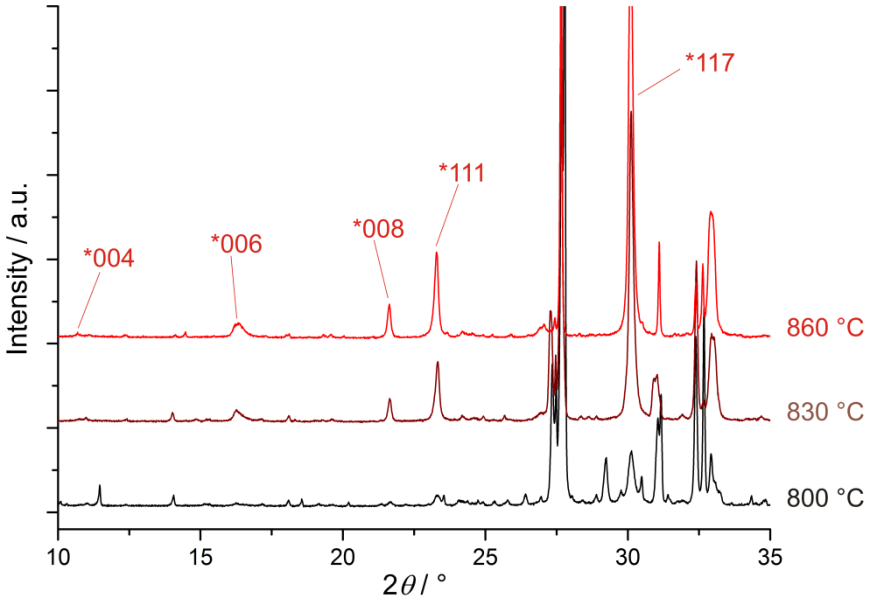

Figure 5.1: XRD data from the products of quenching experiments for MSS of $Bi_5Ti_3Fe_{0.5}Cr_{0.5}O_{15}$, undertaken at three temperatures. Selected Bragg reflections corresponding to $Bi_4Ti_3O_{12}$ have been assigned and are labelled with an asterix.

5.3 *In situ* XRD studies of Aurivillius phase synthesis

All *in situ* XRD experiments described in this chapter were undertaken using Beamline I12 at the Diamond Light Source. The Oxford Diamond *In Situ* Cell (ODISC) in the high-temperature configuration was employed to carry out all reactions.[15] The molten salt synthesis of $n = 4$ Aurivillius phases was first probed on Beamline I12 using EDXRD in March 2012. The feasibility of employing angular-dispersive diffraction to investigate the same reactions was then tested during experiments undertaken in March 2013. Data quality was found to vary significantly between the two techniques.

EDXRD data from all 23 detector elements were summed and the background subtracted from all diffraction spectra using a simple but highly-effective automatic background-estimation algorithm.[16] During *in situ* experiments, data were collected as 55 second scans every 60 seconds for the duration of each reaction. Temperature data were recorded at the end point of each 55 second measurement. During angular-dispersive diffraction experiments, images were recorded with four second exposure at 30 second intervals using the Pixium detector. 2D images of concentric Bragg diffraction rings were converted to 1D diffraction patterns (intensity *vs.* 2θ) using the Fit2D software program. Figure 5.2 contains XRD data obtained from a sample of $Bi_5Ti_3Fe_{0.5}Cr_{0.5}O_{15}$, measured using both angular and energy-dispersive techniques.

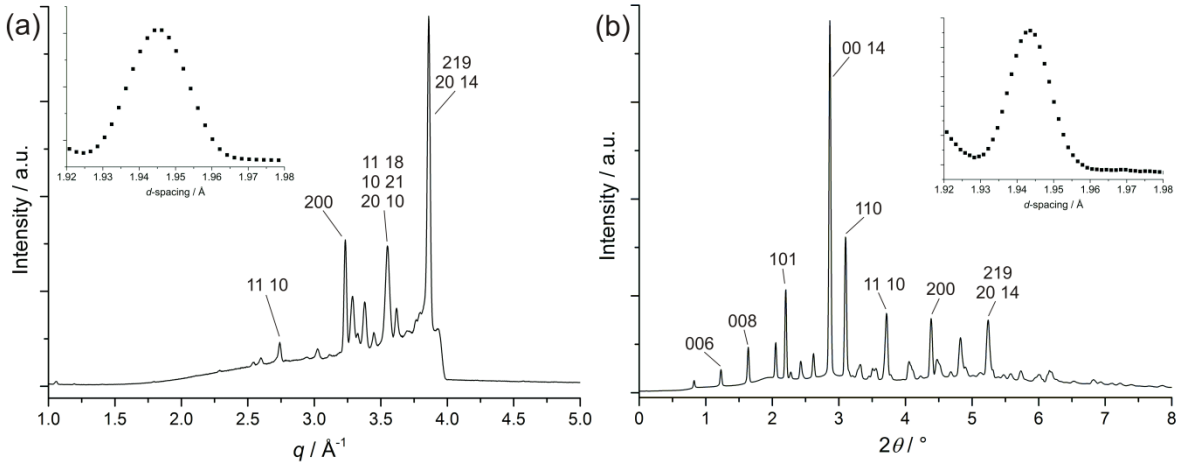

Figure 5.2: *In situ* XRD data for $Bi_5Ti_3Fe_{0.5}Cr_{0.5}O_{15}$ measured at 950 °C using ODISC. (a) A 55 second scan using EDXRD and (b) an angular-dispersive XRD scan with 4 second exposure. INSET FOR BOTH: the (200) product Bragg reflection plotted as a function of *d*-spacing.

The EDXRD technique is less appropriate for studying these systems in real time than angular-dispersive XRD. Because of the absorption edge due to the presence of bismuth, reflections above *ca.* $q = 4.0$ Å^{-1} (where $q = 2\pi/d$) are very low in intensity. Additionally, the fixed angle of the detector at 5° results in reflections at low q (high d-spacing) being excluded from the data. Consequently, high-quality XRD data could only be obtained over a small d-spacing range, *ca.* $1.5 \leq d$ / Å ≤ 3.2, using this technique. Fluorescence peaks due to the presence of bismuth in the reaction mixture were also observed in EDXRD data at the following energies: Kα_1 $E = 77.12$ keV ($q = 3.38$ Å^{-1}), Kα_2 $E = 74.81$ keV ($q = 3.28$ Å^{-1}) and Kβ_1 $E = 87.34$ keV ($q = 3.83$ Å^{-1}). One advantage of employing EDXRD was the ability to optimise the position of the gauge volume to exclude peaks due to the sample vessel.

A comparison of the data resolution from both techniques was undertaken using values for the full width at half maximum (FWHM) of the $Bi_5Ti_3Fe_{0.5}Cr_{0.5}O_{15}$ (200) Bragg reflection, inset in Figure 5.2. The values were obtained using a Gaussian fit to the data and are expressed in Ångstroms to enable comparison between the two data sets. The (200) FWHM for the EDXRD data was 0.019 Å, whereas that for the angular-dispersive data was significantly lower, at 0.013 Å. A smaller FWHM is indicative of better data resolution and this is the case for the angular-dispersive data, despite the (200) Bragg reflection being significantly broader than some reflections observed at lower 2θ. High-resolution data were particularly important for the identification of intermediates during

synthesis of $n = 4$ Aurivillius phases. The large number of crystalline phases which exist prior to product formation, in addition to the similarity in position of many of the Bragg reflections of these phases, made their elucidation very challenging. Higher resolution data, available over a greater *d*-spacing range, made *in situ* studies using angular-dispersive diffraction more insightful.

5.4 Molten salt synthesis of $Bi_5Ti_3Fe_{0.5}Cr_{0.5}O_{15}$

The MSS of $Bi_5Ti_3Fe_{0.5}Cr_{0.5}O_{15}$ was investigated using *in situ* angular-dispersive XRD. Controlled heating of the starting materials (Bi_2O_3, TiO_2, Fe_2O_3, and Cr_2O_3) in the presence of a seven-fold excess of Na_2SO_4 was undertaken. The sample, positioned in an alumina crucible inside a silicon carbide tube, was heated to 950 °C and maintained at this temperature for 55 mins.

5.4.1 Phase identification and characterisation

The contour plot in Figure 5.3 illustrates XRD data measured *in situ* during the molten salt synthesis of $Bi_5Ti_3Fe_{0.5}Cr_{0.5}O_{15}$. The diagram shows diffraction intensity plotted as a function of 2θ and temperature/time. Bragg reflections in the reaction profile can be assigned to known crystalline phases, the most prominent of which are labelled in the figure. The region incorporated in the dotted white box is examined in more detail in Section 5.4.2. Bragg reflections observed at $t = 2$ min can be assigned to the starting material α-Bi_2O_3 and Na_2SO_4 crystalline phases. The presence of both phases was confirmed using a two-phase Rietveld refinement with XRD data measured after 2.5 min, details of which are provided in Appendix E. Reflections corresponding to TiO_2, Cr_2O_3, and Fe_2O_3 are either very low in intensity or obscured by stronger intensity reflections, and are not observed in the data.

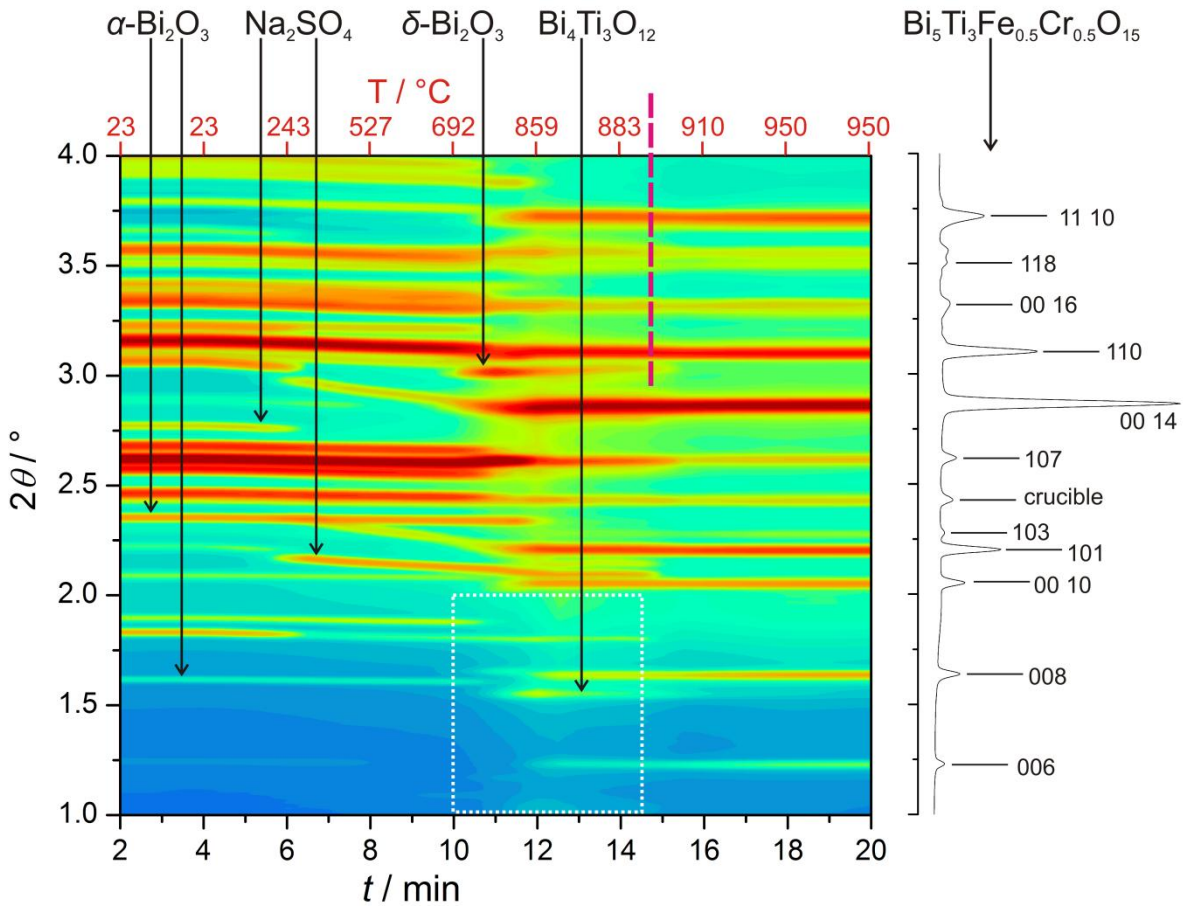

Figure 5.3: Contour plot showing time-resolved angular-dispersive *in situ* XRD data for the synthesis of $Bi_5Ti_3Fe_{0.5}Cr_{0.5}O_{15}$ in Na_2SO_4 flux. Prominent reflections corresponding to crystalline phases in the reaction are labelled and the point at which the Na_2SO_4 salt melts is marked with – – – –. A fully indexed diffraction pattern for the n = 4 material, measured at 950 °C after 25 min, is shown alongside. The data highlighted in the white box are presented in a stack plot in Figure 5.5.

The positions of several starting material reflections due to Na_2SO_4, shift significantly to smaller 2θ during heating, corresponding to thermal expansion of this phase. At elevated temperatures, both Na_2SO_4 and Bi_2O_3 undergo solid-state structural transitions. A phase change from the β- to the α-phase of Na_2SO_4 is clearly evident in the diffraction data (new peaks are most notably observed at 2θ = *ca.* 2.17 and 2.97°, corresponding to the respective (101) and (102) Bragg reflections).[17] The phase change from α-Bi_2O_3 to the fluorite-related δ-Bi_2O_3 was studied during calibration experiments described in Section 2.6.2, and is observed here at *ca.* 730 °C.[18, 19]

At a similar temperature to the bismuth oxide phase change, Bragg reflections corresponding to the high temperature form of the n = 3 Aurivillius compound, $Bi_4Ti_3O_{12}$,[13] appear and grow in intensity. This is consistent with observations from

quenching studies described in Section 5.2. The low-temperature phase of $Bi_4Ti_3O_{12}$ is a commonly encountered side-product of the attempted synthesis of n = 4 Aurivillius compounds (Chapter 4). The formation of this material has been studied in detail using *in situ* XRD (Section 5.1).

Shortly following the initial formation of $Bi_4Ti_3O_{12}$ observed in the XRD data, at a temperature close to the melting point of Bi_2O_3 (824 °C),[20] reflections corresponding to the n = 4 $Bi_5Ti_3Fe_{0.5}Cr_{0.5}O_{15}$ product material appear. The growth of product reflections takes place concurrently with a decline in those of $Bi_4Ti_3O_{12}$, suggesting direct conversion between the two materials. As this transformation occurs, the intensities of the α-Na_2SO_4 reflections also decline to zero, indicating the point at which the salt melts. This physical change acts as an internal temperature calibrant; the temperature recorded by the thermocouple as these XRD data were accumulated is consistent with the melting point of Na_2SO_4, 884 °C. Following a short dwell time at 950 °C, Bragg reflections of $Bi_4Ti_3O_{12}$ steadily decline until the n = 4 product phase exists in isolation.

The structure of the product at 950 °C is typical of that observed for similar Aurivillius phases at high temperatures. Many Aurivillius compounds with even n exhibit symmetry changes beyond a specific temperature unique to that material.[21-23] Above this transition temperature, Aurivillius compounds exist in their aristotype form, with tetragonal *I*4/*mmm* symmetry resulting from minimal tilting of the perovskite-layer oxide octahedra. The high-temperature tetragonal structure model of $Bi_5Ti_3CrO_{15}$ proposed by Giddings *et al.* was used as a starting point for refinement of the partially chromium-doped product phase at 950 °C.[24] Angular-dispersive XRD data from a measurement undertaken after 70 mins (collected during temperature dwell at 950 °C) were subject to Rietveld structure analysis to unequivocally confirm the structure of the high-temperature phase (Figure 5.4). Tables containing detailed structural information from this analysis are provided in Appendix E.

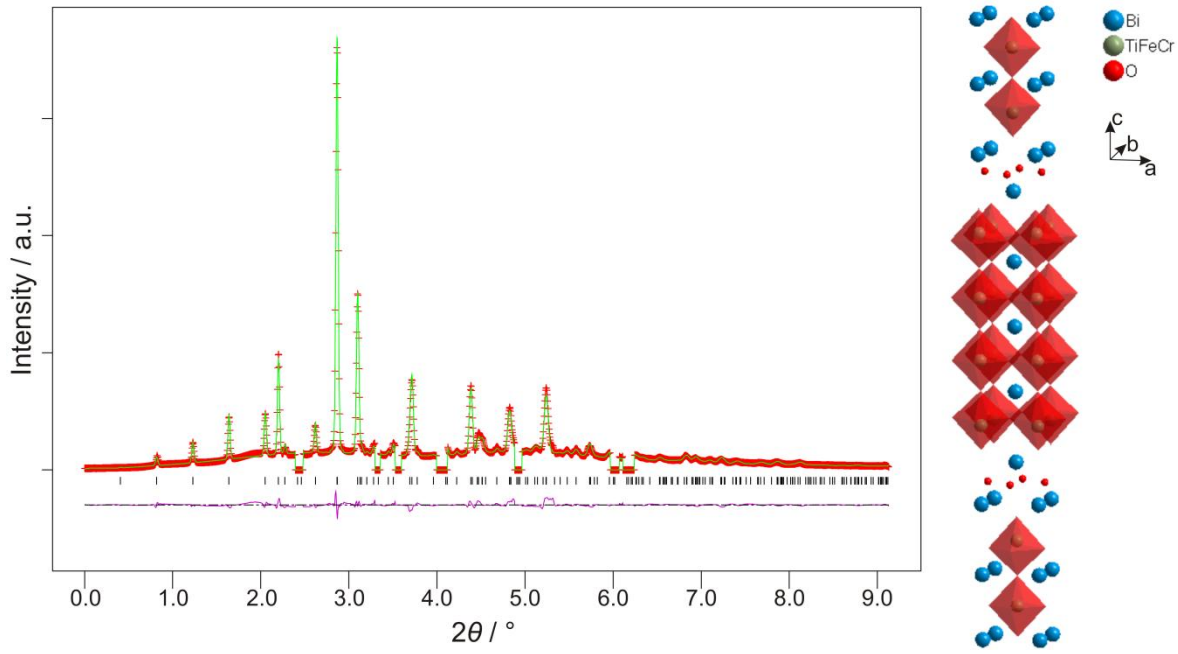

Figure 5.4: Rietveld refinement of a tetragonal *I*4/*mmm* structure model using powder XRD data from an *in situ* scan of $Bi_5Ti_3Fe_{0.5}Cr_{0.5}O_{15}$ at 950 °C. The diagram contains experimental (red), calculated (green) and difference (pink) profiles for the data. Reflections due to the alumina crucible were excluded. Goodness of fit parameters were: $\chi^2 = 1.251$, wRp = 0.0663, and Rp = 0.0508. The unit cell picture generated from the refined model is shown alongside.

Rietveld refinement verifies the formation of a pure product following synthesis in the presence of molten Na_2SO_4. Goodness of fit parameters indicate strong agreement between the data and model. The structural parameters of the $Bi_5Ti_3Fe_{0.5}Cr_{0.5}O_{15}$ material at 950 °C ($a = b = 3.8887(3)$ Å, $c = 41.561(4)$ Å, *I*4/*mmm*) are consistent with the high-temperature structures proposed for both $Bi_5Ti_3CrO_{15}$ ($a = b = 3.87$ Å, $c = 41.10$ Å, *I*4/*mmm* at 700 °C) and $Bi_5Ti_3FeO_{15}$ ($a = b \sim 3.88$ Å, $c \sim 41.85$ Å, *I*4/*mmm* at 800 °C). The atomic positions of all atoms in the material were refined. As expected, the oxide octahedra in the perovskite layer are closer to ideal alignment than in the low-temperature orthorhombic hettotype. As was observed for Rietveld analysis with room-temperature laboratory XRD data (Section 4.3), the positions of the B-site cations in the 'outer' layers of the perovskite block are positioned significantly off-centre with respect to the surrounding oxide ions.

It can be hypothesised that the increased mobility of the reacting species due to the presence of the ionic melt is the drive behind such rapid conversion to the target $n = 4$ Aurivillius phase.

5.4.2 Mechanistic insight

The intricate interconversion between several crystalline phases at high-temperature, as well as the effect of the two melting transitions, was probed in greater detail. The nature of the species present prior to and during product formation was most readily observed in the high *d*-spacing / low 2θ diffraction range. Figure 5.5 shows 10 consecutive *in situ* XRD measurements recorded across the temperature range $692 \leq T / °C \leq 887$ for the MSS of $Bi_5Ti_3Fe_{0.5}Cr_{0.5}O_{15}$. The data correspond to the highlighted region in Figure 5.3.

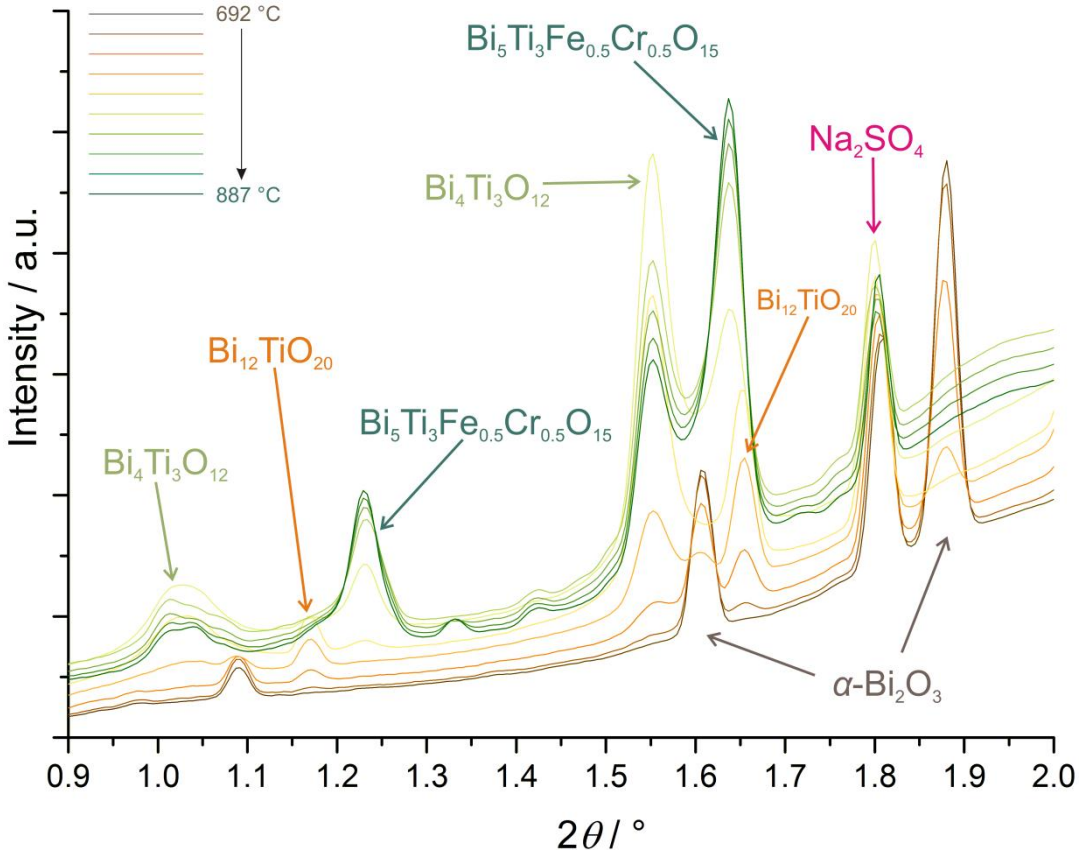

Figure 5.5: Time-resolved *in situ* XRD data for the MSS of $Bi_5Ti_3Fe_{0.5}Cr_{0.5}O_{15}$.

$Bi_4Ti_3O_{12}$ and $Bi_5Ti_3Fe_{0.5}Cr_{0.5}O_{15}$ Aurivillius phase reflections appear in the diffraction data in Figure 5.5 before the reflection corresponding to Na_2SO_4 declines in intensity. This observation confirms that the onset of product formation occurs independently of the melting of the salt. It is also evident from these data that the formation of the $n = 4$ product is closely linked to the decline of the $Bi_4Ti_3O_{12}$ phase. Reflections consistent with the $n = 3$ $Bi_4Ti_3O_{12}$ phase appear and grow rapidly in intensity as the temperature increases beyond 692 °C. However, an immediate steady decrease in intensity of these

reflections commences as soon as the $Bi_5Ti_3Fe_{0.5}Cr_{0.5}O_{15}$ product begins to form. This suggests that $n = 4$ Aurivillius product formation proceeds *via* direct conversion from the very closely structurally related $Bi_4Ti_3O_{12}$ intermediate species.

Low intensity reflections corresponding to the $Bi_{12}TiO_{20}$ compound, with cubic sillenite structure ($a = 10.18$ Å, $I23$),[25] are observed in four diffraction scans in Figure 5.5. Despite the reflections of this phase overlapping with those from materials present in greater quantity, it is clear from these data that $Bi_{12}TiO_{20}$ forms as a short-lived intermediate alongside $Bi_4Ti_3O_{12}$ and prior to $n = 4$ product formation. The $Bi_{12}TiO_{20}$ phase is a closely-related, Ti-stabilised form of γ-Bi_2O_3, which has previously been observed to form during the synthesis of $Bi_3Ti_4O_{12}$.[7, 26]

The integrated intensities corresponding to specific Bragg reflections of three crystalline phases present in the reaction, α-Bi_2O_3 (110), $Bi_4Ti_3O_{12}$ (006), and $Bi_5Ti_3Fe_{0.5}Cr_{0.5}O_{15}$ (006), are plotted in Figure 5.6. These values were calculated using a Gaussian fit to the data. The scan points at which the temperature reached the melting points of Bi_2O_3 and Na_2SO_4 are also labelled in the diagram.

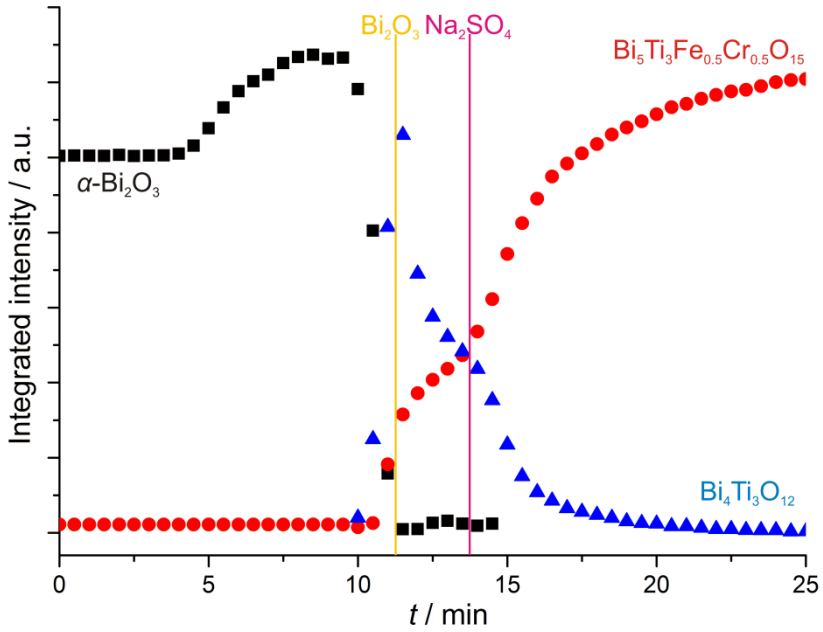

Figure 5.6: Integrated intensity *vs.* time plot for three phases involved in the MSS of $Bi_5Ti_3Fe_{0.5}Cr_{0.5}O_{15}$. The scan points during which the temperature rose above the melting point of Bi_2O_3 (—) and Na_2SO_4 (—) are labelled.

The melting point of the Bi_2O_3 precedes a decline in intensity of the $Bi_4Ti_3O_{12}$ reflections. Direct conversion of $Bi_4Ti_3O_{12}$ to $Bi_5Ti_3Fe_{0.5}Cr_{0.5}O_{15}$ can be inferred from the opposing trends in integrated intensity of the (00*l*) reflections of each phase. An important

observation is the influence of the Na_2SO_4 melting on the species present in the reaction. It is clear that although the onset of product formation is not reliant on the presence of Na_2SO_4 in the reaction mixture, transformation of $Bi_4Ti_3O_{12}$ to $Bi_5Ti_3Fe_{0.5}Cr_{0.5}O_{15}$ is significantly accelerated following melting of the salt. The considerable increase in the rate of integrated reflection intensity change for both intermediate and product Aurivillius phases can be explained by an increase in diffusion rate of the $Bi_4Ti_3O_{12}$, Fe/Cr_2O_3 and Bi_2O_3 reacting species in the sample mixture. Due to the simultaneity of the salt melt and the increase in intermediate to product conversion rate, evidenced by the gradient of the integrated intensity profiles, it can be inferred from Figure 5.6 that the presence of molten salt does aid product formation.

5.4.3 Investigating the high-temperature phase transition

Orthorhombic-tetragonal structure transitions at elevated temperatures have been reported in a number of Aurivillius phases.[22, 27, 28] A structure field map has been constructed for cation-doped analogues with even *n* to illustrate the relationship between Curie temperature, phase-transition temperature and the nature of the dopant.[29] Giddings and co-workers postulated the existence of a discontinuous phase transition of $Bi_5Ti_3CrO_{15}$ from the $A2_1am$ hettotype to the centrosymmetric $I4/mmm$ structure above 660 °C.[24] A similar transition was observed by Snedden *et al.* for the $Bi_5Ti_3FeO_{15}$ material at *ca.* 730 °C.[21] To investigate such a transition in $Bi_5Ti_3Fe_{0.5}Cr_{0.5}O_{15}$, cooling of the product from 950 °C was monitored, with emphasis on detecting growth of any reflections consistent with a structure of different symmetry to that observed in the sample at 950 °C.

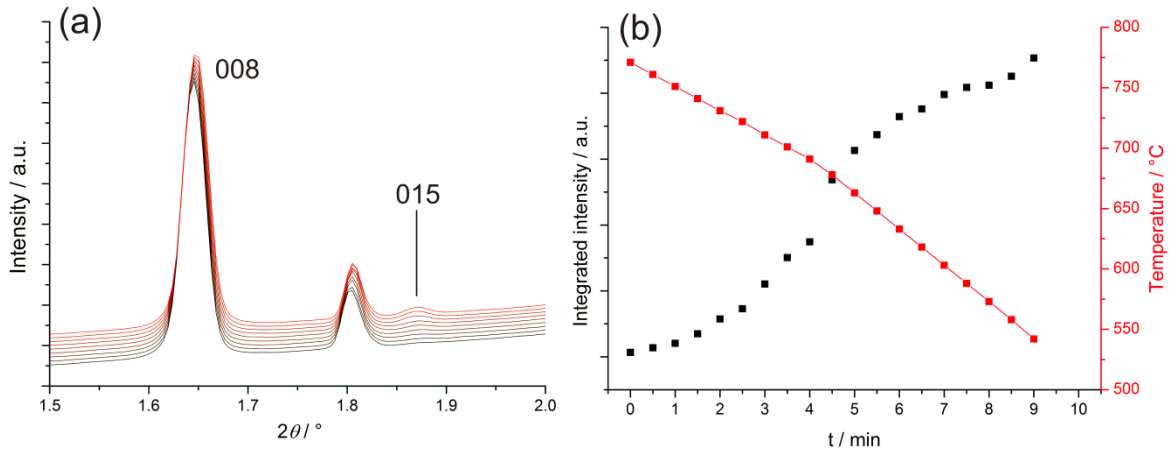

Figure 5.7: (a) Stack plot of *in situ* XRD data illustrating the growth of the (015) Bragg reflection upon sample cooling. Scans were recorded in the temperature range 731 °C (black) to 633 °C (red) in 10 °C increments (first five scans) and 15 °C increments (final four scans). (b) A plot of the change in integrated intensity of the (015) reflection (■) and sample temperature (■) as a function of time.

The use of angular-dispersive XRD was a necessity to study this phase transition. Observation of such low intensity Bragg reflections was not possible using EDXRD on Beamline I12 due to the lower data quality and restricted *d*-spacing range. During the phase transition, the (015) reflection (characteristic of a material with $A2_1am$ symmetry) appears at 2θ = *ca.* 1.87°. This reflection is first observed in measurements recorded at 711 °C and steadily increases in intensity upon cooling (Figure 5.7). The temperature at which this structural transition is observed is significant because it lies between known values for the Curie temperatures (and corresponding structural transitions) of the full Fe- and Cr-doped species.

Rietveld refinement analysis was undertaken using *in situ* data from selected XRD measurements recorded during product cooling. The lattice parameters elucidated from each refinement are plotted as a function of sample temperature in Figure 5.8. The unit cell volume of the low-temperature orthorhombic phase is approximately twice the size of the high-temperature tetragonal form and so $a_{orth} \sim b_{orth} = a_{tet}\sqrt{2}$.

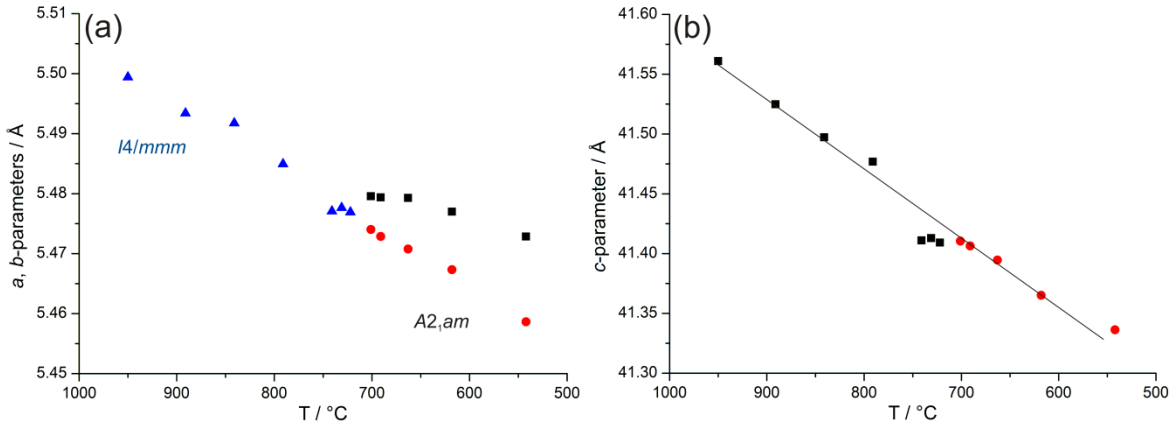

Figure 5.8: Thermal evolution of lattice parameters for $Bi_5Ti_3Fe_{0.5}Cr_{0.5}O_{15}$: (a) *a*- and *b*-parameters (where ▲ represents $a\sqrt{2}$ for *I*4/*mmm* symmetry, and ■ and ● represent *a* and *b* respectively for orthorhombic $A2_1am$ symmetry) and (b) *c*-parameter (where ■ represents *c* for *I*4/*mmm* symmetry, and ● represents *c* for orthorhombic $A2_1am$ symmetry). Lattice parameter error is within the data point.

A smooth trend in the lattice parameter variation with temperature is observed for the parent $Bi_5Ti_3FeO_{15}$ material throughout the orthorhombic-tetragonal phase transition. This is not the case for results from the $Bi_5Ti_3Fe_{0.5}Cr_{0.5}O_{15}$ material, which exhibit small discontinuities in *a*, *b*, and *c* at temperatures close to the observed structure change. This is perhaps suggestive of an indirect transition between the polar orthorhombic and centrosymmetric tetragonal structures, *via* an intermediate phase. Such behaviour has

been observed in similar Aurivillius compounds.[30] It would be particularly significant to observe an intermediate structure with *Amam* symmetry as such a phase was hypothesised, but could not be observed, for $Bi_5Ti_3CrO_{15}$. However, detection of such a short-lived intermediate structural variant requires further investigation to monitor precisely the existence of superlattice reflections throughout the entire temperature region of the phase change.

5.4.4 Discussion

n = 4 Aurivillius phase synthesis proceeds through several structurally related materials. Conversion of the δ-Bi_2O_3 species to form $Bi_4Ti_3O_{12}$ is a significant transformation because the fluorite-like arrangement of atoms in δ-Bi_2O_3 reflects that of the Bi_2O_3 layer in all Aurivillius compounds. Similarly, formation of $Bi_5Ti_3Fe_{0.5}Cr_{0.5}O_{15}$ occurs *via* the n = 3 Aurivillius phase, $Bi_4Ti_3O_{12}$. This material is closely related to the n = 4 Aurivillius product, but with a shortened unit cell in the *c*-direction due to the presence of fewer layers in the pseudo-perovskite blocks of the structure.

Conversion from an n = 3 to an n = 4 Aurivillius structure has previously been monitored using high-resolution transmission electron microscopy (HRTEM).[31] The mechanistic pathway was observed to proceed *via* expansion of the perovskite layers through formation of a complex series of defects at the phase boundary. It is possible that formation of $Bi_5Ti_3Fe_{0.5}Cr_{0.5}O_{15}$ from $Bi_4Ti_3O_{12}$ occurs through a similar layer-by-layer intercalation mechanism. The broad nature of some $Bi_4Ti_3O_{12}$ (00*l*) Bragg reflections at low 2θ is indicative of stacking defects in the *c*-direction of the unit cell, perhaps due to the disordered inclusion of some n = 4 layers at the reaction boundary of the two materials. No indication of an intermediary n = 3/4 systematic intergrowth structure can be inferred from the *in situ* XRD data. However, a small number of very low intensity Bragg reflections that could not be indexed to known crystalline phases, *were* observed during conversion between the two Aurivillius materials (at 2θ = *ca.* 1.34 and 1.42° in Figure 5.5). It is possible that these reflections arise from ordered defects produced during perovskite layer insertion to form the pure n = 4 product.

At no point during the reaction do starting material, intermediate or product phases become dissolved in the sodium sulphate salt. This is due to the low solubility of reagents

in the highly ionic molten flux.[32] Nor do components of the flux interact directly with species in the reaction, forming side-products. The function of the flux has instead been confirmed to be as an accelerant for formation of the final product. This is most likely due to the increase in ionic mobility of the reagents beyond the salt melting point. This finding is complimentary to that of Koch and co-workers, who observed that the rate of formation of $Bi_4Ti_3O_{12}$ was accelerated through implementation of the sol-gel method.[33] To provide further evidence to these conclusions, the synthesis of $Bi_5Ti_3Fe_{0.5}Cr_{0.5}O_{15}$ without salt was investigated, and the results are discussed in the ensuing section.

5.5 Synthesis of $Bi_5Ti_3Fe_{0.5}Cr_{0.5}O_{15}$ without molten salt

The synthesis of $Bi_5Ti_3Fe_{0.5}Cr_{0.5}O_{15}$ was studied in the absence of Na_2SO_4 using *in situ* EDXRD. Solid oxide starting materials (TiO_2, Cr_2O_3, Fe_2O_3, and Bi_2O_3) were ground together using an agate pestle and mortar until a homogeneous mixture was established. The reagents were heated to 950 °C in an alumina crucible, using ODISC in the high-temperature configuration.

5.5.1 Phase identification and mechanistic insight

In situ EDXRD data are compiled in a contour plot in Figure 5.9, alongside the sample temperature profile for the reaction.

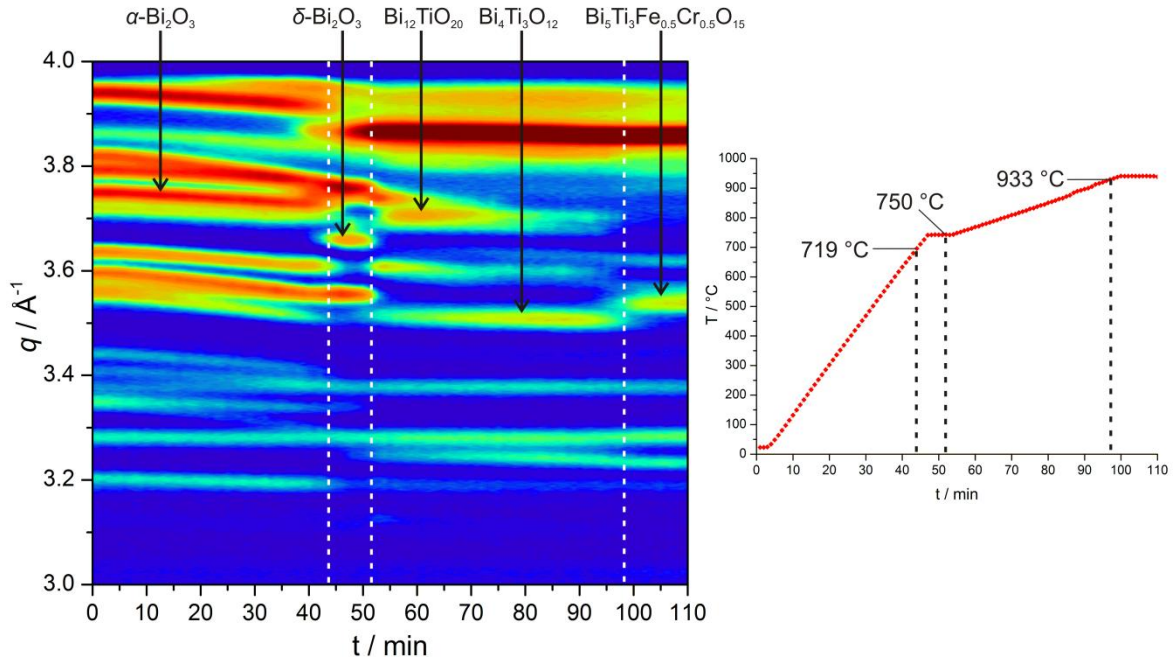

Figure 5.9: Annotated time-resolved *in situ* EDXRD data for the synthesis of $Bi_5Ti_3Fe_{0.5}Cr_{0.5}O_{15}$ in the absence of Na_2SO_4. The sample temperature profile for the reaction is provided alongside the contour plot.

In situ EDXRD data measured during the initial stages of reaction are comparable to results obtained upon heating an isolated sample of Bi_2O_3, discussed in Section 2.6.2. Thermal expansion of the α-Bi_2O_3 starting material is evidenced by the shift in several reflections to lower q upon heating (Figure 5.9). The bismuth oxide phase change at *ca.* 730 °C is observed after 43 mins, most notable through the appearance of the δ-Bi_2O_3 (311) Bragg reflection at $q = 3.68$ Å^{-1}.

The identification of further crystalline phases in the EDXRD data is challenging due to the presence of only a small number of Bragg reflections per phase across this q range. However, a comparison with the angular-dispersive results detailed in Section 5.4 and a consideration of similar studies described in the literature can help to explain the observed reaction profile. Navarro-Rojero and co-workers reported the formation of $Bi_{12}TiO_{20}$ cubic sillenite phase as an intermediate towards formation of $Bi_4Ti_3O_{12}$.[26] This Ti-stabilised form of γ-Bi_2O_3 was also observed as a short-lived intermediate in the MSS of $Bi_5Ti_3Fe_{0.5}Cr_{0.5}O_{15}$ discussed in Section 5.4. The Bragg reflection at $q = 3.71$ Å^{-1} in the EDXRD data is consistent with the overlapping (532) and (611) reflections of this phase. Further evidence for the assignment of this reflection to $Bi_{12}TiO_{20}$ is that its growth and subsequent decline occurs concurrently with the increase in intensity of a reflection at $q = 3.51$ Å^{-1}, the (206) Bragg reflection of $Bi_4Ti_3O_{12}$. This is directly analogous to behaviour observed in the MSS reaction prior to Na_2SO_4 melting. Due to the more gradual incline in temperature of this reaction, the existence of both phases is extended over a greater time period.

One of the most significant observations in the *in situ* data for this reaction is the final crystalline phase conversion observed at *ca.* 933 °C. Following the steady increase in intensity of the $Bi_4Ti_3O_{12}$ (206) Bragg reflection over the temperature range $750 \leq T / °C \leq 900$, a relatively fast decline in intensity of this reflection occurs alongside the emergence of reflections corresponding to a new phase. The most prominent of these, at $q = 3.54$ Å^{-1}, corresponds to the (11 18) reflection of the target $n = 4$ Aurivillius product $Bi_5Ti_3Fe_{0.5}Cr_{0.5}O_{15}$. Figure 5.10 contains extent of reaction (α) *vs.* time information for both phases over the temperature range of the transition.

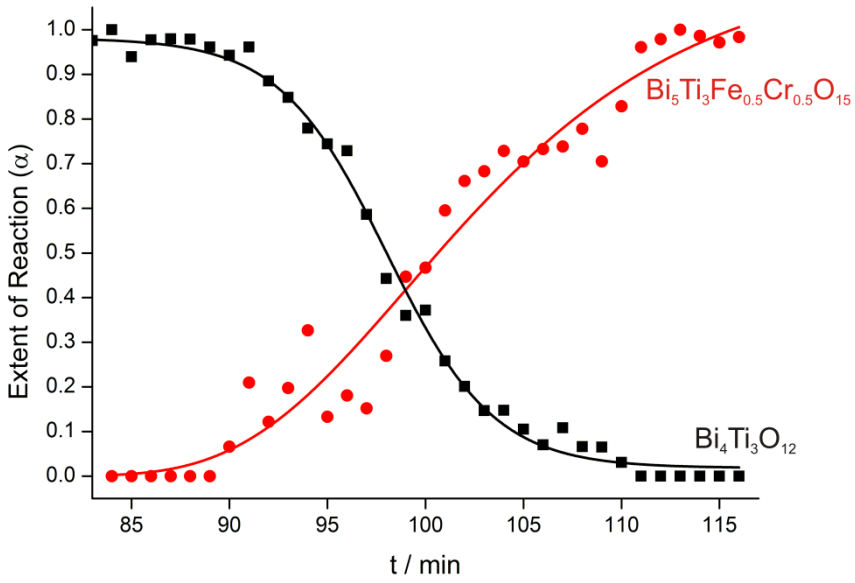

Figure 5.10: Extent of reaction *vs.* time plot for the $Bi_4Ti_3O_{12}$ (■) and $Bi_5Ti_3Fe_{0.5}Cr_{0.5}O_{15}$ (●) reflections during heating to 950 °C. The solid lines are included as a guide.

It is clear from the *in situ* data that despite the absence of the Na_2SO_4 melting transition, rapid and complete conversion to the desired n = 4 product material still takes place in a short time period at a modest temperature. The data in Figure 5.10 indicate that product formation occurs directly *via* the $Bi_4Ti_3O_{12}$ precursor. An interesting feature of this conversion is the shift in the (200) Bragg reflection observed at *ca.* q = 3.24 $Å^{-1}$. This reflection is present in the high-temperature tetragonal forms of both the n = 3 intermediate and n = 4 product Aurivillius phases. It shifts marginally to lower q (higher d-spacing) during formation of $Bi_4Ti_3O_{12}$, but the intensity and position of the reflection remain constant throughout transformation from the n = 3 to the n = 4 species. This is indicative of a process where order is retained perpendicular to the plane of the Aurivillius layers, consistent with the 'layer insertion' mechanism proposed for these systems in Section 5.4.

5.5.2 Discussion

The crystalline phases observed during the synthesis of $Bi_5Ti_3Fe_{0.5}Cr_{0.5}O_{15}$ without salt are directly comparable to those present in the reaction undertaken with salt (aside from the absence of Na_2SO_4 reflections). The rapid rate of n = 4 product formation *via* the related n = 3 compound is perhaps uncharacteristic of the ceramic synthesis method. Typically, such solid-state reactions require pelletized reagents to be heated for several

hours, sometimes days, at temperatures above 1000 °C to reach completion. This is due to the slow diffusion rates between solids in the reacting mixture.

One possible explanation for the rapid rate of $Bi_5Ti_3Fe_{0.5}Cr_{0.5}O_{15}$ formation is that melting of a bismuth-containing oxide species accelerates the rate of reaction. Several studies into the TiO_2-Bi_2O_3 system indicate that the position of the liquidus is dependent on the relative mole fractions of the two reagents.[34, 35] However, in the bismuth-rich region, the temperature at which species in this system transform to the liquid phase varies predominantly over the range 800-900 °C. The behaviour of a Bi_2O_3-type species as both reagent and flux at these temperatures would facilitate greater reagent mobility, as well as significantly faster diffusion of the species itself to the site of reaction. This is consistent with *ex situ* experimentation described by Morozov *et al.*, who postulated that Aurivillius formation takes place only above the melting point of a Bi_2O_3-based surface phase.[36] In fact, Bi_2O_3 itself has been employed to facilitate flux growth of Aurivillius phase single crystals, albeit at temperatures in excess of 1100 °C.[37]

5.6 Monitoring the effects of varying synthesis conditions

The reaction temperature and composition of the molten salt were altered and the resulting impact upon the synthesis of $Bi_5Ti_3Fe_{0.5}Cr_{0.5}O_{15}$ was monitored *in situ*.

5.6.1 Reducing the dwell temperature

Stoichiometric quantities of starting material oxide reagents were mixed with a seven-fold excess of Na_2SO_4, in an attempt to synthesise $Bi_5Ti_3Fe_{0.5}Cr_{0.5}O_{15}$. The mixture was heated to 800 °C using ODISC, and the reaction monitored using *in situ* angular-dispersive XRD. The contour plot and temperature profile for the reaction are shown in Figure 5.11.

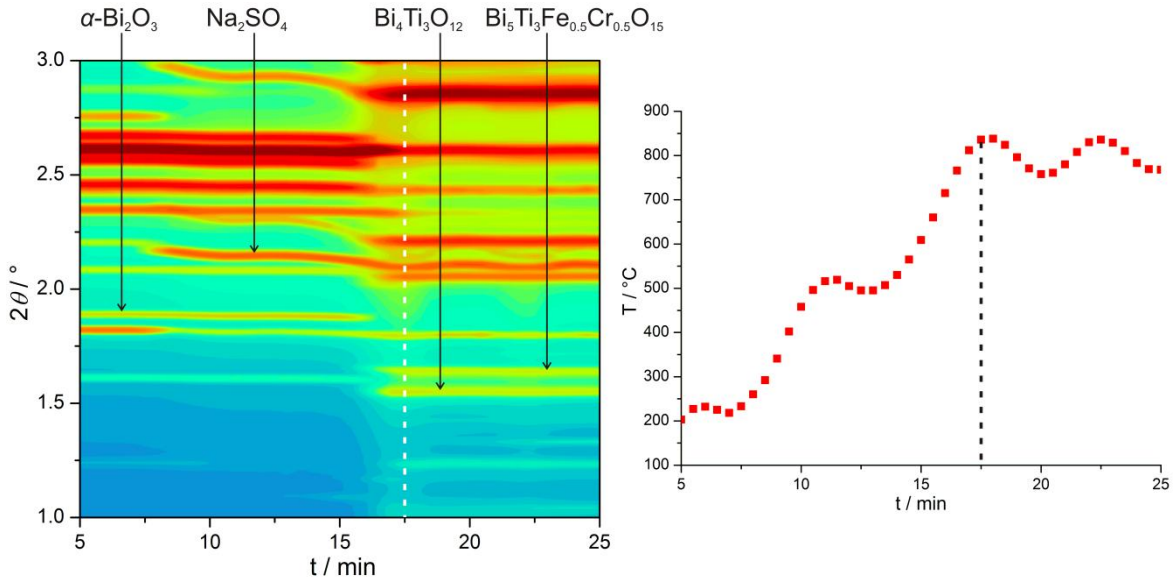

Figure 5.11. Contour plot showing time-resolved angular-dispersive *in situ* XRD data for the synthesis of $Bi_5Ti_3Fe_{0.5}Cr_{0.5}O_{15}$ at *ca.* 800 °C alongside the temperature profile for the reaction. Prominent reflections corresponding to crystalline phases in the contour plot are labelled and the point at which the maximum temperature of 838 °C is reached is signified by the dotted line in each diagram.

The initial stages of formation of $Bi_5Ti_3Fe_{0.5}Cr_{0.5}O_{15}$ proceed *via* an identical mechanism to the MSS reaction monitored at 950 °C. The reaction at *ca.* 800 °C was entirely undertaken below the melting point of Na_2SO_4 and peaks due to the high-temperature phase of this material are observed in XRD data throughout the reaction. The measured sample temperature oscillated above and below the target set-point, which was reflected in the fluctuating position of Bragg peaks corresponding to expansion and contraction of the Na_2SO_4 unit cell.

Formation of the n = 3 Aurivillius phase, $Bi_4Ti_3O_{12}$, again occurs prior to product formation. However, the ensuing rapid conversion to the n = 4 phase, observed upon heating to 950 °C, is not seen here. Instead, reflections corresponding to both materials are still present in the diffraction data following sample temperature dwell at 800 °C for 84 mins. This directly contrasts the observation made by Porob and Maggard, who claim that MSS of phase-pure $Bi_5Ti_3FeO_{15}$ can be undertaken following reaction for 1 hour at 800 °C.[11] The integrated intensities of three reflections, corresponding to α-Bi_2O_3 (110), $Bi_4Ti_3O_{12}$ (006), and $Bi_5Ti_3Fe_{0.5}Cr_{0.5}O_{15}$ (006), are plotted *vs.* time in Figure 5.12 for a 20 min section of the reaction.

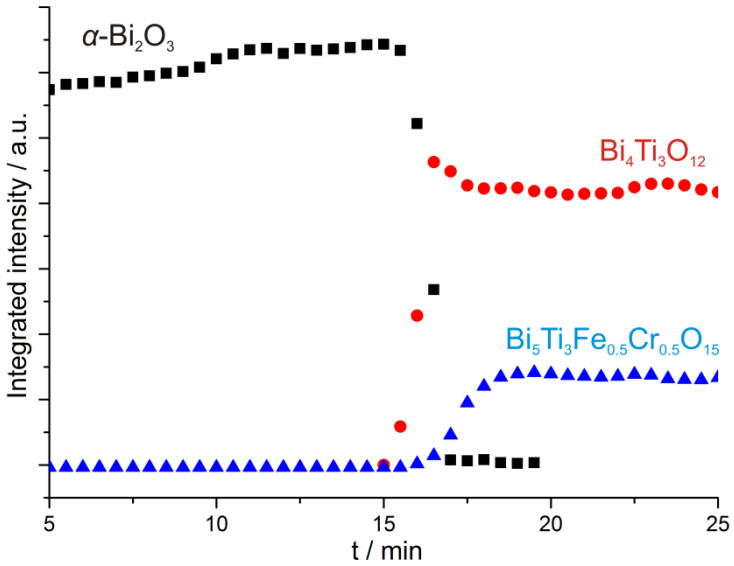

Figure 5.12: Integrated intensity *vs.* time plot for three phases involved in the synthesis of $Bi_5Ti_3Fe_{0.5}Cr_{0.5}O_{15}$ at *ca.* 800 °C.

Following an initial growth period, the integrated intensities of reflections consistent with both n = 3 and n = 4 phases reach a plateau. During temperature dwell at 800 °C, $Bi_4Ti_3O_{12}$ Bragg reflections undergo a very gradual decline in intensity, concurrent with a comparable minor growth in intensity of the $Bi_5Ti_3Fe_{0.5}Cr_{0.5}O_{15}$ reflections. At 800 °C, the rate of conversion to the product material is that expected of a ceramic synthesis reaction where slow kinetics are dictated by the gradual diffusion of solid reagents to the site of reaction.

It is interesting to note the initial rapid growth of the $Bi_5Ti_3Fe_{0.5}Cr_{0.5}O_{15}$ Bragg reflections, approximately 16 mins into the reaction. A corresponding minor decrease in intensity of $Bi_4Ti_3O_{12}$ reflections at this time indicates that conversion to the product

begins, but is quickly hindered. This observation approximately coincides with the sample temperature reaching an initial maximum. It is possible that, due to the temperature overshoot illustrated in Figure 5.11, the temperature of the reacting mixture temporarily rises above the melting point of a bismuth-containing oxide species, thus instigating the rapid conversion previously observed for the salt and no-salt reactions undertaken at 950 °C. The subsequent temperature drop and maintenance below this crucial threshold results in the lack of further reactivity observed. This observation is supported by the increase in 'background' intensity due to amorphous scattering at *ca.* 16 mins (Figure 5.11), which indicates the presence of a non-crystalline phase in the reaction mixture.

5.6.2 Molten salt synthesis using RbCl

The mechanism of MSS of $Bi_5Ti_3Fe_{0.5}Cr_{0.5}O_{15}$ using RbCl salt was probed using *in situ* EDXRD. The melting point of RbCl is 718 °C, below that of any bismuth-containing species present in the reaction. Solid oxide starting materials were mixed with a fifteen-fold excess of the salt. The reaction mixture was heated to 750 °C at 15 °C.min^{-1} followed by heating to 950 °C at 5 °C.min^{-1}. EDXRD data are presented as a contour plot alongside the temperature profile for the reaction in Figure 5.13.

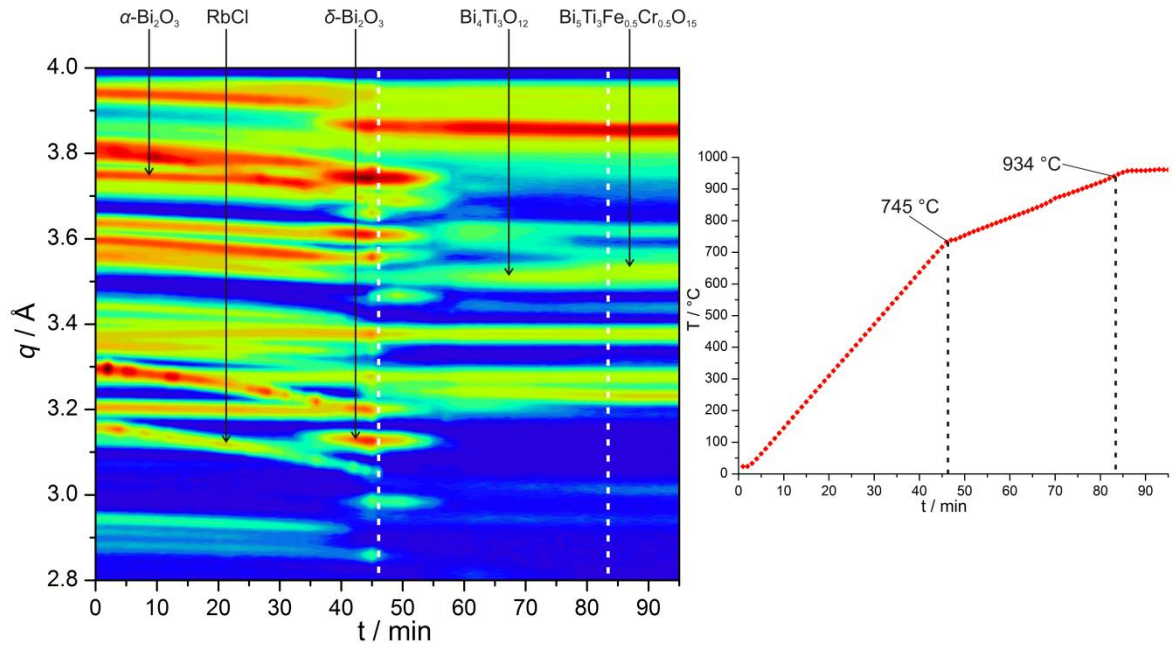

Figure 5.13: Annotated time-resolved *in situ* EDXRD data for the synthesis of $Bi_5Ti_3Fe_{0.5}Cr_{0.5}O_{15}$ in the presence of RbCl. The sample temperature profile for the reaction is provided alongside the contour plot.

The point at which the RbCl salt melts is illustrated by the first dotted line in both profiles. Reflections due to the crystalline salt, labelled in Figure 5.13, decline to zero intensity before the sample temperature reaches 745 °C. This melting transition does not appear to influence the mechanism of the reaction. The various phase changes of Bi_2O_3 proceed in analogous fashion to those observed in the reaction undertaken without salt. Additionally, the final phase conversion from $Bi_4Ti_3O_{12}$ to the n = 4 $Bi_5Ti_3Fe_{0.5}Cr_{0.5}O_{15}$ product, indicated by the second dotted line in each profile, occurs at the same temperature as the no-salt reaction, at 934 °C.

An increase in intensity of all Bragg reflections across the entire q range is observed in data measured shortly prior to and during the melting of the salt, at *ca.* 44 mins into the reaction. It is likely that this is a result of 'settling' of the sample in the path of the X-ray beam as the density of the salt changes upon melting. An increase in quantity of sample in the beam path correlates with a rise in Bragg reflection intensity. In addition to the growth in intensity of reflections due to crystalline phases, the 'background' due to scattering from amorphous materials in the beam path also varies significantly throughout sample heating and the melting of the salt. Diffraction due to scattering from non-crystalline phases was typically observed as a broad asymmetric signal in the data, which can be observed in the EDXRD scan shown in Figure 5.2. This 'background' intensity was modelled using the method of Bruckner,[16] and then subtracted from the raw data. The subtracted intensity obtained following this analysis was plotted as a function of q and time, and the resulting contour plot is provided in Figure 5.14.

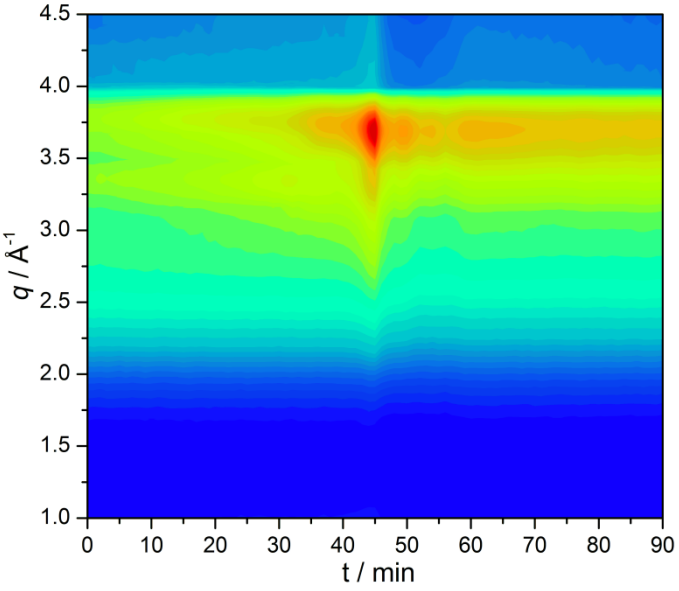

Figure 5.14: Contour plot containing the diffraction due to scattering from amorphous materials, extracted from raw *in situ* EDXRD data for the synthesis of $Bi_5Ti_3Fe_{0.5}Cr_{0.5}O_{15}$ with RbCl salt.

A maximum in the intensity of diffraction due to amorphous scattering coincides with the melting of the RbCl salt, which occurs after *ca.* 44 mins. It is to be expected that such scattering should increase as the material in the X-ray beam transforms from the solid to the liquid phase, due to the decrease in long-range order of the sample. It is interesting to note that the scattering intensity is significantly greater during the melting transition than it is when RbCl exists purely in the liquid phase, at $t > 50$ mins. It is possible that this coincides with additional melting of a Bi_2O_3-related species and the subsequent decay in the background is due to conversion of this material to the final crystalline product.

5.6.3 Discussion

The reaction probed at 800 °C gives the strongest indication yet that the threshold to product formation in these systems is the melting of a Bi_2O_3-based phase. A crucial physical transformation appears to occur in the temperature region $815 \leq T / °C \leq 835$. This observation is consistent with findings detailed in Section 4.5.2, where successful MSS with RbCl salt was observed following temperature dwell for 5 hours at 835 °C (above the Bi_2O_3 melting point of 824 °C) but not at 800 °C.

Variation in diffraction intensity of both Bragg reflections and the background due to scattering, particularly in data measured close to the RbCl melting point, suggests significant particle rearrangement within the sample mixture during reaction. This correlates with preliminary experiments undertaken to monitor change in diffraction intensity as a function of X-ray beam position through the sample. EDXRD scans were undertaken at several positions moving vertically down the centre of the sample crucible during MSS of $Bi_5Ti_3FeO_{15}$ at 950 °C, and it was noted that product reflection intensity increased closer to the base of the sample vessel. It would be interesting to simultaneously monitor the evolution of crystalline phases using *in situ* XRD whilst imaging the position and movement of these phases in the molten flux. The implementation of a beamline at Diamond Light Source capable of such studies is currently in the discussion stage.

5.7 Conclusion

In situ XRD studies revealed that formation of the desired $n = 4$ $Bi_5Ti_3Fe_{0.5}Cr_{0.5}O_{15}$ product proceeds *via* the related $n = 3$ structure, $Bi_4Ti_3O_{12}$. The synthesis reaction goes to completion upon heating to 950 °C in the absence of a molten salt, however the melting transition of Na_2SO_4 was observed to accelerate the rate of product formation. Use of a salt with lower melting point (RbCl) did not alter the mechanism of reaction, nor was the threshold temperature to product formation lowered by this synthetic variation. The results from an analogous reaction undertaken with Na_2SO_4 at *ca.* 800 °C indicated that the melting of a bismuth-containing oxide intermediate may provide the drive required for successful synthesis of $Bi_5Ti_3Fe_{0.5}Cr_{0.5}O_{15}$ in the pure phase.

Significant advances in XRD data processing and analysis have been necessary since Beamline I12 was first commissioned in 2010. A greater quantity of useful information can now be extracted from *in situ* XRD measurements on high-temperature systems using I12. Accumulation of data from all 23 energy-dispersive detector elements, automated batch peak-fitting, diffraction pattern background subtraction, and the trial of angular-dispersive studies have all served to improve data analysis markedly. Rietveld refinement has been successfully undertaken on diffraction data measured using 4 second exposure at temperatures up to 950 °C. Lattice parameters elucidated from these analyses can be plotted *vs.* temperature to monitor subtle phase changes in crystalline materials upon heating and cooling. It is anticipated that batch Rietveld refinement analysis will soon be possible on similar systems.

5.8 References

1. Y. M. Sung, *Crystal Growth & Design*, 2004, **4**, 325-329.
2. W. C. Kwak and Y. M. Sung, *Journal of the European Ceramic Society*, 2004, **24**, 1603-1606.
3. W. C. Kwak and Y. M. Sung, *Journal of Materials Research*, 2002, **17**, 1463-1468.
4. C. H. Lu and J. T. Lee, *Ceramics International*, 1998, **24**, 285-291.
5. S. T. Misture, *Journal of Electroceramics*, 2006, **16**, 167-178.
6. M. S. Haluska, S. Speakman and S. T. Misture, *Advances in X-ray Analysis*, 2002, **45**, 110-116.
7. M. I. Morozov, L. P. Mezentseva and V. V. Gusarov, *Russian Journal of General Chemistry*, 2002, **72**, 1038-1040.

8. M. T. Buscaglia, M. Sennour, V. Buscaglia, C. Bottino, V. Kalyani and P. Nanni, *Crystal Growth & Design*, 2011, **11**, 1394-1401.
9. M. S. Peterson, C. A. Say, S. Speakman and S. T. Misture, *Advances in X-ray analysis*, 2003, **46**, 226-231.
10. Y. Zhao, Y. X. Li, Y. Q. Lu and Y. L. Wang, *Ferroelectrics*, 2010, **404**, 45-49.
11. D. G. Porob and P. A. Maggard, *Materials Research Bulletin*, 2006, **41**, 1513-1519.
12. Zulhadjri, B. Prijamboedi, A. A. Nugroho, N. Mufti, A. Fajar, T. T. M. Palstra and Ismunandar, *Journal of Solid State Chemistry*, 2011, **184**, 1318-1323.
13. J. F. Dorrian, R. E. Newnham, M. I. Kay and D. K. Smith, *Ferroelectrics*, 1971, **3**, 17-27.
14. A. D. Rae, J. G. Thompson, R. L. Withers and A. C. Willis, *Acta Crystallographica Section B-Structural Science*, 1990, **46**, 474-487.
15. S. J. Moorhouse, N. Vranjes, A. Jupe, M. Drakopoulos and D. O'Hare, *Review of Scientific Instruments*, 2012, **83**, 084101-084108.
16. S. Bruckner, *Journal of Applied Crystallography*, 2000, **33**, 977-979.
17. A. J. van den Berg and F. Tuinstra, *Acta Crystallographica, Section B (Structural Crystallography and Crystal Chemistry)*, 1978, **B34**, 3177-3181.
18. C. N. R. Rao, G. V. S. Rao and S. Ramdas, *Journal of Physical Chemistry*, 1969, **73**, 672-675.
19. H. A. Harwig, *Zeitschrift Fur Anorganische Und Allgemeine Chemie*, 1978, **444**, 151-166.
20. P. Shuk, H. D. Wiemhofer, U. Guth, W. Gopel and M. Greenblatt, *Solid State Ionics*, 1996, **89**, 179-196.
21. A. Snedden, C. H. Hervoches and P. Lightfoot, *Physical Review B*, 2003, **67**, 092102.
22. C. H. Hervoches, A. Snedden, R. Riggs, S. H. Kilcoyne, P. Manuel and P. Lightfoot, *Journal of Solid State Chemistry*, 2002, **164**, 280-291.
23. C. H. Hervoches, J. T. S. Irvine and P. Lightfoot, *Physical Review B*, 2001, **64**, 100102-(1-4).
24. A. T. Giddings, M. C. Stennett, D. P. Reid, E. E. McCabe, C. Greaves and N. C. Hyatt, *Journal of Solid State Chemistry*, 2011, **184**, 252-263.
25. D. C. N. Swindells and J. L. Gonzalez, *Acta Crystallographica Section B-Structural Science*, 1988, **44**, 12-15.
26. M. G. Navarro-Rojero, J. J. Romero, F. Rubio-Marcos and J. F. Fernandez, *Ceramics International*, 2010, **36**, 1319-1325.
27. C. H. Hervoches and P. Lightfoot, *Chemistry of Materials*, 1999, **11**, 3359-3364.
28. M. Krzhizhanovskaya, S. Filatov, V. Gusarov, P. Paufler, R. Bubnova, M. Morozov and D. C. Meyer, *Zeitschrift Fur Anorganische Und Allgemeine Chemie*, 2005, **631**, 1603-1608.
29. N. C. Hyatt, I. M. Reaney and K. S. Knight, *Physical Review B*, 2005, **71**, 7.
30. V. Srikanth, H. Idink, W. B. White, E. C. Subbarao, H. Rajagopal and A. Sequeira, *Acta Crystallographica Section B-Structural Science*, 1996, **52**, 432-439.
31. S. Mallick, K. J. Bowman and A. H. King, *Applied Physics Letters*, 2005, **86**, 2.
32. D. E. Bugaris and H.-C. zur Loye, *Angewandte Chemie-International Edition*, 2012, **51**, 3780-3811.
33. R. J. Koch, I. N. Lokuhewa, J. Shi, M. S. Haluska and S. T. Misture, *Journal of Sol-Gel Science and Technology*, 2012, **64**, 612-618.
34. T. M. Bruton, *Journal of Solid State Chemistry*, 1974, **9**, 173-175.
35. J. Lopez-Martinez, A. Romero-Serrano, A. Hernandez-Ramirez, B. Zeifert, C. Gomez-Yanez and R. Martinez-Sanchez, *Thermochimica Acta*, 2011, **516**, 35-39.
36. M. I. Morozov and V. V. Gusarov, *Inorganic Materials*, 2002, **38**, 723-729.
37. J. Tellier, P. Boullay, M. Manier and D. Mercurio, *Journal of Solid State Chemistry*, 2004, **177**, 1829-1837.

Chapter 6: An *In Situ* Study of the Resin-assisted Solvothermal Synthesis of Metal-Organic Frameworks

6.1 Introduction

The Oxford-Diamond *In Situ* Cell (ODISC) was designed as a multifunctional furnace for undertaking time-resolved X-ray diffraction (XRD) studies. It was essential, in the initial stages of use, that the wide versatility of the device was demonstrated. The crystallisation of metal-organic framework (MOF) materials is an important area of study in the field of *in situ* X-ray diffraction. The ability to accurately probe the subtleties of MOF formation under solvothermal conditions, and the corresponding kinetics of their crystallisation, *in situ*, was a crucial aspect of the development of ODISC. This chapter contains the description of a brief *in situ* investigation into the crystallisation of MOFs using ODISC in the hydrothermal configuration. The study employed angular-dispersive XRD and was undertaken using Beamline I12 at the Diamond Light Source. Complementary data was also obtained using EDXRD on Beamline F3 at the DORIS synchrotron in Hamburg.

The range of established approaches to formation of metal-organic frameworks was introduced in Section 1.5. Use of a polymer resin as both template and metal source in solvothermal reactions is a relatively new technique towards MOF synthesis. Functionalised polystyrene resins have been shown to exhibit wide applicability in the fields of polymer-supported catalysis, water purification, and combinatorial synthesis.[1-3] These macroporous resins exist as amorphous, crosslinked, infinite networks of interpenetrating polymer chains with well-developed porous structures.[4] Sulfonated styrene-divinylbenzene (styrene-DVB) beads are commercially available with Na^+ as the cation. Upon stirring in a concentrated solution of transition metal salt, the Na^+ cations in the beads are readily interchanged with a chosen metal ion. The use of metal-exchanged sulfonated styrene-DVB resin beads to direct the bulk synthesis of several novel metal-organic frameworks and layered double hydroxides was reported by Du and co-workers in 2008 and 2009, respectively.[5, 6]

Under solvothermal conditions, metal-exchanged polymer resin exhibits a denaturation temperature at approximately 120 °C, at which point cations are released from the pores into solution. At temperatures slightly below this threshold, metals ions in the active sites

of the polymer resin can react to form a thin coating of product as a 'seeded layer' on the surface of the beads. Following sustained reaction at such temperatures, cations are slowly leached into solution forming product particles in bulk, which can deposit on the seeded layer of the beads. During reaction at higher temperatures, metal ions are steadily leached into solution resulting in a finite number of crystal nucleation sites. The cation concentration gradient around the beads in solution, in addition to the surface interactions with the organic molecules, creates a unique sample environment which has previously facilitated the formation of several novel frameworks.

6.2 Investigating the resin-assisted crystallisation mechanism of $(H_2NMe_2)_2[Co_3(BDC)_4]\cdot y$DMF

Metal-organic frameworks containing 1,4-benzenedicarboxylate (BDC) ligands exhibit several different metal-linker binding modes. Various synthetic routes towards the formation of similar Zn-BDC frameworks, using diethylformamide (DEF) solvent, were reported in 2005-2006.[7-9] Poulsen and co-workers described the solvothermal synthesis of two isostructural coordination polymers comprising chains of cobalt or zinc atoms, interconnected by BDC linkers.[7] The cobalt framework described, $[2(NH_2Et_2)]^{2+}[Co_3(C_8H_4O_4)_4]^{2-}\cdot 3C_5H_{11}NO$, is charge balanced by the $(NH_2Et_2)^+$ linkers that are formed from *in situ* acid-catalysis of the DEF solvent. A detailed charge density study of this material at 16 K was subsequently undertaken by Clausen *et al.*, who observed very different charge distributions for the three uniquely-bound BDC linkers in the framework.[10] More recently, an analogous cobalt-framework synthesised with dimethylformamide (DMF) solvent was reported by Luo *et al.*.[11] The structural relationship between several of these phases, including the synthesis of two novel DMF-derived Co-analogues, has been summarised by Wang and co-workers.[12] BDC-derived MOFs that incorporate by-products from DMF solvent hydrolysis have also been observed for a variety of different metal cations.[13-17]

Phases in the Co-BDC-DEF/DMF systems are distinguished by the coordination environments of cobalt that they exhibit. The structures consist of trimetallic cobalt building units coordinated to eight BDC ligands (Figure 6.1). In each case, a 'central' cobalt(II) atom, bonded to six carboxylate oxygen atoms in distorted octahedral geometry, is flanked by two 'terminal' cobalt(II) atoms that exhibit identical coordination

environments. The terminal cobalt atoms have been shown to bind in a tetrahedral, pyramidal, or octahedral fashion to the surrounding BDC linkers. Acid catalysis of the DEF or DMF solvent results in formation of $(NH_2R_2)^+$ (R = Me or Et), which reside in the pores of the negatively-charged framework alongside neutral solvent molecules to maintain overall electroneutrality.

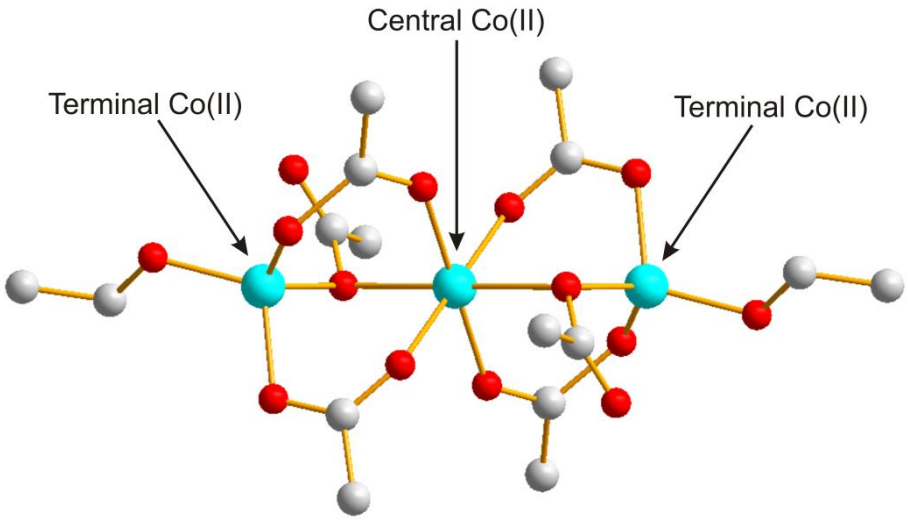

Figure 6.1: Trimetallic building unit observed in Co-BDC-DMF frameworks, where ● represents Co atoms, ● represents O atoms, and ● represents C atoms. BDC units are represented only by the 'carboxylate' functional groups. The terminal cobalt atoms are tetrahedrally coordinated in this case.

Wang and co-workers reported temperature-induced isomerism in the system of Co-BDC-DMF co-ordination polymers.[12] In their work, different coordination modes of the carboxylate linker to the two terminal Co(II) atoms are described, which leads to a corresponding variation in the structural parameters of two analogous frameworks. They report on the existence of 'Co_{oct}-Co_{oct}-Co_{oct}' and 'Co_{tet}-Co_{oct}-Co_{tet}' secondary building units (SBUs) involving the three respective Co(II) atoms shown in Figure 6.1 (where oct and tet correspond to the respective octahedral and tetrahedral binding-modes of BDC to cobalt). Another BDC binding mode, 'Co_{pyr}-Co_{oct}-Co_{pyr}', (where pyr represents pyramidal binding to cobalt) has been observed in an analogous coordination polymer synthesised in the presence of DMF and methanol by Luo *et al.*[11]

In order to investigate the influence of cation-exchanged resin beads in directing the synthesis of Co-BDC framework materials, a systematic *in situ* XRD study was undertaken. The use of polymer resin beads as a source of cobalt metal ions in the solvothermal synthesis of $(H_2NMe_2)_2[Co_3(BDC)_4]\cdot y$DMF was probed. Chemical reactions

were monitored at several synthesis temperatures and the route to product formation, as well as the structure of the final material, was analysed.

6.2.1 In situ *angular-dispersive XRD study*

Cobalt-exchanged polymer resin beads and BDC were added to a solution of DMF and methanol. The mixture was placed inside a PTFE liner and sealed in a stainless-steel autoclave that had been adapted for *in situ* studies. The autoclave was heated at 30 °C.min^{-1} to various dwell temperatures. All temperature data provided in this chapter were recorded using a thermocouple positioned between the sample autoclave and a glassy carbon sheath. A shift in the position of a Bragg reflection corresponding to the PTFE liner ceased within 1 min of the thermocouple temperature reaching a plateaux, which indicated minimal lag between the recorded and the sample temperatures. Angular-dispersive XRD data were recorded with 4 sec exposure at 30 sec intervals during the course of each reaction. An annotated contour plot containing XRD data for the reaction undertaken at 250 °C is shown in Figure 6.2. The temperature profile for the reaction is provided in Appendix E.

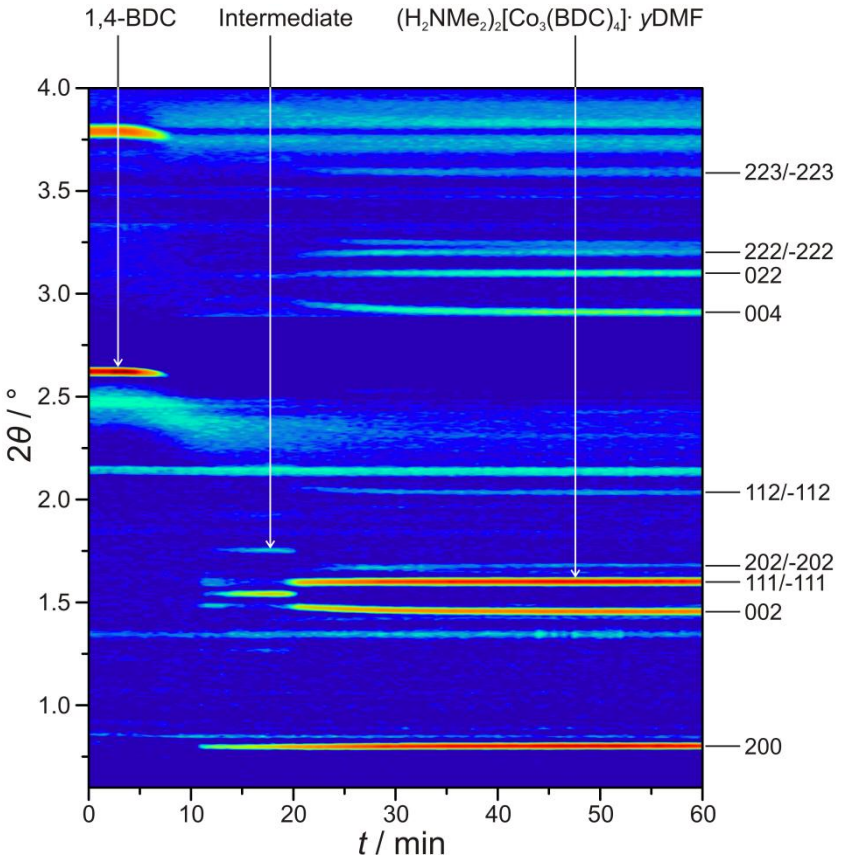

Figure 6.2: Annotated contour plot containing *in situ* angular-dispersive XRD data for the synthesis reaction of $(H_2NMe_2)_2[Co_3(BDC)_4]\cdot y$DMF. The assignment of selected product Bragg reflections is shown.

Reflections corresponding to undissolved BDC are observed during the initial stages of the reaction, which decline to zero intensity upon heating. The temperature of the autoclave reaches 250 °C before 11 mins. After 12 mins, Bragg reflections corresponding to a crystalline intermediate phase grow in intensity, including those observed at 2θ = *ca.* 0.80, 1.54, and 1.75°. After 20 mins, a sharp decline in intensity of intermediate phase reflections is concurrent with the growth of new reflections consistent with the product phase, which subsequently exist in isolation until the reaction reaches completion. Bragg reflections corresponding to the product material can be indexed to the structure of the target framework, $(H_2NMe_2)_2[Co_3(BDC)_4]\cdot y$DMF, which is shown in Figure 6.3. The structural parameters relate closely to those reported in the literature: a = 33.2 Å, b = 9.8 Å, c = 18.2 Å, β = 92.5°, with space group $C2/c$.[10]

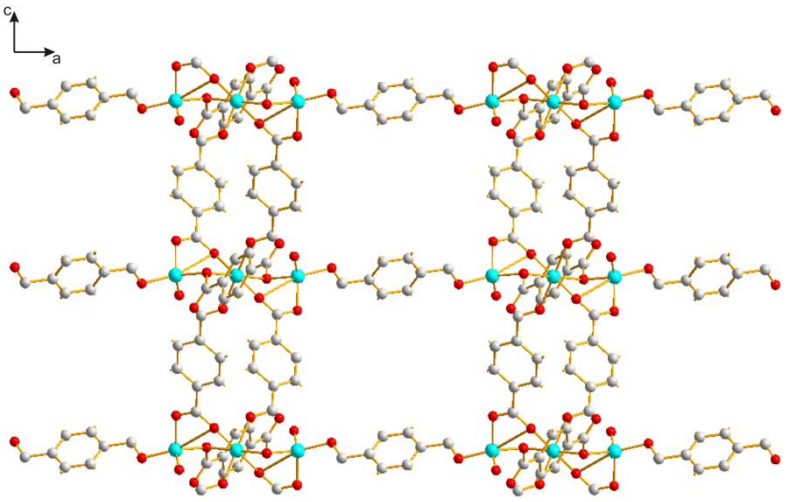

Figure 6.3: The structure of $(H_2NMe_2)_2[Co_3(BDC)_4]\cdot y$DMF, where ● represents Co atoms, ● represents O atoms, and ● represents C atoms. H atoms and solvent molecules have been excluded for clarity.

The reflection at 2θ = 0.80° is observed throughout conversion between the intermediate and product phases. This can be interpreted as an indication that the two materials are structurally related. Indexing of Bragg reflections present in the *in situ* XRD scan recorded after 19 mins indicates that the structure of the intermediate is comparable to a zinc-BDC framework previously reported by Edgar *et al.*, $[Zn_3(BDC)_3(H_2O)_3]\cdot 4$DMF,[18] with a = 12.76 Å, b = 9.81 Å, c = 17.49 Å, β = 106.87°, and space group $P2_1/c$. The structure of this intermediate consists of stacked 'layers' containing the same trimetallic building units as the product, with tetrahedral coordination of the two terminal cobalt atoms to the oxygen atoms in the BDC linkers. In the intermediate, both tetrahedrally

coordinated terminal cobalt(II) atoms are bound to a solvent ligand, which connect *via* hydrogen bonding to crystallographically distinct DMF molecules between the layers. During intermediate to product conversion, a significant structural rearrangement takes place and the cobalt-coordinated solvent molecules become replaced by BDC groups, which bind to cobalt(II) atoms in adjacent layers. The resulting cross-linking 'pillars' create the final 3D porous network, which becomes occupied by disordered solvent molecules. It is possible that the final transformation proceeds *via* solid-state reorganisation between the two related frameworks, as both contain similar trimetallic building units.

The positional shift and integrated intensity of selected reflections corresponding to both phases present during the reaction were analysed using a Gaussian fitting routine and plotted as a function of time (Figure 6.4). From the extent of reaction *vs.* time plot in Figure 6.4(a), it is clear that direct conversion of the intermediate to the product phase occurs.

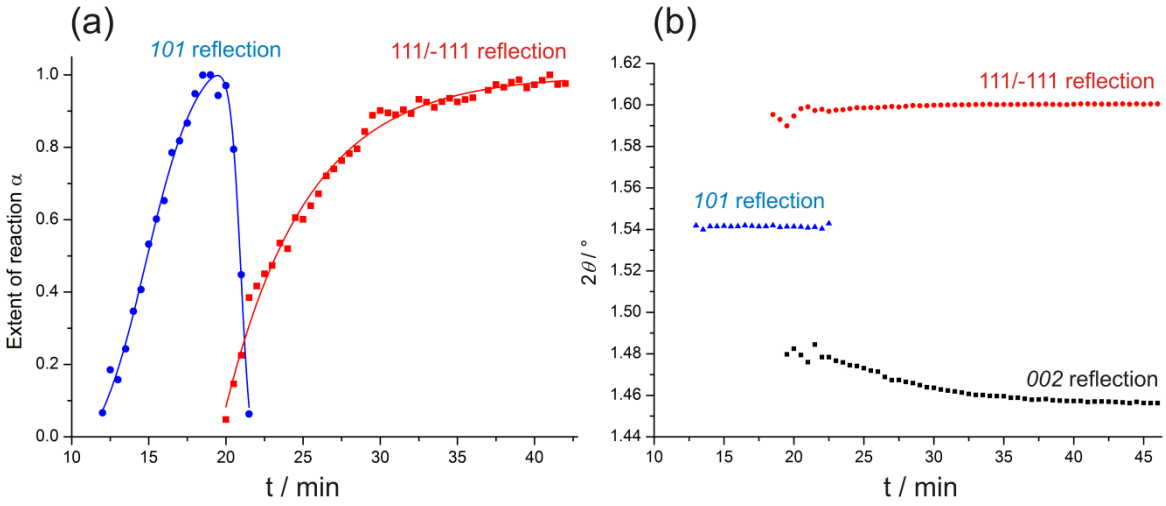

Figure 6.4: Data obtained from intensity integration analysis corresponding to intermediate (●) and product (●,●) reflections, including (a) extent of reaction *vs.* time plot (the solid lines are included as a guide) and (b) reflection position *vs.* time plot.

The changes in position of the intermediate (101) reflection and the product (111/-111) and (002) reflections as a function of time are shown in Figure 6.4(b). During initial formation of the 3D product framework, migration of the (00*l*) reflections to lower 2θ (higher *d*-spacing) signifies a small expansion of the unit cell in the direction perpendicular to the *c*-axis. This axis is orthogonal to the framework 'layers', within

which the three cobalt atoms of the trimetallic building units lie. The shift of the (002) reflection is therefore indicative of an increase in interlayer spacing which can be attributed to a minor preferential alignment of the BDC pillars, as the cobalt-coordinated solvent molecules of the intermediate become replaced. Only product reflections with a component in *l* are observed to shift in this manner.

An attempt at monitoring the synthesis of $(H_2NMe_2)_2[Co_3(BDC)_4]\cdot y$DMF at three other dwell temperatures, 180, 200, and 225 °C, was undertaken. The reduction in synthesis temperature to 200 °C had the effect of prolonging the lifetime of the metastable precursor (see Appendix E). Unfortunately, product reflections observed during analogous syntheses at 180 and 225 °C were of very low intensity and as such, no mechanistic information could be implied from these data.

6.2.2 Structural interpretation of the product frameworks

Following *in situ* monitoring of the reaction mixture, sample autoclaves from reactions at 180, 200, 225, and 250 °C were cooled at 30 °C.min^{-1} to room temperature. The product mixtures were transferred to polypropylene centrifuge tubes and a single scan of 4 sec exposure was undertaken on each sample in monochromatic-beam mode. The resulting 2D images were converted to 1D diffraction patterns and structural analysis on the XRD data was carried out using the Rietveld method. In the case of the sample synthesised at 225 °C, a scan was undertaken on the final product stirring in a glass vial at room temperature in an attempt to remove signals due to the polypropylene vessel, but this resulted in lower intensity data and an increased background. Studying the products suspended in solvent allowed structural effects due to sample drying (and subsequent removal of solvent from the pores of the framework) to be eliminated.

The monoclinic structure proposed by Luo *et al.* was used as a starting model for refinement against the raw data.[11] A good correlation between experimental and modelled data was evident for all samples. Figure 6.5 shows the results of structural refinement with the product of synthesis at 250 °C. Results from the additional product refinements, alongside goodness of fit parameters for all samples, are provided in Appendix E.

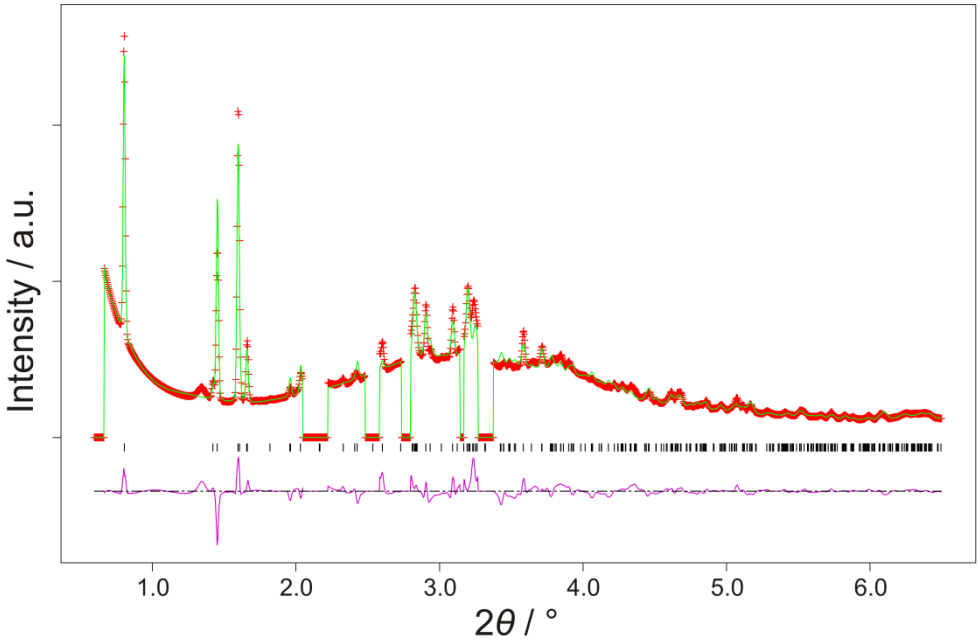

Figure 6.5: Refinement of a monoclinic structure model with angular-dispersive XRD data from a scan of $(H_2NMe_2)_2[Co_3(BDC)_4]\cdot y$DMF (250 °C product) with 4 sec exposure. Raw data is indicated by the red crosses, the green line indicates the refined model data, and the pink line represents the difference between both experimental and modelled data. Regions containing reflections due to the polypropylene sample vessel have been excluded.

A low intensity, broad reflection is observed at 2θ = *ca.* 1.35 ° in the diffraction data from products synthesised at 200 and 250 °C. This can be attributed to the (001) reflection of 'MOF-71', a Co(BDC)(DMF) framework first synthesised by Rosi *et al.*[19] This material differs from the major product through the existence of doubly bridging oxygen-bound DMF linkers in its structure. No such Bragg reflection is observed during *in situ* formation, therefore it is likely that a small amount of MOF-71 forms upon sample cooling in the absence of excess $(NH_2Me_2)^+$, due to insufficient acid catalysis of the DMF solvent. Structural parameters for each product calculated from refinement are provided in Table 6.1. Clearly, the variation in synthesis temperature has a profound influence on the structure of the material formed.

Table 6.1: Unit cell parameters obtained by refinement of a monoclinic structure model against angular-dispersive XRD data for $(H_2NMe_2)_2[Co_3(BDC)_4]\cdot y$DMF synthesised at four temperatures.

Synthesis temperature / °C	**Lattice parameter**				**Unit cell volume / Å^3**
	***a* / Å**	***b* / Å**	***c* / Å**	***β* / °**	
180	33.50 (3)	9.848 (5)	18.151 (9)	95.69 (7)	5959 (10)
200	33.28 (2)	9.775 (3)	18.169 (6)	94.05 (5)	5896 (6)
225	33.48 (4)	9.847 (5)	18.34 (1)	92.55 (8)	6039 (11)
250	33.215 (8)	9.775 (3)	18.372 (6)	89.90 (3)	5965 (5)

The structural model is based on layers of cobalt building units interconnected by BDC ligands. The layers are linked by cross-linking BDC 'pillars' which create a 3D porous framework. Structural data provided in Table 6.1 for the products from resin-assisted synthesis at various temperatures indicate subtle deviations in each case. The *a*- and *b*-lattice parameters fluctuate moderately between samples, and mirror the slight change in overall unit cell volume observed. There is no indication of significant cell expansion or contraction with increase in synthesis temperature, which might be indicative of the extent of solvent incorporation. A clear increase in the *c*-parameter is observed for higher synthesis temperatures, which contrasts the considerable decrease in *β*-angle detected as dwell temperature increased.

The variation in structural parameters of the four new MOFs relative to $(H_2NMe_2)_2[Co_3(BDC)_4]\cdot y$DMF, synthesised at 160 °C by Wang, is illustrated in Figure 6.6. Lattice parameters of two further analogues, synthesised at room temperature by Wang and at 160 °C with DMF/methanol by Luo, are also included in the plot. When positioned consecutively with respect to the relative *β*-angles, it is clear that the newly synthesised materials exhibit structures that are intermediate between the known frameworks. Where the *a*- and *b*-parameters fluctuate slightly above and below 1.00, the *c*-parameter is observed to increase as the *β*-angle decreases across the series.

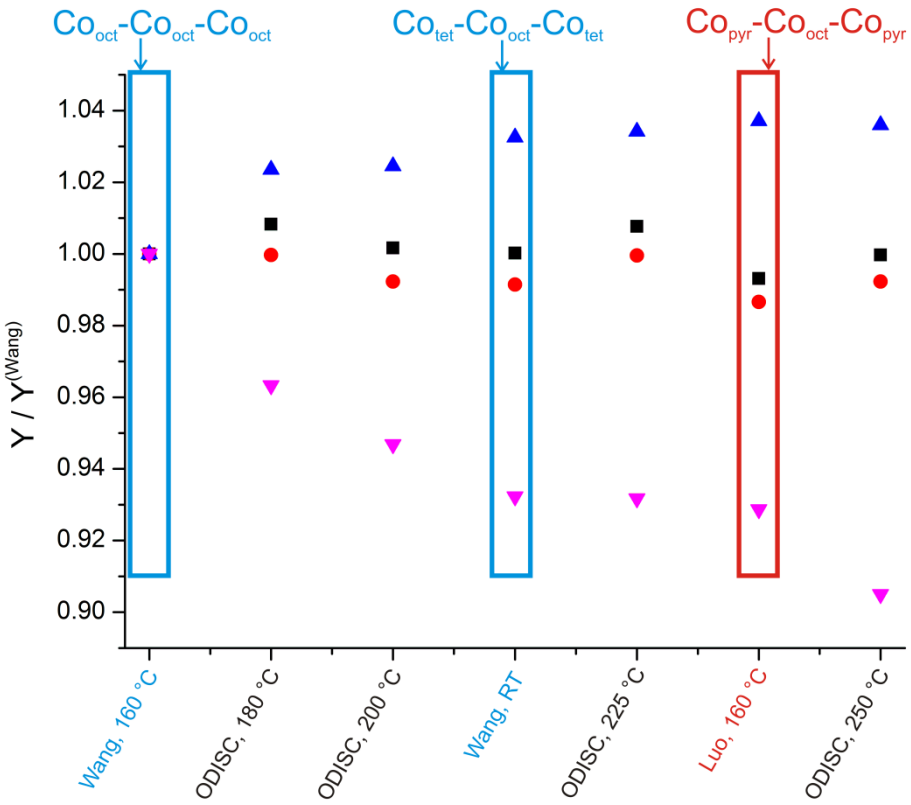

Figure 6.6: Unit cell parameters (Y) relative to the sample synthesised by Wang *et al.* (Y^{wang}): *a*-parameter (■), *b*-parameter (●), *c*-parameter (▲), and *β*-angle (▼). The error in each case is within the range of the data point.

It is possible that the intermediate lattice parameters are indicative of a transformation of the coordination geometry at one of the terminal Co(II) atoms. A change in the ligand coordination at only one Co(II) atom would result in local asymmetry in the system. The existence of asymmetric SBUs, such as Co_{tet}-Co_{oct}-Co_{oct}, Co_{pyr}-Co_{oct}-Co_{oct}, and Co_{tet}-Co_{oct}-Co_{pyr}, was hypothesised by Wang *et al.* (Figure 6.7), but have not been previously observed in this Co-BDC-DMF system. High-resolution synchrotron X-ray diffraction and single-crystal diffraction analysis would provide a more detailed picture of the subtle structural differences across this series. Confirmation of the existence of asymmetric SBUs in the newly synthesised structures would allow a systematic study of the variation in magnetic properties across this series to be undertaken.[20]

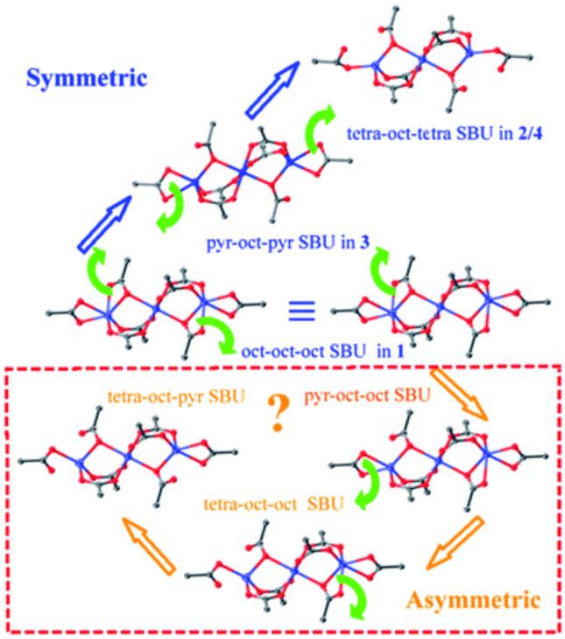

Figure 6.7: Schematic published by Wang *et al.* illustrating the known and hypothesised (in the dashed box) coordination environments in $Co_3(RCOO)_8$ trimetallic building units, where green arrows represent Co–O bond dissociation.[12]

6.2.3 Conclusion

Resin-assisted synthesis of $(H_2NMe_2)_2[Co_3(BDC)_4]\cdot y$DMF proceeds *via* a structurally-related metastable precursor, the structure of which is analogous to a previously reported $[Zn_3(BDC)_3(H_2O)_3]\cdot 4$DMF framework. The increase in network dimensionality from intermediate to product conforms to the trend observed in previous *in situ* studies of framework materials.[21] The observation of a Bragg reflection that remains unchanged throughout the transition indicates that the process is topotactic rearrangement, which is a sensible conclusion given the related structures of the building units of the two materials. Formation of the final product is driven by the onset of a solvent hydrolysis reaction between DMF and H_2O (both of which are components of the intermediate framework), following sustained temperature dwell at the target temperature.

6.3 Probing the crystallisation of frameworks in the Co-NDC-DMF system

A significant number of coordination polymers containing transition metal ions bonded to the 2, 6-naphthalenedicarboxylate (NDC) linker have been reported.[22, 23] Indeed, several unique structures exist in the Co-NDC-DMF system alone. The 3D framework, $[Co_3(NDC)_3(DMF)_4]$, comprises linear trimetallic building units interconnected by NDC ligands. The structure contains two crystallographically unique cobalt atoms: one (the central atom in the building unit) coordinated octahedrally to six NDC ligands, and the other (corresponding to two terminal cobalt atoms) coordinated to four NDC carboxylate oxygen atoms and two DMF molecules.[24, 25] Use of a chloride instead of a nitrate salt as the source of cobalt ions in the reagent mixture results in preferential formation of a different framework, $[Co_3(NDC)_3(DMF)_2(Me_2NH)_2]$.[26] This structure, formed *via* partial decomposition of the DMF solvent, was first synthesised using the resin-assisted approach by Du *et al.* in 2008.[5] Its structure is again composed of Co_3 clusters, with the central atom octahedrally coordinated to six carboxylate oxygen atoms and the terminal atoms coordinated to four carboxylate oxygen atoms, one DMF molecule, and one dimethylamine ligand. A further material in the Co-NDC-DMF family has also been observed as a side-product in the synthesis of $[Co_3(NDC)_3(DMF)_2(Me_2NH)_2]$. This Co(DMF)(NDC) framework was isolated by Du *et al.* as vivid purple, needle-like crystals in very low yield of *ca.* 2%.[27] The structure exhibits only one crystallographically unique cobalt atom, in a distorted octahedral environment coordinated by four NDC carboxylate oxygen atoms and two DMF molecules.

Considering the structural diversity observed in coordination polymers formed using only these three reagents, the system was probed using *in situ* XRD to determine the factors influencing preferential formation of one structure over another. It was of particular interest to observe whether Co(DMF)(NDC), with chain-like 3D structure, could be formed in higher yield as a pure phase.

6.3.1 Resin-assisted synthesis

Angular-dispersive XRD was employed to monitor the resin-assisted solvothermal synthesis of frameworks in the Co-NDC-DMF system. Reactions were undertaken using ODISC in the hydrothermal configuration. Co^{2+}-exchanged resin was treated solvothermally with NDC and DMF at 200, 225, and 250 °C. Autoclaves containing the

reaction mixture were heated at 30 °C.min^{-1} to the dwell temperature and held until the reaction was deemed to have reached completion. Following cooling, the sample was transferred to a polypropylene centrifuge tube and a 4 second scan of the product was undertaken in monochromatic mode. It was found that heating the reaction mixture to both 200 °C and 225 °C resulted in formation of Co(DMF)(NDC) in isolation. No crystalline products were observed to form at 250 °C using *in situ* XRD despite multiple attempts.

The stack plot in Figure 6.8 contains *in situ* XRD data obtained during the formation of Co(DMF)(NDC) from solvothermal treatment at 200 °C. Bragg reflections corresponding to the product phase were indexed using the following parameters: a = 23.5 Å, b = 8.8 Å, c = 7.2 Å, β = 97.8°, and space group $C12/c1$. Reflections consistent with undissolved NDC are observed initially at 2θ = 2.48 and 3.64 °, which decline to zero before the autoclave reaches 200 °C (after 11 mins). All reflections consistent with the Co(DMF)(NDC) phase appear concurrently, 6.5 mins after the dwell temperature is first reached. Bragg reflections corresponding to other crystalline materials are not observed in the *in situ* data, which indicates that the target framework is formed with phase-purity at 200 °C.

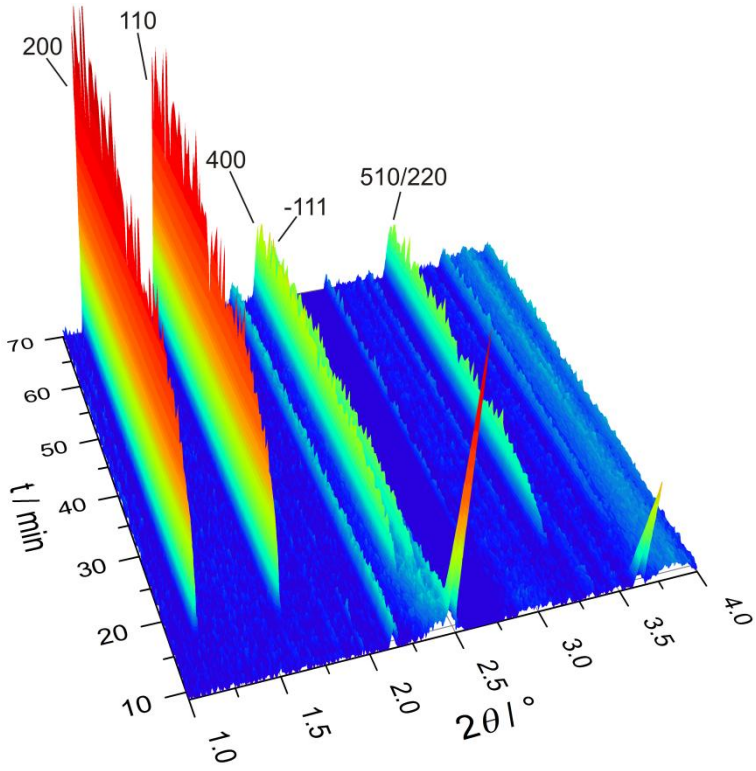

Figure 6.8: 3D stack plot containing *in situ* angular-dispersive XRD data for the synthesis reaction of Co(DMF)(NDC) at 200 °C.

The structure of Co(DMF)(NDC) formed by reaction at 200 °C was verified using Rietveld refinement of a monoclinic structure model, proposed by Du *et al.*,[27] with XRD data recorded from the product phase. The model agrees well with the angular-dispersive X-ray diffraction data. Accurate structural parameters elucidated from refinement are provided in Appendix E. The extent of reaction (α) was calculated for several product Bragg reflections in data from reactions undertaken at both 200 °C and 250 °C. The integrated intensity of each reflection for all time points was calculated using a batch Gaussian fitting procedure. Extent of reaction *vs.* time plots are shown in Figure 6.9.

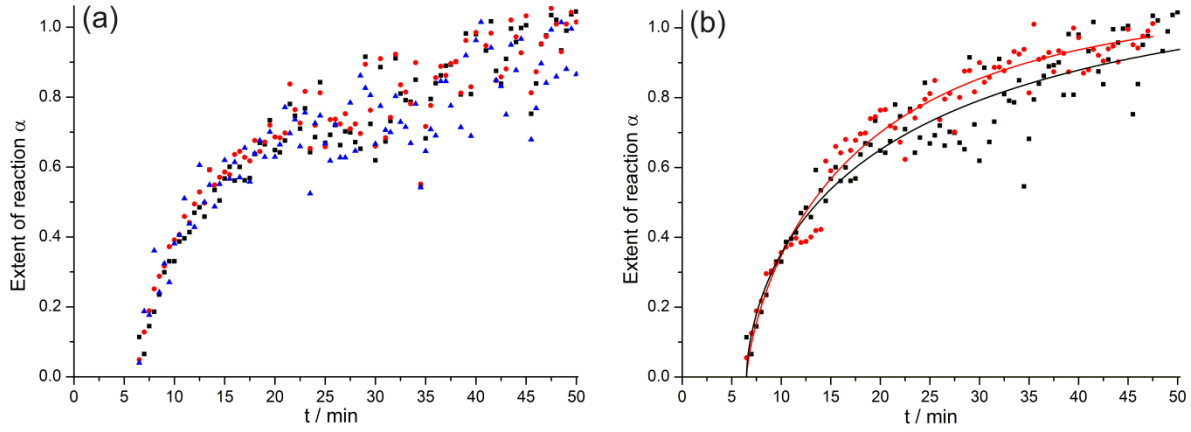

Figure 6.9: Extent of reaction (α) *vs* time (t) curves for the synthesis of Co(DMF)(NDC) including (a) α for the (002) (■), (110) (●), (400) (▲) Bragg reflections from the product formed at 200 °C, and (b) α determined for the (002) Bragg reflections of the product formed at 200°C (■) and 225 °C (●). The data in (b) have been modelled with the Avrami-Erofe'ev rate equation.

The crystallisation curves in Figure 6.9(a) for different Bragg reflections of the same material indicate that crystal growth in this system is isotropic. α *vs.* time data calculated for the (002) Bragg reflection from syntheses at both 200 and 225 °C are compared in Figure 6.9(b). Both data sets have been modelled with the Avrami-Erofe'ev rate law ($\alpha = 1 - \exp\{-[k(t - t_0)]^n\}$),[28-30] and the corresponding Sharp-Hancock plot,[31] alongside kinetic parameters yielded from the fit of the model, is provided in Figure 6.10.

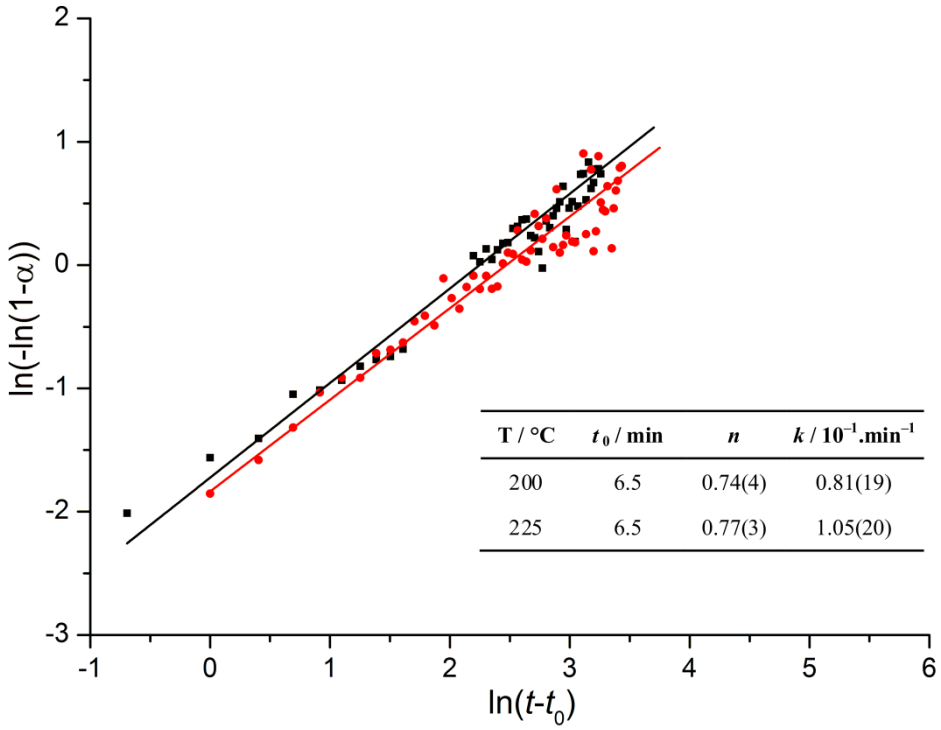

T / °C	t_0 / min	n	k / 10^{-1}.min^{-1}
200	6.5	0.74(4)	0.81(19)
225	6.5	0.77(3)	1.05(20)

Figure 6.10: Sharp-Hancock plots for the synthesis of Co(DMF)(NDC) at 200 °C (●) and 225 °C (■) alongside a table containing kinetic parameters for the reactions, where t_0 is the induction time, n is the Avrami exponent, and k is the rate constant for each reaction.

The value of the Avrami exponent, n, is close to 0.5 for both reactions. This is suggestive of a process that is highly-diffusion controlled.[32] It appears that slow release of cations from the metal-exchanged resin beads into solution is the limiting factor on the rate of product crystallisation. Despite the small difference in synthesis temperatures, the rate constant is noticeably larger upon undertaking the reaction at 225 °C instead of 200 °C.

6.3.2 Nitrate-salt synthesis

The analogous synthesis of Co(DMF)(NDC) using nitrate salt as the source of cobalt was attempted, in order to provide a comparison with the resin-assisted method. NDC was added to an autoclave containing a solution of $Co(NO_3)_2 \cdot 6H_2O$ dissolved in DMF, and the mixture heated to 180 °C. Facilities on Beamline F3 at the DORIS synchrotron were employed to undertake an *in situ* EDXRD study on the solvothermal reaction. 60 second scans were undertaken at 60 second intervals for 1 hour. Selected XRD data are shown in Figure 6.11. The temperature of the autoclave reached 180 °C after 8 mins.

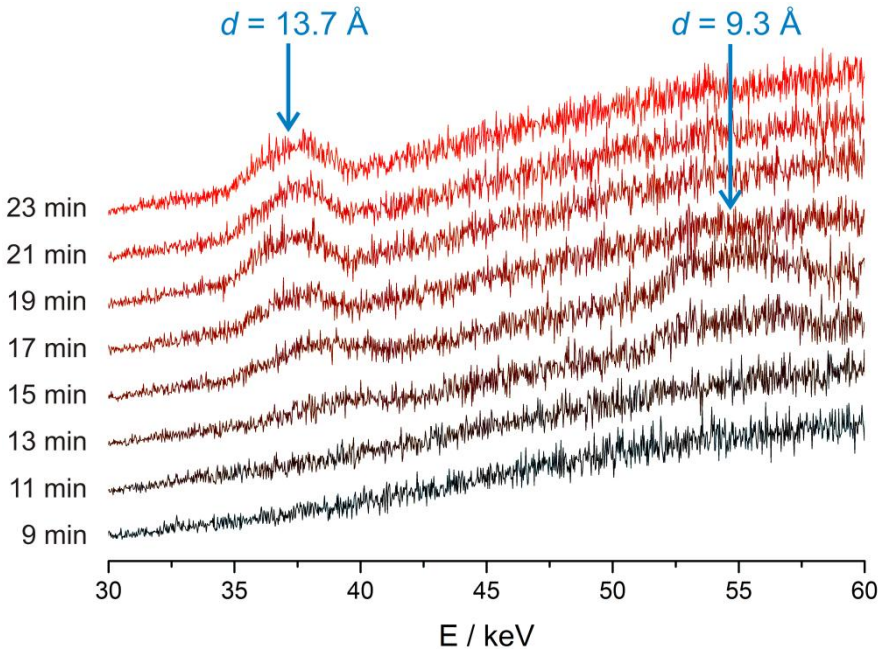

Figure 6.11: *In situ* XRD data recorded during the attempted synthesis of Co(DMF)(NDC).

Despite the considerably poorer data resolution than that obtained using Beamline I12, broad, low intensity Bragg reflections can be observed for more than one phase in the reaction profile. A broad signal, potentially corresponding to two separate Bragg reflections, is observed in the $9.1 \leq d$ / Å ≤ 9.6 region and is consistent with a crystalline intermediate phase. This peak is present in five consecutive 60 second scans and declines in intensity when growth of a product reflection, at *ca.* 13.7 Å, begins after 14 mins. The positions in *d*-spacing of the observed Bragg reflections do not correspond to expected values for reflections consistent with Co(DMF)(NDC).

The observed intermediate peak is instead compatible with the (020) and (011) reflections of $[Co_3(NDC)_3(DMF)_2(Me_2NH)_2]$, with *d*-spacings of *ca.* 9.5 and 9.1 Å respectively. This phase was described in the introduction to Section 6.3 and has been formed under similar solvothermal conditions, but with $CoCl_2$ as the Cobalt(II) source.[26] The position of the product material reflection is coincident with the *d*-spacing of the (011) Bragg reflection of framework $[Co_3(NDC)_3(DMF)_4]$. Liu *et al.* have previously synthesised this material under analogous solvothermal conditions and with the nitrate salt of cobalt.[25]

6.3.3 Discussion

Co(DMF)(NDC) has been successfully synthesised in bulk using the resin-assisted method. Due to the previous preparation of Co(DMF)(NDC) as a very low-yielding side-product, only single-crystal and SEM analyses have been reported for this material. Following discovery of the optimum synthesis conditions for its formation as a pure-phase, comprehensive characterisation of the properties of Co(DMF)(NDC) is now feasible. Of particular interest with cobalt frameworks is the magnetic behaviour of the system.[33]

It is clear that the two synthesis methods proceed *via* dissimilar reaction mechanisms to yield two different products. The controlled release of Co^{2+} ions from the resin-beads into solution leads to diffusion-controlled formation of the Co(DMF)(NDC) framework with chain-like structure of corner-sharing CoO_6 octahedra units. It appears that synthesis with metal nitrate facilitates formation of the pseudo-polymorph, $[Co_3(NDC)_3(DMF)_4]$, containing linear tri-metallic building units. Chen recently reported the one-pot synthesis of both manganese analogues to this system, and hypothesised that the role of the DMF solvent as a ligand was crucial in the preferential formation of one structure over another.[34]

The nature of the product framework formed from metal-salt derived synthesis of the Co-NDC-DMF system has been shown to be dependent upon the counter anion of the cobalt salt starting material.[26] Wang and co-workers previously reported that reaction with the chloride salt leads to formation of $[Co_3(NDC)_3(DMF)_2(Me_2NH)_2]$, whereas reaction with the nitrate salt results in preferential formation of $[Co_3(NDC)_3(DMF)_4]$. They hypothesised that this was due to a combination of the increased basicity afforded by $Cl > NO_3$ and the role of the anions as buffering additives. The results from *in situ* monitoring suggest that synthesis of $[Co_3(NDC)_3(DMF)_4]$ with $Co(NO_3)_2{\cdot}6H_2O$ could proceed *via* conversion from $[Co_3(NDC)_3(DMF)_2(Me_2NH)_2]$.

It is important to discuss the nature of the solvent employed for MOF syntheses described throughout this section. Amongst other reports on the same effect, an investigation by Burrows *et al.* highlights the importance of maintaining consistency in the 'age' of the DMF solvent employed.[9] Reactions undertaken with DMF that had been in the laboratory for several weeks led to formation of frameworks containing substituents resulting from solvent hydrolysis. These products contrasted those from syntheses using 'fresh' solvent.

All *in situ* studies undertaken at Beamline I12 described in this chapter were undertaken during the same beamtime using the same sample of 'fresh' DMF. This is likely to explain the reason for synthesis of Co(DMF)(NDC) as a single major product, in contrast to its formation as a low yielding side-product in the synthesis of $[Co_3(NDC)_3(DMF)_2(Me_2NH)_2]$, observed by Du *et al.* It is possible that use of poorer-quality DMF would lead to closer replication of the reactions undertaken by Du *et al.*

6.4 Conclusion

An *in situ* investigation into the synthesis of two cobalt-containing metal-organic frameworks, $(H_2NMe_2)_2[Co_3(BDC)_4]\cdot y$DMF and Co(DMF)(NDC), has been undertaken using ODISC. Crystallisation under solvothermal conditions has been successfully monitored and a range of structural and kinetic analysis techniques have been applied to the high-quality data obtained from Beamline I12. The effective use of cobalt-exchanged styrene-DVB beads to direct the bulk synthesis of MOFs has been demonstrated. Changes to the dwell temperature had a significant effect on the structure of the $(H_2NMe_2)_2[Co_3(BDC)_4]\cdot y$DMF product. Additionally, exclusive formation of a different product in the Co-NDC-DMF system to that observed for corresponding synthesis with cobalt nitrate as the metal source, demonstrates the pertinence of the resin-assisted method. Slow diffusion of metal ions from the polymer-resin beads into solution was suggested as the principal factor behind selective product crystallisation.

6.5 References

1. A. Akelah and D. C. Sherrington, *Chemical Reviews*, 1981, **81**, 557-587.
2. A. Akelah and D. C. Sherrington, *Polymer*, 1983, **24**, 1369-1386.
3. D. C. Sherrington, *Pure and Applied Chemistry*, 1988, **60**, 401-414.
4. D. C. Sherrington, *Chemical Communications*, 1998, 2275-2286.
5. Y. Du, A. L. Thompson and D. O'Hare, *Chemical Communications*, 2008, 5987-5989.
6. Y. Du, G. Hu and D. O'Hare, *Journal of Materials Chemistry*, 2009, **19**, 1160-1165.
7. R. D. Poulsen, A. Bentien, M. Christensen and B. B. Iversen, *Acta Crystallographica Section B-Structural Science*, 2006, **62**, 245-254.
8. E. Biemmi, T. Bein and N. Stock, *Solid State Sciences*, 2006, **8**, 363-370.
9. A. D. Burrows, K. Cassar, R. M. W. Friend, M. F. Mahon, S. P. Rigby and J. E. Warren, *CrystEngComm*, 2005, **7**, 548-550.
10. H. F. Clausen, J. Overgaard, Y. S. Chen and B. B. Iversen, *Journal of the American Chemical Society*, 2008, **130**, 7988-7996.
11. F. Luo, Y. X. Che and J. M. Zheng, *Crystal Growth & Design*, 2009, **9**, 1066-1071.
12. X.-F. Wang, Y.-B. Zhang, W. Xue, X. L. Qi and X. M. Chen, *CrystEngComm*, 2010, **12**, 3834-3839.
13. P. J. Calderone, D. Banerjee, A. M. Plonka, S. J. Kim and J. B. Parise, *Inorganica Chimica Acta*, 2013, **394**, 452-458.
14. T. Z. Zhang, Y. Lu, Y. G. Li, Z. Zhang, W. L. Chen, H. Fu and E. B. Wang, *Inorganica Chimica Acta*, 2012, **384**, 219-224.
15. S. R. Fan and L. G. Zhu, *Inorganica Chimica Acta*, 2009, **362**, 2962-2976.
16. S. Hausdorf, J. Wagler, R. Mossig and F. Mertens, *Journal of Physical Chemistry A*, 2008, **112**, 7567-7576.
17. S. M. Hawxwell and L. Brammer, *CrystEngComm*, 2006, **8**, 473-476.
18. M. Edgar, R. Mitchell, A. M. Z. Slawin, P. Lightfoot and P. A. Wright, *Chemistry-a European Journal*, 2001, **7**, 5168-5175.
19. N. L. Rosi, J. Kim, M. Eddaoudi, B. L. Chen, M. O'Keeffe and O. M. Yaghi, *Journal of the American Chemical Society*, 2005, **127**, 1504-1518.
20. M. Kurmoo, *Chemical Society Reviews*, 2009, **38**, 1353-1379.
21. L. J. McIntyre, T. J. Prior and A. M. Fogg, *Chemistry of Materials*, 2010, **22**, 2635-2645.
22. Z. Q. Jiang, *Asian Journal of Chemistry*, 2013, **25**, 2347-2348.
23. J. Wang, Y. Zhang, X. Q. Liu, J. Xiao, H. Zhou and A. H. Yuan, *Microporous and Mesoporous Materials*, 2012, **159**, 100-104.
24. S. H. Kim, H. S. Huh and S. W. Lee, *Journal of Molecular Structure*, 2007, **841**, 78-87.
25. B. Liu, R. Q. Zou, R. Q. Zhong, S. Han, H. Shioyama, T. Yamada, G. Maruta, S. Takeda and Q. Xu, *Microporous and Mesoporous Materials*, 2008, **111**, 470-477.
26. X.-F. Wang, Y.-B. Zhang, W.-X. Zhang, W. Xue, H.-L. Zhou and X.-M. Chen, *Crystengcomm*, 2011, **13**, 4196-4201.
27. Y. Du, A. L. Thompson, N. Russell and D. O'Hare, *Dalton Transactions*, 2010, **39**, 3384-3395.
28. M. Avrami, *The Journal of Chemical Physics*, 1939, **7**, 1103-1112.
29. M. Avrami, *The Journal of Chemical Physics*, 1940, **8**, 212-224.
30. M. Avrami, *The Journal of Chemical Physics*, 1941, **9**, 177-184.
31. J. D. Hancock and J. H. Sharp, *Journal of the American Ceramic Society*, 1972, **55**, 74-77.
32. R. J. Francis, S. O'Brien, A. M. Fogg, P. S. Halasyamani, D. O'Hare, T. Loiseau and G. Ferey, *Journal of the American Chemical Society*, 1999, **121**, 1002-1015.
33. Y. Oka and K. Inoue, *Chemistry Letters*, 2004, **33**, 402-403.
34. J. X. Chen, *Chemistry Letters*, 2011, **40**, 886-887.

Chapter 7: Experimental Details

7.1 Analytical techniques

7.1.1 Powder X-ray Diffraction

Laboratory X-ray powder diffraction (XRD) data were recorded using a PANalytical X'Pert Pro diffractometer. This diffractometer operates with Cu Kα radiation ($\lambda(K\alpha_1)$ = 1.54057 Å, $\lambda(K\alpha_2)$ = 1.54433 Å, weighted average λ = 1.54178 Å) in reflection mode at 40 kV and 40 mA. Samples were mounted upon stainless steel plates, which did not produce Bragg reflections in the region of interest. Plates were rotated at 30 rpm during each scan. High resolution X-ray diffraction data was obtained using 0.02 mm Söller slits.

7.1.2 Rietveld Profile Refinement

Structural information is obtained from powder X-ray diffraction data using the Rietveld method.[1] The Rietveld method simulates a pattern based on a trial structure and refines this model against existing data using a least squares fit. Various parameters are refined to achieve an appropriate model for the data, where the similarity of the model to the data is signified by the 'goodness of fit' parameters. S, the sum of the squares, is given by:

$$S = \sum w_i \, (y_i(obs) - y_i(calc))^2 \qquad \textbf{Equation 7.1}$$

where w_i is the weighting factor, $y_i(obs)$ is the observed intensity of the data at the i^{th} step, and $y_i(calc)$ is the calculated intensity from the model at the i^{th} step.

S is minimised using the General Structure Analysis System (GSAS).[1] This computer programme uses a number of parameters to determine the quality of the refinement. Rp is the profile factor, *w*Rp is the weighted profile factor, and χ^2 is the 'goodness of fit' parameter (where χ^2 = 1 is a perfect fit). A visual comparison can also be made using GSAS by superimposing theoretical and observed data on the same plot, with a difference curve to illustrate the extent of agreement. Where Rietveld analysis gave unacceptable goodness of fit parameters, automated reflection indexing was undertaken using Celref.

7.1.3 FTIR Spectroscopy

Infrared measurements were undertaken using a Biorad FTS 6000 FTIR Spectrometer equipped with a DurSamplIR II diamond surface accessory. Data were recorded using attenuated reflectance mode over the range $4000 \geq \nu / cm^{-1} \geq 500$. In each case, 50 scans were recorded at 4 cm^{-1} resolution. Measurements using solid samples were undertaken with the sample in direct contact with a diamond surface. As a result, strong absorptions due to diamond were observed in the region $2400 \geq \nu / cm^{-1} \geq 1750$. This was verified through comparison with signals observed in a background spectrum containing data from only the diamond surface.

7.1.4 Thermogravimetric Analysis

Thermogravimetric analysis (TGA) was carried out using a Netzsch STA 409 PC instrument. Approximately 60 mg of well-ground powder sample was mounted in an alumina crucible, loaded into the internal balance and left to settle for 1 hour. An accurate value for the initial mass was recorded before beginning a measurement. Samples were heated to a chosen temperature (depending on the nature of the sample) at a rate of $5°C.min^{-1}$ under 50 $cm^3.min^{-1}$ flowing H_2/N_2 or argon gas. Where appropriate, the set-point temperature was maintained for 1 hour to ensure complete reduction of the sample.

7.1.5 Elemental Microanalysis

Elemental Microanalysis was performed by Stephen Boyer at the School of Human Sciences, London Metropolitan University. C, H, and N analyses were undertaken using a quantitative combustion technique. Metals analysis was performed with and by Dr. Gareth Williams at London Metropolitan University, using inductively coupled plasma (ICP) atomic emission spectroscopy on a Perkin-Elmer Optima 4300 DV instrument.

7.1.6 Scanning Electron Microscopy and Energy Dispersive X-ray Spectroscopy

Scanning Electron Microscopy (SEM) was performed using a JEOL JSM-840F in the Earth Sciences Department, University of Oxford. Powder samples were mounted onto 32 mm × 10 mm cylindrical metal stubs and scanned using an accelerating voltage of 200 kV. A Link Pentafet EDX detector was used for energy dispersive X-ray spectroscopy (EDX) measurements.

7.1.7 Transmission Electron Microscopy

Transmission Electron Microscopy (TEM) was performed using a JEOL 3000FX Electron Microscope at the Department of Materials, University of Oxford. All measurements were undertaken by Chengle Wang or Hannah Buckley. Solid samples were sonicated for 15 mins in ethanol solvent to disperse the particles prior to analysis, before mounting on a lacey copper grid for use in TEM analysis.

7.1.8 SQUID Magnetometry and the Curie-Weiss Law

Changes in magnetic susceptibility as a function of temperature were measured using a superconducting quantum interference device (SQUID) magnetometer. Measurements were undertaken on a Quantum design MPMS XL magnetometer. Approximately 30 mg of sample were accurately weighed into a 5 mm gelatine capsule, which was positioned inside a plastic cylindrical straw with four capsules at either side. Diamagnetic tape was used at each end to hold the sample in place. All capsules and the straw were pierced with a needle to prevent air becoming trapped. Zero field cooled and field cooled measurements were undertaken over the temperature range $10 \leq T / \mathrm{K} \leq 300$.

The Curie Law outlines the simplest type of paramagnetic behaviour, where the magnetic susceptibility is inversely proportional to temperature, T:

$$\chi = \mathrm{C} / T \qquad \textbf{Equation 7.2}$$

C is the Curie constant and is specific to the compound being studied. This is an ideal model which is not observed by the majority of species. A more applicable model for most paramagnetic behaviour includes a temperature dependent term, θ, the Weiss constant, which is incorporated into the previous equation to give the Curie-Weiss Law:

$$\chi = \mathrm{C} / (T - \theta) \qquad \textbf{Equation 7.3}$$

Again, θ, is characteristic of a substance. When the magnetic susceptibility is fitted to a Curie-Weiss dependence and the Weiss temperature is zero, the material is a paramagnet. For $\theta > 0$, it is ferromagnetic and for $\theta < 0$, it is anti-ferromagnetic. Experimentally determined Weiss temperatures often deviate significantly from the expected $-T_N$ due to an assumption that the molecular field on one sub-lattice depends only on the magnetisation of the other sub-lattice.

7.1.9 Raman Spectroscopy

Raman spectroscopy was performed using a Dilor LabRam 300 instrument, which incorporated a He-Ne laser (632.81 nm). Data were recorded over the range $50 \leq \nu / \mathrm{cm}^{-1} \leq 1500$, at 50 × magnification. The spectrometer was calibrated against a silicon standard with an intense absorption at 520.7 cm^{-1}.

7.1.10 In situ *X-ray Diffraction*

The majority of *in situ* XRD experiments described in this thesis were undertaken using Beamline I12 at the Diamond Light Source. Chapter 2 contains a detailed description of the equipment used to undertake studies on I12. EDXRD measurements employed white-beam with energy range *ca.* $50 \leq E / \mathrm{keV} \leq 150$, whereas angular-dispersive XRD was undertaken at an appropriate specified energy, typically E = *ca.* 53 keV or 83 keV. Detailed background information about *in situ* XRD studies and Beamline I12 is provided in Chapters 1 and 2. In both white-beam and monochromatic modes, sample positions in the beam path were optimised using a capillary of NIST-standard LaB_6 or CeO_2 mounted centrally within the Oxford Diamond *In Situ* Cell (ODISC).[3] XRD scans were undertaken as the sample stage was shifted laterally and vertically with respect to the direction of the X-ray beam, and the position of optimum diffraction from the capillary was maintained

for the duration of the experiment. A darkfield calibration scan was undertaken following each sample measurement when operating in angular-dispersive mode.

During experimentation in energy-dispersive mode, data from each of the twenty-three detector elements are recorded as 4096 energy values, the sequence of which is only approximately the same for all elements. The same is also true of the twenty-three collimator angles. In order to account for this, the NEXUS data file for each experiment contains an array of calibrated *q* values for each element. This enables the intensity data from all elements to be summed against a uniform set of *q* values, using cubic spline interpolation.

In situ EDXRD experiments were also undertaken using Beamline F3 at Hasylab, of the DORIS synchrotron at DESY (Deutsches Elektronen-Synchrotron, Hamburg). The white-beam energy range accessible from the bending magnet on this beamline is *ca.* $15 \leq E \,/\, \text{keV} \leq 65$. LDH intercalation reactions were carried out in borosilicate tubes using the Oxford-Daresbury cell.[2] MOF synthesis was undertaken using steel autoclaves in the hydrothermal configuration of ODISC. The angle of the EDXRD detector was shifted in order to probe the appropriate *d*-spacing range.

In order to calibrate the value of *q* or θ, a standard sample of ettringite or LaB_6 was measured prior to each set of beamtime experiments. A rearrangement of Bragg's Law, followed by substitution of the fundamental constants for real values gives:

$$E = \frac{1}{d}\left(\frac{6.19926}{\sin\theta}\right) \quad \text{(keV)} \qquad \textbf{Equation 7.4}$$

where *E* is in keV, *d* is in Å, and the value of 6.19926 is equal to hc/λ. A subsequent plot of *E vs.* $1/d$ facilitates accurate calculation of θ.

7.1.11 Solid-state reaction kinetics

For integrated intensity analysis, the Xming peak profiling program was employed with a series of scripts written by Dr. Jonathan Burley at the Laboratory of Biophysics and Surface Analysis, University of Nottingham. A Gaussian fitting routine was applied to experimentally observed Bragg reflections to yield values for reflection position, intensity, and width. Data obtained from Beamline F3 at Hasylab were analysed using the

'F3 Tool', a custom-made software package provided by DESY. Typically, reactions which take place in the solid-state are monitored using the change in intensity of Bragg reflections of the materials being studied. Where appropriate therefore, integrated intensity values were converted to the extent of reaction parameter, α. The extent of reaction, α, at a specific time point, *t*, is defined as $\alpha(t) = I_{(hkl)}(t) / I_{(hkl)}^{max}(t)$, where $I_{(hkl)}$ is the integrated intensity of a specific reflection at time *t*, and $I_{(hkl)}^{max}$ is the maximum intensity of that reflection.

Several models exist for the determination of chemical reaction pathways.[4, 5] A common approach for kinetic analysis of solid-state reactions is that derived by Avrami and Erofe'ev. The expression for Avrami-Erofe'ev kinetics has been applied to wide variety of solid-state processes, such as crystallisation and intercalation reactions,[6, 7] and has recently been extended to include separate terms for nucleation and growth.[8] The relationship between α and *t* takes the form:

$$\alpha = 1 - \exp\{-[k(t - t_0)]^n\} \qquad \textbf{Equation 7.5}$$

where t_0 is the induction time for the reaction and *k* is the rate constant. The parameter *n*, referred to as the Avrami exponent, is related to terms describing both nucleation (β) and growth (λ). Hulbert has proposed a series of expected values of *n* for various crystallisation environments, including 1D, 2D, and 3D growth ($1 \leq \lambda \leq 3$) and instantaneous ($\beta = 0$), constant ($\beta = 0$), and deceleratory ($0 \leq \beta \leq 1$) nucleation.[9]

The Sharp-Hancock technique provides a method of obtaining *n*.[10] If a logarithm of the Avrami-Erofe'ev equation is taken, following rearrangement the expression becomes:

$$\ln(\ln(1 - \alpha)) = n\ln k - n\ln(t - t_0) \qquad \textbf{Equation 7.6}$$

As such, a plot of $\ln(\ln(1 - \alpha))$ *vs.* $\ln(t - t_0)$ allows the elucidation of *n* using the gradient, and *k* using the intercept.

7.2 Experimental procedures for Chapter 2

7.2.1Equipment providers

The furnace shell and heating set-up were assembled using commercially available components from Precision Control Systems Inc. & Research Inc., USA. The ChambIR® Model E4 Infrared Heating System uses aluminium elliptical reflectors to IR radiation onto a cylindrical sample in the furnace. Water is circulated through the furnace *via* a Thermal Exchange Ltd. LR6U80-W-CC-5 continuous water-cooling unit.

Glassy carbon tubes were purchased from HTW Hochtemperatur-Werkstoffe GmbH, Germany. Silicon carbide tubes were purchased from Ortech Inc., USA. Recrystallized alumina crucibles (99.7% Al_2O_3) were purchased from NETZSCH-Gerätebau GmbH, UK Branch. High-coercivity, PTFE-coated stirrer bars with samarium cobalt rare-earth magnets were puchased from V&P Scientific Inc. The temperature of the furnace is controlled by a programmable temperature controller, Eurotherm Model 3504, which is connected to a single phase thyristor unit, Eurotherm Model 7100A (Invensys Eurotherm Ltd., USA). The low-temperature culture tube configuration incorporated 12 mm OD culture tubes which were purchased from DURAN®. PTFE-lined magnetic wing stirrers positioned in the tubes were purchased from VWR International.

The ODISC mounting disks, centring tubes, baseplate and support bracket, culture tube ferrule, PTFE autoclave liners, and magnetic stirrer head were constructed by Charles Evans at the University of Oxford Physical and Theoretical Chemistry Laboratory (PTCL) Workshop.

7.2.2 Gold coating

Gold coating was undertaken on the four separate reflectors by Richard Makin in the Thin Films Facility at the University of Oxford, using the following procedure:

"The individual reflector segments were cleaned using an ultrasonic bath of acetone for 20 minutes followed by an ultrasonic bath of IPA for 20 minutes. The components were wiped clean using optical tissue and any remaining dust removed using a CO_2 SNO-clean. After placing in a Leybold L560 coating plant, plasma glow discharge (oxygen plasma) was implemented for 15 minutes at a vacuum of 5×10^{-2} mBar. At 3×10^{-6}

mBar, the thermal evaporation technique was employed to coat the reflector surfaces with chromium to a thickness of 20 nm at evaporation rate 0.1 $nm.s^{-1}$. The surfaces were then coated with gold using thermal evaporation to a thickness of 250 nm at evaporation rate 2 $nm.s^{-1}$. Substrates were rotated inside the chamber to ensure a uniform coating."

7.2.3 Calibration reactions

EDXRD data quality tests were undertaken using a crystalline sample of rutile TiO_2 ($\geq$ 99.9%), purchased from Aldrich. A small amount of anatase TiO_2 impurity in the sample was identified by several low-intensity reflections in the diffraction data, most notably at q = 1.80 $Å^{-1}$ and q = 2.65 $Å^{-1}$.

Temperature calibration scans were undertaken using a sample of Bi_2O_3 ($\geq$ 99.99%), purchased from Alfa-Aesar. The calibration run was undertaken using the high temperature set-up, with 4 g of Bi_2O_3 loaded inside the 11 × 14 mm (ID × OD) alumina crucible, which was positioned in a silicon carbide tube inside the furnace.

7.3 Experimental procedures for Chapter 3

7.3.1 Starting materials

Gibbsite was supplied by Alcoa and was subject to ball-milling using the procedure as follows: 40 g of gibbsite were added to a RETSCH® PM100 ball mill and ground at 100 % speed with clockwise rotation for 45 mins, followed by anticlockwise rotation for 45 mins. Metal nitrate salts were obtained from Alfa Aesar (≥ 98%) and were used as supplied.

7.3.2 MM'Al$_8$-NO$_3$ LDH synthesis

Hydrothermal reactions were undertaken in polytetrafluorethylene (PTFE) lined stainless steel autoclaves. 1 g of activated $Al(OH)_3$ was reacted with 5 mL of a 10 M aqueous solution of each of two metal nitrate hydrates. Autoclaves were heated in a muffle furnace controlled by a Eurotherm device. The reagents were treated hydrothermally at 150 °C for 48 hours in the case of activated gibbsite starting material, and at 225 °C for 110 hours in the case of activated bayerite. Following controlled cooling to room temperature at 5 °C.min^{-1}, the products were vacuum filtered, washed with water, and then dried in air for 2 hours to afford the product powders.

Syntheses of the metal-tuned LDHs and the four-metal LDH were undertaken with different volume ratios of transition metal nitrate salts. The overall solution volume in each case was maintained at 10 mL. The starting materials and observed ratios for the ternary systems are provided in Table 7.1. In the case where an accurate small quantity of nickel nitrate was required, an appropriate 1 mL pipette was used.

Table 7.1: Synthesis conditions for metal-tuned LDHs.

Metal ions		Volume M nitrate solution / mL	Volume M' nitrate solution / mL	Observed M : M' ratio
M	**M'**			
Co	Zn	8.0	2.0	77.6 : 22.4
Co	Zn	6.0	4.0	56.2 : 43.8
Co	Zn	5.0	5.0	51.1 : 48.9
Co	Zn	4.5	5.5	44.0 : 56.0
Co	Zn	4.0	6.0	38.6 : 61.4
Co	Zn	2.0	8.0	17.8 : 82.2
Ni	Zn	5.0	5.0	97.3 : 2.7
Ni	Zn	1.5	8.5	84.9 : 15.1
Ni	Zn	1.0	9.0	68.2 : 21.8
Ni	Zn	0.8	9.2	63.9 : 26.1
Ni	Zn	0.6	9.4	56.3 : 43.7
Ni	Zn	0.5	9.5	45.4 : 54.6
Ni	Zn	0.3	9.7	38.5 : 61.5
Co	Ni	5.0	5.0	97.2 : 2.8
Co	Ni	8.1	1.9	84.2 : 15.8
Co	Ni	9.2	0.8	62.0 : 28.0
Co	Ni	9.4	0.6	56.1 : 43.9
Co	Ni	9.5	0.5	53.7 : 46.3
Co	Ni	9.6	0.4	47.7 : 52.3
Co	Ni	9.7	0.3	40.3 : 59.7
Co	Ni	9.8	0.2	37.8 : 62.2

7.3.3 Intercalation reactions

The sodium salts of all organic intercalates were obtained from Aldrich (≥ 96%). Intercalation experiments were undertaken using glass ampoules, and the reaction mixture stirred using a magnetic teflon-lined stirrer bar located within the ampoule. Reactions that required heating were carried out in an oil bath atop a stirrer-hotplate. In each case, 0.2 g of the LDH was added to 10 mL of water containing a five- or ten-fold excess of the guest ions and the mixtures stirred for periods of 2 – 30 hours. A list of reaction conditions is provided in Table 7.2. Following reaction, the LDH product was recovered using vacuum filtration and washed with deionized water.

Table 7.2: Experimental conditions for LDH intercalation reactions.

Guest	**Reaction conditions (Guest excess, Temp. / ºC, Time /h)**		
	$Co_xZn_{2-x}Al_8$-NO_3	$Ni_xZn_{2-x}Al_8$-NO_3	$Co_xNi_{2-x}Al_8$-NO_3.
Fumarate	(5:1, RT, 24)	(5:1, RT, 24)	(5:1, RT, 24)
Succinate	(10:1, RT, 24)	(10:1, RT, 24)	(10:1, RT, 24)
Terephthalate	(10:1, RT, 4)	(10:1, RT, 4)	(10:1, RT, 4)
2-napthalenesulfonate	(10:1, 60, 30)	(10:1, 60, 30)	(10:1, 60, 30)
Phthalate	(5:1, RT, 2)	(5:1, RT, 4)	(5:1, RT, 4)

7.3.4 In situ *EDXRD*

EDXRD measurements of LDH reactions carried out at Beamline I12 of the Diamond Light Source employed the shifted-detector configuration detailed in Chapter 3. Intercalation experiments were undertaken using a refurbished version of the Oxford-Daresbury hydrothermal cell.[2] 0.2 g of starting material host LDH was stirred in 12 mL water at room temperature and diffraction measurements started. 55 second scans were recorded at 60 second intervals. After a few minutes, a solution containing a ten-fold excess of phthalate was added drop-wise (at a rate of 9.92 cc.hour^{-1} using a Semat International Razel syringe pump) to the reaction mixture and changes in the diffraction data were monitored. The X-ray beam size for all data sets was 0.3 × 0.3 mm, which was

applied using the positions of the entry slits. The data obtained from detector Element 2 were selected for final analysis.

EDXRD measurements of LDH reactions carried out at Beamline F3, Hasylab were also undertaken using the refurbished version of the Oxford-Daresbury hydrothermal cell. 0.5 g of starting material host LDH was stirred in 15 mL water at room temperature and a 5 : 1 excess of an aqueous solution of the guest was added. 60 second scans were undertaken until the reaction was deemed to have reached completion. The angle of the detector was shifted to $2\theta = ca.\ 2.1°$.

7.3.5 In situ *angular-dispersive XRD*

LDH intercalation reactions were monitored using angular-dispersive XRD at Beamline I12, Diamond Light Source. ODISC was employed in the low-temperature configuration. 0.5 g of the LDH host were stirred in 15 mL deionised water at room temperature inside a glassy carbon tube. 10 mL of an aqueous solution containing a five-fold excess of guest anions were added dropwise (at a rate of 6.35 cc.hour^{-1} using a Semat International Razel syringe pump). Images from the 2D detector were recorded with 4 second exposure at 30 second intervals. The energy of the monochromated beam was 53.2442 keV (λ = 0.23286 Å) and the detector was positioned 2501.440 mm from the sample. The X-ray beam size was 0.75 × 0.75 mm.

The LDH synthesis reaction was undertaken using ODISC in the hydrothermal configuration. The temperature of the sample autoclave, recorded using a thermocouple positioned between the glassy carbon sheath and the autoclave, was raised to 250 °C at a rate of 30 °C.min^{-1} and held at that temperature for 102 mins. Sample cooling was then undertaken at a rate of 2 °C.min^{-1} to room temperature. Images from the 2D Pixium detector were recorded with 4 second exposure at 60 second intervals. The X-ray beam size was 0.5 × 0.5 mm.

7.3.6 Crystal growth analysis

The Scherrer equation was used to model sample crystallinity as a function of time for the LDH synthesis reaction probed *in situ*. The equation takes the form:

$$\tau = \frac{K\lambda}{\cos\theta\sqrt{\beta_{obs}^2 - \beta_{std}^2}} \qquad \textbf{Equation 7.7}$$

where τ is the mean crystallite size, K is the shape factor (here assigned 0.89), λ is the X-ray wavelength, β_{obs} is the observed FWHM, β_{std} is the FWHM calculated from a standard, and θ is the Bragg angle. Below is the angular-dispersive X-ray diffraction data for a sample of LaB_6, which was used as the standard for particle size calculation.

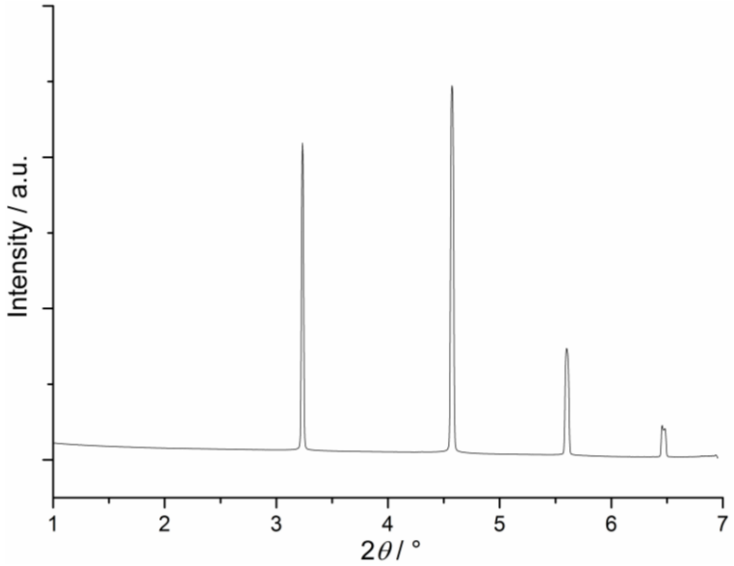

Figure 7.1: Angular-dispersive X-ray diffraction data for a sample of NIST-standard LaB_6.

7.4 Experimental Procedures for Chapter 4

7.4.1 Starting materials

Metal oxide starting materials were purchased from Alfa Aesar or Sigma Alrich with the following purities: Bi_2O_3 (99.999%), TiO_2 (99.99%), V_2O_3 (99.7 %), Cr_2O_3 (99.9 %), Fe_2O_3 (99.99 %), Co_3O_4 (99.99 %), Ga_2O_3 (99.99 %), Na_2SO_4 (99.0 %), K_2SO_4 (99.0 %), and RbCl (99.0 %).

7.4.2 Aurivillius phase synthesis

In the preparation of samples for molten salt synthesis (MSS), stoichiometric amounts of starting material oxides were ground with a seven-fold excess of a combination of solid K_2SO_4/Na_2SO_4 ionic salts in an agate pestle and mortar to produce a homogeneous mixture. The respective masses corresponded to 2 g of the product material. K_2SO_4/Na_2SO_4 were present in a 1 : 1 ratio. Other salts were used as specified. The mixture was placed in an alumina crucible and heated to a specified temperature above the melting point of the respective salt. Samples were heated at 5 °C.min^{-1} and cooled at 2 °C.min^{-1} unless otherwise specified. Following cooling to room temperature, samples were washed with warm deionised water, vacuum filtered, and dried in air for 2 hours. Detailed synthetic parameters for MSS reactions are provided in the relevant sections in Chapter 4.

For reactions undertaken under ceramic synthesis conditions, stoichiometric amounts of starting material oxides were ground using an agate pestle and mortar. This step was particularly important for ceramic synthesis reactions to reduce particle size and achieve a homogeneous mixture of reagents. Following grinding, the reaction mixture was pressed into a pellet of approximately 2 g mass using a 13 mm die at 5 tonnes pressure. The pellet was placed in an alumina crucible and heated to the required temperature. Samples were heated in a muffle furnace at 5 °C.min^{-1} and cooled at 2 °C.min^{-1} unless otherwise specified. Detailed synthetic parameters for ceramic reactions are provided in the relevant sections in Chapter 4.

7.5 Experimental Procedures for Chapter 5

7.5.1 Quenching experiments

Samples were prepared as described in Section 7.4.2. Crucibles containing the reagents were heated to the desired temperature at 5 °C.min^{-1} using a muffle furnace. Immediately on reaching the appropriate quench temperature, the crucible was removed from the oven using long-handled tongs and placed in a Dewar containing liquid nitrogen. The Dewar was left until all liquid nitrogen had evaporated and the products were worked up as described in Section 7.4.2.

7.5.2 In situ *XRD using Beamline I12*

ODISC in the high-temperature configuration was employed to undertake all *in situ* XRD experiments with Aurivillius phases. Stoichiometric quantities of starting material oxides were mixed with a seven-fold excess of just Na_2SO_4. This salt was chosen in preference to the K_2SO_4/Na_2SO_4 eutectic for *in situ* studies due to its well-defined melting point and to minimise the number of crystalline reflections from the flux. Results from *in situ* and *ex situ* experiments indicated that this change in molten salt had no effect on the mechanism or products of Aurivillius phase synthesis. The overall mass of the starting material mixture was greater than that used for laboratory studies to ensure the sample remained in the path of the X-ray beam throughout experimentation. Approximately 4 g of sample was loaded and packed down into an alumina crucible, which was positioned in a silicon carbide tube in the furnace.

EDXRD scans were recorded for 55 seconds at 60 second intervals. During angular-dispersive experimentation, images from the 2D detector were recorded with 4 second exposure at 30 second intervals. The energy of the monochromated beam was 83.5136 keV (λ = 0.14846 Å) and the detector was positioned 900.09 mm from the sample. The X-ray beam size for all data sets was 0.3 × 0.3 mm, which was applied using the positions of the entry slits. Diffraction scans were measured with 4 second exposure at 30 second intervals. In the case of angular-dispersive studies, the silicon carbide tube was raised within the furnace to a height above the X-ray beam path to eliminate peaks due to the crystalline tube. The temperature of the reacting mixture was accurately measured using a thermocouple positioned in contact with the powder sample.

7.6 Experimental Procedures for Chapter 6

7.6.1 General procedures for resin-assisted synthesis

Sulfonated styrene-divinylbenzene (styrene-DVB) beads were purchased in the Na^+ form (DOWEX® MARATHON® C) from Sigma Aldrich. The beads were converted to the Co^{2+} metal-exchanged form by treatment with $CoCl_2$. 6 g of styrene-DVB beads were added to 30 mL of a saturated aqueous solution of $CoCl_2$ and stirred for 3 hours at room temperature. The mixture was vacuum filtered to isolate the beads, and the resulting

cobalt-exchanged beads were washed with deionised water and dried in air. This procedure was repeated a further four times to ensure significant metal ion exchange.

The beads were then used in place of typical metal salt precursors in a variety of solvothermal syntheses.

7.6.2 In situ *XRD studies of resin-assisted synthesis of* $(H_2NMe_2)_2[Co_3(BDC)_4]\cdot y$*DMF*

0.4 g 1,4-BDC were dissolved in 12 ml DMF. 4 mL methanol and 0.5 g cobalt-exchanged resin beads were added to the solution and the mixture placed in a PTFE liner and sealed inside a stainless-steel autoclave.

During *in situ* angular-dispersive XRD measurements, images from the 2D detector were recorded with 4 second exposure at 30 second intervals. The energy of the monochromated beam was 53.2442 keV (λ = 0.23286 Å) and the detector was positioned 2501.440 mm from the sample. The X-ray beam size was 0.5 × 0.5 mm, which was applied using the positions of the entry slits.

7.6.3 In situ *XRD studies of resin-assisted synthesis of Co(DMF)(NDC)*

0.5 g cobalt-exchanged resin beads were added to a solution containing 0.4 g 2,6-naphthalenedicarboxylate dissolved in 16 mL DMF. The mixture was placed in a PTFE liner and sealed inside a stainless-steel autoclave.

During *in situ* angular-dispersive XRD measurements, images from the 2D detector were recorded with 4 second exposure at 30 second intervals. The energy of the monochromated beam was 53.2442 keV (λ = 0.23286 Å) and the detector was positioned 2501.440 mm from the sample. The X-ray beam size was 0.5 × 0.5 mm, which was applied using the positions of the entry slits.

7.6.4 In situ *EDXRD studies of attempted metal-salt synthesis of Co(DMF)(NDC)*

0.5 g 2,6-naphthalenedicarboxylate were dissolved in 6 mL DMF. The solution was added to another solution containing 1.2 g $Co(NO_3)_2\cdot 6H_2O$ dissolved in 8 mL DMF, and

the overall mixture placed in a PTFE liner and sealed inside a stainless-steel autoclave. The autoclave was heated to 180 °C. Facilities on Beamline F3 at the DORIS synchrotron were employed to undertake an *in situ* EDXRD study on the reaction. 60 second scans were undertaken at 60 second intervals for 1 hour. The angle of the detector was shifted to $2\theta = ca.\ 1.4°$.

7.7 References

1. H. M. Rietveld, *Journal of Applied Crystallography*, 1969, **2**, 65-71.
2. J. S. O. Evans, R. J. Francis, D. O'Hare, S. J. Price, S. M. Clark, J. Flaherty, J. Gordon, A. Nield and C. C. Tang, *Review of Scientific Instruments*, 1995, **66**, 2442-2445.
3. S. J. Moorhouse, N. Vranjes, A. Jupe, M. Drakopoulos and D. O'Hare, *Review of Scientific Instruments*, 2012, **83**, 084101-084108.
4. A. Khawam and D. R. Flanagan, *Journal of Pharmaceutical Sciences*, 2006, **95**, 472-498.
5. A. Khawam and D. R. Flanagan, *Journal of Physical Chemistry B*, 2006, **110**, 17315-17328.
6. A. M. Fogg and D. O'Hare, *Chemistry of Materials*, 1999, **11**, 1771-1775.
7. A. M. Fogg, S. J. Price, R. J. Francis, S. O'Brien and D. O'Hare, *Journal of Materials Chemistry*, 2000, **10**, 2355-2357.
8. F. Millange, R. El Osta, M. E. Medina and R. I. Walton, *Crystengcomm*, 2011, **13**, 103-108.
9. S. F. Hulbert, *Journal of the British Ceramic Society*, 1969, **6**.
10. J. D. Hancock and J. H. Sharp, *Journal of the American Ceramic Society*, 1972, **55**, 74-77.

Appendix A

ODISC Supplementary Information

A.1 Furnace controller circuit diagrams

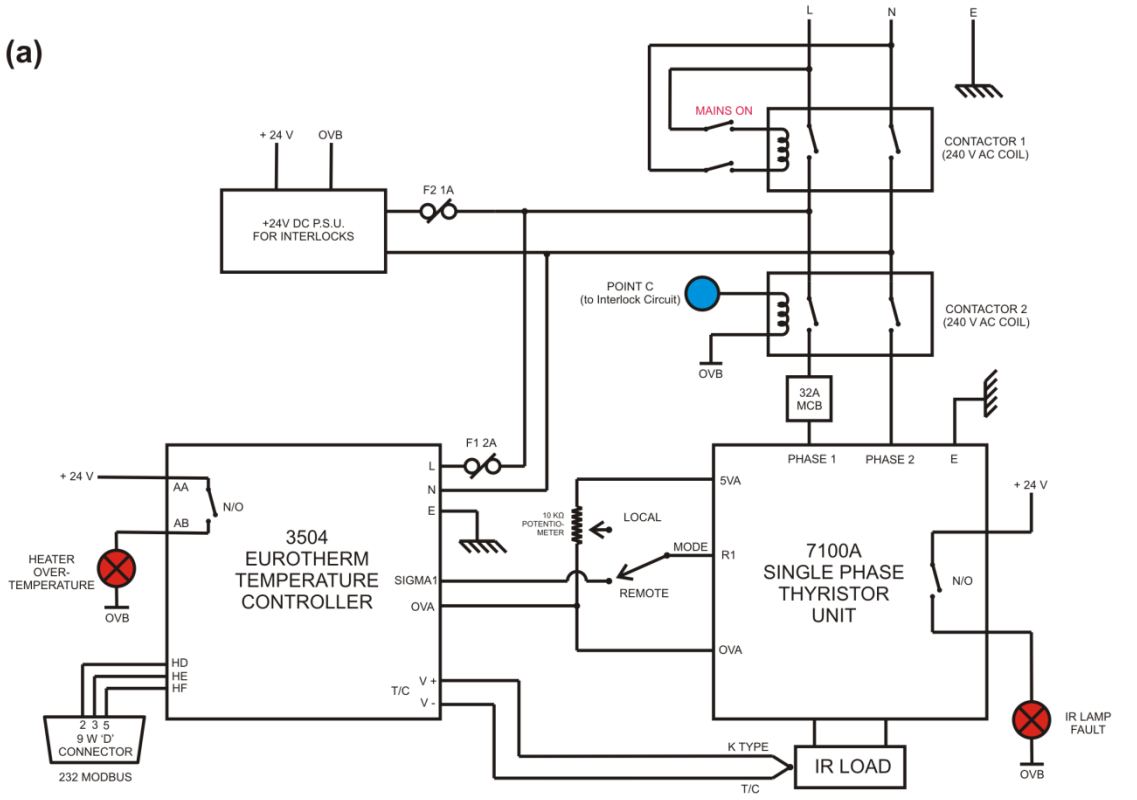

A.2 Proportional Integral Differential (PID) parameters for ODISC configurations

Configuration	Proportional	Integral	Derivative	Max. output
Low-temperature	20	360	60	8%
High-temperature	47.6	34	6	80%
Hydrothermal	142.2	70	12	9.5%
Culture-tube	86.2	50	8	15%

A.3 Metal-sheet configuration for rapid heating

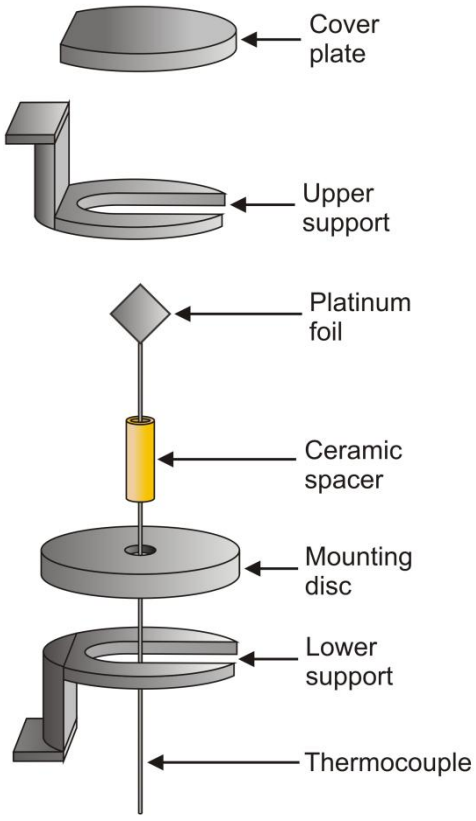

Note: the thermocouple was spot welded to the platinum foil and lowered into the ceramic spacer during experimentation. This was to minimise the effect of direct IR heating of the thermocouple, thus improving the accuracy of temperature measurement.

A.4 PID parameters for slow cooling with metal-sheet configuration

Temperature	Proportional	Integral	Derivative	Max. output
500 °C	584.6	11	2	80%
1000 °C	664.1	9	1	80%

A.5 Feasibility test for sample heating in high-temperature configuration

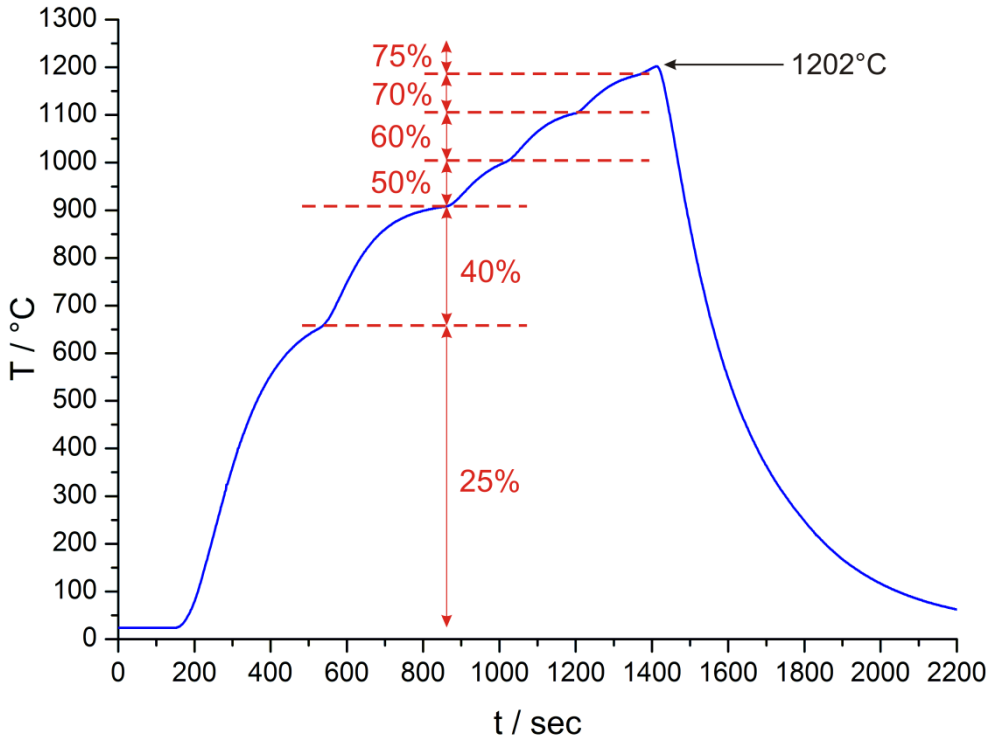

Note: The percentage figures labelled on the temperature profile represent the manually-controlled power output of the furnace.

Appendix B

Elemental Analysis Data

B.1 Elemental analysis details

Elemental analysis data provided in the following sections were obtained using a quantitative combustion technique (for elements C, H, and N) undertaken by Stephen Boyer at the School of Human Sciences, London Metropolitan University, or from energy dispersive X-ray spectroscopy (EDX) measurements (for elements Al, S, Ti, V, Cr, Fe, Co, Ni, Cu, Zn, Ga, Bi) using a JEOL JSM-840F scanning electron microscope in the Earth Sciences Department, University of Oxford.

B.2 Elemental analysis data for Chapter 3

Table B.1: Elemental analysis data for the ternary $[M_xM'_{2-x}Al_8(OH)_{24}](NO_3)_4{\cdot}yH_2O$ LDHs

Formula	Elemental analysis	
	Observed %	Calculated %
$\mathbf{[CoZnAl_8(OH)_{24}](NO_3)_4{\cdot}5H_2O}$	Co: 5.62 Zn: 5.38 Al: 20.60 N: 4.69 H: 2.82	Co: 5.42 Zn: 6.01 Al: 19.86 N: 5.16 H: 3.15
$\mathbf{[Ni_{1.9}Zn_{0.1}Al_8(OH)_{24}](NO_3)_4{\cdot}5H_2O}$	Ni: 10.38 Zn: 0.29 Al: 21.33 N: 5.44 H: 2.80	Ni: 10.32 Zn: 0.61 Al: 19.98 N: 5.19 H: 3.17
$\mathbf{[Co_{0.1}Ni_{1.9}Al_8(OH)_{24}](NO_3)_4{\cdot}4H_2O}$	Ni: 9.88 Co: 0.43 Al: 20.23 N: 5.47 H: 2.81	Ni: 10.51 Co: 0.56 Al: 20.33 N: 5.28 H: 3.04

Table B.2: Elemental analysis data for the characterisable ternary copper-containing LDHs

Formula	Elemental analysis	
	Observed %	Calculated %
$\mathbf{[Co_{1.0}Cu_{1.0}Al_8(OH)_{24}](NO_3)_4 \cdot 7H_2O + \mathit{y}[Cu_2(OH)_3NO_3]}$	Co: 4.23 Cu: 13.21 Al: 18.58 N: 5.15 H: 2.82	Co: 5.26 Cu: 5.67 Al: 19.26 N: 5.00 H: 3.41
$\mathbf{[Cu_{1.0}Zn_{1.0}Al_8(OH)_{24}](NO_3)_4 \cdot 8H_2O + \mathit{y}[Cu_2(OH)_3NO_3]}$	Cu: 12.14 Zn: 4.82 Al: 16.89 N: 5.03 H: 3.32	Cu: 5.55 Zn: 5.71 Al: 18.85 N: 4.89 H: 3.52

Table B.3: Elemental analysis data for the $[Co_{0.5}Ni_{1.1}Zn_{0.4}Al_8(OH)_{24}](NO_3)_4 \cdot 2H_2O$ LDH

Formula	Elemental analysis	
	Observed %	Calculated %
$\mathbf{[Co_{0.5}Ni_{1.1}Zn_{0.4}Al_8(OH)_{24}](NO_3)_4 \cdot 2H_2O}$	Co: 2.87 Ni: 6.41 Zn: 2.50 Al: 21.24 N: 5.44 H: 2.81	Co: 2.87 Ni: 6.28 Zn: 2.54 Al: 20.99 N: 5.45 H: 2.74

Table B.4: Elemental analysis data for the organic intercalates of $[CoZnAl_8(OH)_{24}](NO_3)_4{\cdot}yH_2O$

Formula and Guest	Elemental analysis	
	Observed %	Calculated %
$[CoZnAl_8(OH)_{24}](C_4H_4O_4)_{1.7}(CO_3)_{0.3}{\cdot}6H_2O$ Succinate	Co: 5.30 Zn: 5.36 Al: 22.07 N: 0.00 H: 3.55 C: 7.78	Co: 5.50 Zn: 6.10 Al: 20.14 N: 0.00 H: 4.03 C: 7.96
$[CoZnAl_8(OH)_{24}](C_4H_2O_4)_{1.5}(CO_3)_{0.5}{\cdot}4.5H_2O$ Fumarate	Co: 6.34 Zn: 6.16 Al: 20.88 N: 0.00 H: 3.58 C: 7.64	Co: 5.72 Zn: 6.35 Al: 20.95 N: 0.00 H: 3.52 C: 7.58
$[CoZnAl_8(OH)_{24}](C_8H_4O_4)_{1.6}(CO_3)_{0.4}{\cdot}10H_2O$ Phthalate	Co:5.10 Zn: 4.68 Al: 18.06 N: 0.00 H: 4.48 C: 12.56	Co: 4.85 Zn: 5.38 Al: 17.76 N: 0.00 H: 4.18 C: 13.05
$[CoZnAl_8(OH)_{24}](C_8H_4O_4)_{1.7}(CO_3)_{0.3}{\cdot}9.5H_2O$ Terephthalate	Co: 6.02 Zn: 6.06 Al: 17.72 N: 0.00 H: 4.14 C: 13.72	Co: 4.84 Zn: 5.38 Al: 17.74 N: 0.00 H: 4.13 C: 13.72
$[CoZnAl_8(OH)_{24}](C_{10}H_7SO_3)_3(CO_3)_{0.5}{\cdot}8H_2O$ 2-napthalenesulfonate	Co: 4.90 Zn: 4.35 Al: 13.89 S: 5.39 N: 0.00 H: 4.00 C: 23.84	Co: 3.82 Zn: 4.23 Al: 13.98 S: 6.23 N: 0.00 H: 3.98 C: 23.72

Table B.5: Elemental analysis data for the organic intercalates of $[Ni_xZn_{2-x}Al_8(OH)_{24}](NO_3)_4{\cdot}yH_2O$

Formula and Guest	Elemental analysis	
	Observed %	Calculated %
$[Ni_{1.9}Zn_{0.1}Al_8(OH)_{24}](C_4H_4O_4)_{1.7}(CO_3)_{0.3}{\cdot}7H_2O$ Succinate	Ni: 9.99 Zn: 0.18 Al: 19.78 N: 0.00 H: 4.26 C: 7.82	Ni: 10.29 Zn: 0.60 Al: 19.92 N: 0.00 H: 4.17 C: 7.87
$[Ni_{1.9}Zn_{0.1}Al_8(OH)_{24}](C_4H_2O_4)_{1.8}(CO_3)_{0.2}{\cdot}8H_2O$ Fumarate	Ni: 10.60 Zn: 0.33 Al: 19.51 N: 0.00 H: 3.90 C: 7.96	Ni: 10.11 Zn: 0.59 Al: 19.56 N: 0.00 H: 3.98 C: 8.05
$[Ni_{1.1}Zn_{0.9}Al_8(OH)_{24}](C_8H_4O_4)_{1.6}(CO_3)_{0.4}{\cdot}10H_2O$ Phthalate	Ni: 5.80 Zn: 4.46 Al: 18.03 N: 0.00 H: 4.50 C: 12.70	Ni: 5.32 Zn: 4.85 Al: 17.78 N: 0.00 H: 4.18 C: 13.06
$[Ni_{1.9}Zn_{0.1}Al_8(OH)_{24}](C_8H_4O_4)_{1.8}(CO_3)_{0.2}{\cdot}10.5H_2O$ Terephthalate	Ni: 9.75 Zn: 0.24 Al: 17.54 N: 0.00 H: 4.15 C: 14.05	Ni: 9.00 Zn: 0.53 Al: 17.43 N: 0.00 H: 4.25 C: 14.16
$[Ni_{1.9}Zn_{0.1}Al_8(OH)_{24}](C_{10}H_7SO_3)_{2.9}(CO_3)_{0.55}{\cdot}7H_2O$ 2-napthalenesulfonate	Ni: 7.16 Zn: 0.10 Al: 14.70 S: 5.16 N: 0.00 H: 3.53 C:23.10	Ni: 7.42 Zn: 0.44 Al: 14.37 S: 6.19 N: 0.00 H: 3.89 C: 23.52

Table B.6: Elemental analysis data for the organic intercalates of $[Co_xNi_{2-x}Al_8(OH)_{24}](NO_3)_4{\cdot}yH_2O$

Formula and Guest	Elemental analysis	
	Observed %	Calculated %
$[Co_{0.1}Ni_{1.9}Al_8(OH)_{24}](C_4H_4O_4)_{1.9}(CO_3)_{0.1}{\cdot}10.5H_2O$ Succinate	Co: 0.24 Ni: 8.68 Al: 18.75 N: 0.00 H: 4.58 C:7.99	Co: 0.51 Ni: 9.64 Al: 18.65 N: 0.00 H: 4.58 C: 7.99
$[Co_{0.1}Ni_{1.9}Al_8(OH)_{24}](C_4H_2O_4)_{1.8}(CO_3)_{0.2}{\cdot}7H_2O$ Fumarate	Co: 0.32 Ni: 11.60 Al: 19.90 N: 0.00 H: 3.84 C: 8.15	Co: 0.54 Ni: 10.28 Al: 19.90 N: 0.00 H: 3.87 C: 8.19
$[Co_{1.2}Ni_{0.8}Al_8(OH)_{24}](C_8H_4O_4)_{1.6}(CO_3)_{0.4}{\cdot}10H_2O$ Phthalate	Co: 5.05 Ni: 3.43 Al: 18.33 N: 0.00 H: 4.45 C: 12.63	Co: 5.85 Ni: 3.89 Al: 17.86 N: 0.00 H: 4.20 C: 13.12
$[Co_{0.1}Ni_{1.9}Al_8(OH)_{24}](C_8H_4O_4)_{1.9}(CO_3)_{0.1}{\cdot}11H_2O$ Terephthalate	Co: 0.24 Ni: 8.42 Al: 17.89 N: 0.00 H: 4.26 C: 14.63	Co: 0.47 Ni: 8.87 Al: 17.17 N: 0.00 H: 4.30 C: 14.61
$[Co_{0.1}Ni_{1.9}Al_8(OH)_{24}](C_{10}H_7SO_3)_{2.9}(CO_3)_{0.55}{\cdot}7H_2O$ 2-napthalenesulfonate	Co: 0.21 Ni: 7.55 Al: 14.42 S: 6.15 N: 0.00 H: 3.53 C: 23.65	Co: 0.39 Ni: 7.43 Al: 14.38 S: 6.19 N: 0.00 H: 3.91 C: 23.64

B.3 Elemental analysis data for Chapter 4

For EDX studies with Aurivillius phases, elemental ratios were calculated with respect to a pure sample of $Bi_5Ti_3FeO_{15}$, for which the elemental ratios are known.

Table B.7: EDX data for the $Bi_5Ti_3Fe_{1-x}M_xO_{15}$ (M = V, Cr, Co, Ga) series.

Chemical Formula	Elemental % from EDX	
	Observed	Calculated
$Bi_5Ti_3Fe_{0.9}V_{0.1}O_{15}$*	Ti: 9.41 V: 0.41 Fe: 3.26	Ti: 9.68 V: 0.34 Fe: 3.38
$Bi_5Ti_3Fe_{0.9}Cr_{0.1}O_{15}$	Ti: 10.32 Cr: 0.38 Fe: 4.06	Ti: 9.68 Cr: 0.35 Fe: 3.39
$Bi_5Ti_3Fe_{0.8}Cr_{0.2}O_{15}$	Ti: 10.78 Cr: 0.74 Fe: 3.42	Ti: 9.68 Cr: 0.70 Fe: 3.01
$Bi_5Ti_3Fe_{0.7}Cr_{0.3}O_{15}$	Ti: 10.09 Cr: 1.11 Fe: 2.68	Ti: 9.68 Cr: 1.05 Fe: 2.64
$Bi_5Ti_3Fe_{0.6}Cr_{0.4}O_{15}$	Ti: 10.72 Cr: 1.50 Fe: 2.65	Ti: 9.68 Cr: 1.40 Fe: 2.26
$Bi_5Ti_3Fe_{0.5}Cr_{0.5}O_{15}$	Ti: 10.22 Cr: 1.74 Fe: 2.00	Ti: 9.68 Cr: 1.75 Fe: 1.88
$Bi_5Ti_3Fe_{0.9}Co_{0.1}O_{15}$*	Ti: 10.23 Co: 0.41 Fe: 2.96	Ti: 9.67 Co: 0.40 Fe: 3.39
$Bi_5Ti_3Fe_{0.8}Co_{0.2}O_{15}$*	Ti: 9.87 Co: 0.69 Fe: 3.02	Ti: 9.67 Co: 0.79 Fe: 3.01
$Bi_5Ti_3Fe_{0.8}Co_{0.2}O_{15}$*	Ti: 10.26 Co: 0.93 Fe: 2.62	Ti: 9.67 Co: 1.19 Fe: 2.63
$Bi_5Ti_3Fe_{0.7}Co_{0.3}O_{15}$*	Ti: 10.57 Co: 0.96 Fe: 1.92	Ti: 9.67 Co: 1.59 Fe: 2.26
$Bi_5Ti_3Fe_{0.9}Ga_{0.1}O_{15}$	Ti: 10.09 Ga: 0.45 Fe: 3.45	Ti: 9.67 Ga: 0.47 Fe: 3.38
$Bi_5Ti_3Fe_{0.8}Ga_{0.2}O_{15}$	Ti: 10.15 Ga: 0.91 Fe: 2.79	Ti: 9.66 Ga: 0.94 Fe: 3.00

* indicates samples synthesised alongside additional impurities.

Table B.8: EDX data for the $Bi_5Ti_{3+x}Fe_{1-2x}Ni_xO_{15}$ series.

Chemical Formula	Elemental % from EDX	
	Observed	Calculated
$\mathbf{Bi_5Ti_{3.1}Fe_{0.8}Ni_{0.1}O_{15}}$	Ti: 10.98 Fe: 2.73 Ni: 0.30	Ti: 10.00 Fe: 3.01 Ni: 0.40
$\mathbf{Bi_5Ti_{3.2}Fe_{0.6}Ni_{0.2}O_{15}}$	Ti: 11.39 Fe: 2.11 Ni: 0.58	Ti: 10.33 Fe: 2.26 Ni: 0.79
$\mathbf{Bi_5Ti_{3.3}Fe_{0.4}Ni_{0.3}O_{15}}$	Ti: 11.65 Fe: 1.50 Ni: 0.91	Ti: 10.65 Fe: 1.51 Ni: 1.19

Appendix C

X-ray Diffraction and Structure Refinement Data for New Compounds

Where Rietveld refinement was not possible, X-ray powder diffraction patterns were indexed. The results for new compounds are shown below. The Residual in each case is defined as the calculated *d*-spacing (d_{calc}) minus the observed *d*-spacing (d_{obs}).

C.1 X-ray diffraction data for Chapter 3

C.1.1 Phase-pure nitrate intercalated LDHs

Table C.1: Indexing of $[CoZnAl_8(OH)_{24}](NO_3)_4 \cdot 5H_2O$.
Orthorhombic cell a = 5.282(5) Å, b = 8.904(9) Å, c = 17.03(1) Å

h	*k*	*l*	d_{calc} / Å	d_{obs} / Å	Residual
0	0	2	8.538254	8.512527	-0.02573
0	1	1	7.889929	7.89028	0.000351
0	1	3	4.795664	4.78569	-0.00997
1	1	0	4.58221	4.542868	-0.03934
0	0	4	4.271551	4.256269	-0.01528
0	2	2	3.94968	3.945131	-0.00455
0	1	5	3.191128	3.180405	-0.01072
0	2	4	3.067837	3.076545	0.008708
0	0	6	2.824143	2.837505	0.013362
-1	1	5	2.722085	2.724622	0.002536
2	0	0	2.636432	2.641014	0.004583
2	0	2	2.523808	2.522401	-0.00141
0	1	7	2.334671	2.346204	0.011533
-2	1	3	2.303496	2.312282	0.008785
0	4	0	2.223167	2.226062	0.002895
-2	2	2	2.191846	2.194645	0.002799
2	2	3	2.111119	2.108787	-0.00233
2	2	4	2.009932	2.003926	-0.00601
1	4	2	1.998892	1.994247	-0.00465
0	1	9	1.854045	1.850376	-0.00367
0	3	8	1.730153	1.729504	-0.00065
3	1	1	1.719579	1.718413	-0.00117
-3	0	5	1.562636	1.563964	0.001328
1	0	11	1.486316	1.485282	-0.00103
0	6	0	1.482926	1.484041	0.001115
-1	1	11	1.465006	1.465039	3.31E-05

Table C.2: Indexing of $[Ni_{1.9}Zn_{0.1}Al_8(OH)_{24}](NO_3)_4 \cdot 5H_2O$.

Orthorhombic cell a = 5.322(9) Å, b = 8.909(7) Å, c = 17.00(2) Å

h	***k***	***l***	d_{calc} / Å	d_{obs} / Å	**Residual**
0	0	2	8.609524	8.500047	-0.10948
0	1	1	7.879214	7.890771	0.011556
1	1	0	4.560549	4.568755	0.008206
0	2	1	4.298023	4.308851	0.010827
0	2	2	3.935187	3.94539	0.010203
0	1	5	3.178829	3.176545	-0.00228
0	2	4	3.059601	3.074907	0.015306
0	3	2	2.813683	2.80338	-0.0103
0	2	5	2.70678	2.702652	-0.00413
0	3	3	2.628556	2.630262	0.001706
-2	1	1	2.512669	2.521449	0.008779
0	2	6	2.384708	2.390687	0.005979
2	2	0	2.294776	2.284378	-0.0104
1	3	4	2.213826	2.213644	-0.00018
1	4	2	2.003884	1.996991	-0.00689
-2	3	1	1.965779	1.968395	0.002615
1	2	8	1.808366	1.804345	-0.00402
0	3	8	1.727655	1.728118	0.000463
-1	4	7	1.566167	1.568525	0.002358
0	6	1	1.478588	1.479133	0.000545
-2	5	2	1.457851	1.458529	0.000678
2	4	7	1.397223	1.397022	-0.0002
0	6	5	1.360872	1.360682	-0.00019

Table C.3: Indexing of $[Co_{0.1}Ni_{1.9}Al_8(OH)_{24}](NO_3)_4 \cdot 4H_2O$.

Orthorhombic cell a = 5.306(7) Å, b = 8.890(6) Å, c = 17.06(2) Å

h	***k***	***l***	d_{calc} / Å	d_{obs} / Å	**Residual**
0	0	2	8.488416	8.527502	0.039085
0	1	1	7.848077	7.882993	0.034915
0	1	3	4.810355	4.789378	-0.02098
1	1	0	4.560062	4.556099	-0.00396
0	0	4	4.266681	4.263764	-0.00292
0	2	2	3.932439	3.941488	0.00905
0	1	5	3.179317	3.18461	0.005293
0	2	4	3.054799	3.076929	0.02213
-2	1	1	2.513758	2.514412	0.000654
1	0	7	2.216263	2.214159	-0.0021
-2	2	4	2.002362	2.009253	0.006891
1	2	8	1.810982	1.807269	-0.00371
3	1	1	1.727882	1.725755	-0.00213
-1	5	4	1.566494	1.567699	0.001205
0	6	0	1.482203	1.481588	-0.00062
0	6	2	1.460375	1.45972	-0.00066
0	6	4	1.400281	1.399503	-0.00078

Table C.4: Indexing of $[Co_{0.5}Ni_{1.1}Zn_{0.4}Al_8(OH)_{24}](NO_3)_4 \cdot 2H_2O$.

Orthorhombic cell a = 5.33(1) Å, b = 8.87(2) Å, c = 17.01(6) Å

h	***k***	***l***	d_{calc} / Å	d_{obs} / Å	**Residual**
0	0	2	8.539076	8.51367	-0.02541
0	1	1	7.892033	7.870691	-0.02134
1	1	0	4.568895	4.56985	0.000955
0	2	1	4.281324	4.294447	0.013123
0	2	2	3.946911	3.935342	-0.01157
0	1	5	3.187219	3.179462	-0.00776
0	2	4	3.064541	3.072051	0.007509
2	1	1	2.516826	2.524522	0.007696
2	2	0	2.297401	2.284923	-0.01248
0	4	0	2.218402	2.218951	0.000549
2	2	4	2.008607	2.013232	0.004625

C.1.2 Carboxylate- and sulphonate-intercalated LDHs

Table C.5: Summary of lattice parameters from indexing of powder X-ray diffraction data from the products of MM'Al_8-NO_3 intercalation reactions.

LDH system	Guest	Lattice parameter		
		a **/ Å**	***b*** **/ Å**	***c*** **/ Å**
Co/Zn/Al	Fumarate	5.31(1)	8.81 (2)	21.35 (3)
Co/Zn/Al	Succinate	5.27 (3)	8.54 (8)	21.35 (3)
Co/Zn/Al	Terephthalate	5.284 (9)	8.813 (8)	27.91 (1)
Co/Zn/Al	2-naphthalenesulphonate	5.32 (3)	8.82 (5)	35.5 (1)
Co/Zn/Al	Phthalate	5.32 (2)	8.57 (8)	28.91 (2)
Ni/Zn/Al	Fumarate	5.31 (2)	8.81 (2)	21.49 (3)
Ni/Zn/Al	Succinate	5.26 (2)	8.65 (9)	21.42 (3)
Ni/Zn/Al	Terephthalate	5.291 (9)	8.81 (2)	28.04 (2)
Ni/Zn/Al	2-naphthalenesulphonate	5.30 (5)	8.85 (5)	35.74 (8)
Ni/Zn/Al	Phthalate	5.32 (3)	8.56 (6)	28.85 (2)
Co/Ni/Al	Fumarate	5.31 (2)	8.82 (3)	21.60 (5)
Co/Ni/Al	Succinate	5.26 (3)	8.75 (5)	21.66 (9)
Co/Ni/Al	Terephthalate	5.29 (3)	8.78 (2)	27.98 (3)
Co/Ni/Al	2-naphthalenesulphonate	5.30 (5)	8.85 (4)	35.75 (7)
Co/Ni/Al	Phthalate	5.32 (2)	8.56 (6)	28.88 (2)

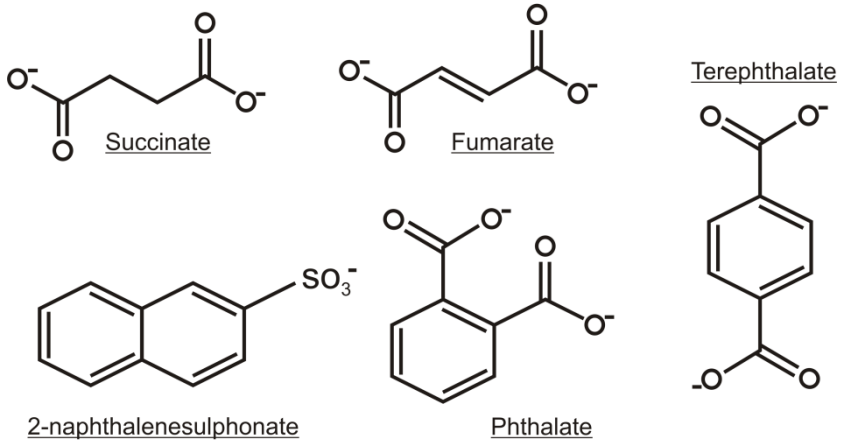

Figure C.1: Structures of the organic anions used for intercalation reactions.

C.2 X-ray diffraction data for Chapter 4

Table C.6: Indexing of $Bi_5Ti_{3.1}Fe_{0.8}Ni_{0.1}O_{15}$.

Orthorhombic cell a = 5.461(2) Å, b = 5.426(2) Å, c = 40.957(16) Å

h	***k***	***l***	d_{calc} / Å	d_{obs} / Å	**Residual**
0	0	4	10.17479	10.24776	0.072967
0	0	6	6.807191	6.831826	0.024635
0	0	8	5.114326	5.123886	0.00956
0	1	5	4.520739	4.527634	0.006895
0	0	10	4.095976	4.099112	0.003136
0	1	7	3.978995	3.982039	0.003044
1	1	1	3.830991	3.835553	0.004562
1	1	3	3.704415	3.707882	0.003467
1	1	5	3.484778	3.486669	0.001891
0	0	12	3.415829	3.415919	9.01E-05
1	1	7	3.217525	3.218424	0.000899
0	1	11	3.073934	3.072702	-0.00123
1	1	9	2.941662	2.94136	-0.0003
2	0	0	2.732341	2.732771	0.00043
0	2	0	2.715666	2.715498	-0.00017
1	1	11	2.679593	2.678442	-0.00115
0	0	16	2.564227	2.561944	-0.00228
2	0	6	2.537756	2.537312	-0.00044
0	2	6	2.52422	2.523465	-0.00076
0	1	15	2.442172	2.441128	-0.00104
2	0	8	2.412576	2.411265	-0.00131
0	2	8	2.400652	2.399374	-0.00128

Table C.7: Indexing of $Bi_5Ti_{3.2}Fe_{0.6}Ni_{0.2}O_{15}$.

Orthorhombic cell a = 5.462(4) Å, b = 5.430(3) Å, c = 40.895(15) Å

h	***k***	***l***	d_{calc} / Å	d_{obs} / Å	**Residual**
0	0	4	10.14218	10.23225	0.090075
0	0	6	6.787963	6.8215	0.033537
0	0	8	5.100898	5.116141	0.015243
0	0	10	4.085559	4.092901	0.007342
1	1	1	3.831968	3.837283	0.005315
1	1	3	3.704567	3.709085	0.004518
0	0	12	3.407231	3.410754	0.003524
1	1	7	3.21582	3.218003	0.002184
1	1	9	2.939396	2.940302	0.000906
2	0	0	2.732585	2.733323	0.000738
0	2	0	2.716467	2.717492	0.001026

h	***k***	***l***	d_{calc} / Å	d_{obs} / Å	**Residual**
0	0	16	2.558138	2.558067	-7.1E-05
2	0	8	2.411515	2.410835	-0.00068
0	2	8	2.400158	2.399948	-0.00021
0	0	18	2.27457	2.273838	-0.00073
0	2	10	2.264589	2.263924	-0.00067
1	1	15	2.228005	2.227015	-0.00099
0	0	20	2.047637	2.046455	-0.00118
2	2	0	1.928006	1.927131	-0.00088
1	1	19	1.881998	1.880398	-0.0016

Table C.8: Indexing of $Bi_5Ti_{3.3}Fe_{0.4}Ni_{0.3}O_{15}$.

Orthorhombic cell a = 5.464(3) Å, b = 5.431(5) Å, c = 40.877(16) Å

h	***k***	***l***	d_{calc} / Å	d_{obs} / Å	**Residual**
0	0	4	10.14799	10.228	0.080014
0	0	6	6.795745	6.818675	0.02293
0	0	8	5.106144	5.113975	0.007831
0	0	10	4.087972	4.091189	0.003216
1	1	1	3.832945	3.837936	0.004991
0	0	12	3.407103	3.409331	0.002229
1	1	9	2.941662	2.940094	-0.00157
2	0	0	2.732341	2.734134	0.001793
0	2	0	2.716387	2.717653	0.001266
0	0	16	2.557785	2.556994	-0.00079
2	1	5	2.336419	2.340463	0.004044
2	0	10	2.273414	2.273221	-0.00019
0	0	20	2.046714	2.045594	-0.00112
2	2	0	1.927813	1.92747	-0.00034
1	1	19	1.881779	1.879876	-0.0019
1	1	19	1.878348	1.879876	0.001527
2	0	18	1.74733	1.747823	0.000493
3	1	9	1.616567	1.61537	-0.0012
2	2	14	1.609839	1.608998	-0.00084

C.3 Rietveld refinement data for Chapter 4

Despite the models from Rietveld analysis appearing to represent the data well, often comparatively high goodness of fit parameters were elucidated from refinement. This was explained by preferred orientation, which resulted in anomalous intensities of some 00*l* Bragg reflections due to highly-textured product platelet particles.

Preferred orientation effects were accounted for in the refinement using the 'March-Dollase' factor for some reflections.

Table C.9: Summary of structural information elucidated from Rietveld refinement analysis using powder XRD data of the $Bi_5Ti_3Fe_{1-x}Cr_xO_{15}$ series.

$Bi_5Ti_3Fe_{1-x}Cr_xO_{15}$	$x = 0.1$	$x = 0.2$	$x = 0.3$	$x = 0.4$	$x = 0.5$
RMM	1483.95	1483.57	1483.18	1482.80	1482.41
Crystal system	Orthorhombic	Orthorhombic	Orthorhombic	Orthorhombic	Orthorhombic
a / Å	5.4704 (2)	5.4684 (2)	5.4675 (2)	5.4651 (2)	5.4640 (2)
b / Å	5.4363 (2)	5.4359 (2)	5.4354 (2)	5.4348 (2)	5.4351 (2)
c / Å	41.157 (1)	41.108 (1)	41.069 (1)	41.017 (2)	40.997 (2)
V / Å^3	1223.97 (9)	1222.0 (1)	1220.47 (8)	1218.3 (1)	1217.5 (1)
Space group	$A2_1am$	$A2_1am$	$A2_1am$	$A2_1am$	$A2_1am$
Laue group	*mmm*	*mmm*	*mmm*	*Mmm*	*mmm*
λ / Å	1.5406	1.5406	1.5406	1.5406	1.5406
Zero point	0.4 (1)	0.2 (2)	1.57 (1)	0.7 (2)	4.9 (1)
Number of variables	35	34	27	28	23
R_p / %	14.22	12.38	17.17	18.15	20.56
wR_p / %	18.76	16.29	22.77	24.09	27.23
χ^2	3.556	1.796	4.564	5.355	82.5

Table C.10: Summary of structural information elucidated from Rietveld refinement analysis using powder XRD data of the $Bi_5Ti_3Fe_{1-x}Co_xO_{15}$ series.

$Bi_5Ti_3Fe_{1-x}Co_xO_{15}$	***x* = 0.1***	***x* = 0.17***	***x* = 0.25***	***x* = 0.3***
Crystal system	Orthorhombic	Orthorhombic	Orthorhombic	Orthorhombic
a / Å	5.47111(9)	5.47239(7)	5.4706(1)	5.4694(2)
b / Å	5.43678(9)	5.43862(8)	5.4318(1)	5.4375(2)
c / Å	41.1695(6)	41.1561(6)	41.146(1)	41.138(1)
V / Å^3	1224.59(5)	1224.90(5)	1223.89(8)	1223.4(1)
Space group	*A*2$_1$*am*	*A*2$_1$*am*	*A*2$_1$*am*	*A*2$_1$*am*
Laue group	*mmm*	*mmm*	*mmm*	*mmm*
λ / Å	1.5406	1.5406	1.5406	1.5406
Zero point	0.52 (9)	7.45 (7)	4.6 (1)	-1.5 (1)
Number of variables	40	26	26	24
R_p / %	11.68	9.49	12.97	14.78
wR_p / %	16.12	12.69	17.46	18.87
χ^2	11.30	5.682	10.88	1.946

* indicates that data for an additional Bi_2O_3 impurity phase was incorporated into the model during Rietveld analysis.

Table C.11: Summary of structural information elucidated from Rietveld refinement analysis using powder XRD data of the $Bi_5Ti_3Fe_{1-x}V_xO_{15}$ and $Bi_5Ti_3Fe_{1-x}Ga_xO_{15}$ series.

	$Bi_5Ti_3Fe_{0.9}V_{0.1}O_{15}$*	**$Bi_5Ti_3Fe_{0.9}Ga_{0.1}O_{15}$**	**$Bi_5Ti_3Fe_{0.8}Ga_{0.2}O_{15}$**
Crystal system	Orthorhombic	Orthorhombic	Orthorhombic
a / Å	5.4701(2)	5.4705(1)	5.4667(1)
b / Å	5.4364(2)	5.4366(1)	5.4337(1)
c / Å	41.166(1)	41.1844(8)	41.2181(8)
V / Å^3	1224.17(9)	1224.86(6)	1224.34(6)
Space group	*A*2$_1$*am*	*A*2$_1$*am*	*A*2$_1$*am*
Laue group	*mmm*	*mmm*	*mmm*
λ / Å	1.5406	1.5406	1.5406
Zero point	0.7 (1)	5.6 (1)	5.58 (9)
Number of variables	30	23	24
R_p / %	15.97	12.73	11.05
wR_p / %	20.92	17.42	14.47
χ^2	3.568	11.97	8.892

* indicates that data for an additional impurity phase was incorporated into the model during Rietveld analysis.

Appendix D

Characterisation data for $Bi_5Ti_3Fe_{1-x}Cr_xO_{15}$

D.1 Thermogravimetric analysis data for $Bi_5Ti_3Fe_{1-x}Cr_xO_{15}$

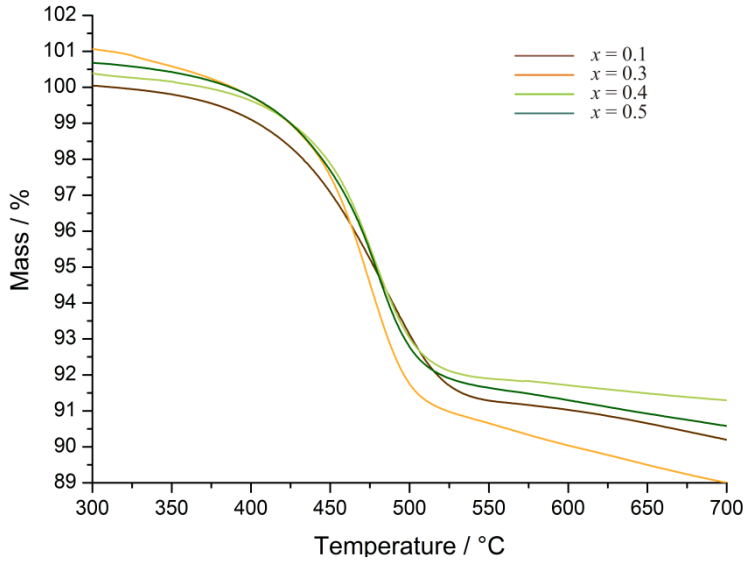

Sample	Parameter	Room temperature	750 °C
	Observed Mass	100.2 %	90.0 %
***x* = 0.1**	RMM	1484.0	1342.4
	Chemical Formula	$Bi_5Ti_3Fe_{0.9}Cr_{0.1}O_{15}$	5Bi, $3TiO_2$, 0.9Fe, $0.05Cr_2O_3$
	Observed Mass	100.3 %	90.7 %
***x* = 0.2**	RMM	1483.6	1344.4
	Chemical Formula	$Bi_5Ti_3Fe_{0.8}Cr_{0.2}O_{15}$	5Bi, $3TiO_2$, 0.8Fe, $0.1Cr_2O_3$
	Observed Mass	100.9 %	90.9 %
***x* = 0.3**	RMM	1483.2	1346.4
	Chemical Formula	$Bi_5Ti_3Fe_{0.7}Cr_{0.3}O_{15}$	5Bi, $3TiO_2$, 0.7Fe, $0.15Cr_2O_3$
	Observed Mass	100.4 %	91.2 %
***x* = 0.4**	RMM	1482.8	1348.4
	Chemical Formula	$Bi_5Ti_3Fe_{0.6}Cr_{0.4}O_{15}$	5Bi, $3TiO_2$, 0.6Fe, $0.2Cr_2O_3$
	Observed Mass	100.8 %	91.7 %
***x* = 0.5**	RMM	1482.4	1350.4
	Chemical Formula	$Bi_5Ti_3Fe_{0.5}Cr_{0.5}O_{15}$	5Bi, $3TiO_2$, 0.5Fe, $0.25Cr_2O_3$

Figure D.1: Thermogravimetric (TGA) raw data and analysis for members of the $Bi_5Ti_3Fe_{1-x}Cr_xO_{15}$ series.

D.2 Magnetic data for $Bi_5Ti_3Fe_{1-x}Cr_xO_{15}$

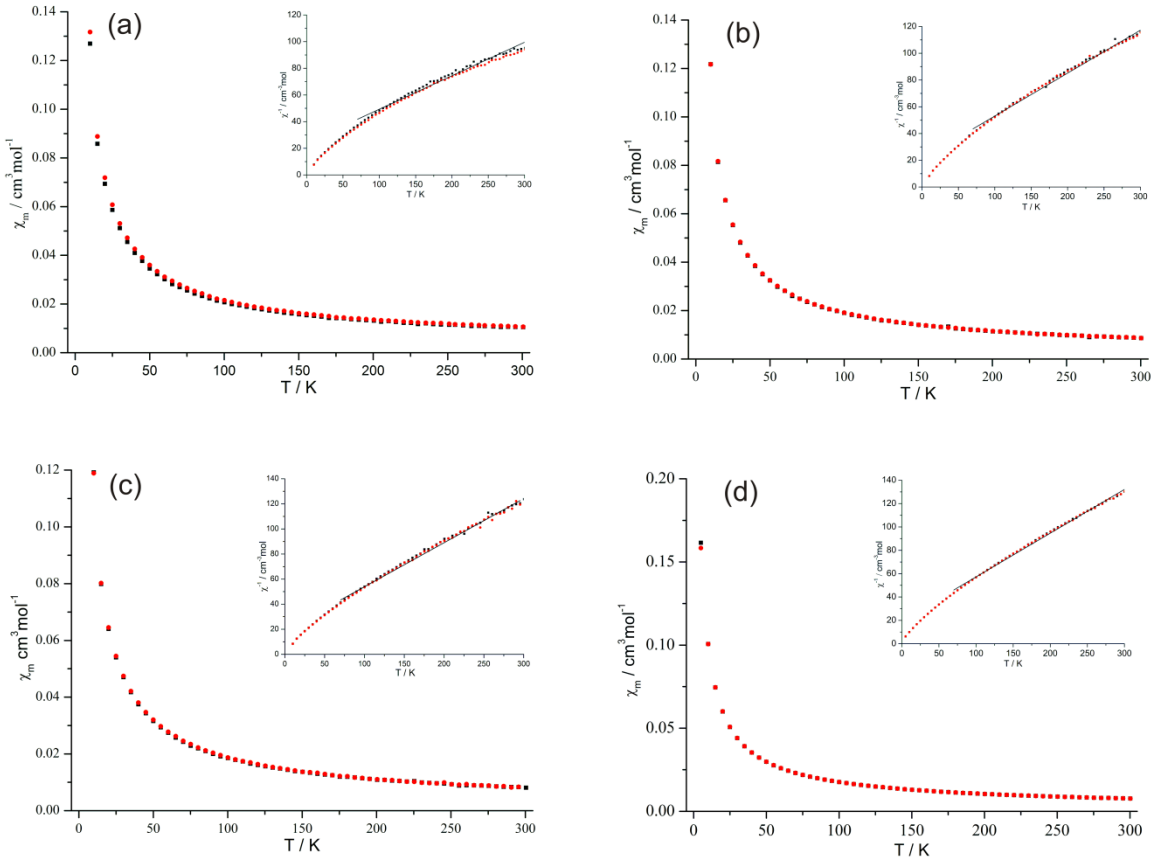

Chromium stoichiometry (x)	Observed μ_{eff} (μ_B)	Weiss Constant (θ) / K	Curie Constant	Curie-Weiss fitting range
0.1	5.64 (4)	− 96.14	3.98	70 – 300 K
0.2	5.00 (6)	− 65.44	3.12	70 – 300 K
0.3	4.77 (5)	− 53.10	2.84	70 – 300 K
0.4	4.62 (4)	− 52.76	2.67	70 – 300 K
0.5	4.75 (5)	− 48.94	2.83	70 – 300 K

Figure D.2: Magnetic data for $Bi_5Ti_3Fe_{1-x}Cr_xO_{15}$. The figure shows zero field cooled (■) and field cooled (●) molar susceptibility (χ_m) *vs.* temperature plots for the (a) x = 0.1 (b) x = 0.2 (c) x = 0.3 (d) x = 0.4 members of the $Bi_5Ti_3Fe_{1-x}Cr_xO_{15}$ series. Reciprocal of χ_m *vs.* temperature plots including fitting of field cooled data to the Curie-Weiss Law are inset in each case. Magnetic data are summarised in the table.

D.3 SEM data for $Bi_5Ti_3Fe_{0.4}Cr_{0.6}O_{15}$

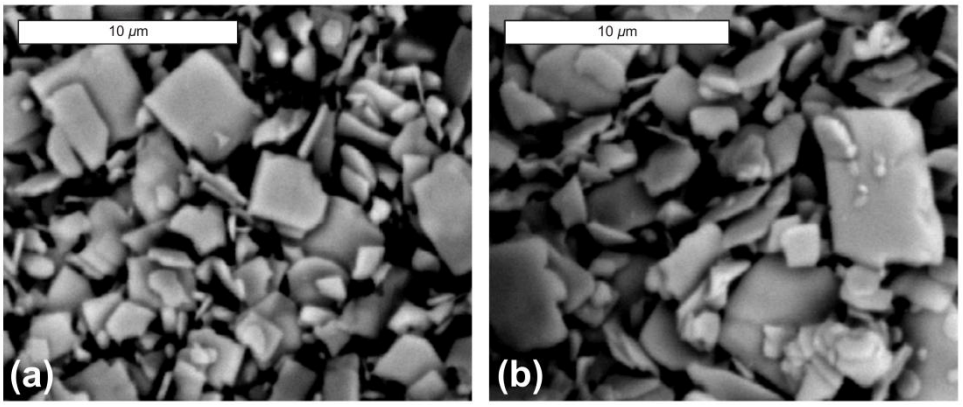

Figure D.3: SEM images for $Bi_5Ti_3Fe_{0.4}Cr_{0.6}O_{15}$ synthesised at 950 °C for (a) 2.5 hours and (b) 12.5 hours

D.4 EDX data for $Bi_5Ti_3CrO_{15}$

Table D.4: Elemental analysis data for Bi_5TiCrO_{15} deduced from EDX experiments.

Reaction conditions	**Observed elemental %**		
	Bi	Ti	Cr
5	59.96	9.36	2.20
7.5	57.94	9.01	2.15
12.5	59.46	9.57	1.62
Ceramic	70.05	9.89	3.48
Expected	70.58	9.70	3.51

Appendix E

Supplementary Data from *In Situ* X-ray Diffraction Studies

E.1 Rietveld refinement data for Chapter 5

E.1.1 Molten salt synthesis of $Bi_5Ti_3Fe_{0.5}Cr_{0.5}O_{15}$ – starting materials

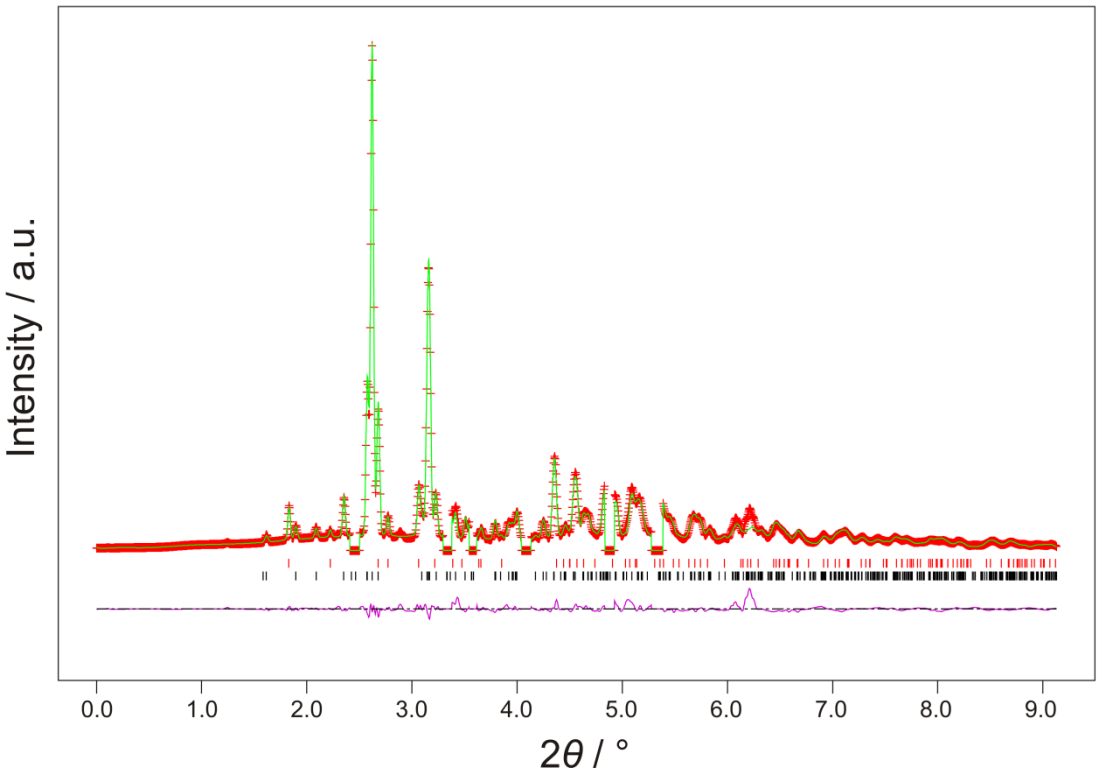

Figure E.1: Difference plot of a two-phase Rietveld refinement with angular-dispersive XRD data from an *in situ* scan of the starting materials prior to heating. The phases α-Bi_2O_3 (black ticks) and Na_2SO_4 (red ticks) are included in the analysis. Reflections due to the alumina crucible were excluded. Goodness of fit parameters were: χ^2 = 4.069, wRp = 0.098, and Rp = 0.0647 for 33 refined variables.

E.1.2 Molten salt synthesis of $Bi_5Ti_3Fe_{0.5}Cr_{0.5}O_{15}$ – product at 950 °C

Table E.1: Summary of structural information from Rietveld refinement with angular-dispersive XRD data obtained from a sample of $Bi_5Ti_3Fe_{0.5}Cr_{0.5}O_{15}$ at 950 °C.

Crystal data	**$Bi_5Ti_3Fe_{0.5}Cr_{0.5}O_{15}$**
RMM	1482.51
Temperature / °C	950
Crystal system	Tetragonal
a / Å	3.8887 (3)
c / Å	41.561 (4)
V / Å^3	628.48 (14)
Space group	*I*4/*mmm*
Laue group	4/*mmm*
λ / Å	0.14846
Zero point	−0.143 (2)
Number of parameters	44
R_p / %	5.08
wR_p / %	6.63
χ^2	1.251

Table E.2: Fractional atomic coordinates of $Bi_5Ti_3Fe_{0.5}Cr_{0.5}O_{15}$ at 950 °C.

Atom	***x***	***y***	***z***	**Occupancy**	**U_{iso}**
Bi1	0.00000	0.00000	0.00000	1.000	0.072(3)
Bi2	0.00000	0.00000	0.10476	1.000	0.072(2)
Bi3	0.00000	0.00000	0.21842	1.000	0.059(2)
Ti1	0.00000	0.00000	0.44975	0.750	0.046(9)
Cr1	0.00000	0.00000	0.44975	0.125	0.005
Fe1	0.00000	0.00000	0.44975	0.125	0.025
Ti2	0.00000	0.00000	0.34532	0.750	0.025(7)
Cr2	0.00000	0.00000	0.34532	0.125	0.005
Fe2	0.00000	0.00000	0.34532	0.125	0.025
O1	0.00000	0.00000	0.50000	1.000	0.10(4)
O2	0.00000	0.50000	0.40493	1.000	0.12(2)
O3	0.00000	0.00000	0.14447	1.000	0.05(2)
O4	0.00000	0.50000	0.30753	1.000	0.009(9)
O5	0.00000	0.00000	0.25000	1.000	0.02(2)
O6	0.00000	0.50000	0.44975	1.000	0.025

E.1.3 Molten salt synthesis of $Bi_5Ti_3Fe_{0.5}Cr_{0.5}O_{15}$ – product cooling

Table E.3: Summary of structural information elucidated from Rietveld refinement analysis, using *in situ* angular-dispersive XRD data from selected $Bi_5Ti_3Fe_{0.5}Cr_{0.5}O_{15}$ scans, recorded during product cooling from 950 °C.

	891 °C	**841 °C**	**791 °C**	**741 °C**	**731 °C**
Crystal system	Tetragonal	Tetragonal	Tetragonal	Tetragonal	Tetragonal
$a = b$ / Å	3.8844 (3)	3.883 (6)	3.8784 (3)	3.8727 (7)	3.8733 (5)
c / Å	41.525 (4)	41.497 (9)	41.477 (5)	41.412 (8)	41.413 (7)
V / Å^3	626.6 (2)	625.8 (3)	623.9 (2)	621.1 (3)	621.3 (3)
Space group	*I*4/*mmm*	*I*4/*mmm*	*I*4/*mmm*	*I*4/*mmm*	*I*4/*mmm*
Laue group	4/*mmm*	4/*mmm*	4/*mmm*	4/*mmm*	4/*mmm*
λ / Å	0.14846	0.14846	0.14846	0.14846	0.14846
Zero point	−0.11 (2)	−0.15 (5)	−0.17 (2)	−0.33 (9)	−0.19 (7)
R_p / %	5.91	15.97	5.03	9.58	5.03
wR_p / %	7.41	20.54	6.78	12.29	6.75
χ^2	1.473	10.26	1.140	3.882	1.137

	722 °C	**701 °C**	**691 °C**	**663 °C**	**618 °C**
Crystal system	Tetragonal	Orthorhombic	Orthorhombic	Orthorhombic	Orthorhombic
a / Å	3.8728 (6)	5.480 (3)	5.479 (3)	5.479 (2)	5.477 (2)
b / Å	3.8728 (6)	5.474 (4)	5.473 (3)	5.471 (2)	5.467 (2)
c / Å	41.409 (7)	41.410 (7)	41.406 (7)	41.395 (7)	41.365 (7)
V / Å^3	621.1 (3)	1242.1 (4)	1241.7 (4)	1240.8 (4)	1238.7 (4)
Space group	*I*4/*mmm*	*A*2$_1$*am*	*A*2$_1$*am*	*A*2$_1$*am*	*A*2$_1$*am*
Laue group	4/*mmm*	*mmm*	*mmm*	*Mmm*	*mmm*
λ / Å	0.14846	0.14846	0.14846	0.14846	0.14846
Zero point	−0.18 (7)	−0.06 (3)	−0.04 (4)	−0.02 (3)	0.05 (4)
R_p / %	5.03	10.74	13.03	10.01	11.62
wR_p / %	6.57	14.11	17.10	13.78	15.40
χ^2	1.071	4.926	7.592	4.691	5.909

E.2 Rietveld refinement data for Chapter 6

E.2.1 Products of $(H_2NMe_2)_2[Co_3(BDC)_4]\cdot y$DMF synthesis

Table E.4: Summary of structural information elucidated from Rietveld analysis with angular-dispersive XRD data obtained from a samples of $(H_2NMe_2)_2[Co_3(BDC)_4]\cdot y$DMF that had been synthesised at different temperatures.

Synthesis temp / °C	**180**	**200**	**225***	**250**
Crystal system	Monoclinic	Monoclinic	Monoclinic	Monoclinic
a / Å	33.50 (3)	33.28 (2)	33.48 (4)	33.215 (8)
b / Å	9.848 (5)	9.775 (3)	9.847 (5)	9.775 (3)
c / Å	18.151 (9)	18.169 (6)	18.34 (1)	18.372 (6)
β / °	95.69 (7)	94.05 (5)	92.55 (8)	89.90 (3)
V / Å^3	5959 (10)	5896 (6)	6039 (11)	5965 (5)
Space group	*C* 1 2/*c* 1	*C* 1 2/*c* 1	*C* 1 2/*c* 1	*C* 1 2/*c* 1
Laue group	2/*mb*	2/*mb*	2/*mb*	2/*mb*
λ / Å	0.23286	0.23286	0.23286	0.23286
Zero point	0.02 (8)	−0.04 (5)	0.05 (9)	0.19 (9)
Number of variables	29	39	29	46
R_p / %	3.68	5.31	0.5	3.90
wR_p / %	5.65	8.08	0.81	5.64
χ^2	0.7820	1.811	0.014	1.073

* Indicates that Rietveld analysis was undertaken with poorer quality XRD data (containing fewer Bragg reflections and a larger contribution from background scattering), hence the smaller goodness of fit parameters.

E.2.2 Product of Co(DMF)(NDC) synthesis

Table E.5: Summary of structural information from Rietveld refinement with angular-dispersive XRD data obtained from a sample of Co(DMF)(NDC) following reaction at 200 °C.

Crystal data	**$CoO_5NC_{15}H_{12}$**
RMM	346.20
Temperature / °C	Room temperature
Crystal system	Monoclinic
a / Å	23.454 (6)
b / Å	8.779 (2)
c / Å	7.2236 (18)
β / °	97.78 (2)
V / Å^3	1473.7 (10)
Space group	*C*2/*c*
Laue group	2/*mb*
λ / Å	0.23286
Zero point	0.3 (1)
Number of variables	35
R_p / %	3.68
wR_p / %	5.35
χ^2	0.8701

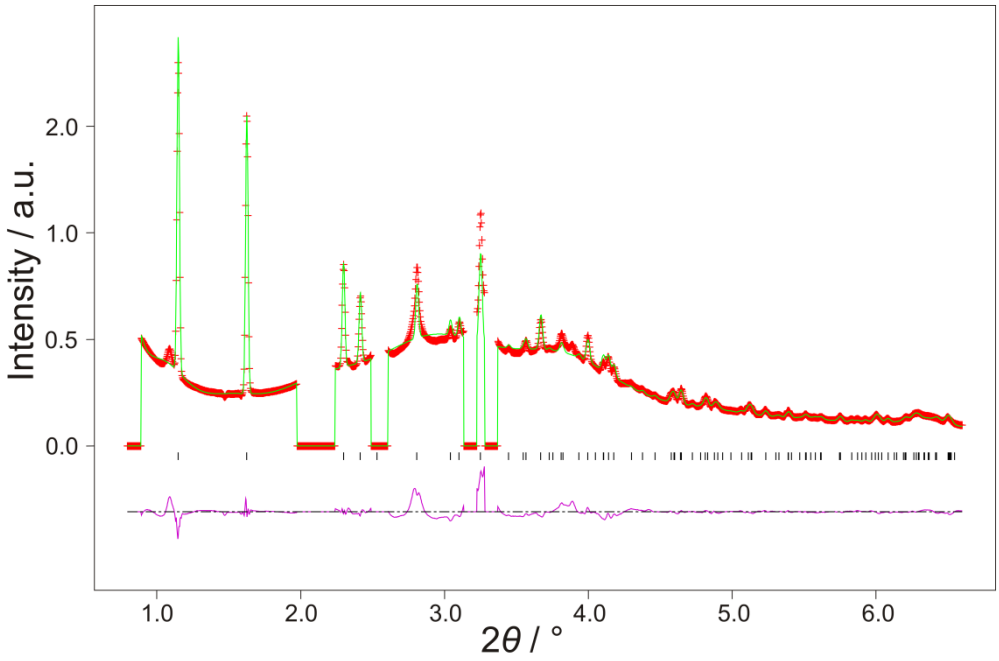

Figure E.2: Difference plot from refinement of a monoclinic structure model with angular-dispersive XRD data from a scan of Co(DMF)(NDC) with 4 sec exposure. Regions containing reflections due to the polypropylene sample vessel were excluded.

E.3 *In situ* XRD data for Chapter 6

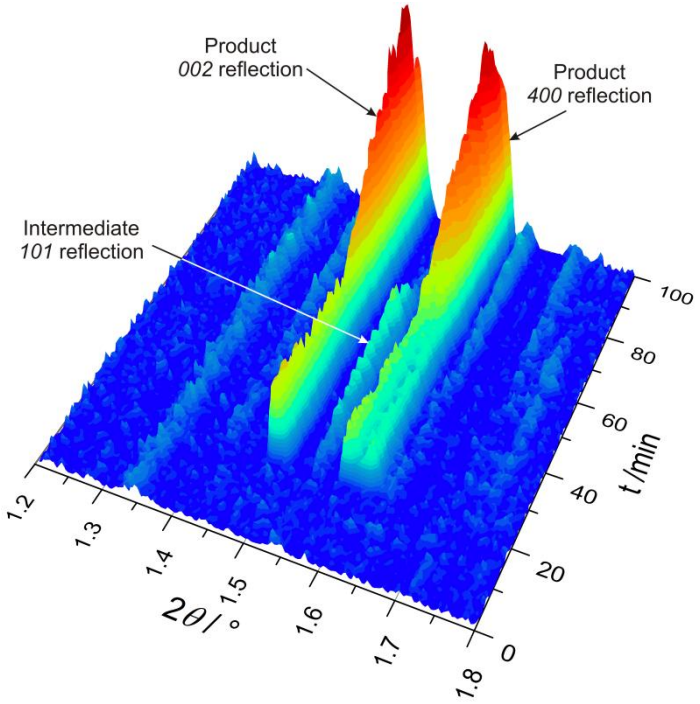

Figure E.3: Stack plot showing *in situ* angular-dispersive XRD data from the resin-assisted synthesis of $(H_2NMe_2)_2[Co_3(BDC)_4]\cdot y$DMF undertaken at 200 °C. The magnified 2θ region illustrates the extended lifetime of a transient intermediate reflection at 2θ = *ca*. 1.54°.

E.4 Miscellaneous temperature profiles

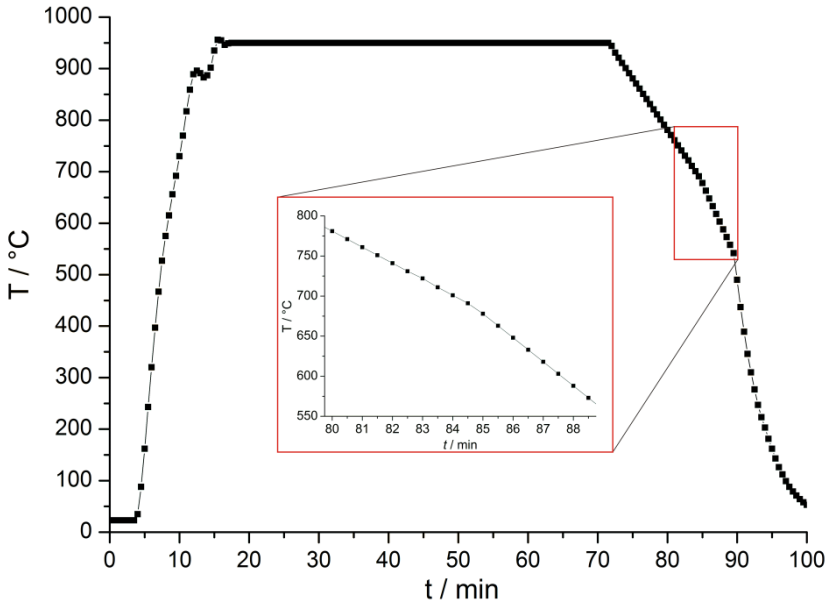

Figure E.4: Temperature data for the synthesis of $Bi_5Ti_3Fe_{0.5}Cr_{0.5}O_{15}$ at 950 °C. The highlighted section corresponds to the region over which the orthorhombic-tetragonal phase transition is observed. The reaction is discussed in detail in Section 5.4.

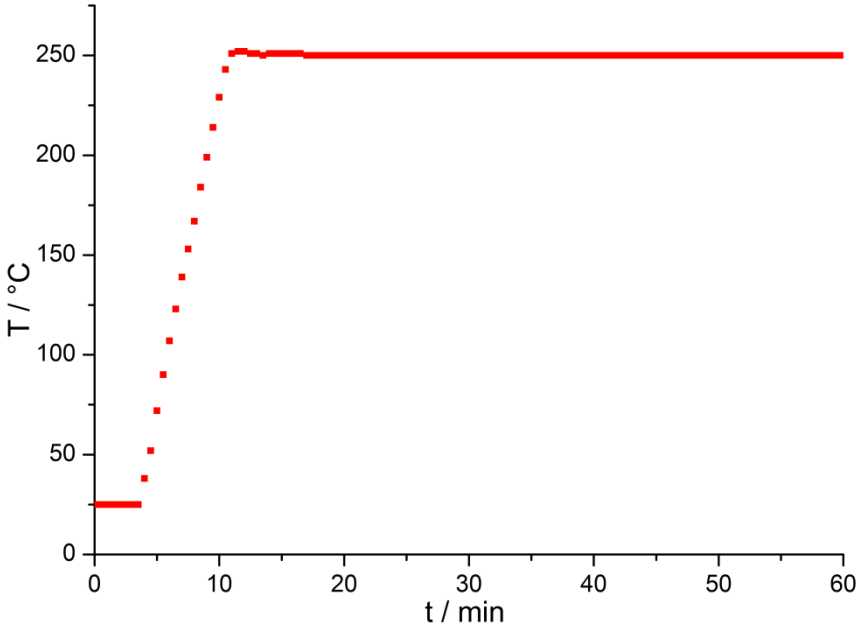

Figure E.5: Temperature data for the synthesis of $(H_2NMe_2)_2[Co_3(BDC)_4]\cdot y$DMF at 250 °C. The reaction is discussed in detail in Section 6.2.

Appendix F

Detailed Parameters from Rietveld Refinement

Table F.1: Parameters from the structural refinement of $Bi_5Ti_3Fe_{0.9}Cr_{0.1}O_{15}$ against powder XRD data.

Atom	*x*	*y*	*Z*	Occupancy	U_{iso}
Bi1	0.286(2)	0.261(1)	0.000	1.0	0.035(2)
Bi2	0.288(2)	0.2263(8)	0.1052(1)	1.0	0.001(1)
Bi3	0.250	0.250	0.219	1.0	0.036(1)
Ti/Cr/Fe1	0.256(7)	0.226(5)	0.4506(2)	0.75/0.025/0.225	0.049(10)
Ti/Cr/Fe2	0.218(4)	0.271(4)	0.3455(2)	0.75/0.025/0.225	0.005
O1	0.336	0.177	0.500	1.0	0.025
O2	0.607	0.546	0.052	1.0	0.025
O3	0.325	0.306	0.405	1.0	0.025
O4	0.533	0.485	0.138	1.0	0.025
O5	0.291	0.203	0.305	1.0	0.025
O6	0.505	0.489	0.251	1.0	0.025
O7	0.033	0.030	0.039	1.0	0.025
O8	0.083	0.032	0.147	1.0	0.025

Table F.2: Parameters from the structural refinement of $Bi_5Ti_3Fe_{0.8}Cr_{0.2}O_{15}$ against powder XRD data.

Atom	*x*	*y*	*Z*	Occupancy	U_{iso}
Bi1	0.246(3)	0.259(2)	0.000	1.0	0.028(2)
Bi2	0.255(2)	0.232(1)	0.1046(1)	1.0	0.019(1)
Bi3	0.250	0.250	0.219	1.0	0.044(1)
Ti/Cr/Fe1	0.316(3)	0.206(3)	0.4508(2)	0.75/0.05/0.20	0.005
Ti/Cr/Fe2	0.206(4)	0.264(4)	0.3439(2)	0.75/0.05/0.20	0.005
O1	0.336	0.177	0.500	1.0	0.025
O2	0.607	0.546	0.052	1.0	0.025
O3	0.325	0.306	0.405	1.0	0.025
O4	0.533	0.485	0.138	1.0	0.025
O5	0.291	0.203	0.305	1.0	0.025
O6	0.505	0.489	0.251	1.0	0.025
O7	0.033	0.030	0.039	1.0	0.025
O8	0.083	0.032	0.147	1.0	0.025

Table F.3: Parameters from the structural refinement of $Bi_5Ti_3Fe_{0.7}Cr_{0.3}O_{15}$ against powder XRD data.

Atom	*x*	*y*	*Z*	Occupancy	U_{iso}
Bi1	0.272(2)	0.243(1)	0.000	1.0	0.034(2)
Bi2	0.280(2)	0.270(1)	0.105(1)	1.0	0.005
Bi3	0.286(3)	0.264(2)	0.218(2)	1.0	0.044(1)
Ti/Cr/Fe1	0.353(4)	0.264(4)	0.4492(2)	0.75/0.075/0.175	0.005
Ti/Cr/Fe2	0.228(5)	0.219(5)	0.3468(2)	0.75/0.075/0.175	0.005
O1	0.336	0.177	0.500	1.0	0.025
O2	0.607	0.546	0.052	1.0	0.025
O3	0.325	0.306	0.405	1.0	0.025
O4	0.533	0.485	0.138	1.0	0.025
O5	0.291	0.203	0.305	1.0	0.025
O6	0.505	0.489	0.251	1.0	0.025
O7	0.033	0.030	0.039	1.0	0.025
O8	0.083	0.032	0.147	1.0	0.025

Table F.4: Parameters from the structural refinement of $Bi_5Ti_3Fe_{0.6}Cr_{0.4}O_{15}$ against powder XRD data.

Atom	*x*	*y*	*z*	Occupancy	U_{iso}
Bi1	0.262(3)	0.250(2)	0.000	1.0	0.024(2)
Bi2	0.252(2)	0.231(1)	0.1048(1)	1.0	0.006(2)
Bi3	0.250	0.250	0.219	1.0	0.025
Ti/Cr/Fe1	0.192(4)	0.219(5)	0.4510(3)	0.75/0.10/0.15	0.016(1)
Ti/Cr/Fe2	0.185(4)	0.281(5)	0.3452(2)	0.75/0.10/0.15	0.005
O1	0.336	0.177	0.500	1.0	0.025
O2	0.607	0.546	0.052	1.0	0.025
O3	0.325	0.306	0.405	1.0	0.025
O4	0.533	0.485	0.138	1.0	0.025
O5	0.291	0.203	0.305	1.0	0.025
O6	0.505	0.489	0.251	1.0	0.025
O7	0.033	0.030	0.039	1.0	0.025
O8	0.083	0.032	0.147	1.0	0.025

Table F.5: Parameters from the structural refinement of $Bi_5Ti_3Fe_{0.5}Cr_{0.5}O_{15}$ against powder XRD data.

Atom	*x*	*y*	*z*	Occupancy	U_{iso}
Bi1	0.250	0.250	0.000	1.0	0.012(2)
Bi2	0.238(2)	0.225(2)	0.1045(1)	1.0	0.012(2)
Bi3	0.250	0.268	0.219	1.0	0.020(2)
Ti/Cr/Fe1	0.315	0.189	0.454	0.75/0.125/0.125	0.005
Ti/Cr/Fe2	0.258	0.277	0.354	0.75/0.125/0.125	0.005
O1	0.336	0.177	0.500	1.0	0.025
O2	0.607	0.546	0.052	1.0	0.025
O3	0.325	0.306	0.405	1.0	0.025
O4	0.533	0.485	0.138	1.0	0.025
O5	0.291	0.203	0.305	1.0	0.025
O6	0.505	0.489	0.251	1.0	0.025
O7	0.033	0.030	0.039	1.0	0.025
O8	0.083	0.032	0.147	1.0	0.025

Table F.6: Parameters from the structural refinement of $Bi_5Ti_3Fe_{0.9}Co_{0.1}O_{15}$ against powder XRD data.

Atom	*x*	*y*	*z*	Occupancy	U_{iso}
Bi1	0.268(3)	0.252(1)	0.000	1.0	0.032(2)
Bi2	0.235(3)	0.2321(7)	0.1054(1)	1.0	0.012(10)
Bi3	0.242(3)	0.2591(8)	0.2177(1)	1.0	0.026(1)
Ti/Co/Fe1	0.306(3)	0.205(3)	0.4485(2)	0.75/0.025/0.225	0.005
Ti/Co/Fe2	0.266(4)	0.273(3)	0.3442(2)	0.75/0.025/0.225	0.005
O1	0.336	0.177	0.500	1.0	0.025
O2	0.607	0.546	0.052	1.0	0.025
O3	0.325	0.306	0.405	1.0	0.025
O4	0.533	0.485	0.138	1.0	0.025
O5	0.291	0.203	0.305	1.0	0.025
O6	0.505	0.489	0.251	1.0	0.025
O7	0.033	0.030	0.039	1.0	0.025
O8	0.083	0.032	0.147	1.0	0.025
Additional Phase:					
Bi_2O_3: space group *P* -4 2_1 *c*, *a* = *b* = 7.84(1) Å, *c* = 5.64(2) Å; wt. frac. = 0.50(2)					

Table F.7: Parameters from the structural refinement of $Bi_5Ti_3Fe_{0.83}Co_{0.17}O_{15}$ against powder XRD data.

Atom	***x***	***y***	***z***	**Occupancy**	**U_{iso}**
Bi1	0.270(2)	0.249(1)	0.000	1.0	0.018(1)
Bi2	0.262(1)	0.245(1)	0.1048(1)	1.0	0.009(1)
Bi3	0.256(3)	0.260(2)	0.219(2)	1.0	0.018(1)
Ti/Co/Fe1	0.308(2)	0.235(1)	0.4505(2)	0.75/0.043/0.207	0.005
Ti/Co/Fe2	0.212(1)	0.273(1)	0.3458(2)	0.75/0.043/0.207	0.005
O1	0.336	0.177	0.500	1.0	0.025
O2	0.607	0.546	0.052	1.0	0.025
O3	0.325	0.306	0.405	1.0	0.025
O4	0.533	0.485	0.138	1.0	0.025
O5	0.291	0.203	0.305	1.0	0.025
O6	0.505	0.489	0.251	1.0	0.025
O7	0.033	0.030	0.039	1.0	0.025
O8	0.083	0.032	0.147	1.0	0.025
Additional Phase:					
Bi_2O_3: space group *P* -4 2_1 *c*, *a* = *b* = 7.828(3) Å, *c* = 5.550(4) Å; wt. frac. = 0.547(9)					

Table F.8: Parameters from the structural refinement of $Bi_5Ti_3Fe_{0.75}Co_{0.25}O_{15}$ against powder XRD data.

Atom	***x***	***y***	***z***	**Occupancy**	**U_{iso}**
Bi1	0.273(1)	0.256(1)	0.000	1.0	0.027(2)
Bi2	0.271(4)	0.249(2)	0.105(1)	1.0	0.018(1)
Bi3	0.255(2)	0.268(2)	0.219(2)	1.0	0.020(1)
Ti/Co/Fe1	0.320(3)	0.231(1)	0.4510(7)	0.75/0.063/0.187	0.005
Ti/Co/Fe2	0.265(1)	0.277(1)	0.354(2)	0.75/0.063/0.187	0.005
O1	0.336	0.177	0.500	1.0	0.025
O2	0.607	0.546	0.052	1.0	0.025
O3	0.325	0.306	0.405	1.0	0.025
O4	0.533	0.485	0.138	1.0	0.025
O5	0.291	0.203	0.305	1.0	0.025
O6	0.505	0.489	0.251	1.0	0.025
O7	0.033	0.030	0.039	1.0	0.025
O8	0.083	0.032	0.147	1.0	0.025
Additional Phase:					
Bi_2O_3: space group *P* -4 2_1 *c*, *a* = *b* = 7.57(2) Å, *c* = 6.06(4) Å; wt. frac. = 0.783(6)					

Table F.9: Parameters from the structural refinement of $Bi_5Ti_3Fe_{0.7}Co_{0.3}O_{15}$ against powder XRD data.

Atom	*x*	*y*	*z*	Occupancy	U_{iso}
Bi1	0.255(2)	0.256(1)	0.000	1.0	0.021(2)
Bi2	0.238(1)	0.245(1)	0.105(1)	1.0	0.013(1)
Bi3	0.250	0.268	0.219	1.0	0.030(1)
Ti/Co/Fe1	0.286(2)	0.253(1)	0.4514(4)	0.75/0.075/0.175	0.005
Ti/Co/Fe2	0.277(2)	0.219(1)	0.3448(2)	0.75/0.075/0.175	0.005
O1	0.336	0.177	0.500	1.0	0.025
O2	0.607	0.546	0.052	1.0	0.025
O3	0.325	0.306	0.405	1.0	0.025
O4	0.533	0.485	0.138	1.0	0.025
O5	0.291	0.203	0.305	1.0	0.025
O6	0.505	0.489	0.251	1.0	0.025
O7	0.033	0.030	0.039	1.0	0.025
O8	0.083	0.032	0.147	1.0	0.025
Additional Phase:					
Bi_2O_3: space group *P* -4 2_1 *c*, *a* = *b* = 7.59(2) Å, *c* = 6.02(3) Å; wt. frac. = 0.815(5)					

Table F.10: Parameters from the structural refinement of $Bi_5Ti_3Fe_{0.9}V_{0.1}O_{15}$ against powder XRD data.

Atom	*x*	*y*	*z*	Occupancy	U_{iso}
Bi1	0.259(3)	0.255(1)	0.000	1.0	0.046(3)
Bi2	0.270(2)	0.231(1)	0.1059(1)	1.0	0.007(1)
Bi3	0.241(3)	0.256(1)	0.2175(1)	1.0	0.037(2)
Ti/V/Fe1	0.290(2)	0.189(1)	0.4544(2)	0.75/0.225/0.025	0.025
Ti/V/Fe2	0.228(2)	0.262(2)	0.3445(5)	0.75/0.225/0.025	0.025
O1	0.336	0.177	0.500	1.0	0.025
O2	0.607	0.546	0.052	1.0	0.025
O3	0.325	0.306	0.405	1.0	0.025
O4	0.533	0.485	0.138	1.0	0.025
O5	0.291	0.203	0.305	1.0	0.025
O6	0.505	0.489	0.251	1.0	0.025
O7	0.033	0.030	0.039	1.0	0.025
O8	0.083	0.032	0.147	1.0	0.025
Additional Phase:					
Bi_2O_3: space group *P* -4 2_1 *c*, *a* = *b* = 7.555(3) Å, *c* = 5.555(4) Å; wt. frac. = 0.62(2)					

Table F.11: Parameters from the structural refinement of $Bi_5Ti_3Fe_{0.9}Ga_{0.1}O_{15}$ against powder XRD data.

Atom	*x*	*y*	*z*	Occupancy	U_{iso}
Bi1	0.289(3)	0.246(1)	0.000	1.0	0.027(1)
Bi2	0.288(3)	0.241(1)	0.1048(1)	1.0	0.0171(8)
Bi3	0.273(2)	0.257(1)	0.2184(1)	1.0	0.0277(8)
Ti/Ga/Fe1	0.315	0.189	0.454	0.75/0.225/0.025	0.005
Ti/Ga/Fe2	0.258	0.277	0.354	0.75/0.225/0.025	0.005
O1	0.336	0.177	0.500	1.0	0.025
O2	0.607	0.546	0.052	1.0	0.025
O3	0.325	0.306	0.405	1.0	0.025
O4	0.533	0.485	0.138	1.0	0.025
O5	0.291	0.203	0.305	1.0	0.025
O6	0.505	0.489	0.251	1.0	0.025
O7	0.033	0.030	0.039	1.0	0.025
O8	0.083	0.032	0.147	1.0	0.025

Table F.12: Parameters from the structural refinement of $Bi_5Ti_3Fe_{0.8}Ga_{0.2}O_{15}$ against powder XRD data.

Atom	*x*	*y*	*z*	Occupancy	U_{iso}
Bi1	0.259(2)	0.251(2)	0.000	1.0	0.031(2)
Bi2	0.241(2)	0.237(1)	0.1053(1)	1.0	0.010(1)
Bi3	0.238(2)	0.263(1)	0.2179(1)	1.0	0.034(1)
Ti/Ga/Fe1	0.293(4)	0.215(3)	0.4491(2)	0.75/0.20/0.05	0.005
Ti/Ga/Fe2	0.206(4)	0.262(4)	0.3444(2)	0.75/0.20/0.05	0.005
O1	0.336	0.177	0.500	1.0	0.025
O2	0.607	0.546	0.052	1.0	0.025
O3	0.325	0.306	0.405	1.0	0.025
O4	0.533	0.485	0.138	1.0	0.025
O5	0.291	0.203	0.305	1.0	0.025
O6	0.505	0.489	0.251	1.0	0.025
O7	0.033	0.030	0.039	1.0	0.025
O8	0.083	0.032	0.147	1.0	0.025

Table F.13: Parameters from the structural refinement of $Bi_5Ti_3Fe_{0.5}Cr_{0.5}O_{15}$ against *in situ* angular-dispersive XRD data recorded at 891 °C.

Atom	*x*	*y*	*z*	Occupancy	U_{iso}
Bi1	0.000	0.000	0.000	1.0	0.075(3)
Bi2	0.000	0.000	0.1045(1)	1.0	0.078(2)
Bi3	0.000	0.000	0.2182(1)	1.0	0.052(2)
Ti/Cr/Fe1	0.000	0.000	0.4492(3)	0.75/0.125/0.125	0.025
Ti/Cr/Fe2	0.000	0.000	0.3450(3)	0.75/0.125/0.125	0.025
O1	0.000	0.000	0.500	1.0	0.025
O2	0.000	0.500	0.0457(6)	1.0	0.025
O3	0.000	0.000	0.4062(7)	1.0	0.025
O4	0.000	0.500	0.1401(7)	1.0	0.025
O5	0.000	0.000	0.3098(9)	1.0	0.025
O6	0.000	0.500	0.250	1.0	0.025

Table F.14: Parameters from the structural refinement of $Bi_5Ti_3Fe_{0.5}Cr_{0.5}O_{15}$ against *in situ* angular-dispersive XRD data recorded at 791 °C

Atom	*x*	*y*	*z*	Occupancy	U_{iso}
Bi1	0.000	0.000	0.000	1.0	0.076(3)
Bi2	0.000	0.000	0.1045(1)	1.0	0.077(2)
Bi3	0.000	0.000	0.2181(1)	1.0	0.066(2)
Ti/Cr/Fe1	0.000	0.000	0.451	0.75/0.125/0.125	0.025
Ti/Cr/Fe2	0.000	0.000	0.3467	0.75/0.125/0.125	0.025
O1	0.000	0.000	0.500	1.0	0.025
O2	0.000	0.500	0.0503	1.0	0.025
O3	0.000	0.000	0.4009	1.0	0.025
O4	0.000	0.500	0.1426	1.0	0.025
O5	0.000	0.000	0.3055	1.0	0.025
O6	0.000	0.500	0.250	1.0	0.025
Additional Phase:					
Na_2SO_4: space group $P6_3/mmc$, $a = b = 5.497(4)$ Å, $c = 7.74(1)$ Å; wt. frac. = 0.16(1)					

Table F.15: Parameters from the structural refinement of $Bi_5Ti_3Fe_{0.5}Cr_{0.5}O_{15}$ against *in situ* angular-dispersive XRD data recorded at 741 °C.

Atom	*x*	*y*	*z*	Occupancy	U_{iso}
Bi1	0.000	0.000	0.000	1.0	0.062(5)
Bi2	0.000	0.000	0.1052(2)	1.0	0.078(4)
Bi3	0.000	0.000	0.2184(1)	1.0	0.051(3)
Ti/Cr/Fe1	0.000	0.000	0.4509(8)	0.75/0.125/0.125	0.031(2)
Ti/Cr/Fe2	0.000	0.000	0.3451(7)	0.75/0.125/0.125	0.010(3)
O1	0.000	0.000	0.500	1.0	0.025
O2	0.000	0.500	0.055(1)	1.0	0.025
O3	0.000	0.000	0.414(1)	1.0	0.025
O4	0.000	0.500	0.144(1)	1.0	0.025
O5	0.000	0.000	0.303(2)	1.0	0.025
O6	0.000	0.500	0.250	1.0	0.025
Additional Phase:					
Na_2SO_4: space group $P6_3/mmc$, $a = b = 5.46$ Å, $c = 7.69$ Å; wt. frac. = 0.17(1)					

Table F.16: Parameters from the structural refinement of $Bi_5Ti_3Fe_{0.5}Cr_{0.5}O_{15}$ against *in situ* angular-dispersive XRD data recorded at 731 °C.

Atom	*x*	*y*	*z*	Occupancy	U_{iso}
Bi1	0.000	0.000	0.000	1.0	0.071(3)
Bi2	0.000	0.000	0.1045(1)	1.0	0.071(2)
Bi3	0.000	0.000	0.2185(1)	1.0	0.068(2)
Ti/Cr/Fe1	0.000	0.000	0.4508(3)	0.75/0.125/0.125	0.062(9)
Ti/Cr/Fe2	0.000	0.000	0.3463(3)	0.75/0.125/0.125	0.024(6)
O1	0.000	0.000	0.500	1.0	0.025
O2	0.000	0.500	0.051(1)	1.0	0.025
O3	0.000	0.000	0.406(1)	1.0	0.025
O4	0.000	0.500	0.1465(7)	1.0	0.025
O5	0.000	0.000	0.3106(9)	1.0	0.025
O6	0.000	0.500	0.250	1.0	0.025
Additional Phase:					
Na_2SO_4: space group $P6_3/mmc$, $a = b = 5.47$ Å, $c = 7.70$ Å; wt. frac. = 0.83					

Table F.17: Parameters from the structural refinement of $Bi_5Ti_3Fe_{0.5}Cr_{0.5}O_{15}$ against *in situ* angular-dispersive XRD data recorded at 722 °C.

Atom	***x***	***y***	***z***	**Occupancy**	**U_{iso}**
Bi1	0.000	0.000	0.000	1.0	0.077(3)
Bi2	0.000	0.000	0.1046(1)	1.0	0.074(2)
Bi3	0.000	0.000	0.2182(1)	1.0	0.066(2)
Ti/Cr/Fe1	0.000	0.000	0.4505(2)	0.75/0.125/0.125	0.037(7)
Ti/Cr/Fe2	0.000	0.000	0.3453(3)	0.75/0.125/0.125	0.025(6)
O1	0.000	0.000	0.5000	1.0	0.025
O2	0.000	0.500	0.0503	1.0	0.025
O3	0.000	0.000	0.4009	1.0	0.025
O4	0.000	0.500	0.1426	1.0	0.025
O5	0.000	0.000	0.3055	1.0	0.025
O6	0.000	0.500	0.2500	1.0	0.025
Additional Phase:					
Na_2SO_4: space group $P6_3/mmc$, $a = b = 5.46$ Å, $c = 7.68$ Å; wt. frac. = 0.82					

Table F.18: Parameters from the structural refinement of $Bi_5Ti_3Fe_{0.5}Cr_{0.5}O_{15}$ against *in situ* angular-dispersive XRD data recorded at 701 °C.

Atom	***x***	***y***	***z***	**Occupancy**	**U_{iso}**
Bi1	0.250	0.250	0.000	1.0	0.072(4)
Bi2	0.250	0.250	0.104	1.0	0.076(3)
Bi3	0.245(2)	0.2559(1)	0.2191(1)	1.0	0.066(2)
Ti/Cr/Fe1	0.314	0.189	0.454	0.75/0.125/0.125	0.05
Ti/Cr/Fe2	0.258	0.277	0.354	0.75/0.125/0.125	0.05
O1	0.336	0.177	0.500	1.0	0.025
O2	0.607	0.546	0.052	1.0	0.025
O3	0.325	0.306	0.405	1.0	0.025
O4	0.533	0.485	0.138	1.0	0.025
O5	0.291	0.203	0.305	1.0	0.025
O6	0.505	0.489	0.251	1.0	0.025
O7	0.033	0.030	0.039	1.0	0.025
O8	0.083	0.500	0.147	1.0	0.025
Additional Phase:					
Na_2SO_4: space group $P6_3/mmc$, $a = b = 5.45$ Å, $c = 7.64$ Å; wt. frac. = 0.23(1)					

Table F.19: Parameters from the structural refinement of $Bi_5Ti_3Fe_{0.5}Cr_{0.5}O_{15}$ against *in situ* angular-dispersive XRD data recorded at 691 °C.

Atom	***x***	***y***	***z***	**Occupancy**	**U_{iso}**
Bi1	0.258(4)	0.220(3)	0.000	1.0	0.025
Bi2	0.274(3)	0.225(2)	0.1045(1)	1.0	0.025
Bi3	0.230	0.268	0.219	1.0	0.025
Ti/Cr/Fe1	0.314	0.189	0.454	0.75/0.125/0.125	0.05
Ti/Cr/Fe2	0.258	0.277	0.354	0.75/0.125/0.125	0.05
O1	0.336	0.177	0.500	1.0	0.025
O2	0.607	0.546	0.052	1.0	0.025
O3	0.325	0.306	0.405	1.0	0.025
O4	0.533	0.485	0.138	1.0	0.025
O5	0.291	0.203	0.305	1.0	0.025
O6	0.505	0.489	0.251	1.0	0.025
O7	0.033	0.030	0.039	1.0	0.025
O8	0.083	0.500	0.147	1.0	0.025
Additional Phase:					
Na_2SO_4: space group $P6_3/mmc$, $a = b = 5.45$ Å, $c = 7.64$ Å; wt. frac. = 0.16					

Table F.20: Parameters from the structural refinement of $Bi_5Ti_3Fe_{0.5}Cr_{0.5}O_{15}$ against *in situ* angular-dispersive XRD data recorded at 663 °C.

Atom	***x***	***y***	***z***	**Occupancy**	**U_{iso}**
Bi1	0.250	0.249	0.000	1.0	0.067(4)
Bi2	0.238	0.245	0.105	1.0	0.070(3)
Bi3	0.230	0.268	0.219	1.0	0.056(3)
Ti/Cr/Fe1	0.314	0.189	0.454	0.75/0.125/0.125	0.05
Ti/Cr/Fe2	0.258	0.277	0.354	0.75/0.125/0.125	0.05
O1	0.336	0.177	0.500	1.0	0.025
O2	0.607	0.546	0.052	1.0	0.025
O3	0.325	0.306	0.405	1.0	0.025
O4	0.533	0.485	0.138	1.0	0.025
O5	0.291	0.203	0.305	1.0	0.025
O6	0.505	0.489	0.251	1.0	0.025
O7	0.033	0.030	0.039	1.0	0.025
O8	0.083	0.500	0.147	1.0	0.025
Additional Phase:					
Na_2SO_4: space group $P6_3/mmc$, $a = b = 5.46$ Å, $c = 7.64$ Å; wt. frac. = 0.20(1)					

Table F.21: Parameters from the structural refinement of $Bi_5Ti_3Fe_{0.5}Cr_{0.5}O_{15}$ against *in situ* angular-dispersive XRD data recorded at 618 °C.

Atom	***x***	***y***	***z***	**Occupancy**	**U_{iso}**
Bi1	0.270	0.225	0.000	1.0	0.025
Bi2	0.292(5)	0.219(2)	0.1042(1)	1.0	0.025
Bi3	0.282(6)	0.260(2)	0.2188(1)	1.0	0.025
Ti/Cr/Fe1	0.314	0.189	0.454	0.75/0.125/0.125	0.05
Ti/Cr/Fe2	0.258	0.277	0.354	0.75/0.125/0.125	0.05
O1	0.336	0.177	0.500	1.0	0.025
O2	0.607	0.546	0.052	1.0	0.025
O3	0.325	0.306	0.405	1.0	0.025
O4	0.533	0.485	0.138	1.0	0.025
O5	0.291	0.203	0.305	1.0	0.025
O6	0.505	0.489	0.251	1.0	0.025
O7	0.033	0.030	0.039	1.0	0.025
O8	0.083	0.500	0.147	1.0	0.025
Additional Phase:					
Na_2SO_4: space group $P6_3/mmc$, $a = b = 5.45$ Å, $c = 7.64$ Å; wt. frac. = 0.28(2)					

Table F.22: Parameters from the structural refinement of $(H_2NMe_2)_2[Co_3(BDC)_4]\cdot y$DMF against *in situ* angular-dispersive XRD data. Refinements with data obtained at 180 °C, 200 °C, 225 °C, and 250 °C were undertaken using the monoclinic structure model proposed by Luo *et al.* and identical atomic parameters were used for all analyses.

Atom	***x***	***y***	***z***	$\mathbf{U_{iso}}$
Co1	0.1537	0.7057	-0.0009	0.025
Co2	0.250	0.750	0.00	0.0100
O1	0.1593	0.813	0.056	0.0250
O2	0.22832	0.81720	0.09541	0.0250
O3	0.15451	1.20900	0.40077	0.0250
O4	0.21438	1.12370	0.43602	0.0250
O5	0.18273	0.48240	0.09223	0.1198
O6	0.20271	0.58700	-0.00831	0.8000
O7	0.10020	0.64630	0.02276	0.0365
O8	0.1272	0.626	-0.232	0.8000
O9	0.08691	0.30980	0.12524	0.8000
O10	-0.00790	-0.12000	0.20710	0.0181
N1	0.09519	0.16080	0.03154	0.8000
N2	0.12346	0.53030	0.19238	0.0188
H21	0.14200	0.55850	0.16120	0.0250
H22	0.10890	0.46480	0.16930	0.8000
N3	0.00	0.09860	0.250	0.5486
C1	0.19393	0.85190	0.11410	0.0990
C2	0.19190	0.93000	0.18481	0.0250
C3	0.22421	0.92870	0.23523	0.0250
H3A	0.24740	0.88110	0.22470	0.0250
C4	0.22218	0.99750	0.30103	0.0250
H4A	0.24390	0.99560	0.33480	0.5640
C5	0.18799	1.06950	0.31715	0.0250
C6	0.15603	1.07350	0.26598	0.0250
H6A	0.13330	1.12380	0.27580	0.0250
C7	0.15779	1.00300	0.20050	0.0250
H7A	0.13600	1.00450	0.16690	0.0250
C8	0.18592	1.14000	0.38981	0.0250
C9	0.20279	0.48490	0.03677	0.0250
C10	0.22782	0.36460	0.01801	0.0250
C11	0.22977	0.25280	0.06499	0.0250
H11A	0.21620	0.25440	0.10850	0.0250
C12	0.24809	0.36090	-0.04721	0.0250
H12A	0.24680	0.43500	-0.07900	0.0250
C13	0.08395	0.55780	-0.02111	0.0250
C14	0.04054	0.52770	-0.01009	0.0250
C15	0.01927	0.59990	0.04095	0.0250
H15A	0.03210	0.66760	0.06890	0.0250
C16	0.02085	0.42800	-0.05065	0.0250

Atom	***x***	***y***	***z***	$\mathbf{U_{iso}}$
H16A	0.03470	0.37870	-0.08510	0.0250
C17	0.10664	0.26020	0.07620	0.0250
H17A	0.13200	0.29640	0.07010	0.0250
C18	0.12108	0.11010	-0.02480	0.0250
H18B	0.12120	0.01150	-0.02350	0.0250
H18A	0.14830	0.14120	-0.01400	0.0250
C19	0.10769	0.15670	-0.10040	0.0250
H19C	0.12560	0.12130	-0.13570	0.0250
H19B	0.10790	0.25430	-0.10220	0.0250
H19A	0.08100	0.12420	-0.11180	0.0250
C20	0.05464	0.10340	0.03560	0.0250
H20B	0.03820	0.16570	0.06270	0.0250
H20A	0.04280	0.09550	-0.01380	0.0250
C21	0.05402	-0.03000	0.07100	0.0250
H21C	0.02690	-0.06190	0.07210	0.0250
H21B	0.06510	-0.02270	0.12040	0.0250
H21A	0.06970	-0.09290	0.04390	0.0250
C22	0.09643	0.64660	0.20700	0.0250
H22B	0.08880	0.69130	0.16100	0.0250
H22A	0.11060	0.71210	0.23830	0.0250
C23	0.05929	0.59990	0.24360	0.0250
H23C	0.04260	0.67700	0.25310	0.0250
H23B	0.06680	0.55560	0.28920	0.0250
H23A	0.04480	0.53730	0.21200	0.0250
C24	0.14467	0.46900	0.25800	0.0250
H24B	0.12490	0.44210	0.29290	0.0250
H24A	0.15850	0.38750	0.24290	0.0250
C25	0.17423	0.56160	0.29550	0.0250
H25C	0.18660	0.51630	0.33740	0.0250
H25B	0.16080	0.64210	0.31140	0.0250
H25A	0.19440	0.58630	0.26200	0.0250
C26	0.01460	-0.02910	0.22760	0.0250
C27	-0.03597	0.16570	0.23140	0.0250
H27B	-0.03870	0.24250	0.26430	0.0250
H27A	-0.05810	0.10410	0.23920	0.0250
C28	-0.03910	0.21610	0.15350	0.0250
H28C	-0.06420	0.26240	0.14510	0.0250
H28B	-0.03770	0.14040	0.12040	0.0250
H28A	-0.01750	0.27780	0.14530	0.0250

Table F.23: Parameters from the structural refinement of Co(DMF)(NDC) against *in situ* angular-dispersive XRD data recorded at 200 °C.

Atom	***x***	***y***	***z***	$\mathbf{U_{iso}}$
Co1	0.500	0.500	0.500	0.025
O1	0.429	0.627	0.386	0.025
O2	0.442	0.648	0.082	0.025
O3	0.500	0.636	0.750	0.025
C1	0.412	0.654	0.216	0.025
C2	0.350	0.700	0.165	0.025
C3	0.319	0.764	0.300	0.025
C4	0.262	0.809	0.253	0.025
C5	0.234	0.784	0.068	0.025
C6	0.176	0.824	0.015	0.025
C7	0.478	0.767	0.741	0.025
C8	0.570	0.897	0.778	0.025
C9	0.477	1.038	0.733	0.025
N1	0.507	0.893	0.741	0.025
H1	0.336	0.777	0.425	0.025
H2	0.242	0.856	0.342	0.025
H3	0.155	0.867	0.101	0.025
H4	0.438	0.775	0.727	0.025
H5	0.500	1.124	0.750	0.025
H6	0.455	1.051	0.833	0.025
H7	0.455	1.048	0.617	0.025
H8	0.584	0.794	0.786	0.025
H9	0.582	0.949	0.891	0.025
H10	0.584	0.947	0.676	0.025

Appendix G

ODISC User Guide

Before use, please refer to the following publication for background information on the function of this equipment:
The Oxford Diamond *In Situ* Cell (ODISC) for Studying Chemical Reactions using Time-Resolved X-ray Diffraction, S. J. Moorhouse *et al.* Rev. Sci. Instrum.

The following is meant as a general guide for use, and does not delve into details of the construction and applications of ODISC.

General Points:

- **The cell should not be left unattended whilst in use.**
- The water and air supplies should be switched off when the cell is unattended.
- When operating in remote mode, the remote shut-off button should be located within reaching distance of the user at all times.
- When connecting cables at the outset, the 32 A power supply to the controller should be connected last. It should also be the first to be removed when disconnecting the equipment.

PID Parameters:

The Eurotherm controller has been programmed to maximise the efficiency and accuracy of heating for each of the different sample configurations. Below is a table of optimum PID parameters that have been obtained by tuning the controller in each configuration:

Parameter	Proportional	Integral	Derivative	Max. Output
Low-Temperature	20	360	60	8%
High-Temperature	47.6	34	6	80 %
Hydrothermal	142.2	70	12	9.5%
Culture Tube	86.2	50	8	15%

NB. The hydrothermal PID parameters detailed above are only applicable when the thermocouple between the autoclave and sheath is driving the heating, not the thermocouple situated inside the autoclave.

Furnace Base-plate:

- Once the base-plate has been secured to the sample stage, the stirrer insert can be positioned when required. The L-shaped steel plate should be placed in alignment with the base-plate to provide an even surface for the stirrer to stand upon.
- The stirrer insert should be located with the front facing away from the support bracket to allow access to the speed dial. It can only be positioned in the base of the cell by opening the chamber doors and sliding the head into the centre of the lower void.
- For safety reasons, when the stirrer insert is not in use, two ceramic bricks should be positioned in the space between furnace and stage to provide protection should any material drop from the cell. This is particularly important when the high-temperature configuration is in use.
- It is advisable at the beginning of a session to ensure the stirrer attachment is working effectively by setting up the appropriate configuration with just the stirrer bar in place. Adjust the insert accordingly before adding the sample.

Loading a Sample:

- Firstly, with the furnace secured in position on the stage, ensure the stirrer head is located centrally in the base by closing the furnace and looking down through the top. Adjust as necessary.
- Now reopen the furnace and abide by the following instructions depending on the set-up:

Low temperature configuration

- Place the mounting disk on the lower support and the centring tube on the upper support.
- With the chamber still open, gently lower the glassy carbon tube through the centring tube at the top, and ensure the bottom rests centrally in the recess of the mounting disk. Use ceramic spacers as required.
- Close the chamber shutter and secure the latch. NB. it may help to lift the latch as you close the chamber halves together.
- Lower the thermocouple into the glassy carbon tube and secure using the ‘nick’ at the top of the centring tube

High temperature configuration

- Place the mounting disk on the lower support and the centring tube on the upper support.
- Position the 0.5 mm thermocouple into the silicon carbide tube and lower in the alumina crucible, ensuring the thermocouple remains between the two.
- With the chamber still open, gently lower the silicon carbide tube through the centring tube at the top, and ensure the bottom rests centrally in the recess of the mounting disk. Use ceramic spacers as required.

- Close the chamber shutter and secure the latch. NB. it may help to lift the latch as you close the chamber halves together.
- Position the 1.5 mm thermocouple in contact with the sample located in the alumina crucible. Secure both thermocouples using the 'nick' at the top of the centring tube.

Hydrothermal configuration

- Place the mounting disk on the lower support.
- Centre the glassy carbon sheath on the mounting disc and lower the autoclave into the sheath.
- Clamp the manifold and autoclave attachments in position above the cell.
- With the chamber still open, position the 0.5 mm thermocouple between the sheath and autoclave and clip into position at the top of the cell.
- Now put the centring plates into position on the upper support, ensuring both the thermocouple and autoclave shaft are centred.
- Close the chamber shutter and secure the latch. NB. it may help to lift the latch as you close the chamber halves together.

Culture tube configuration

- Place the mounting disk on the lower support.
- Centre the glassy carbon sheath on the mounting disc.
- Position the thermocouple inside the culture tube and lower into the sheath.
- If required, position secondary 0.5mm thermocouple between sheath and tube and clip into position at the top of the cell.
- Now put the centring plates into position on the upper support, ensuring both thermocouples are centred.
- Close the chamber shutter and secure the latch. NB. it may help to lift the latch as you close the chamber halves together.
- Ensure the tube is centred in the furnace using the observation window.

WARNING: WHEN OPERATING INSIDE THE CHAMBER, WEAR NITRILE GLOVES AND AVOID CONTACT WITH THE HALOGEN LAMPS (PARTICULARLY THE LAMP LOCATED IMMEDIATELY ON THE RIGHT SIDE AS YOU OPEN THE CHAMBER)

Controller Set-up:

- Once the sample is appropriately set up in the furnace, connection to the controller must be configured.
- All interlocks must be primed in order to achieve communication between the controller and furnace, and this is indicated by the six orange LEDs on the front panel. Only when all six are lit can the "Heater On" switch be pressed.

  - Connect the black chamber shutter cables.
  - Ensure water flow and water temperature values are sensible and the cables are connected to the cooler.
  - Check that air is flowing at an acceptable rate to the furnace lamps.
  - Ensure that the emergency shut off switch on the front of the controller is not pressed down.
  - Ensure that the remote shut off button is not pressed down.
- For any interlocks that are not required (for instance, no air cooling available at F3, HASYLAB) ensure that the corresponding override DIN plug is secured in the back of the controller.

- **BEFORE CONTINUING, CHECK THAT ALL THERMOCOUPLES ARE CONNECTED TO THE CONTROLLER AND ARE SECURE IN POSITION INSIDE THE CELL.**
- Flick the yellow switch over to "Remote Mode", and press the green "Heater On" button.

Removing a Sample:

- The first thing a user should do upon entering the hutch is to ensure the green "Heater" LED on the front of the controller is off. This can be achieved by pressing the emergency stop button on the top of the device, but it is safer just to disconnect the chamber shutter cable, thus opening the interlock circuit.
- The thermocouples can then be removed from the sample environment.
  WARNING: NEVER REMOVE THE THERMOCOUPLE BEFORE DISCONNECTING THE CONTROLLER.
- Depending on the set-up (generally for low temperature and high temperature configurations which have tubes protruding from the top), it is usually best to remove the sample vessel carefully before opening the furnace.
- The chamber shutter door can now be opened. The best way to do this is to open the latch slowly, and then lift the latch to gently open the furnace.
  WARNING: WHEN OPENING THE CHAMBER, ALWAYS HOLD ONTO THE CENTRING TUBE AT THE TOP TO PREVENT IT FROM FALLING.
- Keep an eye on the mounting disk at the bottom of the furnace to ensure it is resting safely on the lower support. Also check the water and air connectors are positioned securely as you open the furnace.
- Now remove the sample vessel (together with the centring plates)

WARNING: WHEN OPERATING INSIDE THE CHAMBER, WEAR NITRILE GLOVES AND AVOID CONTACT WITH THE HALOGEN LAMPS (PARTICULARLY THE LAMP LOCATED IMMEDIATELY ON THE RIGHT AS YOU OPEN THE CHAMBER)